Identification of Offshore Wind Turbine Foundation Properties from Monitoring Data



Emily F. Anderson

Somerville College

University of Oxford

A thesis submitted for the degree of

Doctor of Philosophy

Hilary 2022

Identification of Offshore Wind Turbine Foundation Properties from Monitoring Data

Emily F. Anderson

Somerville College, University of Oxford

A thesis submitted for the degree of Doctor of Philosophy

Hilary 2022

There is a consistent discrepancy between the predicted and measured dynamic responses of in-situ offshore wind turbine (OWT) structures. Underestimation of the foundation soil stiffness is thought to contribute significantly to this difference. Identification of the in-situ foundation properties of OWT from monitoring data would reduce this uncertainty, providing critical feedback to foundation design methods and aiding lifetime reassessment. However, OWT are complex systems that present many challenges from a system identification and optimisation point of view. This is a result of OWT being operational, non-proportionally damped, quasi-axisymmetric systems with multiple flexible bodies.

In this study, a system identification framework for estimating the in-situ foundation stiffness of an OWT is presented using a model updating approach applied to simulated data. The results are shown to accurately replicate the behaviour of the true foundation. For the identification of a coupled springs macro-element foundation model, the compliance terms are found to be better parameters for optimisation and assessment, compared to the stiffness terms.

Through this application, this work demonstrates the challenges introduced by the OWT system complexities, and presents mitigation strategies or alternative techniques compared to the standard approaches used in OWT analysis.

Changes to the dynamic response due to the time dependent varying azimuth angle during idling conditions are explored. The effect is found to be very small in modes that are sensitive to the foundation stiffness, but significant for the mode shapes of some blade-dominant modes.

The non-proportional nature of the aerodynamic damping is shown to result in damped mode shapes whose real parts do not correspond to the undamped mode shapes. A normalisation technique is applied that obtains a close approximation of the undamped mode shapes from the complex damped mode shapes. It is demonstrated that large errors are introduced in the identified foundation behaviour if proportional damping is assumed.

The quasi-axisymmetric nature of an OWT is shown to produce close modes

that are challenging to identify. Use of mode shape correlation criteria shows that despite poor identification of some of the mode shapes, qualified using the MAC, the mode shape subspaces spanned by the close mode pairs, qualified using the S2MAC, are identified successfully. The errors in the identified foundation behaviour are consistently improved with the employment of the S2MAC, when close modes have inhibited the mode shape identification.

Investigations into the matching of identified and numerical model modes for comparison in the model updating method demonstrates that using the MAC to perform this matching can lead to inaccuracies in the updated foundation parameters. The coupled nature of the multiple-flexible-bodied OWT model results in modes with different sensitivities to the foundation parameters, which causes veering and crossing of the frequencies, and large changes in the mode shapes, as these parameters are varied.

In successfully estimating the properties of two foundation models from simulated data, and tackling various complications that arise in the process, this work provides the first steps into a new area of research on the identification of OWT foundation properties from monitoring data.

Acknowledgements

Firstly, I would like to thank my supervisors Ross McAdam and Manolis Chatzis. Without their valuable advice and consistent guidance, this thesis would not have been possible. Their patience and enthusiasm throughout was greatly appreciated.

My experience in Oxford was so enriched by my involvement in the REMS program. It afforded countless opportunities for additional learning and skill development and I loved being part of a cohort of such lovely, interesting people. The same appreciation goes to the Civil Engineering Group. There was always something going on, from the thought-provoking seminars, to the lunchtime tuppaware chats, to the Friday pub sessions.

Across the Jenkin Building and three houses on Cardigan Street, Hurst Street and Marlborough Road, I can't believe my luck in meeting such fun, inspiring and supportive people who have become lifelong friends. Thank you to the great friends I made in my 'home away from home': the climbing gym. They were always on hand to provide a welcome distraction. To all my amazing friends, old and new, I am so grateful for the encouragement and continued friendship.

Last but not least, thank you to my family for their unwavering support.

Contents

1 Introduction **12**

1.1 Context and motivation . . . 13
1.2 Methods and tools . . . 16
1.2.1 Modelling . . . 16
1.2.2 System identification . . . 19
1.3 Relevant system complexities . . . 24
1.3.1 Operational systems . . . 24
1.3.2 Quasi-axisymmetric systems . . . 26
1.3.3 Multiple-flexible-bodied systems . . . 28
1.3.4 Non-proportionally damped systems . . . 30
1.4 Thesis structure . . . 32
1.4.1 Overview . . . 32
1.4.2 Chapter summary . . . 33

2 OWT dynamic behaviour **35**

2.1 Introduction . . . 36
2.2 Modelling . . . 36
2.2.1 Foundation models . . . 36
2.2.2 FAST . . . 38
2.2.3 NREL 5MW sub-models . . . 47
2.3 Modal properties of the NREL 5MW . . . 48
2.3.1 Effect of rotor characteristics . . . 49
2.3.2 Effect of locking the rotor . . . 56
2.3.3 Effect of soil stiffness . . . 60
2.3.4 Effect of inclusion of damping . . . 62
2.4 Summary . . . 65

3 Implications of non-proportional damping **67**

3.1 Introduction . . . 68

3.2 Methodology . . . 69
3.2.1 Model . . . 69
3.2.2 Calculation of modal parameters . . . 75
3.2.3 Non-proportional damping . . . 77
3.2.4 Model linearisation and modal parameters . . . 80
3.2.5 Identification of modal parameters . . . 81
3.2.6 Model updating . . . 83
3.3 Exploring modal behaviour . . . 85
3.3.1 Investigation of non-proportional damping and complex normalisation . . . 86
3.3.2 Identification of modal parameters . . . 90
3.4 Application to model updating . . . 96
3.4.1 Foundation identification: case 1 . . . 97
3.4.2 Foundation identification: all cases . . . 104
3.5 Summary . . . 111

4 Effects of idling data and close modes 113
4.1 Introduction . . . 114
4.2 Methodology . . . 115
4.2.1 Model . . . 115
4.2.2 Calculation of modal parameters . . . 117
4.2.3 Identification of modal parameters . . . 117
4.2.4 Mode shape normalisation and comparison . . . 118
4.2.5 Model updating . . . 121
4.3 Exploring modal behaviour . . . 122
4.3.1 Sensitivity to foundation stiffness . . . 122
4.3.2 Effect of idling rotor . . . 126
4.4 Application to model updating . . . 131
4.4.1 Identification of modal parameters . . . 131
4.4.2 Close mode characterisation . . . 138
4.4.3 Identification of foundation properties . . . 143
4.5 Summary . . . 150

5 Mode veering and crossing during optimisation 152
5.1 Introduction . . . 153
5.2 Methodology . . . 156
5.2.1 Wind turbine model . . . 156
5.2.2 Calculation of modal parameters . . . 157

5.2.3 Mode shape normalisation and comparison 159
5.2.4 Nelson's method 161
5.2.5 Model updating 164
5.3 Exploring mode crossing behaviour 166
5.3.1 Demonstrating mode crossing behaviour of an OWT system . 166
5.3.2 Exploring mode crossing behaviour of a 2DOF system 172
5.3.3 Exploring mode crossing behaviour of an OWT system 181
5.3.4 Discussion 183
5.4 Application to model updating 184
5.4.1 Mode matching 185
5.4.2 Foundation identification: one parameter 191
5.4.3 Foundation identification: three parameters 196
5.5 Summary 199

6 Conclusions **201**
6.1 Introduction 202
6.2 Key contributions 202
6.3 Key recommendations 206
6.4 Future work 207
6.5 Summary 210

References **211**

A Mode shape DOF contributions for Chapter 2 **223**

Nomenclature

Common abbreviations

CS Coupled Springs

DOF Degree(s) of Freedom

DS Depthwise-varying Springs

EMA Experimental Modal Analysis

FA Fore-Aft

FB Flexible Blade (sub-model)

FE Finite Element

MAC Modal Assurance Criterion

MSL Mean Sea Level

N4SID Numerical Algorithms for Subspace State Space System Identification

NREL National Renewable Energy Laboratory

OMA Operational Modal Analysis

OWT Offshore Wind Turbine(s)

PSD Power Spectral Density

RB Rigid Blade (sub-model)

RNA Rotor Nacelle Assembly

S2MAC Subspace of Order 2 Modal Assurance Criterion

SHM Structural Health Monitoring

SS Side-to-Side

SSI-cov/ref Reference-based Covariance Driven Stochastic Subspace Identification Method

Greek alphabet variables

$\boldsymbol{\chi}$ Vector of parameters to be tuned through model updating

$\boldsymbol{\phi}, \boldsymbol{\phi}_u, \boldsymbol{\phi}_d, \boldsymbol{\phi}_R, \boldsymbol{\phi}_L$ Second order system eigenvector/mode shape (Generic, undamped, damped, right, left)

$\boldsymbol{\psi}, \boldsymbol{\psi}_R, \boldsymbol{\psi}_L$ First order system eigenvector/mode shape (Generic, right, left)

$\boldsymbol{\alpha}$ Acceleration data

$\bar{\boldsymbol{\phi}}^C, \bar{\boldsymbol{\phi}}^R$ Complex normalised or real normalised mode shape

$\boldsymbol{\epsilon}_F, \boldsymbol{\epsilon}_C, \boldsymbol{\epsilon}_K, \epsilon_{fi}$ Percentage errors: foundation terms, foundation compliance terms, foundation stiffness terms, modal frequencies

$\boldsymbol{\phi}^{AZ}$ Azimuth-averaged mode shape

γ Real positive linear scaling factor

λ System eigenvalue

ν_G Ground-level lateral monopile displacement

$\nu_{G,i}$ Ground-level lateral displacement of i^{th} mode shape

ω_u, ω_c Circular natural frequency (undamped, damped)

σ Standard deviation

θ_G Ground-level lateral monopile rotation

$\theta_{G,i}$ Ground-level lateral rotation of i^{th} mode shape

φ Tower sub-structure mode shape

${}^s\boldsymbol{\phi}$ Sensor-based mode shape

η Percentage noise level

ζ Modal damping ratio

Latin alphabet variables

$\widetilde{\boldsymbol{A}}_C$ Identified continuous system state matrix

$\widetilde{\boldsymbol{A}}_D$ Identified discrete system state matrix

$\boldsymbol{A}$ System state matrix

$\boldsymbol{B}$ System input matrix

$\boldsymbol{C}_F, \boldsymbol{C}_{CS}$ Coupled springs foundation model compliance matrix

$\boldsymbol{D}$ System damping matrix

$\boldsymbol{E}$ System output matrix

$\boldsymbol{F}$ System feedthrough matrix

$\boldsymbol{G}, \boldsymbol{H}, \boldsymbol{L}, \boldsymbol{N}, \boldsymbol{Q}, p$ Intermediate matrices and scalars for Nelson's method equations

$\boldsymbol{K}$ System stiffness matrix

$\boldsymbol{K}_F, \boldsymbol{K}_{CS}$ Coupled springs foundation model stiffness matrix

$\boldsymbol{M}$ System mass matrix

$\boldsymbol{q}$ System degrees of freedom vector

$\boldsymbol{u}$ System force input vector

$\boldsymbol{v}$ Measurement noise vector

$\boldsymbol{w}$ Process noise vector

$\boldsymbol{x}$ System state vector

$\boldsymbol{y}$ System output vector

$\boldsymbol{y}_k$ Vector of simulated output data

az Azimuth angle

c_{11}, c_{12}, c_{22} Coupled springs foundation model spring compliances (lateral, cross-coupling, rotational)

c_{DS} Depthwise springs foundation model base compliance

DR Direction ratio

F, F^* Generalised forces (active, inertia)

f, f_u, f_c Modal natural frequency (Generic, undamped, damped)

h Load eccentricity: ratio of moment load to horizontal load

I Inertia

i Vibration mode index

J Model updating objective function

k_H, k_M Uncoupled springs foundation model spring stiffnesses (lateral, rotational)

k_{11}, k_{12}, k_{22} Coupled springs foundation model spring stiffnesses (lateral, cross-coupling, rotational)

k_α Stiffness component of 2DOF analytical system

k_{DS} Depthwise springs foundation model base stiffness

s Sensor

t Time

$W_{F,i}, W_{M,i}, W_{S,i}$ Boolean weights for objective function components for the i^{th} mode (Frequency, MAC, S2MAC)

H_G Ground-level applied lateral load

m Total number of identified modes

M_G Ground-level applied moment

N Total number of data points

n Total number of system degrees of freedom

p Total number of azimuth increments

Common subscripts, superscripts and diacritics

$\bar{X}$ Normalised value of X

$\dot{X}$ Time derivative of X

$X(\gamma)$ Value of X when evaluated at γ

$X, \widetilde{X}$ Model vs identified variant of X

X_0 Baseline value of X

X_c, X_d Damped variant of X

X_i X corresponding to vibration mode, i

X_k X at time steps k

X_u Undamped variant of X

X_{CS}, X_{DS} X corresponding to the CS and DS foundation models

X^* Complex conjugate of X

$X^\dagger$ Altered version of X

X^T Nonconjugate transpose of X

Chapter 1

Introduction

1.1 Context and motivation

The demand to decrease global carbon emissions and reliance on fossil fuels has led to the development of a wide range of renewable energy sectors in recent years. Among these, one of the largest and fastest growing is the wind industry which provides 51% of global renewable electricity generation (16% if hydropower and nuclear are included) (BP, 2021). Though only 4.8% of global installed wind capacity is offshore, this value is growing quickly with offshore capacity increasing by 24% a year on average (2016 to 2020) compared to 11% for onshore wind (GWEC, 2021). Offshore wind turbines (OWT) generally see less opposition from the public and have access to more consistent winds, therefore providing higher yield and availability.

81% of European OWT are supported by a monopile foundation (Wind Europe, 2021). This is due to their relatively simple and inexpensive design as well as the availability of design guidance and an existing supply chain, when compared to other foundation options. Monopiles are now being built in deeper water and supporting larger turbines than previously thought feasible, which is leading to new challenges.

As the wind energy industry increases in maturity, so too does the incentive to understand the behaviour and condition of the in-situ structures (Antoniadou, Dervilis, Papatheou, Maguire, & Worden, 2015). This can be done through a process called structural health monitoring (SHM) (Farrar & Worden, 2012), which involves processing and analysing data, acquired over time from sensors placed on the structure, to glean important information about the evolving state of the structure. This information can enhance the operation and maintenance management of the in-situ structures (e.g. Avendaño-Valencia, Abdallah, & Chatzi, 2021; Weijtjens, Iliopoulos, Helsen, & Devriendt, 2015), and provide insight on the design of new structures. The sensors used are wide ranging, measuring a variety of aspects from structural vibrations and strains, to temperature fluctuations and corrosion level.

A common process undertaken as part of SHM is the determination of the modal properties of the structure, e.g. natural frequencies and mode shapes, from mea-

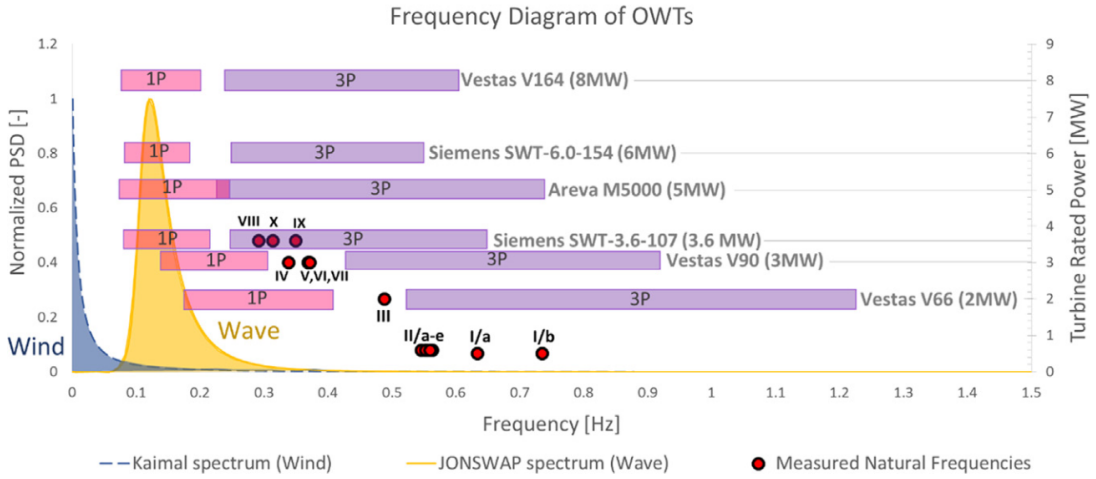


Figure 1.1: Typical wind and wave spectra, rotational speed (1P) and blade passing (3P) frequency bands for six commercial turbines with various measured 1st natural frequencies (Arany et al., 2016).

sured vibration data (Reynders, 2012). A mathematical model of the dynamic system is first identified using system identification techniques, from which the modal properties are then computed using modal analysis. OWT are inherently complex mechanical structures, and as such can cause problems for many of the classical system identification methods. Complexities arise from the fact that OWT systems are operational, quasi-axisymmetric, consist of multiple flexible bodies and are non-proportionally damped. These complexities are described in more detail in Section 1.3.

The 1st natural frequency of an OWT is typically designed to sit in the 'soft-stiff' region between the rotor forcing frequencies: the rotational frequency (1P) and the frequency at which a blade passes the tower (3P) causing a shadow effect (Arany, Bhattacharya, Macdonald, & Hogan, 2016), as shown in Figure 1.1. Also shown are typical wind and wave frequency distributions. Since the 1st natural frequency lies between the forcing frequencies, accurate prediction of an OWT's dynamic properties is paramount. Furthermore, larger turbines have a lower rotational frequency so the trend of increasing turbine size is causing the soft-stiff region to move closer to the wind and wave frequencies. Inaccurate prediction of the 1st natural frequency

could cause it to coincide with a forcing frequency, causing dynamic amplification of deflections, thus increasing fatigue damage and reducing the lifetime of the structure (Bhattacharya, 2014). Estimates of the 1st natural frequency of installed OWT from monitoring data are consistently around 5% higher than the designed natural frequency, and in some cases up to 20% higher (Kallehave, LeBlanc Thilsted, & Troya, 2015). It is hypothesised that this discrepancy could be as a result of underestimation of the soil stiffness (W. G. Versteijlen, Metrikine, & Van Dalen, 2016).

There are inherent uncertainties relating to the foundation behaviour of OWT. Sources of this uncertainty are; conservatism in design (Kallehave, Byrne, Thilsted, & Mikkelsen, 2015), the natural variability of the soil properties, typical site investigation inconsistencies (Nadim, 2015), and difficulties in soil-structure interaction modelling (Doherty & Gavin, 2012). This has an impact on the development of accurate design models and therefore on the nature of the installed structures, including the dynamic behaviour. Furthermore, OWT are typically designed for a 20 to 25 year lifetime and are expected to experience in the order of 10^7 load cycles in this time (Leblanc, Houlsby, & Byrne, 2010). This cyclic loading can cause changes in the stiffness and damping of the soil surrounding the foundation, thereby changing the foundation behaviour over time.

Employing SHM techniques to identify the in-situ foundation stiffness of OWT from monitoring data would reduce the uncertainty in the foundation behaviour, providing critical feedback to foundation design methods and aiding lifetime reassessment. It could also facilitate remote detection of foundation damage, for example scour. This would have positive economical and safety implications since inspection of offshore foundations is notoriously expensive and difficult. The acquired knowledge of the foundation state would allow better planning of maintenance and inspection schedules. On a larger scale, the aggregation of information from multiple OWT over time could provide useful insight for those developing improved design

methods.

In addition, valuable insight would be provided from investigation into the implications of the OWT system complexities on the identification and optimisation of their properties from monitoring data. As well as being valuable to those working in the field of wind turbine SHM, there would likely be transferable knowledge to any systems exhibiting these types of complexities, elaborated upon in Section 1.3.

1.2 Methods and tools

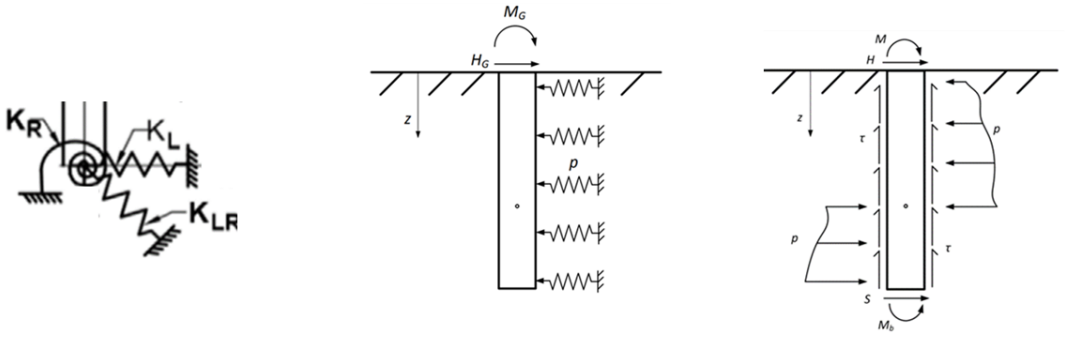
1.2.1 Modelling

OWT are tightly coupled structures operating under complex environmental conditions, thus they must be modelled via so-called integrated analyses (Ashuri, Zaaijer, Martins, Van Bussel, & Van Kuik, 2014). This consists of modelling the dynamic response of all parts of the structure under combined aerodynamic and hydrodynamic loading. Various options exist for modelling OWT. Possible approaches include finite element (FE) (Reddy, 2019) or flexible multi-body dynamics (Bauchau, 2011) formulations. Numerous existing open-source or proprietary software are available, e.g. FAST (NREL, 2022), HAWC2 (DTU, 2022) and Bladed (DNV, 2022), to name a few. These software, among others, are verified and compared in the Offshore Code Comparison Collaboration study (J. Jonkman & Musial, 2010). FAST is used to model the OWT in this thesis. The justification of this choice and more details on the FAST software are given in Section 2.2.2.

As the main application in this thesis aims to estimate the properties of an OWT monopile foundation model, it is important to mention the state of the art of such modelling. Full 3D FE analysis (e.g. Zdravković et al., 2015) of the soil-structure interaction can be performed, but this is computationally intensive, so simplified models are often used that typically represent this interaction with a set of springs.

A macro-element model can be used, where the monopile is represented by a set

of lateral, rotational and optional cross-coupling springs at the mudline level (Arany et al., 2016), as shown in Figure 1.2a. Another option is a depthwise-varying springs approach, often called distributed springs, where the pile is treated as a beam supported by uncoupled lateral springs distributed with depth. In both approaches the springs can be linear or nonlinear. Until recently, the design codes (API, 2010; DNV GL, 2016) recommended following a distributed springs approach, known as the '$p - y$' method (Figure 1.2b). This method consists of independent nonlinear springs distributed with depth that define the relationship between the local lateral resistance, p, and the local lateral displacement, y. The method was initially designed in the mid-20th century using field tests on long slender piles (e.g. Reese & Matlock, 1956) and in recent years its applicability to monopiles, which have a much smaller length to diameter ratio, has been questioned (Byrne et al., 2017). This led to the development of a new method as part of the PISA project, shown in Figure 1.2c. The PISA method involves defining a set of distributed load-displacement, $p - y$, relationships as before plus a set of moment-rotation relationships that represent the effect of shear tractions, τ, on the pile wall due to local pile rotation (Byrne et al., 2017). In addition, the method includes load-displacement and moment-rotation curves at the base of the monopile to account for the horizontal base force, S, and moment, M_b. The REDWIN project developed a sophisticated macro-element model



(a) Macro-element approach, from Arany et al. (2016).

(b) p-y approach, from Byrne et al. (2017).

(c) PISA approach, from Byrne et al. (2015)

Figure 1.2: Diagrams representing simplified approaches to monopile foundation modelling.

that requires the specification of at least one load-displacement response curve (Skau et al., 2018). The REDWIN model is designed to accept curves generated through a number of constitutive models, offering significant flexibility.

The estimation of foundation properties from monitoring data intrinsically requires that the dynamic response of the OWT be sufficiently sensitive to the properties of the foundation. Various studies have shown that this is indeed the case. Mayall et al. (2018) investigated the effect of scour on the structural dynamics of OWT by conducting scale experiments in the Fast Flow Facility at HR Wallingford. The natural frequency of the first three modes was estimated at various local scour depths, and all were found to reduce as the local scour depth increases, with the largest impact on the 2nd mode, then the 3rd mode and the lowest impact on the 1st mode. Damgaard, Ibsen, Andersen, and Andersen (2013) conclude that seabed sediment transportation could be the reason for the time-dependent modal parameters of OWT observed across 1500 rotor-stop tests at four wind farms. Exploring this idea through a numerical study, they found that both backfilling and scour development affect the 1st natural frequency and modal damping ratio. Zaaijer (2006) modelled an OWT, with a coupled springs foundation model, to investigate the sensitivity of the 1st and 2nd natural frequencies to soil parameters. The study found a 4% sensitivity to $\pm$10% variation in the soil friction angle and a 6% decrease due to a local scour hole of twice the pile diameter. Lombardi, Bhattacharya, and Muir Wood (2013) conducted cyclic loading experiments on a scale monopile in Kaolin clay and observed a substantial decrease in the 1st natural frequency and increase in damping over 32,400 load cycles due to soil softening. In summary, there is general agreement in published literature that changes in foundation stiffness have a significant impact on an OWT's dynamic response.

1.2.2 System identification

System identification is the process of predicting the mathematical model of a system that connects the inputs to the outputs (Ljung, 1987). When applied to structures, the measured outputs are commonly the accelerations and strains of the structure. The inputs are typically the loads applied, however these are difficult to measure, therefore so-called output-only methods, which assume that the unmeasured inputs follow a convenient statistical distribution, are often used (Reynders, 2012).

System identification methods have been widely applied to wind turbine structures over a number of decades (James, Carne, & Lauffer, 1995) using dynamic data obtained from the structure with sensors, e.g. accelerometers. These applications cover a wide range of aims including the determination of modal properties, i.e. natural frequencies, mode shapes and damping (Devriendt, Jordaens, De Sitter, & Guillaume, 2013; Van der Valk & Ogno, 2014), as well as state estimation that can be used for the purpose of fatigue estimation (Tatsis, Chatzi, & Lourens, 2017).

Modal identification

The original and simplest system identification methods typically come under the headings of experimental modal analysis (EMA) and operational modal analysis (OMA) (Brincker & Kirkegaard, 2010). For EMA, the structure is excited by measured forces induced by a shaker or an impact force, e.g. a hammer. The modal parameters are extracted from the dynamic response using methods such as peak picking, circle fitting and frequency domain decomposition (Brincker, Zhang, & Andersen, 2001). It is very difficult to apply a controlled force of sufficient magnitude to an OWT. The closest equivalent to an impact test is a rotor stop test (e.g. W. Versteijlen, Metrikine, Hoving, Smid, & De Vries, 2011), where the rotor is suddenly stopped after rotating at high speed. These can be successful, however the input forces from wind and waves are not accounted for.

OMA involves extracting the modal parameters from the dynamic response to

operational loading alone, making use of only the measured outputs (output-only). This is used when the operational loading cannot be neglected or it is not possible to excite the structure artificially. The input is typically assumed to be a stationary white noise random excitation, i.e. have broadband frequency spectra. This assumption is reasonable to a certain extent for OWT when the rotor is parked, i.e. the rotor is restricted from rotating. However, it is not applicable to operating OWT since the driving forces of the wind, waves and rotor all introduce 'coloured' noise at particular frequencies. The effect of driving forces on identification has been illustrated for bridges by P. Brewick and Smyth (2015) and is likely of similar or greater importance for OWT. The reader is referred to Zhang, Brincker, and Andersen (2009) for an overview of different OMA techniques. One of the first examples of output-only modal analysis on wind turbines can be found in James et al. (1995) and there are many recent works (e.g. Oliveira, Magalhaes, Cunha, & Caetano, 2018; Weijtjens, Verbelen, De Sitter, & Devriendt, 2016).

One sub-group of OMA methods is subspace identification methods (Shokravi et al., 2020). 'Subspace' refers to the fact that the models are obtained from the row and column spaces of specific matrices generated with the data (Van Overschee & De Moor, 1996). Typically, these methods identify the components of the general linear dynamic system model in state-space form. No assumptions are made on the underlying structure of the state-space matrices. State-space form allows n^{th} order systems to be represented as 1^{st} order differential equations. Two such subspace methods that have been widely used and proven to be robust, N4SID (Van Overschee & De Moor, 1994) and SSI-cov/ref (Peeters & De Roeck, 1999), are employed in this thesis. More detail on state-space form and N4SID are given in Sections 3.2.2 and 3.2.5 respectively, and on SSI-cov/ref in Section 4.2.3.

Structural identification

The methods mentioned thus far are capable of identifying the modal properties of the structure. For example the subspace methods identify the system state matrix, from which an eigenanalysis extracts the eigenvalues and eigenvectors. The mathematical basis of the identified state matrix is not the same form as the physical basis of the structure it represents, but some arbitrary unknown transformation of it. It is, therefore, not possible to directly extract structural properties from the identified matrices. Current research is tackling this limitation, for example Chatzis, Chatzi, and Smyth (2015) developed an algorithm, termed T-SSID, that can transform the identified matrices into the correct physical form of the system. However, a minimum number of measurements at specific locations must be available.

A common approach to extend modal identification to the identification of structural properties is so-called model updating (Mottershead & Friswell, 1993). This involves optimising a vector of parameters, corresponding to unknown model structural properties, to minimise the difference between identified modal properties and the corresponding model predictions (M. Friswell & Mottershead, 1995). Implementations can be deterministic (using a frequentist approach) or stochastic (using a Bayesian approach) (Simoen, De Roeck, & Lombaert, 2015).

A frequentist approach means the measured data is used to estimate the value of the property directly and therefore the uncertainty can only be gleaned from how the property estimates vary over different datasets from the system. The opposite is a Bayesian approach, which gives a fundamental way of quantifying the uncertainties (Peterka, 1981). The unknowns and the measurements are characterised with probability distributions and used by a system model to calculate the probability distributions of the properties of interest. An example of a Bayesian model updating application by Argyris, Papadimitriou, Panetsos, and Tsopela (2020) uses the Markov Chain Monte Carlo method. A Bayesian method that does not first require the calculation of the system modal properties is the Kalman Filter (Kalman,

1960). The basic Kalman Filter is applicable to linear dynamic systems with known parameters and estimates the states only. Recent advances allow the estimation of more than just the states, such as joint state-parameter (Moireau, Chapelle, & Le Tallec, 2008), joint input-state (Lourens et al., 2012) and joint input-state-parameter (Naets, Croes, & Desmet, 2015) algorithms. These parameters could correspond to structural properties of the systems.

Structural identification of OWT foundations in the literature

W. G. Versteijlen et al. (2017) used a model updating technique to identify the foundation characteristics of a monopile, excited by a hydraulic shaker, prior to installation of the wind turbine. Fallais and Lourens (2016) applied a coupled input-state-parameter estimation method (Naets et al., 2015) to synthetic vibration data from a reduced-order model OWT support structure subject to wave loading. An equivalent hydrodynamic loading input and support structure stiffness parameter were simultaneously identified.

Various studies have conducted field experiments on OWT aiming to quantify the value of the soil damping. Typically rotor stop tests are performed to determine the overall OWT modal parameters, and then a combination of signal analysis and numerical computations are used to estimate how much each damping source: structural, hydrodynamic, aerodynamic and soil, contributes to the measured total modal damping. In terms of logarithmic decrement soil damping, Tarp-Johansen et al. (2009) estimate 3.5 – 5%, W. Versteijlen et al. (2011) estimate 9.5% and Damgaard et al. (2013) estimate 6%.

Structural identification has not been widely applied for the purpose of estimating the foundation properties of OWT, likely due to poor predictive modelling capabilities and a lack of benchmark data for validation. Foundation identification is an interesting area of research for many other structures, hence there is much to be learnt from investigation of such methods to other applications. A few examples

are given here.

Sunder and Sanni (1984) identified the foundation stiffness of an offshore platform using a model updating technique. The foundation was a caisson grouted to a deep pile. They used a 4^{th} order quasi-structural model (tuned to a more complex model) with linear horizontal, rotational and coupling springs at the mudline. Using accelerometer data from each of three decks and a fourth location near the water level, estimates of the spring stiffnesses were obtained.

Sanayei and Davis (2016) took measurements of the static response of a bridge column under traffic loading to determine the vertical, horizontal, rotational and coupling stiffnesses of the foundation. Strain, displacement and tilt gauges were placed in a particular layout allowing calculation of the linear variation of vertical force and moment. The system matrices are partitioned in such a way that the forces and displacements in the column can be used to determine the foundation stiffness matrix.

Palanisamy and Sim (2015) propose a scour monitoring method, through identification of the foundation stiffness reduction, using the Extended Kalman Filter (Mariani & Corigliano, 2005) algorithm (an extension to the Kalman Filter for non-linear systems). The method is shown to perform well on simulated data of a bridge pier generated with an FE model. Accelerations from two locations towards the top of the pier are processed by the Extended Kalman Filter algorithm which then estimates the stiffness of a number of distributed linear springs representing the foundation. Scour essentially removes the springs, so the scour depth is detected by how many springs are identified as having negligible stiffness.

There are additional complexities when identifying OWT, as will be discussed in Section 1.3, so the methods from other industries must be transferred with caution.

In summary, the OWT industry has seen significant research in applying EMA, e.g. rotor stop test, and OMA techniques to measured acceleration data. This allows estimation of natural frequencies, mode shapes and total system modal damping.

Regarding application to the foundation, most research has consisted of analysing the effect of different foundation conditions, e.g. scour or a stiffness change, on the OWT dynamic response through scaled model experiments or computational modelling. There is a gap in the literature for investigation of foundations through system identification applied to monitoring data of OWT structures.

1.3 Relevant system complexities

1.3.1 Operational systems

When compared to time-invariant structures, such as (non-moving) bridges or buildings, there are various inherent challenges that arise from the operational nature of OWT.

OWT have multiple operational modes depending on the wind speed magnitude. At very low wind speeds the OWT is idling, between cut-in and cut-out wind speeds it is operating, and above cut-out it is either idling or parked, depending on the conditions. When the OWT is idling it is not producing power but the rotor is free to rotate. Typically the blades are pitched to an angle that results in slow rotor rotation. OWT have a rated power, the maximum power they are designed to produce, that corresponds to a specific rated rotor speed. The rated wind speed is the lowest wind speed that can achieve the rated power output, with the blades pitched for maximum power output, i.e. pitched to the fine angle, typically defined as 0°. For the NREL 5MW reference turbine the cut-in and cut-out wind speeds are $3m/s$ and $25m/s$ respectively, and the rated wind speed, rotor speed and power are $11.4m/s$, $12.1rpm$ and 5MW respectively (J. Jonkman, Butterfield, Musial, & Scott, 2009).

Between the cut-in and the rated wind speeds, the operational mode is characterised by maximising power output, so the blade pitch is constant at 0° and the rotor speed is dependent on the wind speed. Between the rated wind speed and the

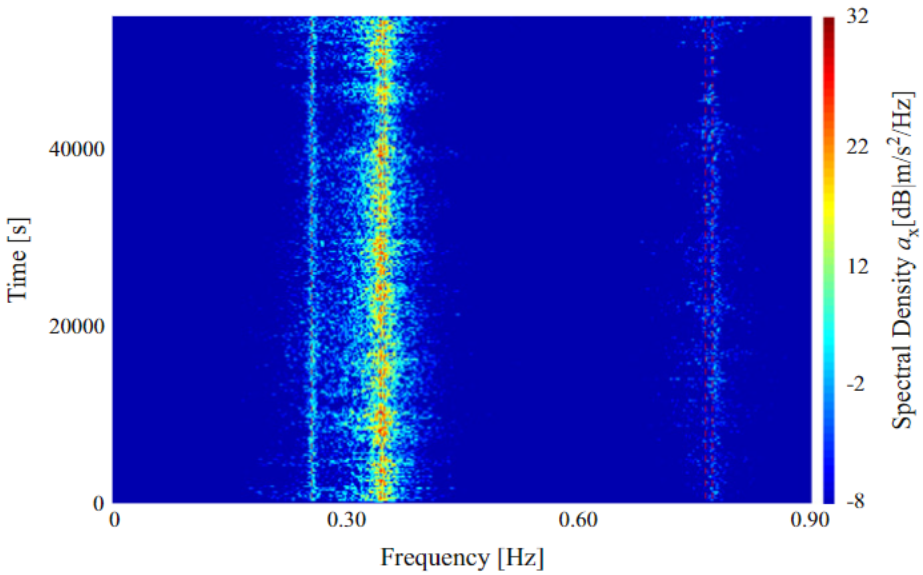


Figure 1.3: Spectrogram of side-to-side accelerations for an operating offshore wind turbine at Wind Park V. The rotational rotor frequency, 1P, the first damped eigenfrequency (~ 0.33Hz) and the blade passing frequency, 3P, are clearly represented in the plot (Damgaard et al., 2013).

cut-out wind speed, the operational mode is instead characterised by regulating the power output, i.e. limiting it to the maximum rated power, which is achieved by pitching the blades to ensure the rotor speed is constant at the rated rotor speed. Above the cut-out wind speed the brake can be applied to lock the rotor or the blades can be pitched to an angle that minimises the rotational speed to protect the OWT from damage.

Many system identification methods, e.g. OMA methods, work under the assumptions that the structural properties are time invariant and the excitation is of white noise nature. When an OWT is operating, the rotor rotation introduces significant time variance to the structure and harmonic components to the excitation, hence violating both of these assumptions (Tcherniak, Chauhan, & Hansen, 2011). Figure 1.3 shows the spectrogram of accelerometer data from an operating OWT (Damgaard et al., 2013), clearly displaying the 1P and 3P excitations introduced by the rotor rotation. The effect of coloured excitations in operational data of mechanical structures, and methods for their removal, are presented by Jacobsen, Anderson,

and Brincker (2007) and Peeters, Cornelis, Janssens, and Van der Auweraer (2007), and Manzato et al. (2014) investigate approaches for OWT. As the rotor is restricted from rotating when in parked conditions, these assumption violations are largely avoided, so monitoring data from such conditions are often favoured (e.g. Devriendt, Weijtjens, El-Kafafy, & De Sitter, 2014). However, parked conditions do not occur frequently in practice, so data from idling conditions are often used as these conditions are more prevalent (e.g. Devriendt, Magalhaes, et al., 2014; Van der Valk & Ogno, 2014) and the 1P and 3P excitations occur at very low frequencies. Though the rotor is rotating very slowly in idling conditions, this rotation does introduce variation of the structural geometry with time. This would clearly affect the rotor mode shapes as the blades are changing position, and may affect the tower portion of the mode shapes through coupling. This is investigated in Section 4.3.2.

1.3.2 Quasi-axisymmetric systems

Axisymmetric systems are those that display rotational symmetry about an axis, for example, a cylinder or a cone. Systems that are nearly axisymmetric, such as a wind turbine, are referred to in this thesis as quasi-axisymmetric systems. Such systems exhibit pairs of modes with closely spaced natural frequencies, herein referred to as close modes. The implications of close modes have been studied for various quasi-axisymmetric structures; for example, tall buildings (Au & Brownjohn, 2019), lighthouses (Brownjohn et al., 2018), and steel masts (Reynders, Pintelon, & De Roeck, 2008).

As close modes are characterised by their closely spaced frequencies, they inherently cause problems for system identification methods that operate in the frequency-domain, but their impact on time-domain methods is gaining prominence. Au, Li, and Brownjohn (2021) have developed the ‘uncertainty law’ for close modes which provides analytical expressions for the uncertainty and achievable precision of the identified properties of close modes, independent of the identification method em-

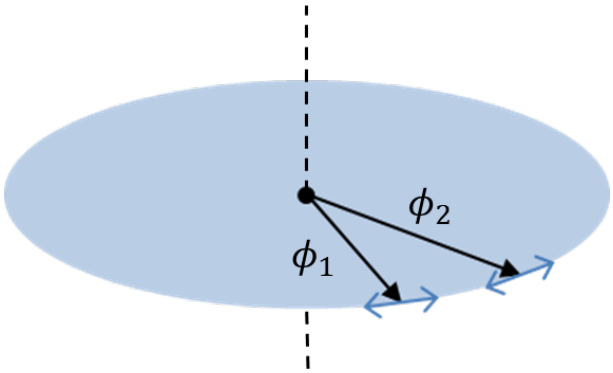


Figure 1.4: Mode shape subspace for close modes (adapted from Au and Brownjohn (2019)).

ployed.

For a perfectly axisymmetric structure, the eigenvalues are repeated and mode shapes cannot be determined uniquely (Wilkinson, 1965) but as existing within a subspace around the axis of symmetry (Brincker & Lopez-Aenlle, 2015), as depicted in Figure 1.4. Whilst for a quasi-axisymmetric structure the eigenvalues are unique and the mode shapes can be defined along orthogonal bases theoretically, in practice system identification methods can struggle to correctly identify the mode shapes of the close modes. Instead, the methods identify some vector within the subspace spanned by the theoretical mode shapes of the close mode pair. Typically, the result is identified mode shapes that resemble the theoretical mode shapes rotated by some arbitrary angle about the axis of symmetry.

In a quasi-axisymmetric structure with two orthogonal planes of vibration that are uncoupled, one would expect to detect mode shapes that lie entirely in each of those planes. However, the existence of close modes can lead to incorrectly identified mode shapes with components in both planes of vibration. This can have implications on the information inferred from these mode shapes. For example, in a model updating method the identified mode shapes are often compared to the model mode shapes by calculating the correlation between them using the Modal Assurance Criterion (MAC) (Allemang & Brown, 1982). The MAC would indicate a poor correlation between such mode shapes if they appear to vibrate in different

planes. As a result, D'Ambrogio and Fregolent (2003) developed an extension of the MAC, called the S2MAC (subspace of order 2 Modal Assurance Criterion), to provide additional insight in the case of repeated or close eigenvalues. The S2MAC provides a higher-order MAC that quantifies the correlation between an individual mode shape and the subspace spanned by a pair of mode shapes. For the relevant formulae see Section 4.2.4. In the model updating example given, this would be applied by comparing the identified mode shape (with incorrect vibration direction) to the subspace spanned by the corresponding pair of close modes from the model.

1.3.3 Multiple-flexible-bodied systems

OWT structures consist of multiple flexible bodies, e.g. the tower and blades. These individual elements have inherent modes of vibration when treated as individual systems. When the elements are combined into the full OWT structure, the modes of vibration of the individual elements couple together so that the full structure presents coupled vibration modes that contain contributions from multiple of these elements.

This poses a variety of challenges for both modelling and system identification. From the modelling point of view, this indicates that a full integrated analysis must be performed to get an accurate understanding of the dynamic behaviour, even if only one element is of interest, as they are not independent of one another. Furthermore, when updating or optimising the parameters of a model, it is common to track the model's vibration modes, and the coupled modes of the OWT model would all change to a different extent depending on their sensitivity to the varying parameter. Hence mode veering and/or mode crossing could occur. Mode veering is when the frequencies of the modes approach one another and then diverge (i.e. 'veer') away without crossing, in a particular region of the varying model parameter (Leissa, 1974). In contrast, mode crossing is when the frequencies of the modes approach and then cross one another, such that their rank, with respect to their

relative frequency magnitudes, swaps with one another. This may have significant implications on a model updating method, for example, in which the identified modal properties from sensor measurements must be matched with these model modal properties, that are varying (and perhaps crossing) as the model is updated.

Some applications may require the inclusion of a mode tracking technique. Eldred, Venkayya, and Anderson (1995) demonstrated two methods for tracking the vibration modes during the weight minimisation of a wing model: the higher order eigenpair perturbation algorithm (Eldred, Lerner, & Anderson, 1992) and the cross-orthogonality check method (Gibson, 1992). Nelson's method (Nelson, 1976) can be used to calculate the eigenvalue and eigenvector derivatives. The eigenderivative calculation for undamped systems was originally presented by Fox and Kapoor (1968), before Nelson (1976) presented a more widely applicable approach that only requires the eigenvector of interest, as opposed to the previous approach that required all eigenvectors. Adhikari (1999) extended the Fox and Kapoor method to non-proportionally damped systems, Lee, Kim, and Jung (1999) extended Nelson's method to self-adjoint damped systems and subsequently M. I. Friswell and Adhikari (2000) extended Nelson's method further to non-proportionally damped non-self-adjoint systems. The effect of mode veering/crossing and the associated need to track the modes as a parameter changes will be discussed further in Chapter 5.

Finally, sensors are typically located in the nacelle and sometimes on the tower, but rarely on the blades. Given that the modes all contain some contribution from both tower and blade bending, a large proportion of information is lost without blade sensors, potentially rendering some modes unidentifiable. In many cases this means that only a subset of the total modes of the structure (within a target frequency range) would be identified. This point is discussed further in Chapter 5.

1.3.4 Non-proportionally damped systems

When formulating the equations of motion for a system, typically the mass, stiffness and damping are all included, representing the damped system. Damping is notoriously difficult to accurately model (Rao, 2011) and is often subject to simplifications, for example being assumed to be proportional to the mass and stiffness. For a generalised form of proportional damping the reader is referred to Adhikari's works (e.g. Adhikari, 2000). In certain situations it can be useful to formulate the undamped system, represented by the mass and stiffness alone. Accurate modal identification of damping from monitoring data is highly challenging (P. T. Brewick & Smyth, 2013), so the comparison of identified modal properties with the corresponding model modal properties is one such situation where utilising the undamped system might be beneficial. However, to allow comparison with the undamped model, one must understand how the damping in the monitored structure would affect the identified modal properties and how the undamped modal properties could be extracted.

Firstly considering natural frequencies: the eigenvalues calculated from a damped system are complex-valued, whereas those from an undamped system are real-valued. Lallement and Inman (1995) showed that the natural frequencies calculated by taking the absolute values of the complex eigenvalues of the damped state-space system are not exactly equivalent to the natural frequencies calculated from the same system with no damping. In fact, the authors state that the assumption of their equivalence is a common misconception. Specifically, the authors show that these two sets of natural frequencies are not equal when the system is non-proportionally damped. Though they would be equivalent for a system with exact proportional damping, this is extremely unlikely in reality. Fortunately, the difference between the two sets of frequencies is typically small, and often considered negligible, although in some cases it is worth further consideration, especially for systems with considerable non-proportional damping.

Rayleigh (1877) showed that undamped modes satisfy an orthogonality condition

that allows the uncoupling of the equations of motion, such that multiple degree of freedom (DOF) systems can be considered as a collection of single DOF systems. If a system exhibits proportional damping then this convenient condition is preserved and the mode shapes from the undamped and damped systems would therefore be equal. Systems that are non-proportionally damped exhibit complex-valued mode shapes (Ibrahim, 1983). When the damping is nearly proportional, i.e. when the damping matrix is diagonally dominant (Woodhouse, 1998), the real part of the damped mode shapes give a good approximation of the real-valued undamped mode shapes. When the off-diagonal damping terms are comparable to the diagonal terms in magnitude then it is not diagonally dominant. In such a case the system is considered non-proportionally damped, and hence the damped mode shapes are not equivalent to the undamped mode shapes.

Various authors have developed methods to attempt to transform the complex-valued damped mode shapes to approximations of the real-valued undamped mode shapes. A sample of the methods are given here, and the reader is referred to the referenced works for more details. In 1980, Fillod (1980) presented the proof for a mode shape scaling method, later named by Sinha (2005) as the 'rescaling of complex modal vectors technique'. In 1983, Ibrahim (1983) presented two approaches titled 'using an oversized mathematical model' and 'using assumed modes'. In 1986, Wei, Allemang, and Brown (1986) presented a 'time domain subspace iteration method'. Fillod's method is applied in this thesis, as explained in Section 3.2.3.

Various works that utilise or present the identification of OWT mode shapes (e.g. Devriendt, Magalhaes, et al., 2014; Shirzadeh, Weijtjens, Guillaume, & Devriendt, 2015) do not explicitly mention what method is used to transform the complex-valued identified mode shapes to real-valued mode shapes. The assumption is therefore that either the absolute value of the complex values was taken, or the imaginary components were discarded. Ibrahim (1983) demonstrates that, for non-proportionally damped systems, the former option can introduce large errors in

subsequent calculations that utilise these mode shapes, and the implications of the latter option is investigated in Chapter 3 of this thesis.

1.4 Thesis structure

1.4.1 Overview

Sections 1.1 to 1.3 have motivated why foundation identification from monitoring data would be useful to the wind industry and why OWT present many complexities from a modelling and SHM point of view. This thesis will explore a variety of these complexities, within the context of using a model updating approach to estimate the foundation stiffness of a modelled OWT from simulated tower accelerometer data. The extension to real monitoring data will be discussed through the suggestions for future work.

Particular attention is given to the demonstration of the challenges introduced by the OWT complexities, and the presentation of mitigation strategies or alternative techniques compared to the standard approaches.

Through the OWT model updating application, this work provides insight for those wanting to:

- estimate foundation properties of a coupled springs model from monitoring data, of any structure
- perform modal identification of an OWT, either under parked or idling conditions
- perform modal identification of a non-proportionally damped system
- perform modal identification of a quasi-axisymmetric system
- conduct optimisation of a multiple-flexible-bodied system

The contents of Chapters 3, 4 and 5 are each in final preparations for submission as journal articles. A portion of the work from Chapter 4 was also published in a conference paper (Anderson, McAdam, & Chatzis, 2021). Finally, some collaborative work in the research group on field monitored data that uses findings from this thesis has recently been submitted as a journal article (McAdam, Chatzis, Kuleli, Anderson, & Byrne, 2022).

1.4.2 Chapter summary

Chapter 1 provides context and motivation for the identification of OWT foundation properties from monitoring data, and the exploration of the impact of OWT system complexities. The relevant literature is also summarised.

Chapter 2 investigates the dynamic behaviour of OWT as predicted by the aeroelastic simulation software FAST. The effect on the dynamic response is explored for a variety of aspects: the blade flexibility and pitch angle, locking the rotor vs leaving it free to rotate, the inclusion of damping and the soil stiffness. This work provides context on the general dynamic behaviour of OWT and further motivates the need to explore the impact of the system complexities on identification.

Chapter 3 addresses the complexity associated with non-proportional damping, through a model updating foundation identification application. The method estimates the stiffnesses of a linear coupled springs macro-element foundation model from simulated tower acceleration data of a simplified parked OWT model, via an output-only identification of the structure's modal properties. The source of the non-proportional damping, and the implications on the foundation identification of both ignoring it and acknowledging it are explored. In the latter case, an existing method is used to transform the affected damped mode shapes to undamped mode shapes. Insights on the feasibility and optimal form of the foundation identification are also presented.

Chapter 4 numerically analyses the effect of close modes and idling conditions

on the identification of OWT foundation properties, again using a model updating approach. This chapter applies the approach to simulated tower acceleration data from idling conditions of the full FAST OWT model, with two linear foundation representations. These are a coupled springs macro-element and a set of depthwise-varying springs. The impact on the identification of ignoring or acknowledging the close modes is explored, through the application of the MAC and S2MAC computations of mode shape correlation.

Chapter 5 investigates the mode veering and crossing that occur during foundation stiffness variation of the undamped and damped OWT models, as a result of the coupled nature of this multiple-flexible-bodied system. An analytical 2-degree-of-freedom system (2DOF) is used to explore when and why modes may or may not cross, and Nelson's method is applied to analytically track a consistent mode. The influence on the model updating process due to the mode veering and/or crossing, and the variation of the modal properties during optimisation, is investigated. Particular focus is given to the process, and impact on the optimisation, of matching the subset of identified modes with the corresponding numerical modes of the model. Again, the application in this chapter is the identification of a linear coupled springs macro-element foundation model.

Finally, **Chapter 6** summarises the key contributions and implications for the field that can be drawn from the work in this thesis. Possible extensions and ideas for future work, that have arisen from this research, are also suggested.

Chapter 2

OWT dynamic behaviour

2.1 Introduction

The aim of this chapter is to give detail on the OWT modelling that is used throughout this thesis, present the general dynamic behaviour of an OWT and demonstrate how these systems exhibit the complexities introduced in Section 1.3.

The effect on the OWT dynamic behaviour of various scenarios is explored through modelling: locking the rotor vs leaving it free to rotate; varying the blade pitch, the blade stiffness and the foundation stiffness; and calculating the undamped or damped properties. This work provides context and background understanding for the issues tackled in Chapters 3, 4 and 5.

2.2 Modelling

2.2.1 Foundation models

The soil-structure interaction of a monopile is typically modelled as a set of depthwise-varying or ground level statically equivalent coupled springs that provide reaction to the specified loading. In this study both forms of the foundation model are investigated, and are termed depthwise springs (DS) and coupled springs (CS) respectively.

The DS model consists of a set of depthwise-varying springs that govern the load-displacement response of the soil with depth. In this study, the soil stiffness is modelled as zero at the surface and linearly increasing with depth to a maximum value, k_{DS}, at the foot of the monopile, as shown in Figure 2.1. This relatively simple distribution of subgrade modulus represents a baseline case of homogeneous soil. The structural properties of the monopile are used both above and below the mudline to the penetration depth of 36m.

The CS model is a single macro-element model, where a set of statically equivalent linear lateral, rotational and cross-coupling springs at the mudline level are used to represent the embedded monopile, as shown in Figure 2.1. The structural

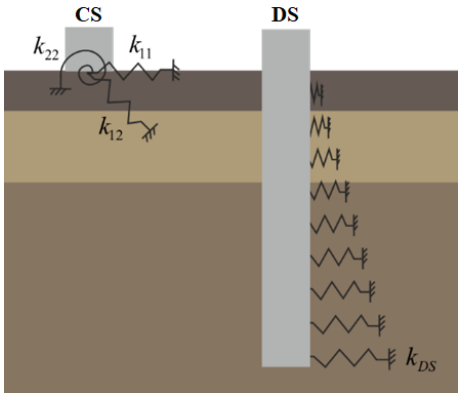


Figure 2.1: Offshore wind turbine model foundation representation. In the DS model the spring length is proportional to the stiffness.

properties of the monopile are only used above the mudline. The set of coupled springs are assembled into a foundation stiffness matrix, $\boldsymbol{K}_F$, that governs the load displacement response by:

$$\begin{Bmatrix} H_G \\ M_G \end{Bmatrix} = \boldsymbol{K}_F \cdot \begin{Bmatrix} \nu_G \\ \theta_G \end{Bmatrix} = \begin{bmatrix} k_{11} & k_{12} \\ k_{12} & k_{22} \end{bmatrix} \cdot \begin{Bmatrix} \nu_G \\ \theta_G \end{Bmatrix} \tag{2.1}$$

where H_G and M_G are ground-level applied lateral load and moment and ν_G and θ_G are ground-level lateral displacement and rotation respectively.

To ensure they are physically meaningful, the spring stiffnesses of the DS model must be positive and the $\boldsymbol{K}_F$ matrix of the CS model must have a positive determinant, hence positive eigenvalues.

All soil properties are assumed to be axisymmetric about the vertical axis. As a consequence, the stiffness matrix defined in Eq. 2.1 is applicable individually in the fore-aft (FA) and side-to-side (SS) planes of motion. The FA and SS directions are depicted in Figure 2.2. There is no coupling of the foundation stiffness matrix between the DOF belonging to the FA and SS planes. The model updating procedure used in this thesis aims to estimate the three parameters of the CS macro-element $\boldsymbol{K}_F$, and the DS model base stiffness, k_{DS}. The CS foundation model is used in all chapters of this thesis, while the DS model is only used in Chapter 4.

Soil damping has not been modelled in this thesis. Soil radiation damping is not considered as it is a phenomenon that occurs at higher frequencies than those of the loading and modes that dominate the behaviour of OWT (Carswell et al., 2015). The contribution from soil hysteric material damping, which would require nonlinear foundation modelling, is considered to be larger, but the contribution is predominantly dependent on the magnitude of the foundation displacements. Therefore, it would only provide a small contribution during idling conditions (modelled in Chapter 4), which consist of low winds and small displacements. Overall, it is not expected that the inclusion of soil damping in the OWT model would have a notable influence on the qualitative outcomes of this thesis.

2.2.2 FAST

The OWT simulation code to be used was chosen based on a comparison of the complexity, accuracy and adaptability of existing codes. In terms of the complexity, it was necessary to find a unified system model that integrates sophisticated models for each element of an OWT, i.e. the aero-elastic, hydrodynamic, structural and soil behaviour. The software must also include a sophisticated time integration technique to ensure accuracy. The final condition was that it must be possible to adapt the source code to meet the specific requirements necessary for this research, which was potentially the most restrictive, as most software is proprietary (e.g. HAWC, Bladed). The wind turbine simulation software FAST was determined to be the best fit for the criteria, specifically FAST v7 (J. Jonkman & Buhl, 2005) due to the versatility of the foundation modelling capability, available at the time of conducting this research. References to the FAST software hereafter will relate to FAST v7.

FAST is a dynamic time-domain tool that simulates horizontal axis wind turbines under hydro and aerodynamic loading. Written in Fortran, the tool has been developed by the United States Department of Energy's National Renewable En-

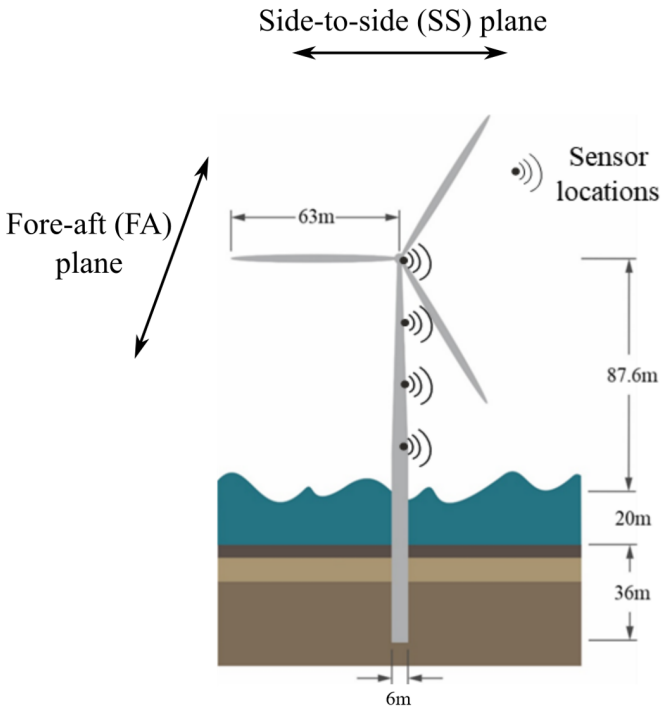


Figure 2.2: NREL 5MW offshore wind turbine model dimensions and indicative sensor locations.

ergy Laboratory (NREL). The model includes simulation of the support structure, tower, nacelle, rotor and the control and drive systems. In this thesis, the NREL 5MW reference turbine (J. Jonkman et al., 2009) is modelled. The NREL 5MW is a conventional three-bladed upwind, variable-speed, blade-pitch-to-feather-controlled turbine with dimensions as shown in Figure 2.2. This model is used in this thesis to generate simulated data, to calculate numerical model modal properties, and is also the model used in the model updating step.

Also shown in Figure 2.2 are the indicative sensor locations of the model set-up used in this thesis. The sensor set-up consists of four biaxial accelerometers, measuring in both the FA and SS directions. The sensors are placed at heights of 10, 35, 60 and 87m above the mean sea level (MSL), which is 20m above the seabed. Those virtually placed sensors in the model are used for simulating the tower accelerometer data and obtaining the mode shapes of the structure in the sensor basis.

FAST fundamentals

The core of the program is the multi-body and modal-dynamics formulation of the nonlinear equations of motion:

$$\boldsymbol{M}(\boldsymbol{q}, t)\ \ddot{\boldsymbol{q}} = -\boldsymbol{f}(\dot{\boldsymbol{q}}, \boldsymbol{q}, t) \tag{2.2}$$

using Kane's method (Kane & Levinson, 1985), where $\boldsymbol{q}$ is the vector of DOF of the system, $\boldsymbol{M}$ is the mass matrix and $\boldsymbol{f}$ is a vectoral function of $\dot{\boldsymbol{q}}$, $\boldsymbol{q}$ and t, time. The rigid bodies of the model are represented with translational and rotational DOF, while the DOF of the flexible bodies are characterised using a linear truncated modal representation. It should be noted that FAST is not based on a finite element formulation. The reader is referred to Shabana (2020) and Clough and Penzien (2003) for more information on multi-body dynamics and modal truncation respectively. The specific equations used in FAST can be found in the 'Unofficial FAST Theory Manual' which is discussed and can be requested through the referenced forum post (NREL, 2016).

The key to Kane's method is the determination of a set of generalised coordinates, q_j, corresponding to the DOF of the system, which are differentiated to give generalised velocities, $\dot{q}_j$, where j refers to a specific DOF. For each generalised coordinate, the generalised active forces, F_j, and inertia forces, F_j^*, are then calculated and summed as shown in Eqs. 2.3 and 2.4, where F is a force on the body, and m_k and r_k are the body mass and position vector respectively, for a specific body k of M total bodies.

$$F_j + F_j^* = 0 \tag{2.3}$$

where

$$F_j = \sum_{k=1}^{M} \frac{\partial v_k}{\partial \dot{q}_j} \cdot F, \quad F_j^* = \sum_{k=1}^{M} \frac{\partial v_k}{\partial \dot{q}_j} \cdot \left(-m_k \frac{dv_k}{dt} \right), \quad v_k = \frac{dr_k}{dt} \tag{2.4}$$

In FAST, first the generalised coordinates corresponding to the enabled DOF are set. The FAST DOF are discussed later in this section and diagrammatically represented in Figure 2.5 of Section 2.2.3. Then the kinematics are calculated and used along with the system properties, specified in input files, to construct the equations of motion (Eq. 2.2). Finally, the loads and motions are calculated by solving the equations of motion.

Time integration: To integrate the equations of motion over time, FAST uses a 4th order Runge-Kutta method for the first three time steps, then an Adams-Bashforth predictor and Adams-Moulton corrector integration scheme for the following time steps.

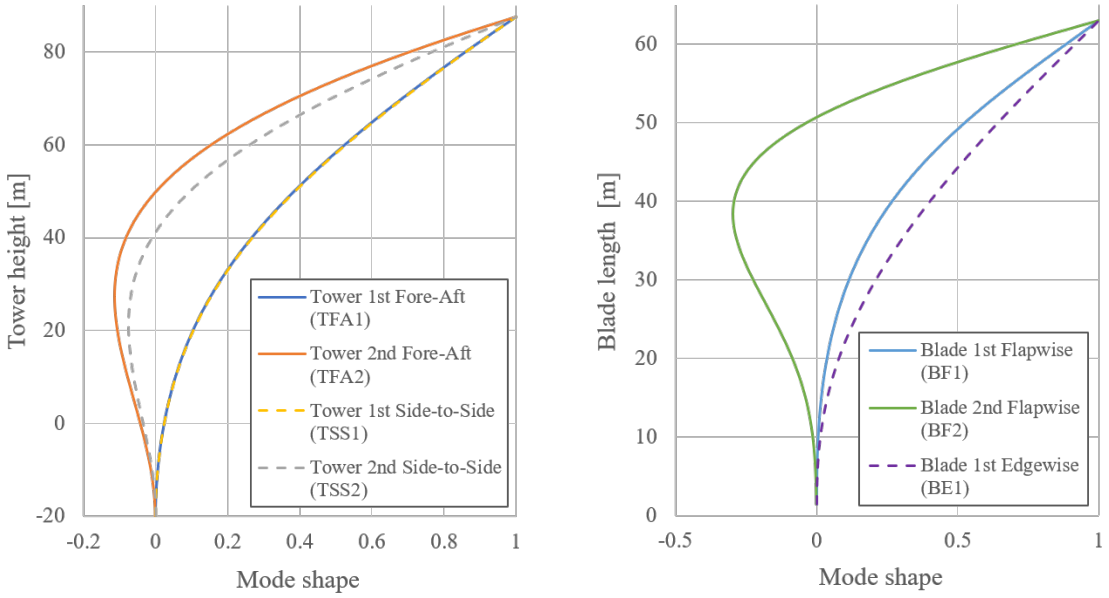
Aerodynamics: The forces are calculated using steady and/or unsteady blade element moment theory or the generalised dynamic wake model (J. Jonkman et al., 2008). Steady blade element moment theory is applied in this thesis. The wind data are generated using TurbSim, which is "a stochastic, full-field, turbulent-wind simulator" (B. J. Jonkman & Kilcher, 2012). A time-series of wind-speed vectors is produced. The blade geometry and airfoil data are provided by the user. Dynamic stall using the Beddoes-Leishman model (Leishman & Beddoes, 1989) may be included, but is not applied in this work.

Structural dynamics: The dynamics for the flexible components of the structure, the tower and blades, are modelled using a linear truncated modal representation of the sub-structures. The overall order of the wind turbine model is reduced as a consequence of this modal reduction approach. The tower is modelled as one sub-structure element with four DOF, associated with the first four tower mode shapes. These DOF are calculated using an existing in-house simplified FE model of the

wind turbine with Euler-Bernoulli elements for the tower, a rigid lumped mass representing the rotor nacelle assembly (RNA) and a coupled springs macro-element or depthwise-varying springs for the foundation. This FE model is discussed in more detail later in the section, in the discussion of alterations. Axial and torsional DOF are not modelled. The mode shapes of this simplified model, referred to herein as tower sub-structure mode shapes, are found through an eigenanalysis and are then truncated to retain the first four mode shapes; the 1$^{\text{st}}$ and 2$^{\text{nd}}$ in the FA direction, and the 1$^{\text{st}}$ and 2$^{\text{nd}}$ in the SS direction. The sub-structure mode shapes are each approximated by a 6$^{\text{th}}$ order polynomial function of the position along the tower from the ground level, or monopile toe depending on the foundation model used, towards the nacelle, with the 0$^{\text{th}}$ and 1$^{\text{st}}$ order terms set to zero. The sum of the polynomial coefficients must add to 1 to ensure the shape has a normalised deflection of 1 at the tower-top. The general shapes of the tower sub-structure mode shapes are given in Figure 2.3a. The corresponding DOF, q_{TFA1}, q_{TFA2}, q_{TSS1} and q_{TSS2} respectively, shown later in Figure 2.5a, are the variables that scale these sub-structure mode shapes over time.

The blades are modelled in a similar way; each blade is one sub-structure element with three DOF representing the blade dynamic bending shapes. Specifically these DOF correspond to two flapwise bending mode shapes, q_{BF1} and q_{BF2} and one edgewise, q_{BE1}, and they are found with a simplified FE model provided by NREL, called BModes (Bir, 2007). BModes models the blades with Euler-Bernoulli elements and a fixed boundary condition at the blade root. The general shapes of these blade sub-structure mode shapes are given in Figure 2.3b, and the DOF are shown diagrammatically later in Figure 2.5a.

There are four additional DOF that correspond to the translation and rotation of the structure's base with respect to the two horizontal axes. These are the surge, sway, pitch and roll DOF, denoted by q_{Sg}, q_{Sw}, q_P and q_R respectively. These are located at the mudline for the CS model and at the base of the monopile for the



(a) Tower sub-structure

(b) Blade sub-structure

Figure 2.3: Normalised mode shapes used in FAST for the tower (left) and blade (right) bending DOF.

DS model. Finally, there are two further DOF that represent the flexibility of the drivetrain and varying azimuth angle of the generator, q_{DrTr} and q_{GeAz} respectively, bringing the total number of DOF, hence number of structural modes, to 19. All of these DOF are shown later in Figure 2.5a of Section 2.2.3. A final DOF allowing the RNA to yaw (i.e. rotate about a vertical axis to face the wind) is also possible in FAST. This DOF is disabled in all simulations used in this thesis, meaning the yaw DOF is modelled as rigid and fixed at a particular orientation. FAST integrates the non-linear equations of motion, as shown in Eq. 2.2, to determine the realisations of the DOF, $\boldsymbol{q}$, (consisting of the translations, rotations and sub-structure mode shape scalars) over time.

Control: Dynamic link libraries provide blade pitch, rotor variable-speed and nacelle yaw control, although these capabilities are disabled in the simulations for this thesis as operational conditions are not analysed.

Hydrodynamics: FAST uses Morison's equation for the calculation of the hydrodynamic loads with viscous drag and inertia, added mass and relative kinematics

considered (J. Jonkman et al., 2008). It is also possible to model drag loads due to a current. The wave kinematics are represented using Airy linear wave theory and can be chosen to be regular (plane progressive) or irregular (JONSWAP/Pierson-Moskowitz). There is also the option of including wave stretching, which allows the extension of the Airy theory above the MSL. The hydrodynamics are first order. The water is modelled as flat, i.e. no waves, for all the analyses in this thesis.

Analysis: FAST has two analysis options: a time marching simulation and a linearisation. The former simulates the full behaviour of the OWT when subject to aerodynamic and hydrodynamic loads, and outputs loads and motions with time at any node in the structure.

The linearisation generates a linearised representation of the nonlinear OWT equations of motion at a specific realisation of the state vector. The state vector consists of the displacements and velocities of the DOF, known as the operating point. FAST computes the linear state matrices by numerically linearising the system by perturbing it about the operating point. If the rotor is rotating, then linearisation is performed at multiple rotor azimuth angles to form periodic matrices that are then averaged. The resulting linear representation allows the user to perform an eigenanalysis for determination of the modal properties. The corresponding equations for the linearisation process are presented in Section 3.2.4.

Alterations

A number of alterations were made to the FAST source code to enable the necessary functionality.

- For the linearisation analysis function, FAST currently allows the user to specify certain initial conditions, and choose whether the model is linearised about an operating point equal to those initial conditions or a steady state operating point that is calculated internally by running the FAST code starting with those initial conditions. Those initial conditions consist of only a subset of the

total DOF in the state vector. The author altered the source code so that the user can specify the operating point for the entire state vector.

- Also in the linearisation analysis, the author multiplied the perturbation used in the numerical linearisation calculation by a factor of 1×10^{-3}. This reduction was applied as the existing magnitude was found to be resulting in numerical inaccuracies for certain foundation realisations.

- The properties of the foundation models, e.g. stiffnesses, are embedded in the fortran source files, so altering them requires recompiling the source code. The author modified the source code so that these properties are defined in the input files, so that altering them no longer requires recompilation.

Requiring just alterations to the default inputs, as opposed to the source code, the modifications that resulted in stable linearisation and time marching functionality were:

- compilation in double precision (the FAST code is distributed with single precision as the default);

- reduction of the integration time step to 0.00125 seconds;

- alteration of the output precision to be of the format 'ES40.32E3' which corresponds to scientific form with 40 characters, 32 digits to the right of the decimal point and 3 digits in the exponent.

NREL provides a program called BModes (Bir, 2007), which can be used to perform the aforementioned eigenanalysis of a simplified wind turbine model that results in defining the properties of the tower sub-structure. However the output precision of the eigenanalysis conducted within BModes was found to be insufficient for this study. This was investigated by varying the foundation stiffness matrix,

$\boldsymbol{K}_F$, using a linear scaling factor:

$$\boldsymbol{K}_F = \gamma \boldsymbol{K}_{F0} \tag{2.5}$$

where $\boldsymbol{K}_{F0}$ is a baseline stiffness matrix and γ is a real positive number, and then calculating the tower sub-structure mode shapes, φ, for each case using BModes. For ease of presentation the mode shape contribution at mid-tower is taken for each case and normalised by dividing by the corresponding mid-tower contribution for the baseline foundation case as follows:

$$\bar{\varphi}_{i,\gamma}\left(mid\right) = \frac{\varphi_i\left(mid,\ \gamma \boldsymbol{K}_{F0}\right)}{\varphi_i\left(mid,\ \boldsymbol{K}_{F0}\right)} \tag{2.6}$$

where i denotes the vibration mode.

Figure 2.4 shows $\bar{\varphi}_{i,\gamma}\left(mid\right)$ against γ for modes 1 and 3, for a narrow range of γ values around 1. It can be seen that there is large variation in the BModes output, which is not expected for such small variations in the values of γ. This was verified to be due to numerical errors through comparison with other software. Such numerical errors provide sufficient variability in the subsequent predicted dynamic behaviour to

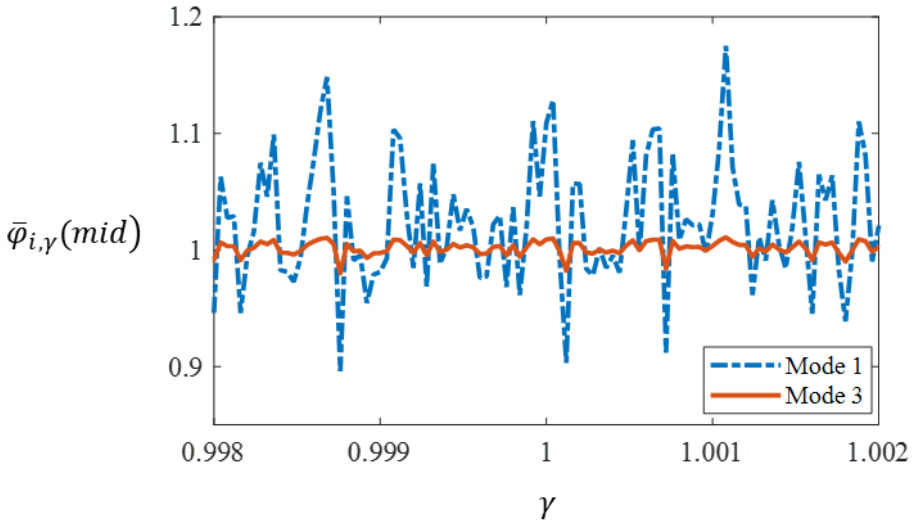


Figure 2.4: BModes normalised mid-tower mode shape contribution, $\bar{\varphi}_{i,\gamma}\left(mid\right)$, against foundation stiffness scaling factor, γ.

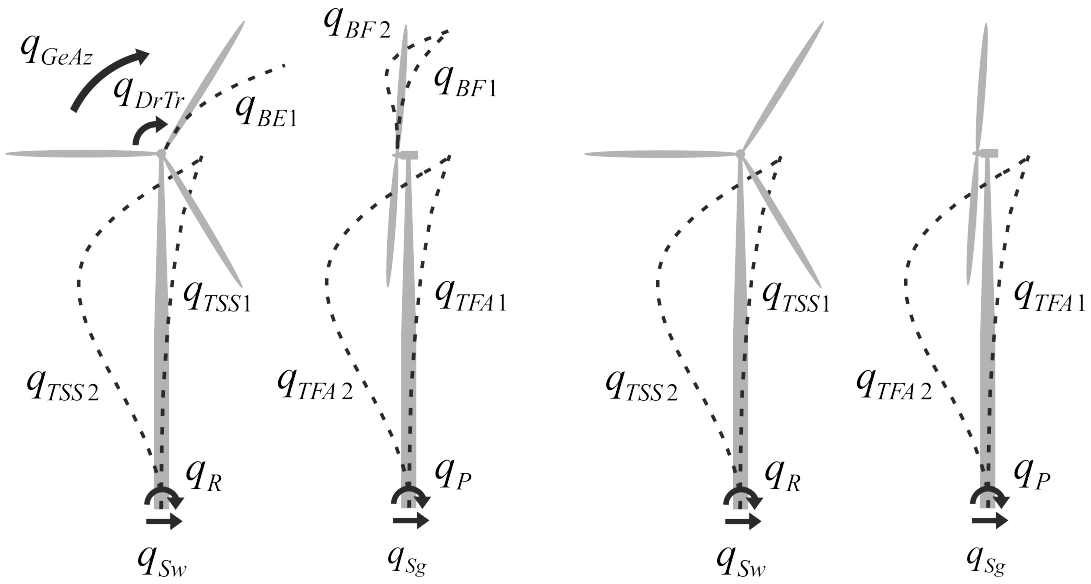
cause issues with the optimisation convergence during the model updating procedure applied in this thesis. An equivalent in-house Euler-Bernoulli FE program, from here-on called the Oxford 1D model, which does not suffer from the same inaccuracy with varied foundation stiffness, has therefore been used to generate these mode shapes in place of BModes.

2.2.3 NREL 5MW sub-models

Two sub-models of the NREL 5MW OWT are used throughout this thesis. The first includes all the DOF other than yaw, as discussed in Section 2.2.2 and shown in Figure 2.5a, and is termed **sub-model FB** (flexible blades). The model is set up to replicate the OWT under idling conditions, so the generator DOF, q_{GeAz}, is enabled to allow the rotor to rotate and the blades are pitched to 14°, resulting in an idling rotor speed of $3rpm$ subject to a wind speed of $3m/s$. Sub-model FB is used in this chapter and Chapters 4 and 5.

The second sub-model models the blades and the drivetrain as rigid, eliminating the coupling between the vibrational responses of the tower and the rotor blades and drivetrain. The generator DOF is also disabled which has the effect of restricting the rotor from rotating, simulating the wind turbine being parked. This sub-model is termed **sub-model RB** (rigid blades), and is depicted in Figure 2.5b. It is used in this chapter and Chapter 3.

In this chapter alone, to explore the effect on the dynamic response of locking the rotor vs leaving it free to rotate, the generator DOF is actually both enabled and disabled in turn, for both sub-models RB and FB. In subsequent chapters it is disabled for the RB model and enabled for the FB model as previously described. Additionally, the impacts of varying the blade pitch, the blade stiffness and the foundation stiffness on the dynamic behaviour of the OWT sub-model FB are explored. Finally, the effect of including or excluding the modelled damping matrix in the calculation of the modal properties is investigated.



(a) Sub-model FB (b) Sub-model RB

Figure 2.5: Sub-model degrees of freedom.

2.3 Modal properties of the NREL 5MW

The modal properties of the model are calculated through an eigenanlysis. A full description of this process with the relevant formulae is given in Section 3.2.2. In Sections 2.3.1 to 2.3.3, the modal properties are calculated without the inclusion of the damping, resulting in undamped frequencies and mode shapes. The inclusion of damping is explored in Section 2.3.4. In all sections of this chapter, the foundation is modelled with the coupled springs representation.

The number of modes that will be calculated from a model is equal to the number of DOF of the model. Only a subset of these modes are generally of interest, firstly because there is typically a frequency range of interest and sensors are often only placed on a subset of the structural components, but also because the characteristics of the specific modelling approach can result in some modes that are unlikely to be representative of the true modes of the real structure. For example, in FAST a number of non-physical modes with high frequencies are introduced through the process of modelling the tower sub-structure with modally reduced polynomial shape DOF for the flexible portion and rigid translational and rotational DOF of the base.

Overall, there are four modes of interest for sub-model RB and 13 modes of interest for sub-model FB of the NREL 5MW. The modes of each sub-model are sorted in order of increasing frequency and referred to as RB 1 to 4 and FB 1 to 13. The frequencies of these modes are typically in the range of $0 - 2.5$ Hz.

The full OWT model mode shapes are shown for various different scenarios in this section (e.g. Figure 2.7). The magnitude of the bending of the flexible sub-structure elements is exaggerated for ease of viewing (note that in some cases this scaling causes an apparent lengthening or shortening of the blade mode shapes, but this does not affect the key interpretations and should be ignored). The black dash-dot line shows the undeformed tower and rotor. Note that the undeformed rotor geometry is plotted at the deformed tower-top. The red solid line shows the deformed tower. When the relevant DOF are enabled, the yellow dash lines show the rotor deformed with q_{GeAz} only, and the blue dash lines show the rotor deformed with both q_{GeAz} and q_{DrTr}. The green solid lines show the rotor deformed with all DOF. These different rotor representations allow the reader to distinguish the varying contributions of each DOF. Appendix A also contains tables presenting the DOF contribution values for further detail if required.

The 'direction' of vibration of a mode is a term frequently used in this chapter and thesis and refers to the overall direction of the mode's vibration in the FA-SS plane, i.e. when observing the mode shape from a bird's eye view. If a mode shape is dominated by DOF that vibrate in the FA plane, then that mode is said to vibrate in the FA direction and referred to as a FA mode. The same logic applies for a SS mode.

2.3.1 Effect of rotor characteristics

In this section the undamped modal properties of the NREL 5MW are analysed for a variety of rotor characteristics, through modelling in FAST.

Blade and drivetrain flexibility

Firstly, the frequencies and mode shapes of both rigid blade, RB, and flexible blade, FB, sub-models are compared with the rotor free to rotate, to see the influence of modelling the rotor blade and drivetrain flexibility.

Figure 2.6 depicts the mode shapes of the OWT sub-model RB with the rotor free to rotate. The frequencies are given under the corresponding mode labels. The modes appear in the following order. The 1st mode exhibits the behaviour that one would expect from the 1st order mode of a beam (referred to as 1st order shape), in the FA plane. The 2nd mode is a 1st order shape SS mode. Then the 3rd and 4th modes correspond to 2nd order shape FA and SS modes respectively.

Figure 2.7 depicts the mode shapes of the OWT sub-model FB with the rotor free to rotate, and the blades pitched to 14°. Ten additional DOF are included in the FB sub-model, the nine blade bending DOF and the drivetrain torsion DOF, adding ten modes to the model, nine of which are considered here. The close proximity of

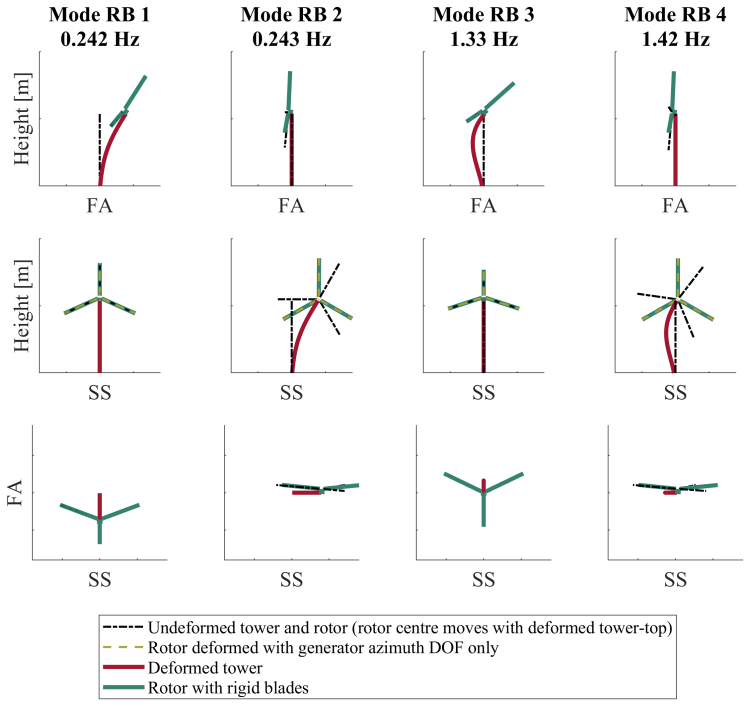


Figure 2.6: Mode shapes and frequencies of the undamped OWT sub-model RB (rigid blades) with rotor free to rotate.

the frequencies of vibration of the constituent OWT sub-structure elements results in modes that contain contributions from tower, drivetrain and blade bending DOF, referred to as DOF coupling. This is particularly pertinent for the 2nd order shape bending modes of the tower sub-structure, which have fundamental frequencies that sit between the fundamental frequencies of the blade sub-structure modes. This is

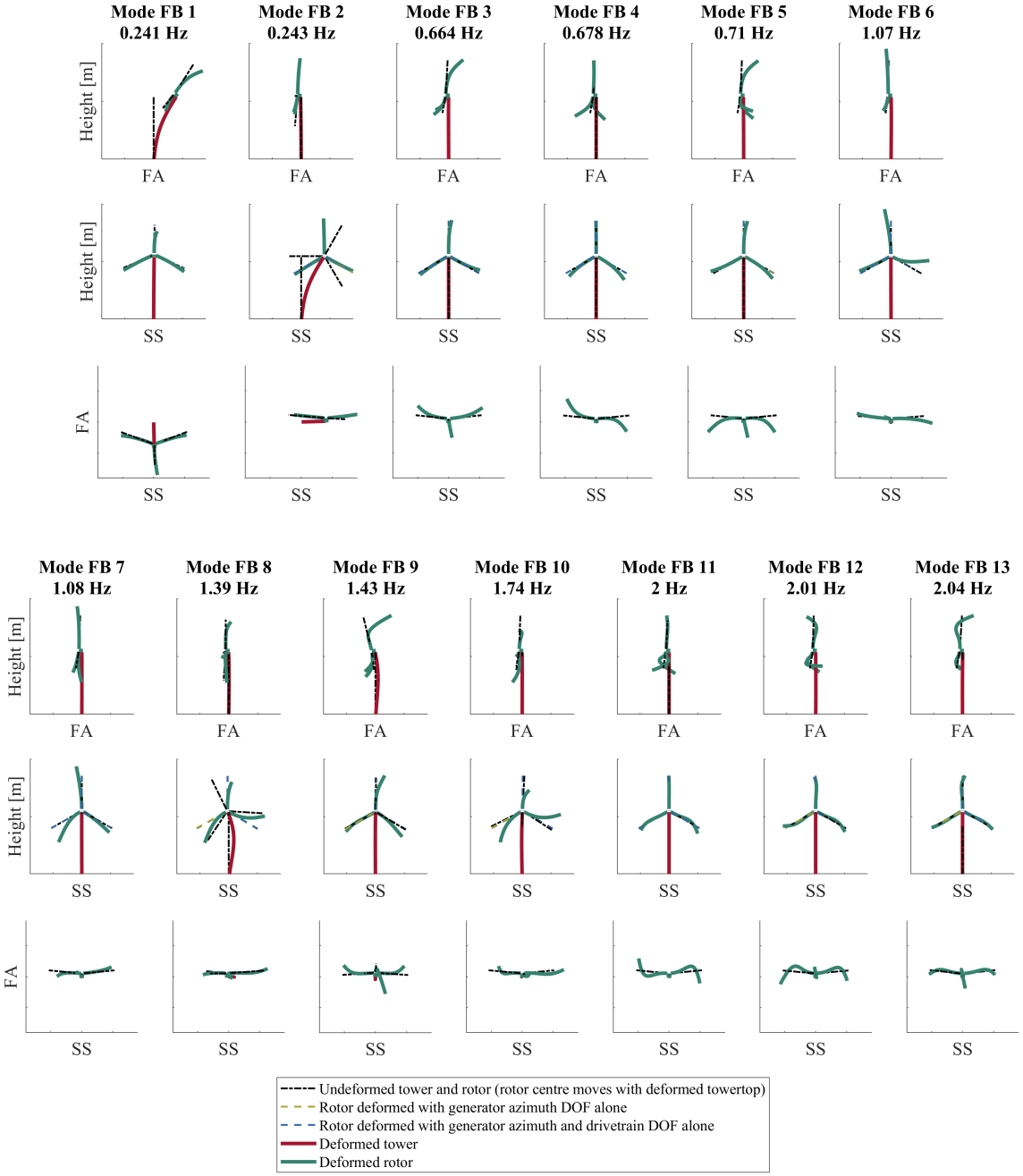


Figure 2.7: Mode shapes and frequencies of the undamped OWT sub-model FB (flexible blades) with rotor free to rotate.

explored in more detail in Chapter 5.

Comparing Figures 2.6 and 2.7, the first two mode shapes, FB 1 and FB 2, are similar to RB 1 and RB 2. There is a slight change to the frequency, when comparing mode FB 1 to RB 1, which can be attributed to coupling with the 1st order flapwise bending DOF of the vertical blade in mode FB 1 (as observed in the upper left plot of Figure 2.7). The FB sub-model then has five modes, FB 3 to FB 7, that appear to predominantly contain blade bending DOF contributions of various combinations of 1st order flapwise (q_{BF1}) or edgewise (q_{BE1}) blade bending or both. Though small in comparison to the magnitude of the blade bending DOF contributions, these modes all also contain some degree of contribution from the tower bending DOF.

Modes FB 8 and FB 9 bear most resemblance to RB 3 and RB 4, according to the frequency magnitudes and tower mode shape. However, the mode shapes of FB 8 and FB 9 vibrate in the SS and FA planes respectively, in contrast to modes RB 3 and RB 4 which vibrate in the FA and SS planes respectively. This change could be attributed to the significant coupling of the tower and blade bending DOF in modes FB 8 and FB 9. Mode FB 10 also exhibits a small contribution from the 2nd order SS tower bending DOF, and both modes FB 8 and FB 10 also present notable contributions from the drivetrain DOF, which appears to couple with the SS tower and edgewise blade bending DOF. Drivetrain DOF contributions can be delineated by comparing the blue and yellow dashed rotor representations in the figure. These can be difficult to see as a result of the scaling, so refer to the tables of Appendix A for the values of the DOF contributions if necessary. Modes FB 11 to 13 are predominantly dominated by 2nd order flapwise blade bending DOF, but also contain some contributions from other blade and tower bending DOF.

Another way of observing the impacts of the blade flexibility is to observe how the mode frequencies change as the degree of the blade flexibility is varied. The blade stiffness is varied by altering the Young's modulus of the material. Figure 2.8 shows the sub-model FB frequencies against normalised blade stiffness across

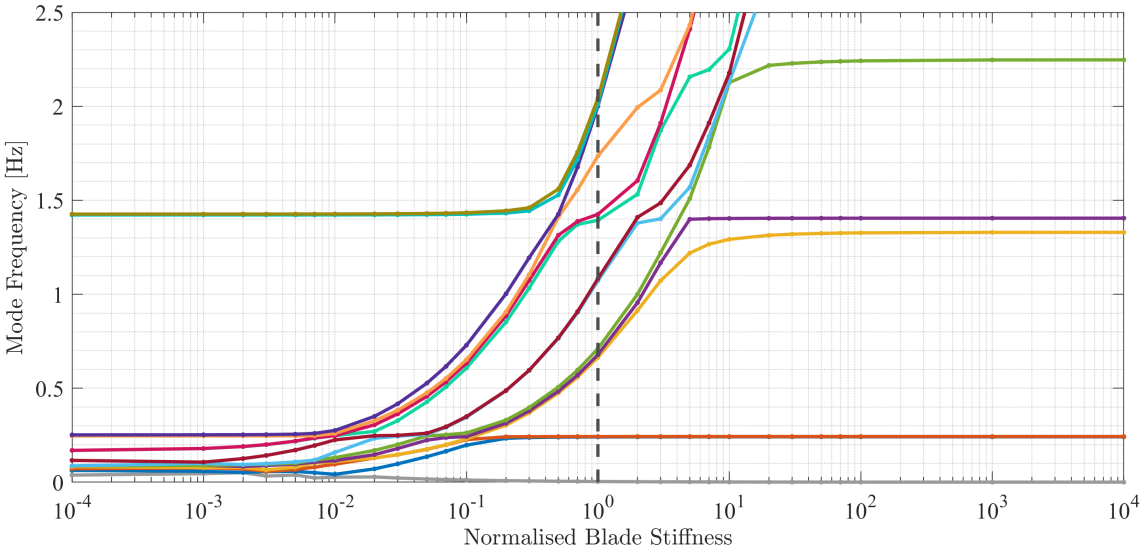


Figure 2.8: Mode frequency with changing blade stiffness for the undamped OWT sub-model FB with rotor free to rotate. The dots on the lines indicate the analysis points, and the vertical grey dashed line indicates the blade stiffness of the original OWT sub-model FB.

varying orders of magnitude, with the grey dashed line indicating the blade flexibility modelled in the baseline sub-model FB (as shown for Figure 2.7). Each colour represents the i^{th} mode at every blade stiffness, with the modes being sorted in order of increasing frequency.

Figure 2.8 demonstrates that some mode frequencies are more sensitive to the blade flexibility than others, represented by the gradients of the lines. Two consistently horizontal lines can be seen at $\sim$ 0.25 Hz, which correspond to modes FB 1 and FB 2 at a normalised blade stiffness of 1. Although these horizontal lines represent different mode numbers (according to the sorting definition) as the blade flexibility varies, they show that there are always two modes whose frequencies are virtually insensitive to the blade flexibility. These modes are dominated by the 1$^{\text{st}}$ order tower bending DOF, q_{TFA1} and q_{TSS1}. The predominantly horizontal lines at $\sim$ 1.4 Hz, representing modes dominated by q_{TFA2} and q_{TSS2}, are also relatively unchanged across the blade stiffness range, although they are affected slightly more in the blade stiffness range from 2×10^{-1} to 2×10^{1}. In this range, there is strong coupling between the 2$^{\text{nd}}$ order shape tower bending and the blade bending DOF.

The lines of substantive gradients correspond to modes that are dominated by various combinations of the blade bending DOF. When the blade stiffness is very high, the model is equivalent to the sub-model RB with the drivetrain DOF also enabled.

In summary, investigating the impact of the blade flexibility on the modes demonstrates the strong coupling between the vibrations of the OWT sub-structure elements and indicates the difficulty in characterising individual modes. In addition, this analysis highlights the importance of accurately modelling the RNA, showing the detail that is lost when a simplified rigid RNA is modelled.

Blade pitch

If the blade pitch were changed, the DOF coupling in each mode (i.e. the combinations of the DOF contributing to each mode) would change, and the data shown in Figure 2.8 would be slightly different. The flapwise and edgewise blade bending DOF do not align exactly with the FA and SS axes respectively, predominantly due to the blade pitch, but also due to the rotor shaft tilt and blade pre-coning. The blades can be pitched at any angle, commonly between 0 and 90°, depending on the operational mode. At 0° the flapwise blade DOF aligns approximately with the FA axis, and at 90° with the SS axis. This variation can have a significant impact on the modes of the structure, as will be shown in this section.

Figure 2.9 shows the frequencies of the OWT sub-model FB as the blade pitch angle is varied from 0 to 90°. The figure shows that the blade pitch affects the frequencies of many of the modes, as it causes a change in the specific combinations of the DOF coupling together. This can be observed by looking at the mode shapes, hence the effect of the blade pitch on the mode shape of an example mode, mode FB 9 (pink in Figure 2.9), is shown in Figure 2.10. As the blade pitch changes, the mode shapes show that the blade flapwise bending DOF changes gradually from approximately aligning with the FA axis at a blade pitch of 0° to aligning with the SS axis at a blade pitch of 90°. The direction of the blade bending DOF clearly

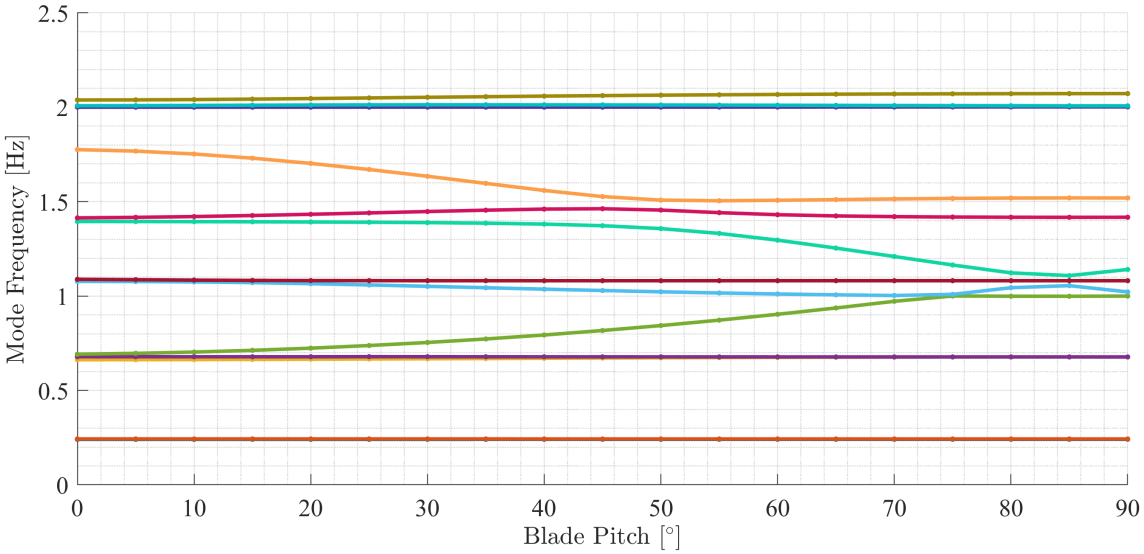


Figure 2.9: Mode frequency with changing blade pitch angle for the undamped OWT sub-model FB with rotor free to rotate. The dots on the lines indicate the analysis points.

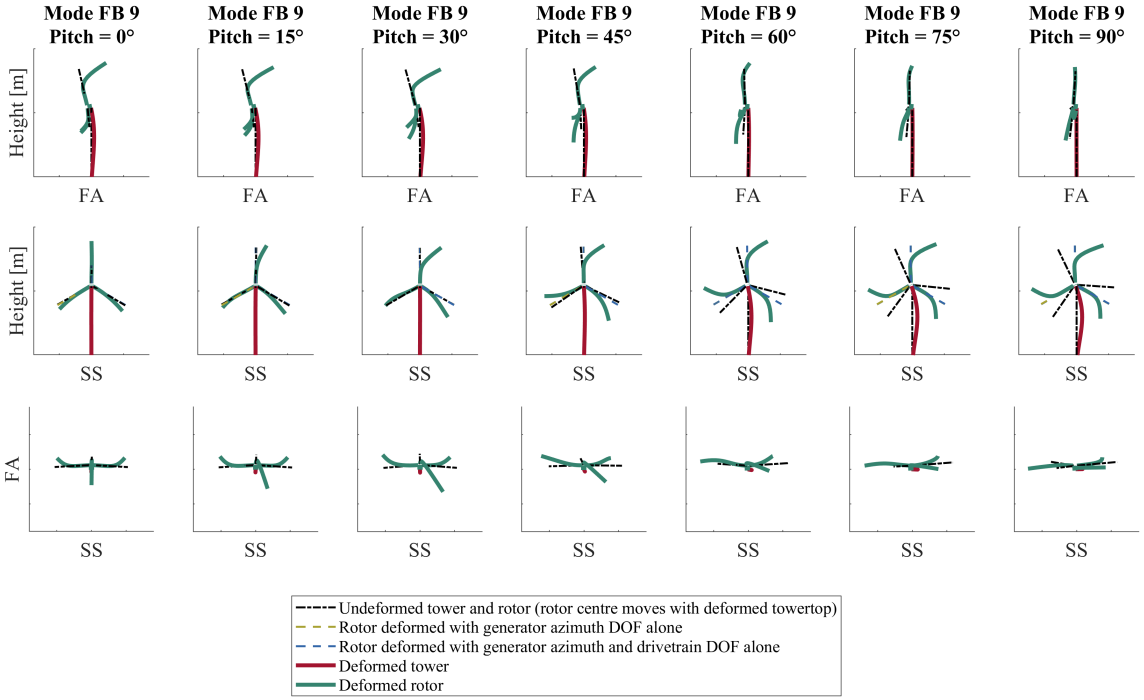


Figure 2.10: Mode shape with changing blade pitch angle for mode 9 of the OWT sub-model FB with rotor free to rotate.

affects the relevant participation of the tower bending DOF, as the tower portion of the mode shape gradually changes from bending in the FA direction at a blade pitch of 0° to the SS direction at a blade pitch of 90°. The opposite effect occurs for mode FB 10 (light orange in Figure 2.9). During changes in pitch for this mode,

the tower portion of the mode shape gradually changes from the SS direction to the FA direction. This means that at a blade pitch of 14°, as shown in Figure 2.7, a pair of modes around 1.4 Hz is seen with the lower vibrating in the SS direction and the higher in the FA, whereas at a blade pitch of 70°, for example, the lower mode vibrates in the FA direction and the higher in the SS.

This investigation demonstrates the extent of the temporal variability introduced to the system properties when the OWT is in an operational mode that involves changes to the blade pitch. Not only does the change in direction of the blade bending impact the rotor mode shape, but the coupling of that blade bending with the tower bending can significantly impact the tower portion of the mode shapes, as demonstrated with mode FB 9 in Figure 2.10. The system identification of data from operating conditions was not considered in this thesis. However, the time variability introduced by the rotor rotation in idling conditions is investigated in Chapter 4.

2.3.2 Effect of locking the rotor

As discussed in Section 1.3.1, during idling and operational conditions the rotor is free to rotate, as has been modelled so far, and in parked conditions a brake is applied to restrict the rotor rotation. The effect of this locking of the rotor on the modal properties of the OWT is investigated with FAST.

Table 2.1 lists the inertia of the RNA when the rotor is free to rotate or locked, as the two conditions are characterised by different effective inertias of the RNA. When the rotor is free to rotate, the inertia about the rotor shaft is not transferred to the supporting structure, but it is transferred when the brake is applied. The shaft is tilted upwards by 5° so does not exactly align with the FA-FA axis, instead lying in the FA-z plane (with the z-axis being vertical), hence why the free rotor case has a non-zero I_{FA-FA} and why there is a small difference between I_{zz} and I_{FA-z} for the two cases. The inertia term about the side-to-side axis, I_{SS-SS}, remains unchanged.

Table 2.1: Rotor nacelle assembly modelled inertias.

Inertia term	Rotor free [kgm^2]	Rotor locked [kgm^2]
I_{FA-FA}	2.99e5	3.86e7
I_{SS-SS}	2.35e7	2.35e7
I_{zz}	2.51e7	2.53e7
I_{FA-z}	-1.31e6	-1.30e6

Figure 2.11 shows the mode shapes and frequencies of the OWT sub-model RB with the rotor locked and Table 2.2 compares the frequencies with those of the sub-model RB with the rotor free to rotate. Comparing with the mode shapes for the free rotor case in Figure 2.6, it can be seen that the rotor face rotates with the tower-top in the locked case, and it only translates in the free case, because the joint between the rotor hub and the rotor is a pin in the latter. Looking at the frequencies in Table 2.2 shows that the FA modes, RB 1 and 3 in the free rotor case and RB 2 and 4 in the locked rotor case, are unaffected by the locking of the rotor. This is

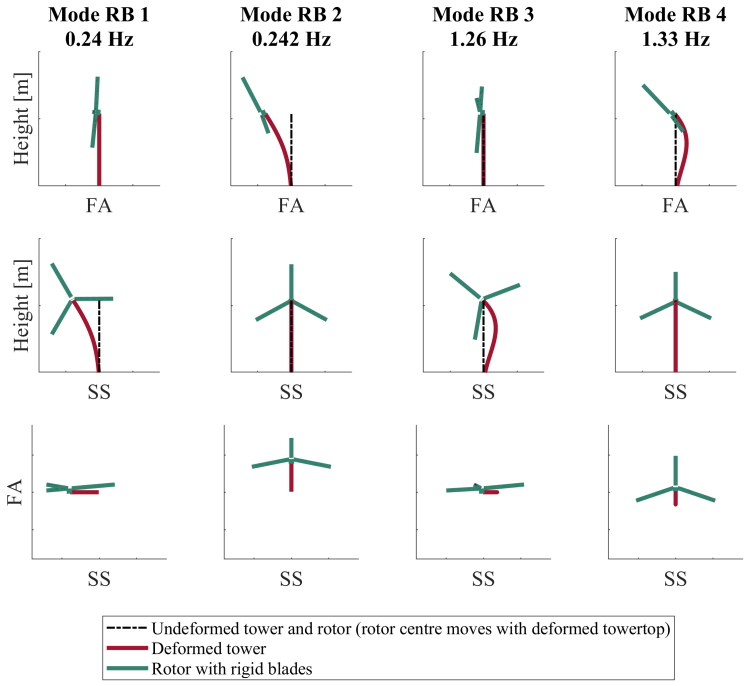


Figure 2.11: Mode shapes and frequencies of the undamped OWT sub-model RB (rigid blades) with rotor locked.

Table 2.2: Comparison of the frequencies of modes 1 to 4 of the OWT sub-model RB when the rotor is locked or free to rotate.

Mode, i	Rotor free f_i [Hz]	Rotor locked f_i [Hz]
RB 1	0.2416	0.2405
RB 2	0.2431	0.2416
RB 3	1.330	1.259
RB 4	1.416	1.330

because these modes are affected by the inertia about the SS-SS axis, I_{SS-SS}, which remains unchanged. In contrast, the frequencies of the SS modes decrease due to the increase in the inertia about the FA-FA axis, I_{FA-FA}. If the usual convention of naming the modes in order of increasing frequency is followed, then locking the rotor has the overall effect that the vibration direction of each mode swaps from SS to FA or FA to SS. So for example, the 1$^{\text{st}}$ mode would be expected to be a SS mode when the rotor is locked, as opposed to a FA mode when the rotor is free, and so on.

Figure 2.12 shows the mode shapes and frequencies of the OWT sub-model FB with locked rotor. The effect on the model with flexible blades is more complex given the introduction of the blade and drivetrain flexibility DOF. Between the locked rotor and free rotor cases, the modes are compared and matched based on their frequency and mode shape resemblance. Comparing Figure 2.12 with the free rotor case, shown in Figure 2.7, shows that the 1$^{\text{st}}$ SS mode is affected in the same way as with sub-model RB, that is the frequency decreases and it becomes the mode with the lowest frequency. Many of the other modes are not significantly impacted in terms of their mode shapes, though a small decrease in the frequencies is generally seen as a result of the increased inertia. After matching the most obvious mode pairs, it appears through a process of elimination that the modes FB 8 and 10 from Figure 2.7, with frequencies of 1.39 and 1.74 Hz bear most resemblance to the modes FB 3 and 10 in Figure 2.12, with frequencies of 0.575 and 1.52 Hz. The larger

impact on these modes could be as a result of the combination of the flexibility of the drivetrain and the change in inertia of the RNA that transfers to the tower.

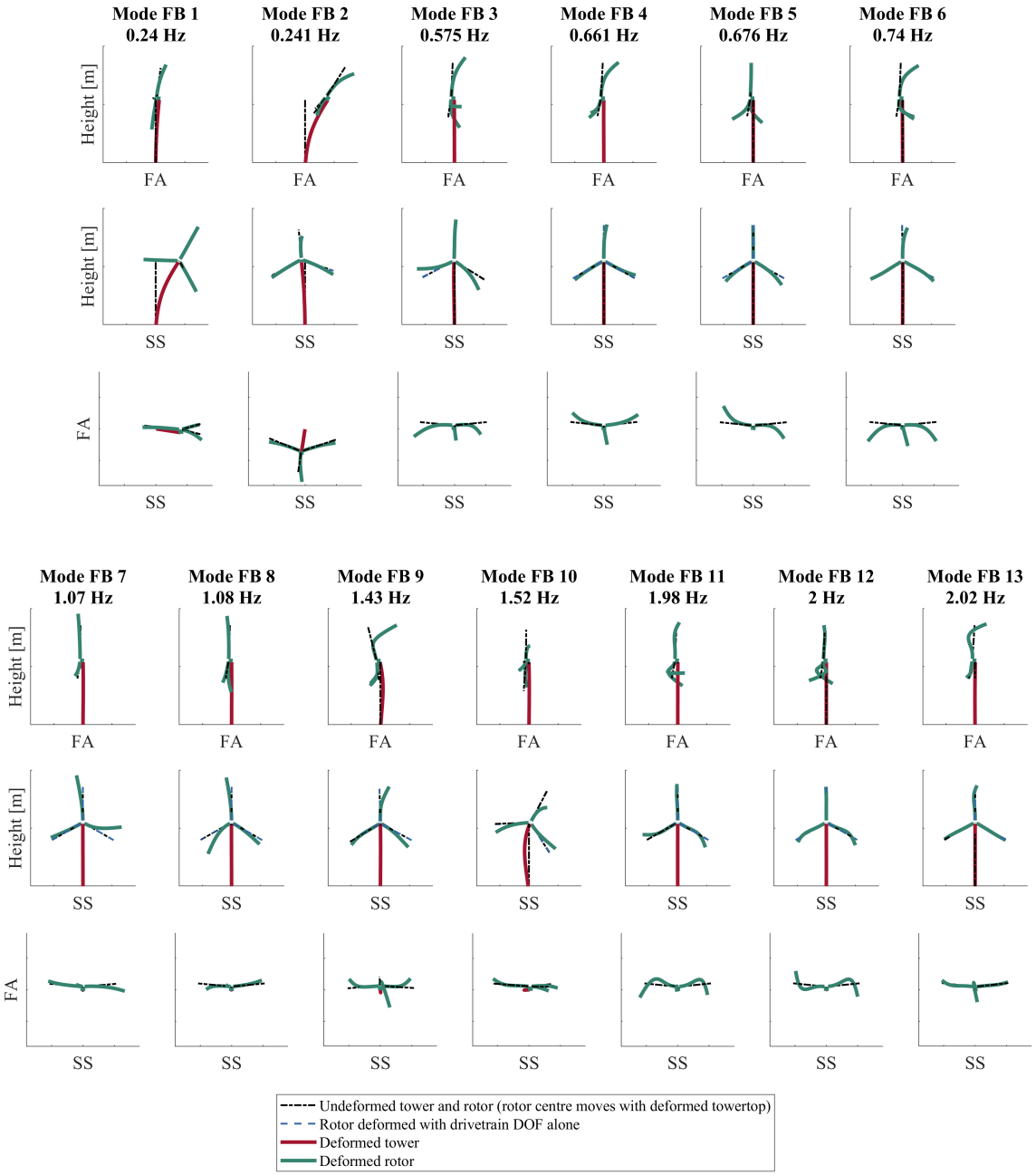


Figure 2.12: Mode shapes and frequencies of the undamped OWT sub-model FB (flexible blades) with rotor locked.

2.3.3 Effect of soil stiffness

In order to develop an approach to identify foundation characteristics from modal properties, it is first important to explore the sensitivity of the modal behaviour to the foundation stiffness.

Figure 2.13 shows the frequencies of the OWT sub-model RB against γ (defined in Eq. 2.5). γ corresponds to the multiplication factor on the foundation stiffness and as such can also be considered as a normalised foundation stiffness. The frequencies of all four modes show sensitivity to the foundation stiffness, with the higher two modes displaying greater sensitivity than the lower two modes.

Figure 2.14 shows the frequencies of the OWT sub-model FB against γ. As already shown, the OWT exhibits strong coupling between its DOF, so the effect of changing the foundation stiffness on the modes of sub-model FB is much more intricate. As with the rigid blades model, sensitivity of the frequencies to the foundation stiffness is observed, indicating that foundation identification is likely to be feasible.

As touched upon in Section 1.3.3, the different sensitivities of the frequency of each mode with respect to the foundation stiffness means that mode veering and/or

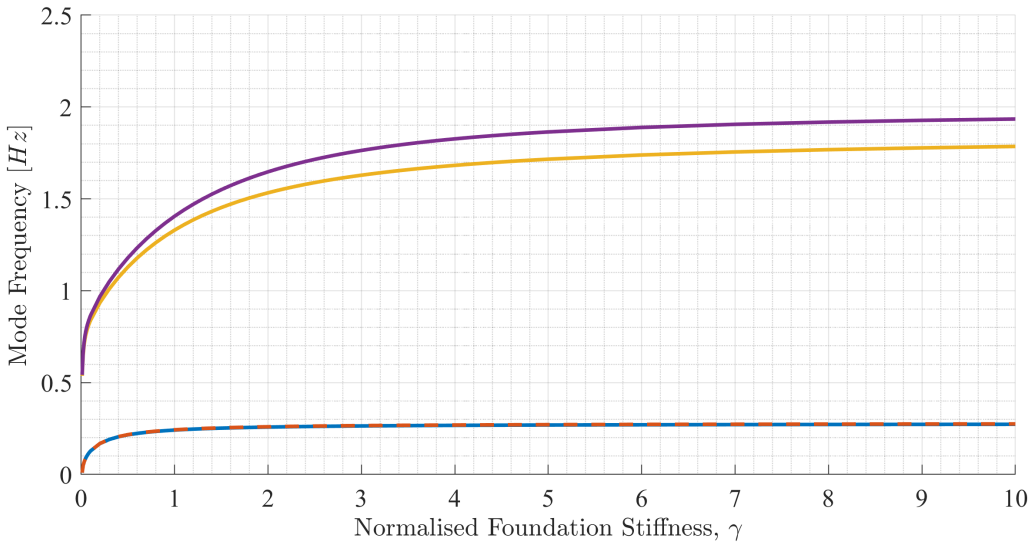


Figure 2.13: Effect of the normalised foundation stiffness, γ, on the frequencies of the undamped OWT sub-model RB.

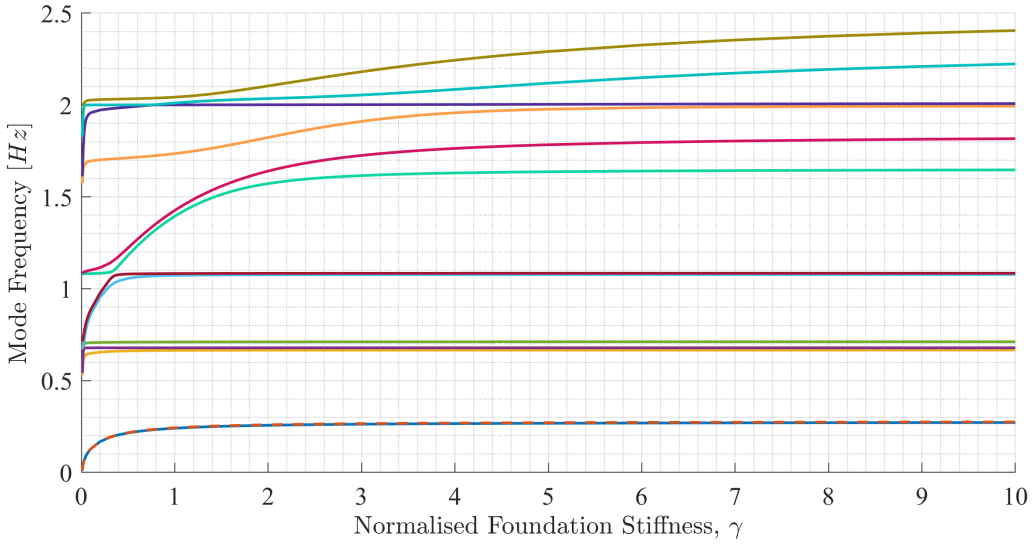


Figure 2.14: Effect of the normalised foundation stiffness, γ, on the frequencies of the undamped OWT sub-model FB.

crossing can occur. This effect can be seen in Figure 2.14. Whether the modes actually cross each other or not has significant implications for model updating. Each identified mode must be matched with its corresponding model-estimated mode for comparison in the updating algorithm. This is not a straightforward task since the numerical model modal properties change as the updating algorithm progresses. The mode veering and crossing make it difficult to interpret the mode matches. Even when looking at the overall picture of the frequencies against γ, as shown in Figure 2.14, it is not possible to tell whether the modes cross one another or not, so implementing an automated procedure in a model updating algorithm would likely be a challenge. This is investigated in more detail in Chapter 5.

Figure 2.14 (as well as Figures 2.8 and 2.9) also clearly shows that the OWT model presents many pairs or even groups of modes with very similar frequencies, i.e. close modes. The existence of close modes for quasi-axisymmetric structures was outlined in Section 1.3.2. Both Figures 2.13 and 2.14 show that the degree of separation between the close modes is dependent on the foundation stiffness magnitude. The implications of close modes for analysing and identifying properties of an OWT is the focus of Chapter 4 of this thesis.

2.3.4 Effect of inclusion of damping

As discussed in Section 1.3.4, OWT exhibit non-proportional damping. When this damping is included with an eigenanalysis, the resulting eigenvalues and eigenvectors, which give the natural frequencies and mode shapes, are both complex-valued. This section shows undamped and damped frequencies and mode shapes. The equations for calculating these modal parameters are given later in Sections 3.2.2 and 5.2.2, but in short the properties are calculated through an eigenanalysis of the system. For undamped properties, only the system mass and stiffness matrices are used, and for damped properties the mass, stiffness and damping matrices are used.

Table 2.3 shows the natural frequencies calculated from the undamped OWT sub-model FB compared with those calculated by taking the absolute values of the complex eigenvalues of the same model with damping included. Lallement and Inman

Table 2.3: Comparison of the frequencies of the OWT sub-model FB (with rotor free to rotate) when calculated with or without the damping included.

Mode, i	Undamped model frequency [Hz]	Damped model frequency [Hz]	Percentage difference [%]
FB 1	0.2407	0.2411	0.2
FB 2	0.2430	0.2430	0.003
FB 3	0.6641	0.6651	0.1
FB 4	0.6784	0.6797	0.2
FB 5	0.7104	0.7088	0.2
FB 6	1.0720	1.0714	0.06
FB 7	1.0830	1.0819	0.1
FB 8	1.3944	1.3947	0.02
FB 9	1.4264	1.4265	0.006
FB 10	1.7355	1.7363	0.05
FB 11	2.0007	1.9991	0.08
FB 12	2.0108	2.0088	0.1
FB 13	2.0428	2.0401	0.1

(1995) showed that although these two sets of frequencies are frequently assumed to be equivalent, they are in fact different when the system is non-proportionally damped. Table 2.3 shows differences from 0.003% to 0.2% between the two sets for the OWT sub-model FB. This could be considered negligible for many applications, though in Chapter 5 of this thesis, the mode veering and crossing behaviour, based on the frequencies, is shown to be different for the undamped and damped OWT models.

When the damping is included, due to its non-proportional nature, the calculated mode shapes are complex-valued. Numerical modelling using FAST indicated that a prominent source of the non-proportional damping is aerodynamic damping, described in Chapter 3. Figure 2.15 shows the sensor-based mode shapes, in

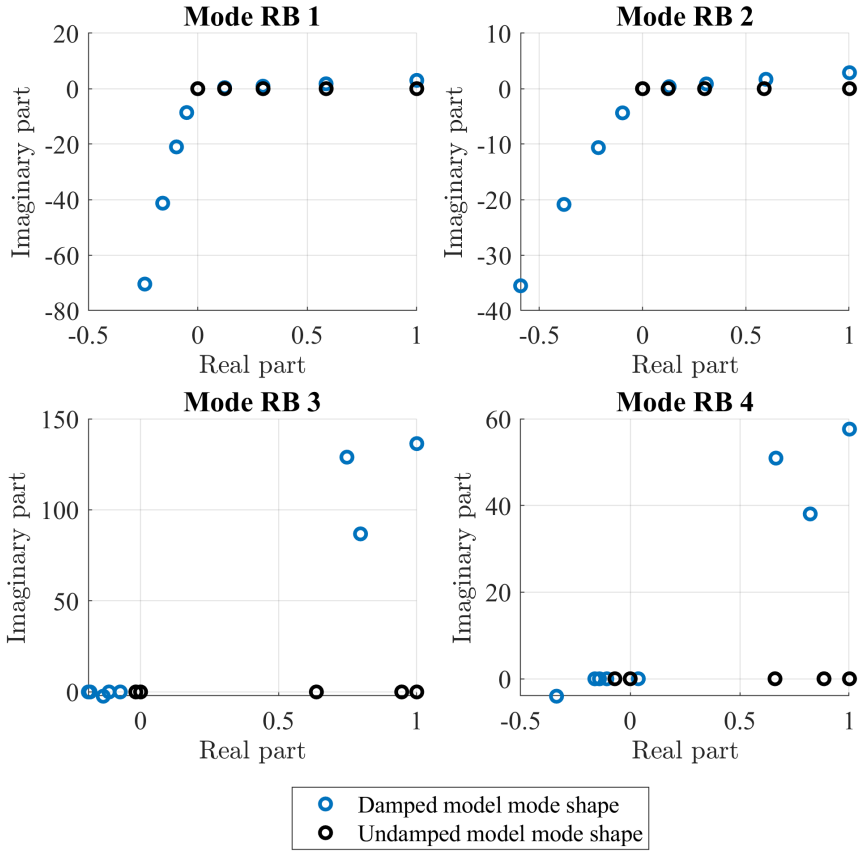


Figure 2.15: Components of the complex sensor-based mode shapes of modes 1 to 4 of the OWT sub-model RB at a wind speed of 15 m/s. The mode shape component at four points on the tower, in both the FA and SS directions, is shown. Note the different scales on the horizontal and vertical axes.

the complex plane, of modes 1 to 4 of the OWT sub-model RB at a wind speed of $15m/s$, comparing those from the damped to the undamped model. The mode shapes consist of four points on the tower in each of the FA and SS directions, corresponding to the sensor locations indicated in Figure 2.2. The mode shapes are all scaled such that the largest real part of each mode shape vector is equal to 1. The figure confirms that the mode shapes display significant complexity.

If someone were to assume that the damping were proportional, they might therefore assume that the damped mode shape real components are representative of the undamped mode shapes, and ignore the imaginary parts. Figure 2.16 shows the mode shapes that would result if this process were applied to the complex mode shapes shown in Figure 2.15. Comparing with the undamped model mode shapes, it can be seen in Figure 2.16 that ignoring the imaginary components would result

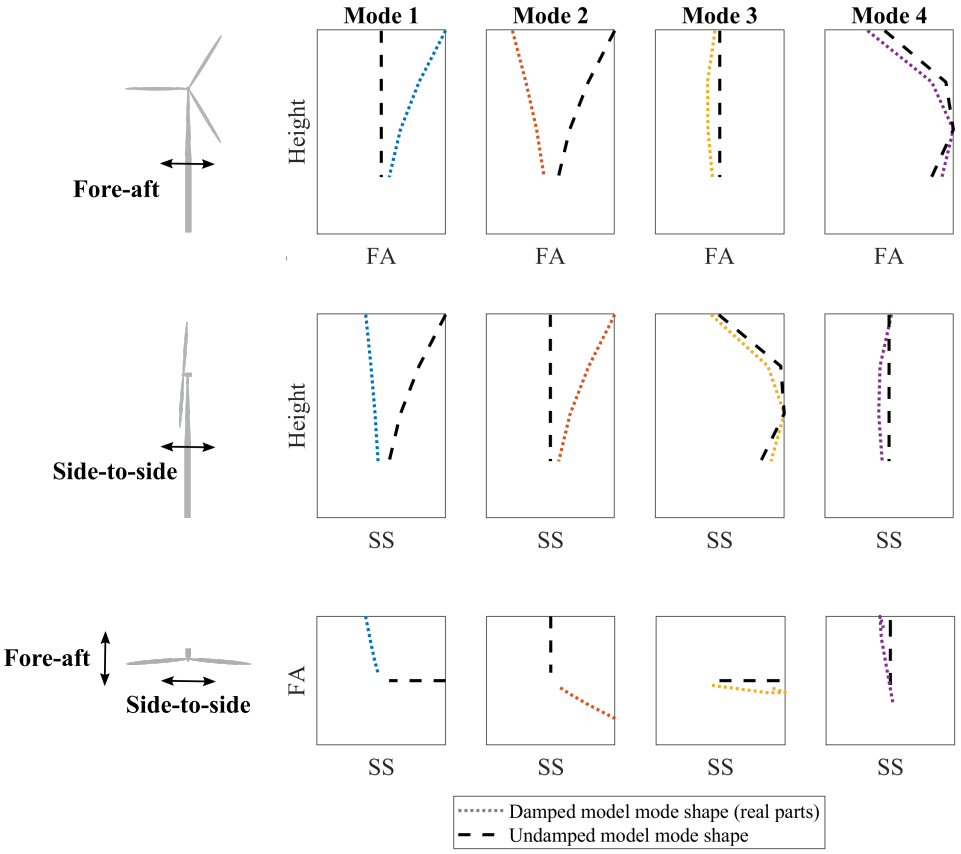


Figure 2.16: Comparison of the real parts of the damped model mode shapes against the undamped model mode shapes, of modes 1 to 4 of the OWT sub-model RB at a wind speed of 15 m/s.

in large misinterpretations of the 1st and 2nd modes, which almost appear to vibrate in the perpendicular direction.

In many civil engineering applications, the assumption of proportional damping is sufficient since the damping is nearly proportional, so the imaginary parts of the mode shapes can be ignored without the introduction of large errors. However, this initial investigation suggests that this is not the case for OWT structures. In the relevant literature looking at system identification of OWT, the treatment of the complex mode shapes is not explicitly described. Devriendt, Magalhaes, et al. (2014) knowingly or unknowingly step around this issue by enforcing that the modal phase collinearity (Pappa, Elliott, & Schenk, 1993) gives a value greater than 0.8, where 1 means entirely real-valued and the lower the modal phase collinearity the more complex the mode shape. They report that physical modes were not classified in some datasets as a result of this restriction on the complexity of the mode shape. Figure 9 from the paper shows the evolution of the identified mode shapes across the monitoring period, and deviations from exactly FA and SS directions can be seen. In the paper these are attributed to small errors in the yaw angle or asymmetries in the foundation structure and soil conditions. However, these are likely to be a result of either the approximation of real mode shapes from complex mode shapes or from the effect of close modes as described in Section 1.3.2.

The effects of OWT non-proportional damping and methods for navigating it are investigated further in Chapter 3.

2.4 Summary

This chapter elaborated on the system complexities introduced in Section 1.3, putting them into the context of the current application: the identification of OWT foundation stiffness using a model updating approach. This was achieved through various parametric studies of the NREL 5MW OWT using FAST.

This chapter demonstrates the importance of using a fully integrated aero-elastic model with structural representation of all elements to accurately model the dynamic response of an OWT. With a simplified model, many of the complexities that have been illustrated would not be evident, and the difference between the model predictions and the true structural behaviour it aims to represent could be significant.

A key finding from this chapter is the inconsistent nature of the vibration directions of the OWT modes. The key modes from a foundation identification perspective are those that are sensitive to the foundation and these modes tend to have significant tower contributions. The application in this thesis focuses on SHM of OWT using sensors on the tower alone and not on the blades, which is most common in practice, so only the tower portion of the mode shapes is identified. Therefore, correctly identifying and understanding the shape and vibration direction of the tower mode shapes of these modes is of paramount importance. The tower portions of these modes (if defined by sorting them in order of frequency magnitude) have been shown to change in vibration direction when the rotor is free to rotate, as opposed to when locked, and/or when the blade pitch is varied. Furthermore, the existence of non-proportional damping has been shown to potentially affect the interpretation of the vibration direction of the mode shapes, as has the existence of close modes (as discussed in Section 1.3.2). This indicates how easily the identified modes from monitoring data could be incorrectly characterised between FA or SS modes. The implications on subsequent applications of those modes, such as within a model updating approach, could be significant. This highlights the importance of using an accurate model, adapted to the specific operational mode, to understand the expected characteristics of those modes, in particular their expected vibration direction.

Chapter 3

Implications of non-proportional damping

3.1 Introduction

Chapter 1 highlighted how uncertainty about in-situ OWT foundation behaviour is believed to contribute significantly to discrepancies observed between the predicted and measured behaviour of OWT. This motivates the development of SHM techniques to estimate the in-situ foundation stiffness of OWT from monitoring data. This chapter investigates the identification of a coupled springs macro-element foundation model from simulated monitoring data of the NREL 5MW OWT, using a model updating approach.

Modal analysis is a widely employed technique for assessing changes in behaviour of wind turbines (e.g. Oliveira et al., 2018; Weijtjens et al., 2016). As explained in Section 1.2.2, this can be extended to identify the characteristics of structural components using model updating, where the difference between identified modal parameters from sensor data and the corresponding model predictions are minimised, in order to optimise a vector of unknown model properties. For the application in this chapter, the unknown model properties are the compliance properties of the foundation model and the modal parameters are the identified frequencies and mode shapes, obtained from simulated tower accelerometer data, using an OMA approach.

As discussed in Sections 1.3.4 and 2.3.4, structures that are non-proportionally damped will exhibit complex mode shapes (Ibrahim, 1983). With some structures, it is possible to assume proportional damping without introducing large errors in analyses. However, the work in this chapter demonstrates that OWT appear not to be one of these structures. A normalisation technique originally developed by Fillod (1980), and applied experimentally to a glass sheet by Sinha (2005), is used in this chapter to obtain a close approximation of the normal undamped mode shapes from the complex damped mode shapes of the OWT.

The wind turbine model, modal identification, mode shape normalisation and model updating methods are explained in Section 3.2 and the techniques are applied in Sections 3.3 and 3.4. In Section 3.3, the use of the mode shape normalisation

technique is motivated and demonstrated through numerical modelling of the OWT, and the source of the non-proportional damping is explored. The OWT frequencies and tower mode shapes are then identified from the simulated data, for a variety of cases with differing characteristics. The characteristics explored are the wind speed, the noise level in the simulated data, and the foundation stiffness magnitude. The foundation parameters are then estimated using model updating in Section 3.4, followed by a discussion of the potential sources of error, the specific form of the foundation best suited for optimisation and the impact of the mode shape normalisation on the results.

3.2 Methodology

3.2.1 Model

In this chapter, the foundation identification and effect of non-proportional damping are investigated using the simplified OWT sub-model RB, as presented in Section 2.2.3, modelled using FAST v7 (J. Jonkman & Buhl, 2005). The DOF of sub-model RB are shown in Figure 3.1 and the dimensions and sensor locations are shown in Figure 3.2a. Four biaxial accelerometers are used for the simulated tower accelerometer data and for obtaining the mode shapes of the structure in the sensor basis. Sub-model RB will simply be referred to as the model or OWT model for the remainder of this chapter.

One additional alteration has been made to the model, that is a change in the inertia of the RNA. This alteration, and the other modelling simplifications are detailed and justified as follows:

- The blades have been modelled as rigid, eliminating coupling between the vibrational responses of the tower and the blades.
- The data have been simulated for parked conditions, i.e. with a stationary

rotor, across a range of wind speeds with the blades pitched to 0°.

- The inertia of the RNA about the shaft axis has been increased by 1×10^8 kgm^2 ($\sim$ 250%) to increase the separation between the frequencies of the first two vibration modes.

The above simplifications have been introduced so that the effect of interest illustrated in this chapter, that of non-proportional damping (discussed in Section 3.2.3), is isolated from other effects. The effects that are removed are; the modal coupling between the blades and the tower, the presence of non-stationary and coloured excitations during turbine operation (Manzato et al., 2014), and the existence of close modes (Au et al., 2021). Each of these effects introduces a complexity to the identification procedure that can be addressed with complementary approaches. These are investigated in Chapters 4 and 5. Whilst it is important to be aware of these effects, the alterations made to minimise their effect do not compromise the qualitative findings in this chapter related to non-proportional damping and model updating.

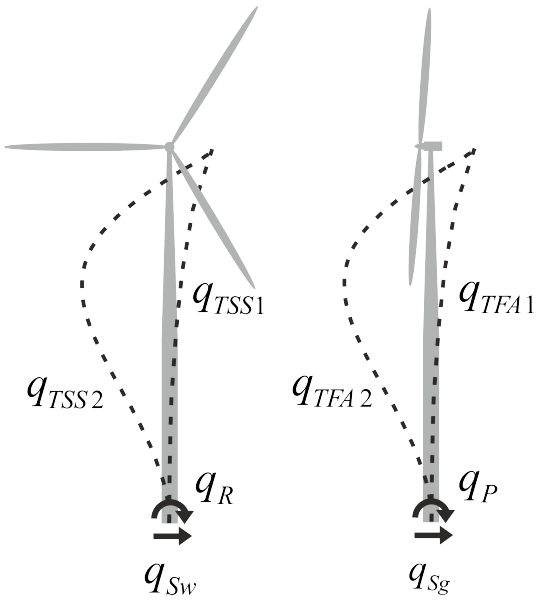
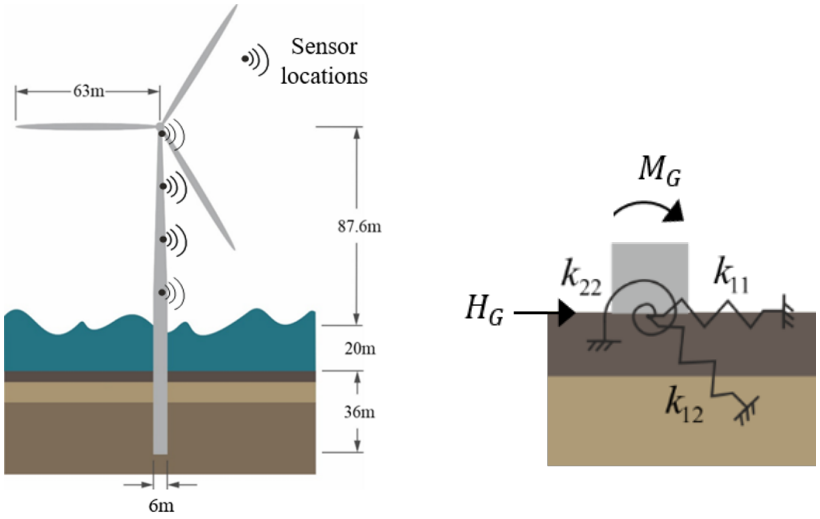


Figure 3.1: Model degrees of freedom.



(a) (b)

Figure 3.2: NREL 5MW OWT model dimensions (a) and foundation representation (b).

Foundation modelling

The soil-structure interaction in this chapter is modelled with a macro-element model, where the embedded monopile is represented by a set of statically equivalent linear springs at the mudline level.

One possible form of this macro-element consists of two uncoupled springs, a lateral, k_H, and a rotational, k_M, that govern the load displacement response by:

$$\begin{Bmatrix} H_G \\ M_G \end{Bmatrix} = \begin{bmatrix} k_H & 0 \\ 0 & k_M \end{bmatrix} \cdot \begin{Bmatrix} \nu_G \\ \theta_G \end{Bmatrix} \tag{3.1}$$

where ν_G and θ_G are the ground-level lateral displacement and rotation respectively and H_G and M_G are the ground-level applied horizontal and moment loads. These uncoupled springs are tuned to be statically equivalent to the embedded monopile, but are limited to being equivalent at one particular load eccentricity, h, which is the ratio of moment load to horizontal load, given by:

$$h = \frac{M_G}{H_G} \tag{3.2}$$

h is commonly used in static analyses (e.g. Byrne et al., 2020). In practice, the loading conditions vary with time, for example when the wind speed changes, and therefore h varies with time. This causes the foundation response to change as the motion of the embedded monopile, and the mobilisation of the soil reactions, also varies. Thus the stiffness response of the embedded monopile is dependent on h, and corresponds to a different set of statically equivalent k_H and k_M for each h.

This variation can be captured with a macro-element consisting of three coupled springs, a lateral, k_{11}, a rotational, k_{22}, and a cross-coupling spring, k_{12}, as shown in Figure 3.2b. These coupled springs are assembled into a foundation stiffness matrix, $\boldsymbol{K}_F$, that governs the load displacement response by:

$$\begin{Bmatrix} H_G \\ M_G \end{Bmatrix} = \begin{bmatrix} k_{11} & k_{12} \\ k_{12} & k_{22} \end{bmatrix} \cdot \begin{Bmatrix} \nu_G \\ \theta_G \end{Bmatrix} \tag{3.3}$$

This coupled springs model is able to replicate the ground-level static behaviour of the embedded monopile under loading of any eccentricity, h. The OWT foundation in this chapter is modelled in this way, and the soil properties are assumed to be axisymmetric about the vertical axis. The coupled spring stiffnesses can be related to the equivalent uncoupled spring stiffnesses using:

$$k_H = \frac{k_{11}k_{22} - k_{12}^2}{k_{22} - hk_{12}} \tag{3.4}$$

$$k_M = \frac{h \cdot k_{11}k_{22} - k_{12}^2}{hk_{11} - k_{12}} \tag{3.5}$$

These equations allow the simplification of the coupled stiffness matrix into its principal behaviours, its overall horizontal and rotational stiffness, for a given h.

Plotting the relationships given in Eqs. 3.4 and 3.5, for a given set of k_{11}, k_{12} and k_{22}, provides a convenient way to compare the behaviour of different foundation matrices (McAdam et al., 2022), such as comparing the matrices estimated through

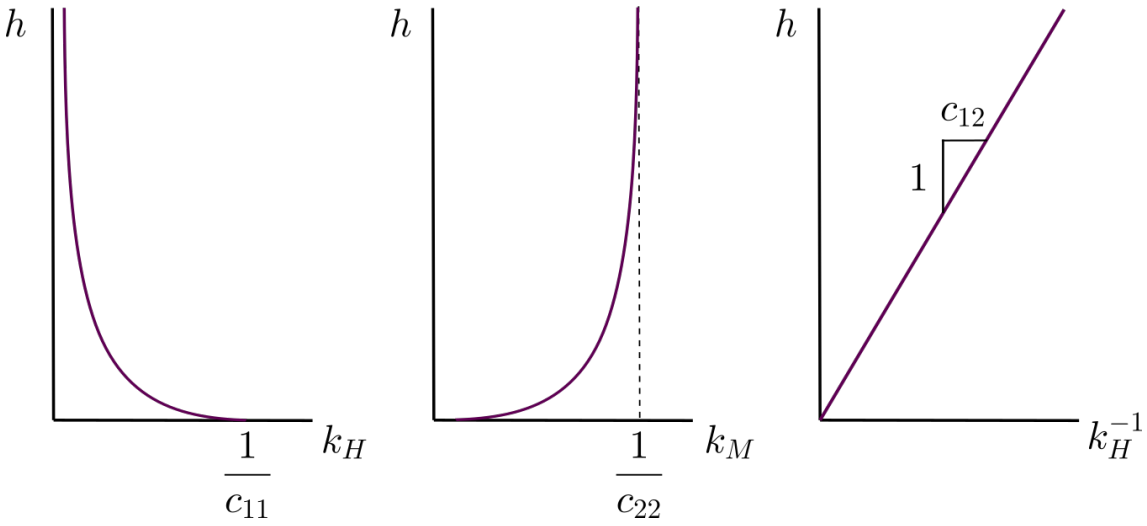


Figure 3.3: Indicative diagram of the relationships between equivalent lateral and rotational stiffnesses (k_H and k_M) and load eccentricity (h). Also shown are the salient features that correspond to the terms of the compliance matrix, $\boldsymbol{C}_F$.

model updating against the 'true' numerical model foundation matrix. Figure 3.3 gives an indicative representation of these relationships with varied load eccentricity, h.

The terms of the compliance matrix, $\boldsymbol{C}_F$, are the inverse of the macro-element stiffness matrix, $\boldsymbol{K}_F$:

$$\boldsymbol{C}_F = \boldsymbol{K}_F^{-1} = \frac{1}{k_{11}k_{22} - k_{12}^2} \begin{bmatrix} k_{22} & -k_{12} \\ -k_{12} & k_{11} \end{bmatrix} = \begin{bmatrix} c_{11} & c_{12} \\ c_{12} & c_{22} \end{bmatrix} \tag{3.6}$$

and correspond to salient features of the foundation relationships shown in Figure 3.3. Furthermore, the coupled spring compliances can be related to the uncoupled springs stiffnesses using:

$$k_H = \frac{1}{c_{11} + hc_{12}} \tag{3.7}$$

$$k_M = \frac{h}{c_{12} + hc_{22}} \tag{3.8}$$

so each uncoupled spring stiffness is only dependent on two coupled compliance

terms, whereas they are dependent on all three coupled stiffness terms (Eqs. 3.4 and 3.5). It will be shown later in this chapter that the compliance matrix terms are found to provide a better basis for comparison of the foundation behaviour than the stiffness matrix terms. This is potentially as a result of their simpler relation with the uncoupled spring form (Eqs. 3.7 and 3.8) and correspondence to salient points on the $h - k_H$ and $h - k_M$ curves, though this is not investigated further. Therefore, the aim of the model updating method is to estimate these three coupled spring compliances, c_{11}, c_{12} and c_{22}.

An effective load eccentricity, h_i, can also be approximated for the i^{th} vibration mode by combining Eqs. 3.2 and 3.3 to give:

$$h_i = \frac{k_{12}v_{G,i} + k_{22}\theta_{G,i}}{k_{11}v_{G,i} + k_{12}\theta_{G,i}} \tag{3.9}$$

where $v_{G,i}$ and $\theta_{G,i}$ are the ground-level lateral and rotational displacements of the i^{th} mode shape, which can be extracted from a model modal analysis. In this structure it was observed that the higher the mode, i, the lower the eccentricity, h_i. These effective load eccentricities can be plotted on the curves shown in Figure 3.3 and give an indication of the relationship between the foundation response and a particular mode, as will be used in Section 3.4.2. For the structure in this chapter, the h_i associated with the first four vibration modes (those with the lowest frequencies) are in the range of 18-108m.

3.2.2 Calculation of modal parameters

The continuous-time equation of motion, in second order form, for a viscously damped n-DOF system is:

$$\boldsymbol{M}\ddot{\boldsymbol{q}}(t) + \boldsymbol{D}\dot{\boldsymbol{q}}(t) + \boldsymbol{K}\boldsymbol{q}(t) = \boldsymbol{u}(t) \tag{3.10}$$

and for an undamped system is:

$$\boldsymbol{M}\ddot{\boldsymbol{q}}(t) + \boldsymbol{K}\boldsymbol{q}(t) = \boldsymbol{u}(t) \tag{3.11}$$

where $\boldsymbol{M}$, $\boldsymbol{D}$ and $\boldsymbol{K}$ are the $n \times n$ mass, damping and stiffness matrices respectively, $\boldsymbol{u}(t)$ is the force vector and $\boldsymbol{q}(t)$ is the $n \times 1$ response vector, each element of which corresponds to a DOF. For the eight DOF NREL 5MW (sub-model RB) used in this chapter, $\boldsymbol{q} = \{q_{Sg}, q_{Sw}, q_R, q_P, q_{TFA1}, q_{TSS1}, q_{TFA2}, q_{TSS2}\}$ (shown in Figure 3.1) and the force inputs are due to the wind and the resistive forces of the soil springs and the water (still water is assumed so no waves are modelled).

The eigenvalues, $\lambda_{u,i}$, and corresponding eigenvectors, $\boldsymbol{\phi}_{u,i}$, for the undamped system can be found by solving the generalised eigenvalue problem given by:

$$\lambda_{u,i}\boldsymbol{M}\boldsymbol{\phi}_{u,i} = \boldsymbol{K}\boldsymbol{\phi}_{u,i} \quad \boldsymbol{\phi}_{u,i} \neq 0 \quad i = 1, 2, ...n \tag{3.12}$$

where i denotes the vibration mode. $\boldsymbol{\phi}_u$ will be referred to as undamped mode shapes.

To find the eigenvalues, $\lambda_{d,i}$, and corresponding eigenvectors, $\boldsymbol{\phi}_{d,i}$, for the damped system the following equation must be solved:

$$\left(\lambda_{d,i}^2\boldsymbol{M} + \lambda_{d,i}\boldsymbol{D} + \boldsymbol{K}\right)\boldsymbol{\phi}_{d,i} = 0 \quad \boldsymbol{\phi}_{d,i} \neq 0 \quad i = 1, 2, ...n \tag{3.13}$$

To find $\lambda_{d,i}$ and $\boldsymbol{\phi}_{d,i}$ exactly, the system is solved in first order state-space form.

The introduction of the state vector $\boldsymbol{x}(t) = \left\{ \begin{array}{c} \boldsymbol{q}(t) \\ \dot{\boldsymbol{q}}(t) \end{array} \right\}$ enables the transformation of Eq. 3.10. into state-space form as follows:

$$\dot{\boldsymbol{x}}(t) = \boldsymbol{A}\boldsymbol{x}(t) + \boldsymbol{B}\boldsymbol{u}(t), \ \boldsymbol{y}(t) = \boldsymbol{E}\boldsymbol{x}(t) + \boldsymbol{F}\boldsymbol{u}(t) \tag{3.14}$$

where $\boldsymbol{y}(t)$ is the output vector, $\boldsymbol{B}$, $\boldsymbol{E}$ and $\boldsymbol{F}$ are the input, output and feedthrough matrices and the state matrix, $\boldsymbol{A}$, is given by:

$$\boldsymbol{A} = \left[\begin{array}{cc} \boldsymbol{0} & \mathrm{I} \\ -\boldsymbol{M^{-1}K} & -\boldsymbol{M^{-1}D} \end{array} \right] \tag{3.15}$$

The damped system can now be solved using the standard eigenvalue problem (in terms of one matrix) given by:

$$\boldsymbol{A}\boldsymbol{\psi}_{d,i} = \boldsymbol{\psi}_{d,i}\lambda_{d,i} \quad \boldsymbol{\psi}_{d,i} \neq 0 \quad i = 1, 2, ...2n \tag{3.16}$$

where there are $2n$ values of $\lambda_{d,i}$ and vectors of $\boldsymbol{\psi}_{d,i}$ occurring in complex conjugate pairs, with each pair corresponding to a DOF. For simpler relation with the undamped eigenvalues and eigenvectors, the damped eigenvalues and eigenvectors are ordered such that the complex conjugate pairs occur in the i^{th} and $(n+i)^{th}$ positions (for $i = 1$ to n). $\boldsymbol{\psi}_d$ are the eigenvectors of the first order linear (state-space) system. $\boldsymbol{\psi}_d$ (basis $\boldsymbol{x}$), are related to the second order form eigenvectors, $\boldsymbol{\phi}_d$ (basis $\boldsymbol{q}$), by:

$$\boldsymbol{\psi}_{d,i} = \left\{ \begin{array}{c} \boldsymbol{\phi}_{d,i} \\ \lambda_{d,i}\boldsymbol{\phi}_{d,i} \end{array} \right\} \tag{3.17}$$

$\boldsymbol{\phi}_d$ will be referred to as damped mode shapes. It is worth noting that $\boldsymbol{\phi}_u$ are real-valued vectors and $\boldsymbol{\phi}_d$ are complex-valued.

The mode shapes are transformed from the state vector, $\boldsymbol{x}$, basis or the DOF,

$\boldsymbol{q}$, basis to the output vector, $\boldsymbol{y}$, basis (sensor basis) as follows:

$$^{s}\boldsymbol{\phi}_d = \boldsymbol{E}\boldsymbol{\psi}_d = \boldsymbol{E}^{\dagger}\boldsymbol{\phi}_d \tag{3.18}$$

where ^{s} denotes the sensor basis, $\boldsymbol{E}$ is the output matrix as introduced in Eq. 3.14 and $\boldsymbol{E}^{\dagger}$ is an alteration of $\boldsymbol{E}$ with all rows but only columns 1 to n of a total $2n$. This procedure allows for comparison of numerical model and identified mode shapes, as the latter is available in the sensor basis (shown in Section 3.2.5). The undamped sensor-based mode shapes can be found using:

$$^{s}\boldsymbol{\phi}_u = \boldsymbol{E}^{\dagger}\boldsymbol{\phi}_u \tag{3.19}$$

$\boldsymbol{\lambda}_d$ and $\boldsymbol{\lambda}_u$ are the diagonal matrices of eigenvalues for the damped and undamped cases respectively. The damping ratios, $\boldsymbol{\zeta}$, are calculated from $\boldsymbol{\lambda}_d$ by:

$$\zeta_i = -\frac{Re\left(\lambda_{d,i}\right)}{|\lambda_{d,i}|} \tag{3.20}$$

where $\lambda_{d,i}$ refers to the i^{th} diagonal element of λ_d.

The natural frequencies, $\boldsymbol{f}$, can be calculated from either $\boldsymbol{\lambda}_d$ or $\boldsymbol{\lambda}_u$ as follows:

$$f_i = \frac{\sqrt{\lambda_{u,i}}}{2\pi} \cong \frac{|\lambda_{d,i}|}{2\pi} \quad i = 1, 2, ...n \tag{3.21}$$

The values differ slightly, as shown previously in Table 2.3, but the discrepancy is negligible in all the examples studied in this chapter. Throughout the thesis, unless otherwise stated, the modes are sorted in ascending order of the values of the frequencies, so that mode 1 refers to the mode with the lowest frequency, f_1.

3.2.3 Non-proportional damping

Rayleigh (1877) showed that undamped modes satisfy an orthogonality condition

that allows the uncoupling of the equations of motion such that multiple DOF systems can be considered as a collection of independent single DOF systems. If a system exhibits proportional damping then this convenient condition is preserved and $\boldsymbol{\phi}_d$ and $\boldsymbol{\phi}_u$ would therefore be equivalent (subject to a normalisation). An example of a proportional damping model is 'Rayleigh/classical damping' represented by:

$$\boldsymbol{D} = \alpha\boldsymbol{M} + \beta\boldsymbol{K} \tag{3.22}$$

where α and β are real positive constants. For a generalised form of proportional damping the reader is referred to Adhikari's works (Adhikari, 2000).

Exact proportional damping is rare in reality and typically systems are considered either 'nearly' proportionally or non-proportionally damped. The distinction is made based on whether the damping matrix, $\boldsymbol{D}$, is considered diagonally dominant (Woodhouse, 1998). If the off-diagonal terms are comparable to the diagonal terms in magnitude then it is not diagonally dominant and therefore the system is considered non-proportionally damped.

The scaling of mode shapes is arbitrary and therefore a normalisation convention must be chosen. A common convention involves setting the largest component to unity and scaling the other values accordingly. For undamped mode shapes, $\boldsymbol{\phi}_u$, which are real-valued, this process is given by:

$$\bar{\boldsymbol{\phi}}_{u,i} = \frac{\boldsymbol{\phi}_{u,i}}{\max(\boldsymbol{\phi}_{u,i})} \tag{3.23}$$

For damped mode shapes, $\boldsymbol{\phi}_d$, this process is more complicated as the components are complex-valued. Often damping is assumed to be proportional, so the imaginary part is ignored and they are normalised in a similar fashion to the un-

damped mode shapes as follows:

$$\bar{\boldsymbol{\phi}}_i^R = \frac{Re\left(\boldsymbol{\phi}_{d,i}\right)}{\max\ \left(Re\left(\boldsymbol{\phi}_{d,i}\right)\right)} \tag{3.24}$$

which is termed 'real normalisation' in this thesis and denoted with superscript ^{R}.

When the damping is nearly proportional, this procedure will give a good approximation of the undamped mode shapes, but not when there is significant non-proportional damping in the system, i.e. when $\boldsymbol{D}$ is not diagonally dominant. For these situations it appears beneficial to use the following alternative normalisation technique originally presented by Fillod (1980):

$$\bar{\boldsymbol{\phi}}_i^C = Re\left(\frac{\boldsymbol{\phi}_{d,i}}{\phi_{d,i,j}}\right) \tag{3.25}$$

where j is the vector element that maximises $|\phi_{d,i,j}|$. This process is termed 'complex normalisation' in this thesis and is denoted with superscript ^{C}. It should be noted that Sinha (2005) indicates that the extent of the applicability of this method to different generalised forms of non-proportional damping should be investigated, but this is not considered in this thesis. However, this thesis does present an example for which the complex normalisation process successfully converts the complex damped mode shapes to a close approximation of the real undamped mode shapes.

It should also be noted that in the literature, the term 'real normalisation' frequently refers to the process of deriving real-valued mode shapes from complex-valued mode shapes, so both of the normalisation techniques outlined above would be described using this umbrella term. However, in this thesis, real normalisation refers to the process given by Eq. 3.24 and complex normalisation refers to the process given by Eq. 3.25.

In summary, when a system can be approximated as proportionally damped, both $\bar{\boldsymbol{\phi}}_i^R$ and $\bar{\boldsymbol{\phi}}_i^C$ provide good approximations of $\bar{\boldsymbol{\phi}}_{u,i}$, but if the contributions of non-proportional damping cannot be ignored, only $\bar{\boldsymbol{\phi}}_i^C$ serves as a good approximation.

As a result, the similarity between $\bar{\boldsymbol{\phi}}_i^R$ and $\bar{\boldsymbol{\phi}}_i^C$ can be used as an indication of the presence of non-proportional damping in a system, as is done in Section 3.3.1 of this chapter.

The FAST wind turbine model predicts significant non-proportional damping, as a result of aerodynamic rotor loading, that causes the damped mode shapes, $\boldsymbol{\phi}_d$, to differ significantly from the undamped mode shapes, $\boldsymbol{\phi}_u$. The rotor aerofoils generate lift forces perpendicular to the direction of the blade resultant velocity. These velocity dependent forces, which vary with changing wind speed, are a source of damping to the structure. This damping appears in the off-diagonal elements of the damping matrix due to the perpendicular nature of the force-velocity interaction, violating the condition of diagonal dominance. Therefore, the resulting damping matrix has significant contributions from non-proportional damping. The off-diagonal terms of the damping matrix can consequently couple the dynamic behaviour of the FA and SS directions of the tower motion.

Section 3.3.1 uses the OWT model to demonstrate the resulting relationship between the wind speed and the dynamic behaviour and successful application of the complex normalisation technique to transform the complex-valued damped mode shapes to close approximations of the real-valued undamped mode shapes.

3.2.4 Model linearisation and modal parameters

The equations of motion (Eq. 2.2) of the wind turbine are nonlinear, so the first step in finding the modal parameters is a linearisation of the model about a specific operating point, which corresponds to specific values of the state vector, $\boldsymbol{x} = \begin{Bmatrix} \boldsymbol{q} \\ \dot{\boldsymbol{q}} \end{Bmatrix}$. This operating point could be chosen as any realisation of the state vector or specifically the steady state point. The linearisation procedure is presented in the FAST user guide (J. Jonkman & Buhl, 2005), where the mass, stiffness and damping ma-

trices are found as follows:

$$\boldsymbol{M} = \boldsymbol{M}|_{op} \tag{3.26}$$

$$\boldsymbol{K} = \left[\frac{\partial \boldsymbol{M}}{\partial \boldsymbol{q}}\ddot{\boldsymbol{q}} + \frac{\partial \boldsymbol{f}}{\partial \boldsymbol{q}}\right]\Bigg|_{op} \tag{3.27}$$

$$\boldsymbol{D} = \frac{\partial \boldsymbol{f}}{\partial \dot{\boldsymbol{q}}}\Bigg|_{op} \tag{3.28}$$

where the symbol $|_{op}$ indicates that the quantity is evaluated at the operating point vector. Eq. 3.27 is consistent with the mechanical engineering definition of linearised stiffness for systems with moving parts. This definition includes an additional term that allows for the inclusion of stiffening effects caused by accelerating masses, e.g. gyroscopic effects of the rotor when rotating. The derivatives in the above equations are calculated in the software numerically by applying a finite difference scheme, which requires a perturbation of $\boldsymbol{x} = \left\{ \begin{array}{c} \boldsymbol{q} \\ \dot{\boldsymbol{q}} \end{array} \right\}$ about the operating point. In this chapter the operating point used is the steady state vector of the wind turbine states under gravitational loading and wind loading at the mean wind speed. $\ddot{\boldsymbol{q}}$ are calculated by FAST using Eq. 2.2 and the specified $\boldsymbol{q}$ and $\dot{\boldsymbol{q}}$.

The modal parameters are then found using the equations described in Section 3.2.2. Whether the calculated parameters are damped or undamped will be specified with each investigation in Sections 3.3 and 3.4.

FAST also calculates the output matrix, $\boldsymbol{E}$, which is used to transform the FAST DOF mode shapes into the sensor-based mode shapes (Eqs. 3.18 and 3.19).

3.2.5 Identification of modal parameters

The identification of the modal parameters of the system from the simulated data will be achieved using a subspace state-space system identification method called

N4SID (Van Overschee & De Moor, 1994). 'Subspace' refers to the fact that the models are obtained from the row and column spaces of specific matrices generated with the data, and the model components are identified in 'state-space' form. The full algorithm is effectively outlined by Van Overschee and De Moor, but in summary, the method identifies the unknown $\widetilde{\boldsymbol{A}}_D$, $\widetilde{\boldsymbol{B}}_D$, $\widetilde{\boldsymbol{E}}$ and $\widetilde{\boldsymbol{F}}$ matrices of the discrete system describing the transition of the system between steps k and $k+1$, in state space form as:

$$\boldsymbol{x}_{k+1} = \widetilde{\boldsymbol{A}}_D \boldsymbol{x}_k + \widetilde{\boldsymbol{B}}_D \boldsymbol{u}_k + \boldsymbol{w}_k, \qquad \boldsymbol{y}_k = \widetilde{\boldsymbol{E}} \boldsymbol{x}_k + \widetilde{\boldsymbol{F}} \boldsymbol{u}_k + \boldsymbol{v}_k \tag{3.29}$$

where $\boldsymbol{w}$ and $\boldsymbol{v}$ are the process noise and measurement noise vectors respectively. The steps $k = 1 \ldots N$ are sampled with a finite sampling time step Δt. The method requires the input, $\boldsymbol{u}$, and output, $\boldsymbol{y}$, data to identify all state matrices, or output data alone to identify $\widetilde{\boldsymbol{A}}_D$ and $\widetilde{\boldsymbol{E}}$, as is the case in this study.

The identified discrete state matrix is then converted to the state matrix of the equivalent continuous state-space system using:

$$\widetilde{\boldsymbol{A}}_C = \frac{\log\left(\widetilde{\boldsymbol{A}}_D\right)}{dt} \tag{3.30}$$

where log is the matrix logarithm. The $\widetilde{\boldsymbol{A}}_C$ matrix is used to find the identified modal parameters using Eqs. 3.16, 3.20 and 3.21 giving $\widetilde{\boldsymbol{\psi}}_d$, $\widetilde{\boldsymbol{\zeta}}$ and $\widetilde{\boldsymbol{f}}$. The identified mode shapes are damped since the $\widetilde{\boldsymbol{A}}_C$ matrix includes damping contributions. All identified parameters are indicated with the accent $\widetilde{\ }$.

While the $\boldsymbol{A}$ matrix assembled from the numerical matrices of the model (Eq. 3.15) is in a physical basis, the basis of the identified $\widetilde{\boldsymbol{A}}_D$ matrix corresponds to some unknown transformation of the physical basis of the model. Therefore, it is not possible to extract information about the structural matrices directly from $\widetilde{\boldsymbol{A}}_D$ without further resolution of the unknown transformation. Instead, structural information is obtained through the model updating process, which compares the

numerical model and identified modal parameters. To enable their comparison, both sets of mode shapes must be in the sensor basis.

The identified output matrix, $\widetilde{\boldsymbol{E}}$, transforms the identified eigenvectors into the sensor-based mode shapes as follows:

$$^{s}\widetilde{\boldsymbol{\phi}}_{d} = \widetilde{\boldsymbol{E}}\widetilde{\boldsymbol{\psi}}_{d} \tag{3.31}$$

where the additional superscript ^{s} denotes the sensor basis.

3.2.6 Model updating

The goal of modal-model updating is to tune a vector of parameters of the model so that its modal properties match those identified from sensor data. This is achieved in this chapter by minimising the following objective function, $J(\boldsymbol{\chi})$:

$$J(\boldsymbol{\chi}) = \sum_{i=1}^{m} \left[\left(\frac{f_i(\boldsymbol{\chi}) - \widetilde{f}_i}{\widetilde{f}_i} \right)^2 + \left(1 - \mathrm{MAC}\left({}^{s}\bar{\boldsymbol{\phi}}_{u,i}(\boldsymbol{\chi}),\ {}^{s}\widetilde{\bar{\boldsymbol{\phi}}}_{i}^{C} \right) \right) \right] \tag{3.32}$$

where m is the number of identified modes used for comparison and $\boldsymbol{\chi}$ is the vector of parameters to be tuned. In this chapter $m = 4$ and $\boldsymbol{\chi}$ are the foundation macro-element compliance parameters, c_{11}, c_{12} and c_{22}. Although satisfactory convergence was also achieved in this work when the objective function was formulated solely with the frequencies, the results presented utilise the frequencies and mode shapes for generality. Although factors are often used to weight the different contributions to the objective function, no such technique was applied in this work.

$f_i(\boldsymbol{\chi})$ and ${}^{s}\bar{\boldsymbol{\phi}}_{u,i}(\boldsymbol{\chi})$ are the numerical model modal parameters realised for a specific $\boldsymbol{\chi}$ following the procedures set out in Sections 3.2.2 and 3.2.4. ${}^{s}\bar{\boldsymbol{\phi}}_{u,i}(\boldsymbol{\chi})$ are undamped mode shapes calculated using Eq. 3.12, transformed to the sensor basis with Eq. 3.19 and finally normalised with Eq. 3.23.

$\widetilde{f}_i$ and ${}^{s}\widetilde{\bar{\boldsymbol{\phi}}}_{i}^{C}$ are the identified modal parameters estimated using the procedures

set out in Sections 3.2.2 and 3.2.5. ${}^{s}\widetilde{\widetilde{\boldsymbol{\phi}}}_i^C$ are damped mode shapes calculated from $\widetilde{\boldsymbol{A}}_C$ using Eq. 3.16, then transformed to the sensor basis using Eq. 3.31 and finally complex normalised using Eq. 3.25.

The MAC (Allemang & Brown, 1982) gives a value between 0 and 1 that indicates the degree of correlation between two mode shapes, using the following equation:

$$\mathrm{MAC}\left(\boldsymbol{\phi}_i, \widetilde{\boldsymbol{\phi}}_i\right) = \frac{\left|\boldsymbol{\phi}_i \widetilde{\boldsymbol{\phi}}_i^{\,*}\right|^2}{\boldsymbol{\phi}_i \boldsymbol{\phi}_i^{\,*} \widetilde{\boldsymbol{\phi}}_i \widetilde{\boldsymbol{\phi}}_i^{\,*}} \tag{3.33}$$

where * denotes the complex conjugate.

The MATLAB fminsearch optimisation algorithm, which uses the Nelder-Mead simplex algorithm (Lagarias, Reeds, Wright, & Wright, 1998), is adopted to minimize the objective function of Eq. 3.32. This is an unconstrained nonlinear optimisation algorithm that finds the minimum of a multi-variable function, starting from a user-specified initial estimate. The algorithm uses a derivative-free direct search method. This derivative-free method was found to give more consistent results than the derivative-based approach fminunc, applied with numerically calculated derivatives, since J was found to be non-smooth with respect to $\boldsymbol{\chi}$ for various cases in this thesis. Throughout the thesis, 'tolX' and 'tolFun', the relative tolerances on the optimisation current point and function value, are 1×10^{-6}.

The model used in this study is unbiased, as the same model is used for simulating the data and the model updating procedure, so the effect of modelling errors is removed. In practice, field monitoring data would be generated by other processes that are not exactly captured by the model used for the updating. For identification using field data, the model must be a reasonable and unbiased approximation of the physical process that generated the data. For a discussion on the effects of a potential bias in the model, see Song's works (e.g. Song, Behmanesh, Moaveni, & Papadimitriou, 2019).

3.3 Exploring modal behaviour

All the results presented in this chapter adopt the model wind turbine parked with the rotor locked and the blades pitched to 0°. All structural properties are as specified for the NREL 5MW reference turbine (J. Jonkman et al., 2009) other than the RNA inertia which is given in Table 3.1 (z denotes the vertical axis). See Figure 3.2a for the main model dimensions. The baseline foundation stiffness matrix, $\boldsymbol{K}_{F0}$, and equivalent compliance matrix, $\boldsymbol{C}_{F0}$, are given in the following equations:

$$\boldsymbol{K}_{F0} = \begin{bmatrix} 0.0257 & 0.225 \\ 0.225 & 2.63 \end{bmatrix} \times 10^{11} \text{ N/m} \tag{3.34}$$

$$\boldsymbol{C}_{F0} = \boldsymbol{K}_{F0}^{-1} = \begin{bmatrix} 1.55 & -0.133 \\ -0.133 & 0.0152 \end{bmatrix} \times 10^{-9} \text{ m/N} \tag{3.35}$$

Table 3.1: Rotor nacelle assembly modelled inertias.

Inertia, I, term	Reference NREL 5MW [kgm^2]	Modified [kgm^2]
I_{FA-FA}	3.9e7	1.4e8
I_{SS-SS}	2.3e7	2.3e7
I_{zz}	2.5e7	2.5e7
I_{FA-z}	-1.3e6	-1.0e7

In Section 3.3.1 the source of the non-proportional damping is investigated through forward modelling of the OWT model, with the original reference NREL 5MW RNA inertia given in Table 3.1, at a variety of wind speeds.

In Section 3.3.2 the model, with the modified RNA inertia, is used to generate simulated data. The system identification method N4SID is then applied to these data to identify the modal parameters.

3.3.1 Investigation of non-proportional damping and complex normalisation

Non-proportional damping, as explained in Section 3.2.3, is explored in this thesis by investigating the relationship between the speed of the wind excitation and the model mode shapes, using FAST. The model was linearised at wind speeds ranging from 0 to 20 m/s, providing the system $\boldsymbol{M}$, $\boldsymbol{K}$, $\boldsymbol{D}$ and $\boldsymbol{E}$ matrices. The damped mode shapes, $\boldsymbol{\psi}_d$, are then calculated by solving the eigenvalue problem given by Eq. 3.16, then transformed to the sensor basis using Eq. 3.18 and real normalised using Eq. 3.24 to give ${}^s\bar{\boldsymbol{\phi}}^R$. The real normalisation method is used here to demonstrate the effect of the damping. The undamped mode shapes, $\boldsymbol{\phi}_u$, are calculated by solving the eigenvalue problem given by Eq. 3.12, transformed to the sensor basis using Eq. 3.19 and finally normalised using Eq. 3.23 to give ${}^s\bar{\boldsymbol{\phi}}_u$.

Figure 3.4 shows a plan view of the resulting undamped, ${}^s\bar{\boldsymbol{\phi}}_u$, and damped, ${}^s\bar{\boldsymbol{\phi}}^R$, sensor-based mode shapes at a variety of wind speeds. The figure demonstrates that the inclusion of damping results in mode shapes whose components are not purely in either of the FA or SS directions, but have elements of comparable magnitude in both principle directions.

To further demonstrate this coupling, a direction ratio, DR, is calculated for each vibration mode shape, ${}^s\bar{\boldsymbol{\phi}}^R$, as follows:

$$DR = \frac{{}^s\bar{\boldsymbol{\phi}}^R_{1,FA}\,(top)}{{}^s\bar{\boldsymbol{\phi}}^R_{1,SS}\,(top)}, \frac{{}^s\bar{\boldsymbol{\phi}}^R_{2,SS}\,(top)}{{}^s\bar{\boldsymbol{\phi}}^R_{2,FA}\,(top)}, \frac{{}^s\bar{\boldsymbol{\phi}}^R_{3,FA}\,(mid)}{{}^s\bar{\boldsymbol{\phi}}^R_{3,SS}\,(mid)}, \frac{{}^s\bar{\boldsymbol{\phi}}^R_{4,SS}\,(mid)}{{}^s\bar{\boldsymbol{\phi}}^R_{4,FA}\,(mid)} \tag{3.36}$$

where FA and SS denote the components of the mode shape along the FA and SS vibration planes respectively, and *top* and *mid* refer to the sensor at the top and middle cross-sections of the tower respectively. This is because the coupling is most dominant at the top sensor for modes 1 and 2 and the middle sensor for modes 3 and 4.

Figure 3.5 shows the relationship between DR and the wind speed for each

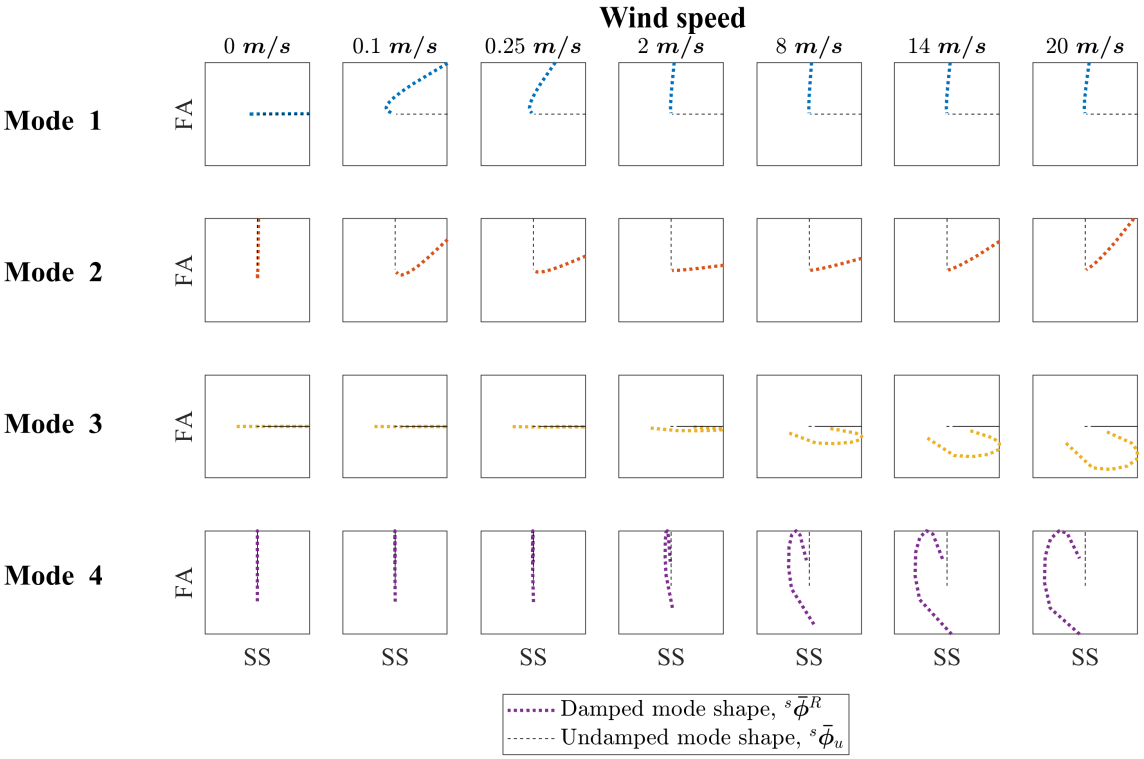


Figure 3.4: Plan view of mode shapes of the OWT model with reference NREL 5MW RNA inertia properties, showing directional coupling with wind speed.

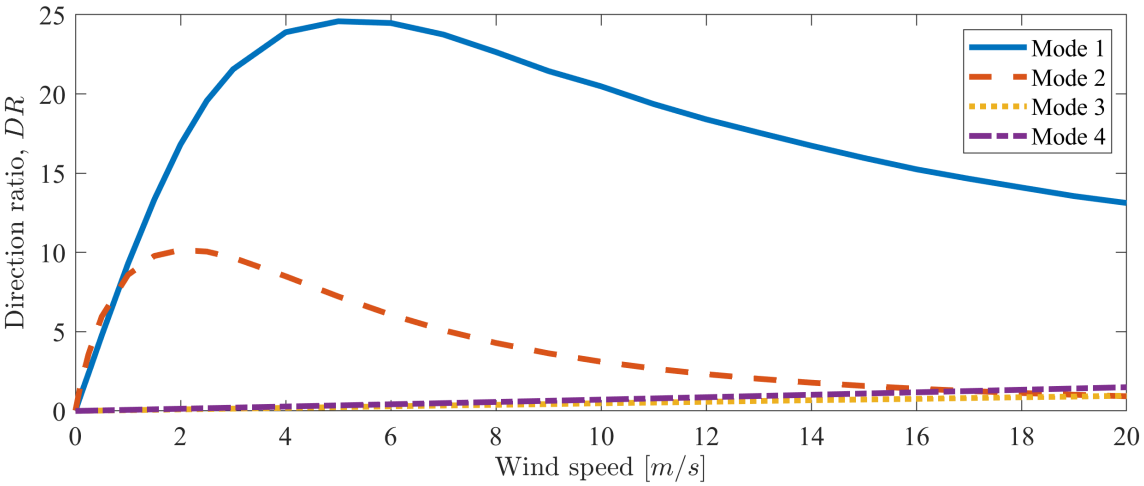


Figure 3.5: Variation of mode shape direction ratio with wind speed for modes 1 to 4.

vibration mode. It can be seen in both Figures 3.4 and 3.5 that at zero wind speed ${}^s\bar{\phi}^R$ present as entirely SS or FA, in agreement with ${}^s\bar{\phi}_u$, but even at very low wind speeds, for example 0.25 m/s, modes 1 and 2 appear to vibrate in the planes perpendicular to the respective planes of vibration for the undamped structure.

Similar effects on the higher modes appear at higher wind speeds.

This result shows that if one were to assume nearly proportional damping, expecting the arising mode shapes to be independent of damping and hence use the real normalisation procedure, one could be misled as to the true nature of the mode, disregard the data as erroneous or seek to tune the model to correct the perceived 'discrepancy'.

In order to match the predicted and measured behaviour during model updating, the model would need to be capable of accurately predicting ${}^{s}\bar{\boldsymbol{\phi}}^{R}$. This would require an accurate representation of the aerodynamics and wind conditions during the monitoring period, in order to replicate the structure's damping matrix very closely, with an emphasis on the non-diagonal elements that result in the non-proportional behaviour. Hence, it would be highly challenging for models without close representation of the blades to be able to predict SS and FA modes that accurately matched those observed. This is a common problem for offshore wind support structure designers, since the detailed rotor properties are often commercially confidential.

Modelling damping is highly challenging (Rao, 2011) and in practice typical aerodynamic rotor models are unlikely to capture the aerodynamic damping with sufficient fidelity across all operational conditions. Furthermore, accurate modal identification of damping is even more challenging (P. T. Brewick & Smyth, 2013). Therefore, it would be highly beneficial to identify the undamped mode shapes of a structure directly and compare to an undamped model.

Normalising the mode shapes with the complex normalisation technique to give ${}^{s}\bar{\boldsymbol{\phi}}^{C}$ (using Eq. 3.25) and comparing with the previously calculated ${}^{s}\bar{\boldsymbol{\phi}}^{R}$ allows the comparison of the two normalisation techniques. Figure 3.6 compares these mode shapes with the corresponding undamped mode shapes at a wind speed of 8 m/s. The close match seen between ${}^{s}\bar{\boldsymbol{\phi}}^{C}$ and ${}^{s}\bar{\boldsymbol{\phi}}_{u}$ demonstrates that the complex normalisation procedure provides mode shapes that are close approximations of the undamped mode shapes.

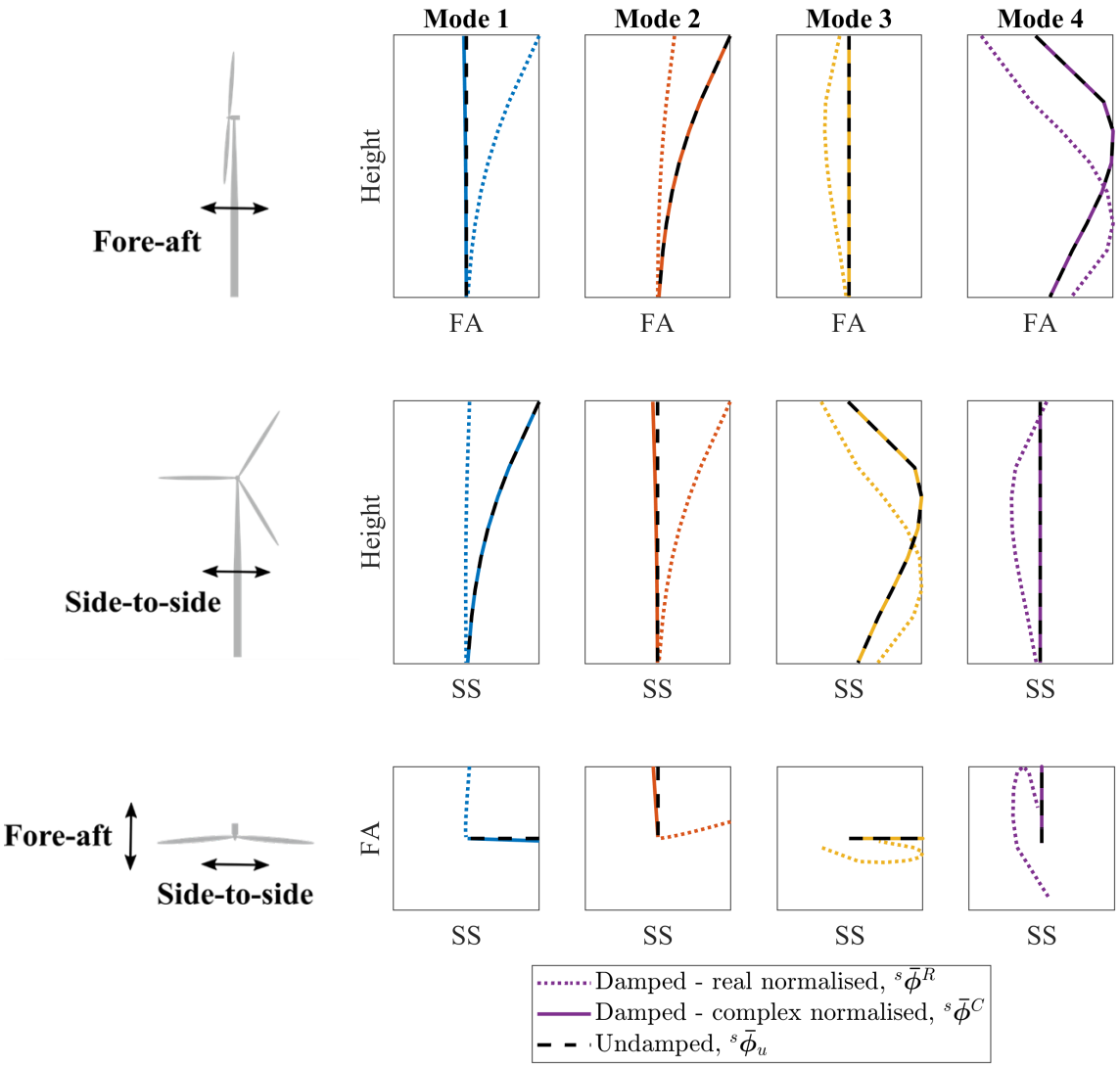


Figure 3.6: Comparison of FAST predicted undamped mode shapes against damped mode shapes, normalised using either real or complex normalisation, at a wind speed of 8 m/s.

It is acknowledged that the non-proportional damping predicted in this thesis will be subject to modelling inaccuracy, but this finding demonstrates how susceptible a wind turbine's dynamic properties are to aerodynamic damping. Thus estimation of the undamped mode shapes, using a technique such as the complex normalisation method, may provide valuable information when using these mode shapes for subsequent applications, such as model updating.

3.3.2 Identification of modal parameters

The wind turbine model was used to generate simulated data for the seven parameter cases shown in Table 3.2.

Table 3.2: Parameter values for simulated data cases.

Case	Wind speed $[\frac{m}{s}]$	Noise level [%]	Foundation
1	12	0.1	$\boldsymbol{K}_{F0}, \boldsymbol{C}_{F0}$
2	12	1	$\boldsymbol{K}_{F0}, \boldsymbol{C}_{F0}$
3	12	5	$\boldsymbol{K}_{F0}, \boldsymbol{C}_{F0}$
4	3	1	$\boldsymbol{K}_{F0}, \boldsymbol{C}_{F0}$
5	25	1	$\boldsymbol{K}_{F0}, \boldsymbol{C}_{F0}$
6	12	1	$0.5\boldsymbol{K}_{F0}, 2\boldsymbol{C}_{F0}$
7	12	1	$2\boldsymbol{K}_{F0}, 0.5\boldsymbol{C}_{F0}$

The synthetic wind data were generated with a stochastic turbulent wind simulator, TurbSim (B. J. Jonkman & Kilcher, 2012), using the International Electrotechnical Commission Kaimal Model (IEC, 2005) with wind turbulence characteristic 'B' and mean wind speed as given in Table 3.2 . All cases were simulated with stationary water.

For each case, the simulated output data are accelerations in the FA and SS directions for four sensors, $s_j, j = 1...4$, located at heights of 10, 35, 60 and 87m respectively above the MSL, which is 20m above the seabed, as depicted in Figure 3.2a. The acceleration data, $\boldsymbol{\alpha}$, are gathered in the following vector:

$$\begin{aligned}\boldsymbol{y}_{k0} = \{&\boldsymbol{\alpha}_{FA}(s_4), \boldsymbol{\alpha}_{SS}(s_4), \boldsymbol{\alpha}_{FA}(s_3), \boldsymbol{\alpha}_{SS}(s_3), \boldsymbol{\alpha}_{FA}(s_2), \boldsymbol{\alpha}_{SS}(s_2), ... \\ &\boldsymbol{\alpha}_{FA}(s_1), \boldsymbol{\alpha}_{SS}(s_1)\}^T\end{aligned} \tag{3.37}$$

where $\boldsymbol{y}_{k0}$ denotes that this is a discrete-time output vector sampled with time step, k. The '0' subscript signifies that this is the raw signal that is yet to be contaminated with noise.

The data were sampled at a frequency of 100 Hz ($k = 0.01s$) for a length of 20 minutes giving $N = 60001$ data points for each signal. FAST was used to simulate 35 minutes of data and the first 15 minutes were discarded to ensure any transient behaviour was omitted. The acceleration output signals were then contaminated with Gaussian white noise to form the eight discrete-time output signals, $\boldsymbol{y}_k$, to be supplied to the identification method. This process is demonstrated by the following equations for the calculation of the 1st contaminated output signal, $\boldsymbol{y}_k(1)$:

$$\boldsymbol{y}_k(1) = \boldsymbol{y}_{k0}(1) + \frac{\eta}{100}\sqrt{\frac{1}{N}\sum_{k=1}^{N}\left|d\boldsymbol{y}_{k0}(1,k)\right|^2} \tag{3.38}$$

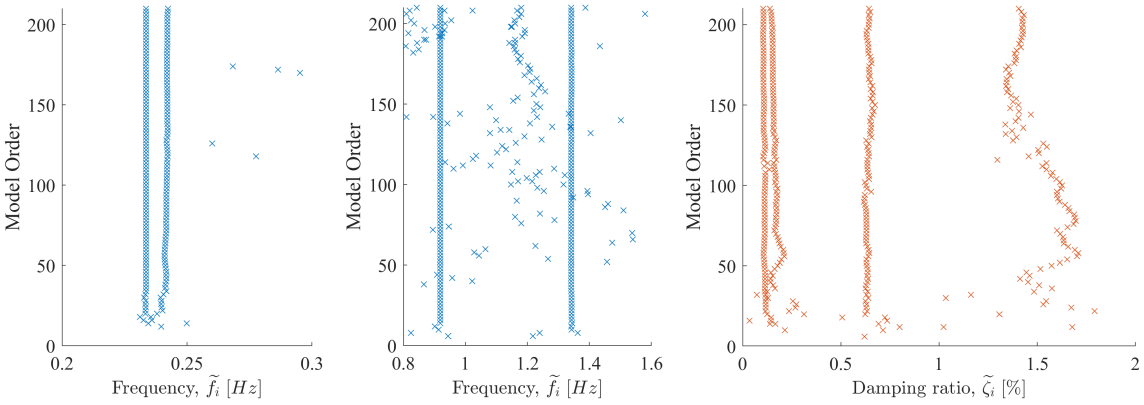
where the raw signal, $\boldsymbol{y}_{k0}(1)$, is contaminated with the noise level, η, multiplied by the root-mean-square of the detrended raw signal, $d\boldsymbol{y}_{k0}(1)$:

$$d\boldsymbol{y}_{k0}(1) = \boldsymbol{y}_{k0}(1) - \frac{1}{N}\sum_{k=1}^{N}\boldsymbol{y}_{k0}(1,k) \tag{3.39}$$

with noise levels, η, given in Table 3.2 .

The system identification method N4SID was applied to the simulated output data, $\boldsymbol{y}_k$, for the seven parameter cases. The input data, $\boldsymbol{u}_k$, are not used and are considered as unmeasured since it is not practical to measure these in reality. Therefore, N4SID calculates estimates of $\widetilde{\boldsymbol{A}}_D$ and $\widetilde{\boldsymbol{E}}$ of the discrete system, given in Eq. 3.29, for a specified system order. The order of a system is twice the number of DOF, which for the numerical model in this chapter is 8. However, an order much higher than 16 is needed to identify the system, with the extra modes corresponding to modelling of the noise terms, due to $\boldsymbol{u}_k$ not being provided to N4SID.

The equivalent continuous system $\widetilde{\boldsymbol{A}}_C$ is calculated using Eq. 3.30, followed by subsequent solution of the eigenvalue problem (Eq. 3.16) to give the identified modal parameters $\widetilde{\boldsymbol{\phi}}_d$ and $\widetilde{\boldsymbol{\lambda}}_d$. $\widetilde{\boldsymbol{\phi}}_d$ are then transformed to the sensor basis (Eq. 3.31) and either real (Eq. 3.24) or complex (Eq. 3.25) normalised to give ${}^s\widetilde{\boldsymbol{\phi}}^R$ or



(a) (b) (c)

Figure 3.7: Stabilisation diagrams, showing identified modal properties at varying model order, for case 2 – (a) frequencies for modes 1 and 2, (b) frequencies for modes 3 and 4, (c) damping ratios.

${}^s\widetilde{\boldsymbol{\phi}}^C$ respectively. Finally $\widetilde{\boldsymbol{f}}$ and $\widetilde{\boldsymbol{\zeta}}$ are calculated from $\widetilde{\boldsymbol{\lambda}}_d$ with Eqs. 3.20 and 3.21.

The order of the system was gradually increased in increments of 2 to achieve stabilisation. An example stabilisation diagram is shown in Figure 3.7 for parameter case 2 (outlined in Table 3.2).

In this chapter, stabilisation is deemed to be achieved at an order when the identified frequencies and damping ratios appear to be practically invariant as the model order is increased. A model order of 200 was used across all cases.

Tables 3.3 to 3.5 compare the identified modal parameters with the model modal parameters for the seven cases. The identified complex normalised mode shapes, ${}^s\widetilde{\bar{\boldsymbol{\phi}}}^C$, are compared to the model undamped mode shapes, ${}^s\bar{\boldsymbol{\phi}}_u$, using the MAC (Eq. 3.33).

Table 3.3 compares the effect of the noise level (cases 1 to 3). There is a slight positive correlation between the noise level and the overall match between the identified and model parameters, but in general there is very little difference, which suggests that, up to a reasonable limit, the quality of the sensor is not of paramount importance.

Table 3.4 compares the effect of the wind speed, showing the results for cases 2, 4 and 5. 3 m/s and 25 m/s are the cut-in and cut-out wind speeds respectively

Table 3.3: Comparison of model natural frequencies (f_i) and mode shapes (${}^s\bar{\boldsymbol{\phi}}_{u,i}$) against identified natural frequencies ($\widetilde{f}_i$) and mode shapes (${}^s\widetilde{\bar{\boldsymbol{\phi}}}_i^C$), for cases 1 - 3 (varied noise level).

Mode, i	f_i [Hz]	$\widetilde{f}_i$ [Hz]			MAC $\left({}^s\bar{\boldsymbol{\phi}}_{u,i},\ {}^s\widetilde{\bar{\boldsymbol{\phi}}}_i^C \right)$		
		$\eta = 0.1\%$	$\eta = 1\%$	$\eta = 5\%$	$\eta = 0.1\%$	$\eta = 1\%$	$\eta = 5\%$
1	0.234	0.234 (-0.009%)	0.234 (-0.006%)	0.234 (-0.005%)	1.000	1.000	1.000
2	0.242	0.242 (-0.086%)	0.242 (-0.065%)	0.242 (-0.008%)	1.000	1.000	1.000
3	0.919	0.919 (-0.016%)	0.919 (-0.015%)	0.919 (-0.014%)	1.000	1.000	1.000
4	1.343	1.341 (-0.14%)	1.342 (-0.099%)	1.342 (-0.096%)	1.000	1.000	1.000

(% error) shown in brackets

Table 3.4: Comparison of model natural frequencies (f_i) and mode shapes (${}^s\bar{\boldsymbol{\phi}}_{u,i}$) against identified natural frequencies ($\widetilde{f}_i$) and mode shapes (${}^s\widetilde{\bar{\boldsymbol{\phi}}}_i^C$), for cases 2, 4 and 5 (varied wind speed).

Mode, i	f_i [Hz]	$\widetilde{f}_i$ [Hz]			MAC $\left({}^s\bar{\boldsymbol{\phi}}_{u,i},\ {}^s\widetilde{\bar{\boldsymbol{\phi}}}_i^C \right)$		
		3 m/s	12 m/s	25 m/s	3 m/s	12 m/s	25 m/s
1	0.234	0.234 (-0.018%)	0.234 (-0.006%)	0.234 (0.014%)	0.995	1.000	0.988
2	0.242	0.242 (-0.087%)	0.242 (-0.065%)	0.242 (-0.15%)	1.000	1.000	0.999
3	0.919	0.919 (0.011%)	0.919 (-0.015%)	0.920 (0.043%)	1.000	1.000	1.000
4	1.343	1.340 (-0.024%)	1.342 (-0.099%)	1.343 (-0.063%)	1.000	1.000	1.000

(% error) shown in brackets

Table 3.5: Comparison of model natural frequencies (f_i) and mode shapes (${}^s\bar{\boldsymbol{\phi}}_{u,i}$) against identified natural frequencies ($\widetilde{f}_i$) and mode shapes (${}^s\widetilde{\bar{\boldsymbol{\phi}}}_i^C$) for cases 2, 6 and 7 (varied foundation stiffness).

Mode, i	f_i [Hz]			$\widetilde{f}_i$ [Hz]			MAC $\left({}^s\bar{\boldsymbol{\phi}}_{u,i},\ {}^s\widetilde{\bar{\boldsymbol{\phi}}}_i^C\right)$		
	$0.5\boldsymbol{K}_{F0}$	$\boldsymbol{K}_{F0}$	$2\boldsymbol{K}_{F0}$	$0.5\boldsymbol{K}_{F0}$	$\boldsymbol{K}_{F0}$	$2\boldsymbol{K}_{F0}$	$0.5\boldsymbol{K}_{F0}$	$\boldsymbol{K}_{F0}$	$2\boldsymbol{K}_{F0}$
1	0.211	0.234	0.248	0.211 (0.032%)	0.234 (-0.006%)	0.248 (0.059%)	0.972	1.000	0.954
2	0.217	0.242	0.258	0.216 (-0.26%)	0.242 (-0.065%)	0.258 (0.002%)	1.000	1.000	1.000
3	0.841	0.919	0.977	0.842 (0.049%)	0.919 (-0.015%)	0.977 (0.039%)	1.000	1.000	1.000
4	1.144	1.343	1.543	1.139 (-0.44%)	1.342 (-0.099%)	1.544 (0.13%)	1.000	1.000	1.000

(% error) shown in brackets

for this turbine, so a wide range of typical conditions have been covered with these investigations. There are only small differences between the parameters identified at each wind speed, which indicates that a preference towards using data measured at a particular wind speed is not necessary.

Table 3.5 compares the effect of the foundation stiffness, using cases 2, 6 and 7. Once again the identification errors are small and vary slightly but with no significant trend over the examined range of stiffnesses.

The impact of the modal identification errors on the foundation identification will be investigated in Section 3.4.2.

Looking across all the results, although $\widetilde{f}_1$ is generally the most accurately identified frequency, ${}^s\widetilde{\bar{\boldsymbol{\phi}}}_1^C$ is the least accurately identified mode shape. The SS mode frequencies ($\widetilde{f}_1$ and $\widetilde{f}_3$) are consistently identified with greater accuracy than the FA ($\widetilde{f}_2$ and $\widetilde{f}_4$). The damping ratios are poorly identified, which is typically the case for output only identification methods (P. T. Brewick & Smyth, 2013), so damping is not adopted for optimisation during the model updating method.

Figure 3.8 compares both identified ${}^s\widetilde{\bar{\boldsymbol{\phi}}}^R$ and ${}^s\widetilde{\bar{\boldsymbol{\phi}}}^C$ against the model ${}^s\bar{\boldsymbol{\phi}}_u$ to

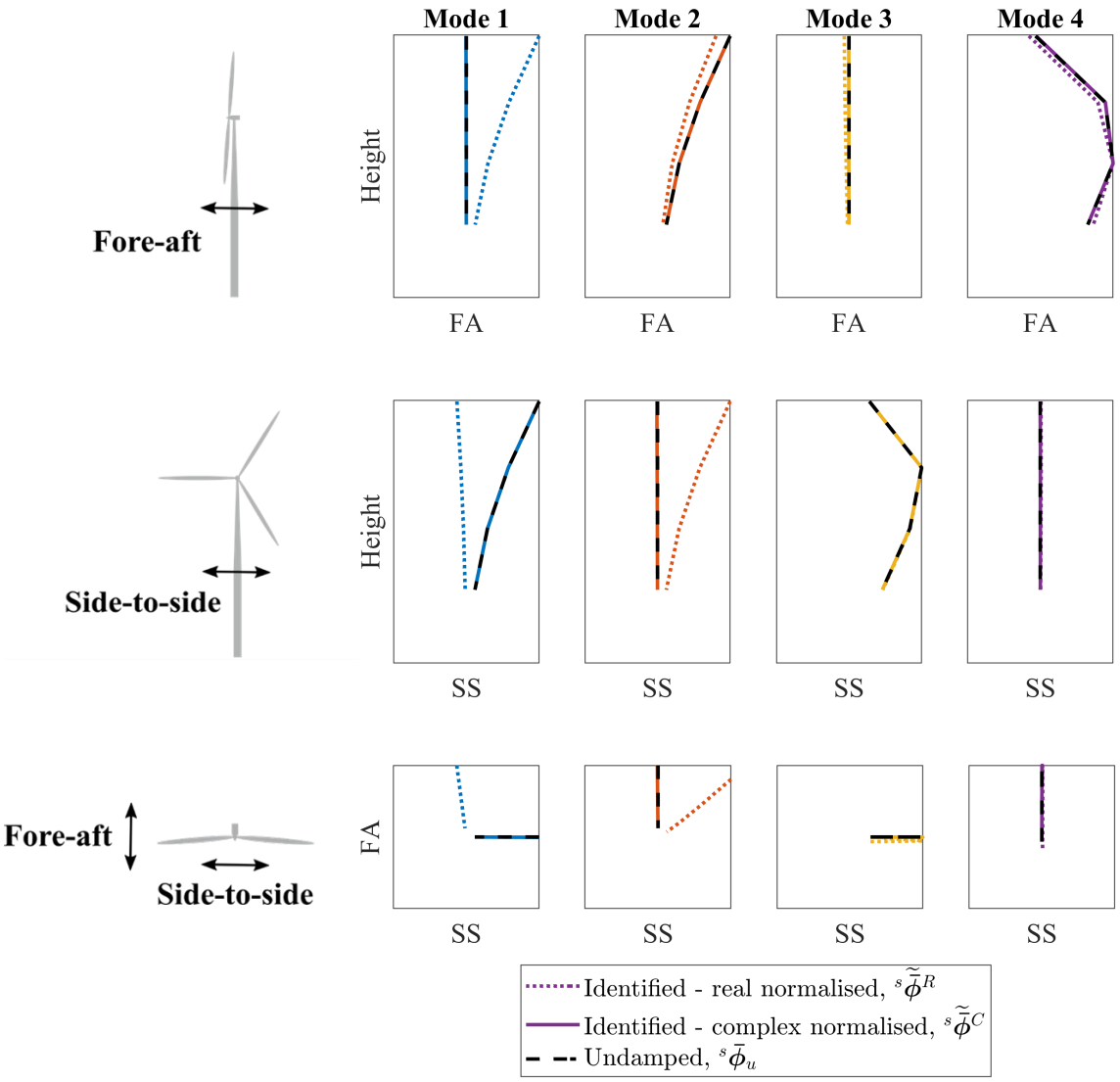


Figure 3.8: Comparison of model undamped mode shapes (${}^s\bar{\phi}_{u,i}$) against identified damped mode shapes, normalised using either real or complex normalisation (${}^s\tilde{\bar{\phi}}_i^R$ or ${}^s\tilde{\bar{\phi}}_i^C$), for case 1.

show the difference between the identified mode shapes processed with the real and complex normalisation techniques for case 1. The corresponding MAC values are given in Table 3.6.

Figure 3.8 highlights the importance of the complex normalisation procedure if an accurate estimate of the undamped model mode shapes, ${}^s\bar{\phi}_u$, is desired. In general there is very good agreement between ${}^s\tilde{\bar{\phi}}^C$ and ${}^s\bar{\phi}_u$, as reflected in the MAC values given in Table 3.6. Furthermore, it can be seen in Figure 3.8 that the discrepancy between ${}^s\tilde{\bar{\phi}}^R$ and ${}^s\bar{\phi}_u$ is significant. Consideration of ${}^s\tilde{\bar{\phi}}^R$ alone may lead

Table 3.6: MAC of model undamped mode shapes (${}^s\bar{\boldsymbol{\phi}}_{u,i}$) compared with identified mode shapes normalised with either the real or complex normalisation techniques (${}^s\tilde{\bar{\boldsymbol{\phi}}}_i^R$ or ${}^s\tilde{\bar{\boldsymbol{\phi}}}_i^C$ respectively), for case 1.

Mode, i	MAC $\left({}^s\bar{\boldsymbol{\phi}}_{u,i},\ {}^s\tilde{\bar{\boldsymbol{\phi}}}_i^C \right)$	MAC $\left({}^s\bar{\boldsymbol{\phi}}_{u,i},\ {}^s\tilde{\bar{\boldsymbol{\phi}}}_i^R \right)$
1	1.0000	0.0164
2	0.9999	0.3802
3	1.0000	0.9954
4	1.0000	0.9890

to the erroneous assumption that the 1st vibration mode is a FA mode, and perhaps consequently that the 2nd vibration mode is a SS mode. The potential impact on the foundation identification, of those erroneous, yet phenomenologically reasonable (based on ${}^s\tilde{\bar{\boldsymbol{\phi}}}^R$) conclusions, is investigated in Section 3.4.1 for this specific case (case 1).

3.4 Application to model updating

This section focuses on the model updating application, using the modal parameters identified in Section 3.3.2.

Section 3.4.1 details the foundation identification procedure for a specific case at a wind speed of 12 m/s. The form of the foundation properties best suited for optimisation and comparison is explored and the impact of normalising the mode shapes using the 'real' and 'complex' techniques is compared.

Section 3.4.2 explores the potential sources of errors in the foundation identification results and compares the effect of wind speed, foundation stiffness and the data signal-to-noise ratio on the foundation identification.

3.4.1 Foundation identification: case 1

This section details the foundation identification model updating procedure for case 1. Case 1 consists of simulated data that have been contaminated with 0.1% white noise (Eq. 3.38) for a wind turbine with the baseline foundation stiffness, $\boldsymbol{K}_{F0}$, at a wind speed of 12 m/s, as shown in Table 3.2.

Identifying compliance vs stiffness terms

The identified modal parameters ($^s\widetilde{\widetilde{\boldsymbol{\phi}}}^C$ and $\widetilde{\boldsymbol{f}}$) for case 1, which were presented in Section 3.3.2 (Table 3.3 and Figure 3.8), are used to identify the foundation properties with the objective function given in Eq. 3.32. Both the stiffness properties and the compliance properties are trialled as the optimisation parameters, to compare their suitability.

Table 3.7 shows the identified $\widetilde{\boldsymbol{K}}_F$ and $\widetilde{\boldsymbol{C}}_F$ matrices, where the initial estimate given was $2\boldsymbol{K}_{F0}$ (or equivalently stated $0.5\boldsymbol{C}_{F0}$). $\boldsymbol{\epsilon}_K$ and $\boldsymbol{\epsilon}_C$ are the corresponding percentage errors, with respect to the true values, $\boldsymbol{K}_{F0}$ and $\boldsymbol{C}_{F0}$.

Firstly focusing on $\widetilde{\boldsymbol{C}}_F$, the model updating process shows good performance in reducing the error in the terms of the compliance matrix, $\boldsymbol{\epsilon}_C$, from the initial estimate at 50% of the true values. To give some context to the residual foundation compliance errors, when calculating the foundation macro-element parameters equivalent to a given set of soil profile parameters, it is not uncommon to see differences on the order of 100% when choosing different methods for this calculation (McAdam, Bajrić, Chatzis, Byrne, & Vanden Haute, 2020). Two common methods for this calculation are the $p-y$ method (API, 2010; DNV GL, 2016) or PISA

Table 3.7: Identified stiffness matrix, $\widetilde{\boldsymbol{K}}_F$, and compliance matrix, $\widetilde{\boldsymbol{C}}_F$, estimated through model updating, for case 1.

Case	$\widetilde{\boldsymbol{K}}_F$ [N/m]	$\boldsymbol{\epsilon}_K$ [%]	$\widetilde{\boldsymbol{C}}_F$ [m/N]	$\boldsymbol{\epsilon}_C$ [%]
1	$\begin{bmatrix} 0.0949 & 0.782 \\ 0.782 & 7.04 \end{bmatrix} \times 10^{11}$	$\begin{bmatrix} 269 & 247 \\ 247 & 168 \end{bmatrix}$ %	$\begin{bmatrix} 1.25 & -0.139 \\ -0.139 & 0.0154 \end{bmatrix} \times 10^{-9}$	$\begin{bmatrix} -19.4 & 4.3 \\ 4.3 & 1.2 \end{bmatrix}$ %

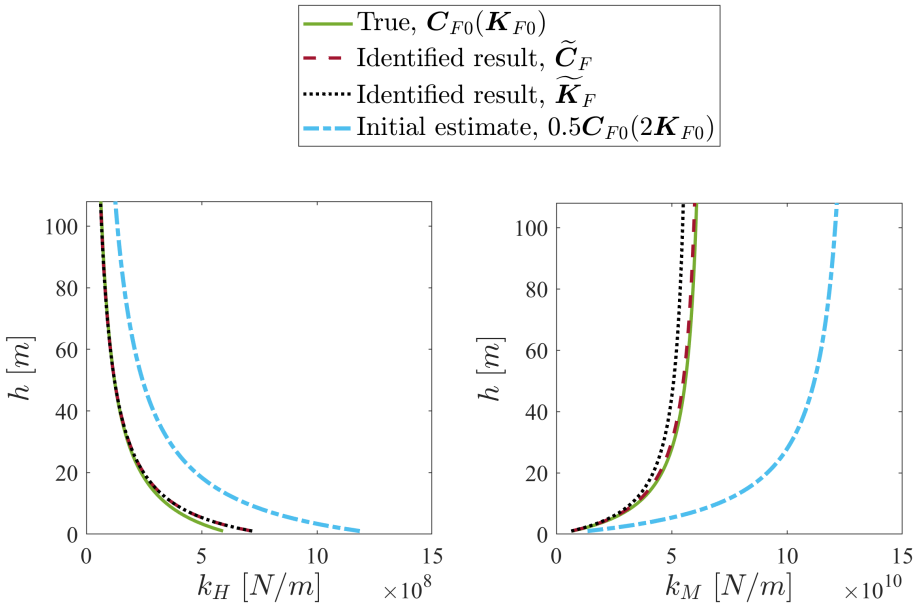


Figure 3.9: Variation of equivalent lateral and rotational stiffness (k_H and k_M) with load eccentricity (h), for the true, initial estimate and model updated foundation stiffness and compliance matrices (identified results), for case 1.

(Byrne et al., 2017). Focusing on $\widetilde{\boldsymbol{K}}_F$ in Table 3.7, the errors, $\boldsymbol{\epsilon}_K$, are much larger, and would not suggest that the foundation properties have been identified well.

As discussed in Section 3.2.6 plotting the h, k_H and h, k_M relationships given in Eqs. 3.4 and 3.5 provides an effective way to compare the behaviour of the model and identified foundations. Figure 3.9 shows these relationships for the identified foundation for case 1, comparing the true values calculated with $\boldsymbol{K}_{F0}$ (solid green line) against the identified values calculated with $\widetilde{\boldsymbol{C}}_F$ (dashed red line) and $\widetilde{\boldsymbol{K}}_F$ (dotted black line), and the initial estimate values (dash-dot blue line) calculated with $2\boldsymbol{K}_{F0}$ ($0.5\boldsymbol{C}_{F0}$). The close match between the green, red and black lines in the figure shows that the foundation behaviour is identified well, regardless of the significant apparent errors in the individual values of $\widetilde{\boldsymbol{K}}_F$ shown in Table 3.7. This demonstrates that, while using either $\boldsymbol{K}_F$ or $\boldsymbol{C}_F$ as the optimisation parameters leads to a good identification of the effective stiffness response (shown with Figure 3.9), analysing the errors, $\boldsymbol{\epsilon}_K$, in the individual terms of the coupled stiffness matrix $\boldsymbol{K}_F$ alone would likely lead to the conclusion of a poor identification. This suggests that the individual terms of $\boldsymbol{K}_F$ do not form a good basis for comparison of the foundation

Table 3.8: Matrices $\underline{\widetilde{\boldsymbol{C}}_F}$ and $\underline{\widetilde{\boldsymbol{K}}_F}$, found through inversion of the identified foundation matrices $\widetilde{\boldsymbol{K}}_F$ and $\widetilde{\boldsymbol{C}}_F$, and the associated errors compared to the true foundation properties.

Case	$\underline{\widetilde{\boldsymbol{C}}_F}$ [m/N]	$\underline{\boldsymbol{\epsilon}_C}$ [%]	$\underline{\widetilde{\boldsymbol{K}}_F}$ [N/m]	$\underline{\boldsymbol{\epsilon}_K}$ [%]
1	$\begin{bmatrix} 1.25 & -0.139 \\ -0.139 & 0.0169 \end{bmatrix} \times 10^{-9}$	$\begin{bmatrix} -19.3 & 4.6 \\ 4.6 & 11.1 \end{bmatrix}$ %	$\begin{bmatrix} 0.0221 & 0.199 \\ 0.199 & 1.80 \end{bmatrix} \times 10^{13}$	$\begin{bmatrix} 8600 & 8800 \\ 8800 & 6800 \end{bmatrix}$ %

behaviour, as matrices with very different values can represent foundations with very similar behaviour.

Furthermore, Table 3.8 shows $\underline{\widetilde{\boldsymbol{C}}_F}$ and $\underline{\widetilde{\boldsymbol{K}}_F}$, which are calculated by inverting matrices $\widetilde{\boldsymbol{K}}_F$ and $\widetilde{\boldsymbol{C}}_F$ respectively, and the associated errors, $\underline{\boldsymbol{\epsilon}_C}$ and $\underline{\boldsymbol{\epsilon}_K}$ found when comparing these to the true values, $\boldsymbol{C}_{F0}$ and $\boldsymbol{K}_{F0}$. On inverting $\widetilde{\boldsymbol{K}}_F$ to $\underline{\widetilde{\boldsymbol{C}}_F}$, it transpires that the result does actually correspond to a reasonable approximation of the true foundation compliances (as shown with $\underline{\boldsymbol{\epsilon}_C}$), and inverting $\widetilde{\boldsymbol{C}}_F$ results in stiffnesses, $\underline{\widetilde{\boldsymbol{K}}_F}$, that have even larger errors than those of $\widetilde{\boldsymbol{K}}_F$ (Table 3.7). This provides further evidence that in the case of identifying the stiffnesses, the problem is not a poorly performing optimisation, but a poor basis for comparison.

The compliances that are optimised directly, $\widetilde{\boldsymbol{C}}_F$, have smaller errors than those inverted from the identified stiffnesses, $\underline{\widetilde{\boldsymbol{C}}_F}$. So it is reasonable to conclude that the compliances are better conditioned for optimisation, as well as clearly giving a better basis for comparison with the true foundation properties. A possible explanation is because the form of the compliance matrix gives a more direct representation of the foundation behaviour, as the $\boldsymbol{C}_F$ terms correspond to physical aspects of the h, k_H and h, k_M relationships, as shown in Figure 3.3 in Section 3.2.1. In addition, Eqs. 3.4 and 3.5 demonstrated that the uncoupled spring stiffnesses, k_H and k_M, are dependent on all three coupled stiffness terms, whereas Eqs. 3.7 and 3.8 showed that they are each only dependent on two of the coupled compliance terms.

Investigating the propagation of errors when converting $\widetilde{\boldsymbol{C}}_F$ to $\underline{\widetilde{\boldsymbol{K}}_F}$, Eq. 3.40 shows how the errors in the stiffness matrix terms, $\underline{\boldsymbol{\epsilon}_K}$, are calculated from the

errors in the compliance matrix terms, $\boldsymbol{\epsilon}_C$, using:

$$\begin{aligned} \underline{\boldsymbol{\epsilon}_K} &= \begin{bmatrix} \underline{\epsilon_{k11}} & \underline{\epsilon_{k12}} \\ \underline{\epsilon_{k12}} & \underline{\epsilon_{k22}} \end{bmatrix} \\ &= \frac{c_{11}c_{22} - c_{12}^2}{c_{11}c_{22}(\epsilon_{c11}\epsilon_{c22} + \epsilon_{c11} + \epsilon_{c22} + 1) - c_{12}^2(\epsilon_{c12} + 1)^2} \begin{bmatrix} \epsilon_{c22} + 1 & \epsilon_{c12} + 1 \\ \epsilon_{c12} + 1 & \epsilon_{c11} + 1 \end{bmatrix} - 1 \end{aligned} \tag{3.40}$$

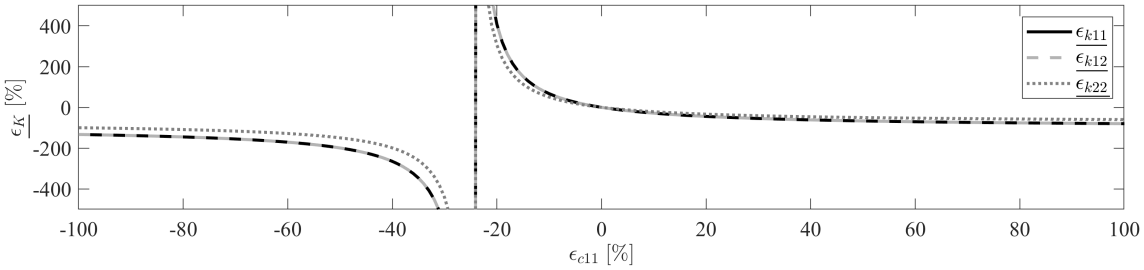
where ϵ_{c11}, ϵ_{c12} and ϵ_{c22} are the errors on the foundation compliance terms.

$\underline{\boldsymbol{\epsilon}_K}$ are dependent on the $\boldsymbol{C}_F$ terms as well as the error terms, $\boldsymbol{\epsilon}_C$, and it can be seen that a particular combination of $\boldsymbol{C}_F$ and $\boldsymbol{\epsilon}_C$ could cause the denominator to be equal to zero. This would result in a singularity and cause $\underline{\boldsymbol{\epsilon}_K}$ to be equal to infinity. This is represented graphically in Figure 3.10, which shows the relationships between the error terms, $\underline{\boldsymbol{\epsilon}_K}$ and $\boldsymbol{\epsilon}_C$, given compliance terms equal to $\boldsymbol{C}_{F0}$.

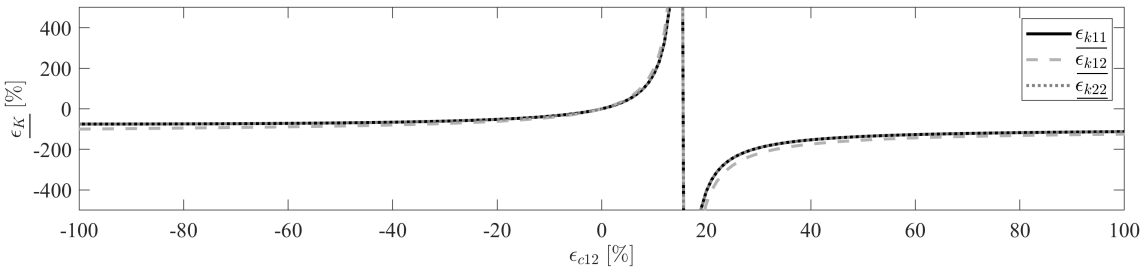
In Figures 3.10a, 3.10b and 3.10c the terms ϵ_{c11}, ϵ_{c12} and ϵ_{c22} are varied respectively between -100% and 100% (with the remaining two $\boldsymbol{\epsilon}_c$ terms in each case equal to zero). The resulting $\underline{\boldsymbol{\epsilon}_K}$ terms are plotted on the y-axis with different line styles, as per the legend. The figure confirms that certain combinations of the $\boldsymbol{\epsilon}_C$ terms cause the $\underline{\boldsymbol{\epsilon}_K}$ terms to tend toward infinity. For the particular case investigated in this section, case 1, the specific combination of $\boldsymbol{C}_{F0}$ and $\boldsymbol{\epsilon}_C$ terms happens to result in this asymptotic behaviour, causing the large errors in $\underline{\widetilde{\boldsymbol{K}}_F}$ presented in Table 3.8.

Finally, Table 3.9 compares the calculated modal parameters of the true model with foundation $\boldsymbol{K}_{F0}$ against those calculated with the model with foundation stiffness $\underline{\widetilde{\boldsymbol{K}}_F}$. The two sets of frequencies differ by a maximum of 0.3% and the MAC between the two sets of mode shapes is 1 for each mode, rounded to five significant figures, indicating almost exact correlation. These results demonstrate further evidence that the dynamic behaviour has been well identified, despite the large apparent errors in $\underline{\widetilde{\boldsymbol{K}}_F}$.

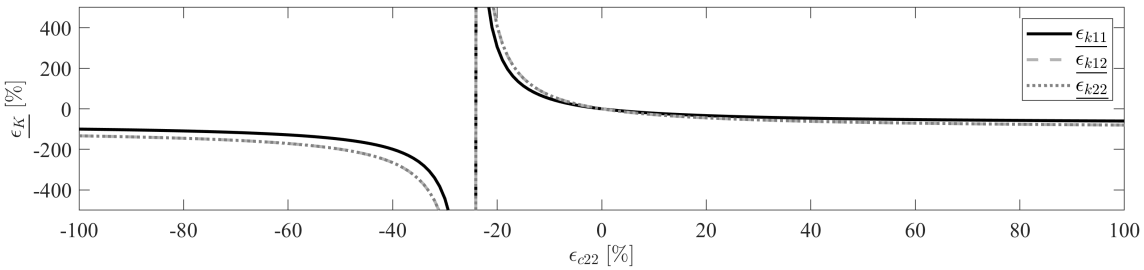
In summary, this work leads to the conclusion that the compliance terms of a coupled springs foundation matrix provide a better measure for comparison, rather



(a) Varying ϵ_{c11} ($\epsilon_{c12} = 0$, $\epsilon_{c22} = 0$)



(b) Varying ϵ_{c12} ($\epsilon_{c11} = 0$, $\epsilon_{c22} = 0$)



(c) Varying ϵ_{c22} ($\epsilon_{c11} = 0$, $\epsilon_{c12} = 0$)

Figure 3.10: Variation of the stiffness matrix error terms, $\boldsymbol{\epsilon}_K$, with ϵ_{c11} (a), ϵ_{c12} (b) and ϵ_{c22} (c). In each case the remaining two $\boldsymbol{\epsilon}_c$ terms are equal to zero. The singularities seen correspond to values that cause the denominator of Eq. 3.40 to be equal to zero.

Table 3.9: Comparison of the modal parameters predicted by the model when formulated with either the true ($\boldsymbol{K}_{F0}$) or identified ($\underline{\widetilde{\boldsymbol{K}}_F}$) foundation stiffness for case 1.

Mode, i	$f_i(\boldsymbol{K}_{F0})$ [Hz]	$f_i(\underline{\widetilde{\boldsymbol{K}}_F})$ [Hz]	MAC $\left({}^s\bar{\boldsymbol{\phi}}_{u,i}\left(\boldsymbol{K}_{F0}\right),\ {}^s\bar{\boldsymbol{\phi}}_{u,i}\left(\underline{\widetilde{\boldsymbol{K}}_F}\right)\right)$
1	0.234	0.233 (-0.27%)	1.0000
2	0.242	0.242 (-0.21%)	1.0000
3	0.919	0.918 (-0.13%)	1.0000
4	1.343	1.346 (0.19%)	1.0000

(% error) shown in brackets

than the stiffness terms, to enable analysis of the true foundation behaviour. Hence, the foundation identification results presented hereafter will compare $\boldsymbol{C}_F$ and the h, k_H and h, k_M relationships.

Model updating using real vs complex normalised mode shapes

As shown in Figure 3.8, consideration of the real normalised mode shapes, ${}^s\widetilde{\bar{\boldsymbol{\phi}}}^R$, alone would suggest that the first and second modes were FA and SS modes respectively, whereas the undamped mode shapes, ${}^s\bar{\boldsymbol{\phi}}_{u,i}$, demonstrate that they are in fact SS and FA respectively. The influence on the accuracy of the identified foundation parameters, through adoption of these two sets of mode shapes in the model updating objective function, is explored in this section.

The model updating method compares the mode shapes and frequencies of the SS modes and the FA modes separately; the mode direction for each identified mode is assumed to be specified by the user. So when considering ${}^s\widetilde{\bar{\boldsymbol{\phi}}}^R$ alone, the 1st identified mode appears to vibrate in the FA direction and is therefore paired with the 2nd model mode, which also vibrates in the FA direction, resulting in an objective function that compares $\widetilde{f}_1$ to f_2 (and $\widetilde{f}_2$ to f_1 applying the same logic to the 2nd identified mode). Consideration of ${}^s\widetilde{\bar{\boldsymbol{\phi}}}^C$, however, results in an objective function that compares the compatible modes, as the predicted vibration directions of the complex normalised damped mode shapes match those of the undamped model mode shapes.

Table 3.10 compares the identified foundation compliance matrices, $\widetilde{\boldsymbol{C}_F}$, when model updating of case 1 adopts either ${}^s\widetilde{\bar{\boldsymbol{\phi}}}^C$ or ${}^s\widetilde{\bar{\boldsymbol{\phi}}}^R$ when formulating the objective function. $\boldsymbol{\epsilon}_C$ gives the percentage errors compared to $\boldsymbol{C}_{F0}$ and J gives the final objective function value. Figure 3.11 shows the corresponding identified foundation behaviour by plotting the equivalent h, k_H and h, k_M relationships.

Adopting the real normalised mode shapes, ${}^s\widetilde{\bar{\boldsymbol{\phi}}}^R$, to formulate the model updating objective function for estimating the foundation compliance matrix, $\widetilde{\boldsymbol{C}}_F^R$, results in

Table 3.10: Comparison of identified compliance matrices found through model updating using mode shapes normalised with the real or complex techniques for case 1.

Case	Normalisation technique	$\widetilde{\boldsymbol{C}}_F$ [m/N]	$\boldsymbol{\epsilon}_C$ [%]	J
1	Complex	$\begin{bmatrix} 1.25 & -0.139 \\ -0.139 & 0.0154 \end{bmatrix} \times 10^{-9}$	$\begin{bmatrix} -19 & 4.3 \\ 4.3 & 1.2 \end{bmatrix}$ %	3.5×10^{-6}
1	Real	$\begin{bmatrix} 5.41 & -0.582 \\ -0.582 & 0.0626 \end{bmatrix} \times 10^{-3}$	$\begin{bmatrix} 3.5 \times 10^{8} & -4.4 \times 10^{8} \\ -4.4 \times 10^{8} & 4.1 \times 10^{8} \end{bmatrix}$ %	2.02

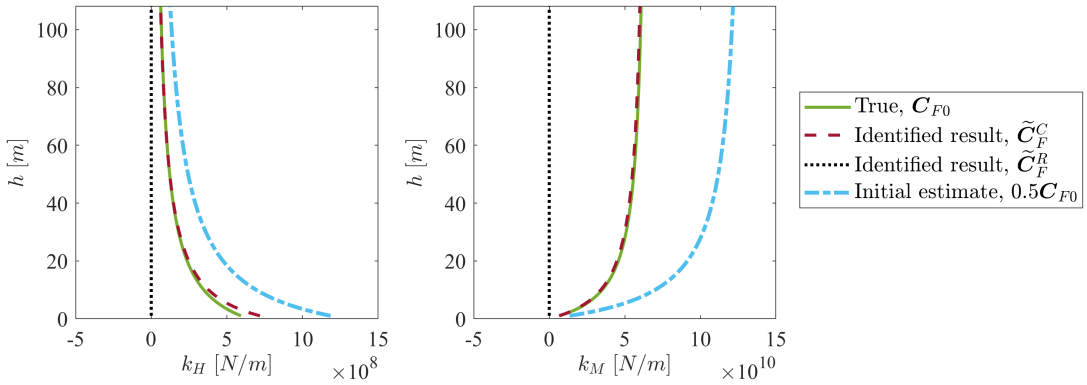


Figure 3.11: Variation of equivalent lateral and rotational stiffness (k_H and k_M) with load eccentricity (h), when real or complex normalised mode shapes are adopted for the model updating, for case 1.

significant overestimation of the magnitude of the true values (Table 3.10). This corresponds to a very low stiffness, as seen in the plots of h vs k_H and k_M in Figure 3.11 with the black dotted lines. Figure 3.11 shows that using ${}^s\widetilde{\bar{\boldsymbol{\phi}}}^R$ in the model updating procedure leads to a poor foundation estimate that would not represent the true foundation behaviour. The final value of J for the real normalisation case, found in Table 3.10, shows that the objective function has not been well satisfied, indicating that the form of the objective function is poor. As explained above, consideration of ${}^s\widetilde{\bar{\boldsymbol{\phi}}}^R$ results in the objective function comparing incompatible mode frequencies, i.e. $\widetilde{f}_1$ to f_2 and $\widetilde{f}_2$ to f_1. However, the user may reasonably assume that the high objective function value be a result of modal identification errors or modelling error. Unfortunately, there is no clear way for the user to know from the

results that the real normalised mode shapes are resulting in a badly chosen objective function that is leading to large errors in the identified foundation parameters.

3.4.2 Foundation identification: all cases

This section explores the foundation identification across all of the cases presented in Table 3.2, looking at the effect, if any, of the wind speed, noise level, foundation stiffness magnitude and initial estimate on the results. This exploration aims to test the feasibility and reliability of the model updating method across a range of realistic conditions.

Sensitivity to initial estimate

The sensitivity of the foundation identification to the initial estimate of $\boldsymbol{C}_F$ is investigated for case 2. Case 2 consists of simulated data that have been contaminated with 1% white noise (Eq. 3.38) for a wind turbine with the baseline foundation stiffness, $\boldsymbol{K}_{F0}$, at a wind speed of 12 m/s, as shown in Table 3.2. Four model updating tests of case 2, with different initial estimates corresponding to $0.25\boldsymbol{C}_{F0}$, $0.5\boldsymbol{C}_{F0}$, $2\boldsymbol{C}_{F0}$ and $4\boldsymbol{C}_{F0}$, yielded results of $\widetilde{\boldsymbol{C}}_F$ where individual parameters differed by a maximum of 0.004%. This indicates a very low sensitivity to the initial estimate, within the examined region from $0.25\boldsymbol{C}_{F0}$ to $4\boldsymbol{C}_{F0}$. Note that a constraint exists on the initial estimate of the parameters; the determinant of the corresponding stiffness matrix, $\boldsymbol{K}_F$, must be positive.

The foundation identification results presented hereafter are optimised with an initial estimate corresponding to half the true foundation compliance matrix (or equivalently stated, double the true stiffness matrix) of the model for that particular case. For cases 1 to 5 this corresponds to an initial estimate of $0.5\boldsymbol{C}_{F0}$, but for cases 6 and 7, which have different true foundation compliances, the initial estimates are $\boldsymbol{C}_{F0}$ and $0.25\boldsymbol{C}_{F0}$ respectively.

Exploring sources of foundation identification errors

This section explores the $\widetilde{\boldsymbol{C}}_F$ matrices and corresponding errors, $\boldsymbol{\epsilon}_C$, that result from applying the foundation identification model updating approach to the identified modal parameters given in Section 3.3.2, for parameter cases 1 to 5, shown in Table 3.2.

Table 3.11 shows the $\widetilde{\boldsymbol{C}}_F$ results for cases 2, 4 and 5 which are the different wind speed cases with $\eta = 1\%$ and foundation $\boldsymbol{K}_{F0}$. These cases highlight that the foundation behaviour can be identified well at a variety of wind speeds. This also results in excellent fidelity of the profiles of equivalent lateral and rotational stiffness, which are not presented for brevity.

Table 3.12 shows the results for cases 1 to 3, which are the different noise level cases at a wind speed of 12 m/s with foundation $\boldsymbol{K}_{F0}$. In Section 3.3.2, Table 3.3 showed marginally larger errors in the modal parameters identified from data with lower noise level. The $\widetilde{\boldsymbol{C}}_F$ results in Table 3.12 reflect this trend with the $\widetilde{c}_{11}$ identification, but the opposite trend is seen with the errors in the other compliance parameters. i.e. larger errors are seen at higher noise levels.

Generally, larger errors in the identified modal parameters appear to result in larger $\boldsymbol{\epsilon}_C$, as expected. However, noting that the foundation parameters are coupled, resulting in a non-linear optimisation problem, certain modal parameters are likely

Table 3.11: Model updated identified compliance matrices, comparing cases 2, 4 and 5 (varying wind speed).

Case	Wind speed [m/s]	$\widetilde{\boldsymbol{C}}_F$, [m/N]	$\boldsymbol{\epsilon}_C$ [%]
4	3	$\begin{bmatrix} 1.36 & 0.143 \\ 0.143 & 0.0151 \end{bmatrix} \times 10^{-9}$	$\begin{bmatrix} -12 & 7.5 \\ 7.5 & -0.8 \end{bmatrix}$ %
2	12	$\begin{bmatrix} 1.34 & 0.142 \\ 0.142 & 0.0149 \end{bmatrix} \times 10^{-9}$	$\begin{bmatrix} -13 & 6.3 \\ 6.3 & -1.9 \end{bmatrix}$ %
5	25	$\begin{bmatrix} 1.45 & 0.146 \\ 0.146 & 0.0147 \end{bmatrix} \times 10^{-9}$	$\begin{bmatrix} -6.7 & 9.4 \\ 9.4 & -3.4 \end{bmatrix}$ %

Table 3.12: Model updated identified compliance matrices, comparing cases 1, 2 and 3 (varying noise level).

Case	Noise level, η	$\widetilde{\boldsymbol{C}}_F$ [m/N]	$\boldsymbol{\epsilon}_C$ [%]
1	0.1%	$\begin{bmatrix} 1.25 & 0.139 \\ 0.139 & 0.0154 \end{bmatrix} \times 10^{-9}$	$\begin{bmatrix} -19 & 4.3 \\ 4.3 & 1.2 \end{bmatrix}$ %
2	1%	$\begin{bmatrix} 1.34 & 0.142 \\ 0.142 & 0.0149 \end{bmatrix} \times 10^{-9}$	$\begin{bmatrix} -13 & 6.3 \\ 6.3 & -1.9 \end{bmatrix}$ %
3	5%	$\begin{bmatrix} 1.41 & 0.143 \\ 0.143 & 0.0146 \end{bmatrix} \times 10^{-9}$	$\begin{bmatrix} -9.3 & 7.4 \\ 7.4 & -4.3 \end{bmatrix}$ %

to have higher implicit influence on the identified foundation parameters. Nelson's adjoint method (Nelson, 1976), for example, could be used in such investigations into the relative parameter sensitivities, but this is not applied here.

Comparing the magnitude of the modal parameter errors in Tables 3.3 and 3.4 ($< 0.2\%$) to the foundation parameter errors in Tables 3.11 and 3.12 (2 to 20%), highlights the degree of sensitivity of the foundation predictions to the modal parameter errors. The likely explanation is that during the minimisation of the objective function, the objective function gradient with respect to the foundation parameters is low, so small modal parameter errors result in significantly magnified foundation compliance errors, $\boldsymbol{\epsilon}_C$.

Sensitivity of foundation compliance errors to modal parameter errors and underlying foundation properties

The expected sensitivity of the foundation estimation errors to the stiffness magnitude of the foundation, varied with cases 6, 2 and 7, is investigated with forward modelling of the OWT. Each foundation compliance parameter is multiplied in turn by a range of values between 1 and 1.1, and the resulting pseudo-objective function, $\underline{J}$ is calculated using Eq. 3.41 with the 'identified' modal parameters being substituted with the model modal parameters realised with the underlying 'true' foundation, $2\boldsymbol{C}_{F0}$, $\boldsymbol{C}_{F0}$ or $0.5\boldsymbol{C}_{F0}$ depending on the case. Eq. 3.41 shows an exam-

ple calculation for case 2 ($\boldsymbol{C}_{F0}$).

$$\underline{J}(\boldsymbol{\chi}) = \sum_{i=1}^{m} \left[\left(\frac{f_i(\boldsymbol{\chi}) - f_i(\boldsymbol{C}_{F0})}{f_i(\boldsymbol{C}_{F0})} \right)^2 + \left(1 - \text{MAC}\left({}^s\bar{\boldsymbol{\phi}}_{u,i}(\boldsymbol{\chi}),\ {}^s\bar{\boldsymbol{\phi}}_{u,i}(\boldsymbol{C}_{F0}) \right)\right) \right]$$

$$\boldsymbol{\chi} = \begin{cases} \begin{bmatrix} \bar{c}_{11}c_{11} & c_{12} \\ c_{12} & c_{22} \end{bmatrix} & \text{for } \bar{c}_{11} = \{1, 1.01 ... 1.1\} \\ \begin{bmatrix} c_{11} & \bar{c}_{12}c_{12} \\ \bar{c}_{12}c_{12} & c_{22} \end{bmatrix} & \text{for } \bar{c}_{12} = \{1, 1.01 ... 1.1\} \\ \begin{bmatrix} c_{11} & c_{12} \\ c_{12} & \bar{c}_{22}c_{22} \end{bmatrix} & \text{for } \bar{c}_{22} = \{1, 1.01 ... 1.1\} \end{cases} \tag{3.41}$$

This process was performed for cases 6, 2 and 7 and termed soft, medium and stiff respectively. In Figure 3.12, the normalised compliance parameter, $\bar{c}_{11}$, $\bar{c}_{12}$ and $\bar{c}_{22}$, is plotted against the value of the pseudo-objective function, $\underline{J}$. The normalised compliance parameters act as a proxy for the expected errors in the estimated compliance parameters, $\widetilde{c}_{11}$, $\widetilde{c}_{12}$ and $\widetilde{c}_{22}$. The value of $\underline{J}$ acts as a proxy for the combined error in the identified modal parameters. For context, the identified modal parameters for cases 1 to 7, shown in Tables 3.3 to 3.5, result in equivalently calculated pseudo-objective function values between 0.0001 and 0.046. Overall, an approximate expected sensitivity of the errors in $\widetilde{c}_{11}$, $\widetilde{c}_{12}$ and $\widetilde{c}_{22}$ to the combined errors in the identified modal parameters, $\widetilde{\boldsymbol{f}}$ and ${}^s\widetilde{\bar{\boldsymbol{\phi}}}^C$, is reflected in the gradients of the lines in Figure 3.12, with steeper meaning more sensitive.

Analysis of the gradients of the lines in Figure 3.12 indicates that the stiffer the underlying foundation, the higher the sensitivity to modal parameter errors and therefore higher errors are expected in the identified foundation parameters, $\widetilde{\boldsymbol{C}}_F$. This trend is seen to a certain extent in the $\widetilde{\boldsymbol{C}}_F$ results for cases 2, 6 and 7, shown in Table 3.13, although the partially random nature of the modal identification makes it difficult to draw conclusions from individual cases.

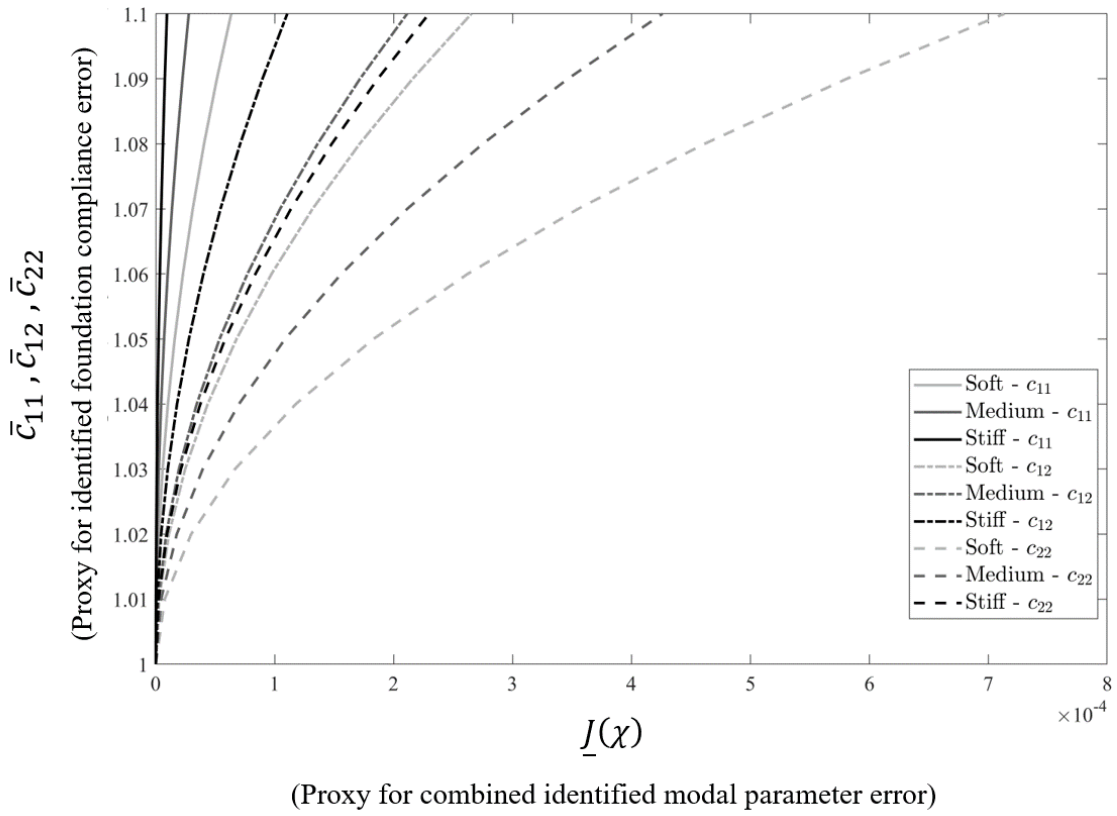


Figure 3.12: Normalised foundation compliance against the corresponding pseudo-objective function value, for the NREL 5MW modelled with soft, medium and stiff foundations. This indicates the sensitivity of the estimated foundation parameter errors to the combined errors in the identified modal parameters.

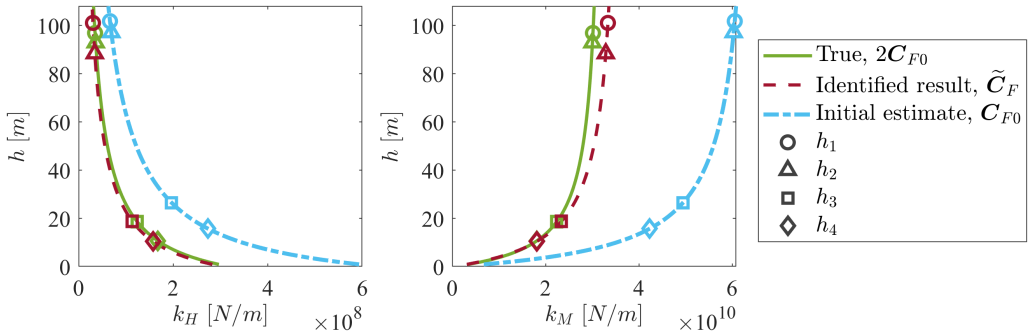
Table 3.13: Model updated identified compliance matrices, comparing cases 2, 6 and 7 (varying foundation stiffness).

Case	Foundation	$\widetilde{\boldsymbol{C}}_F$ [m/N]	$\boldsymbol{\epsilon}_C$ [%]
6	$0.5K_{F0}$, $2C_{F0}$	$\begin{bmatrix} 3.42 & -0.296 \\ -0.296 & 0.0271 \end{bmatrix} \times 10^{-9}$	$\begin{bmatrix} 4.3 & 11 \\ 11 & -11 \end{bmatrix}$ %
2	K_{F0}, C_{F0}	$\begin{bmatrix} 1.34 & -0.142 \\ -0.142 & 0.0149 \end{bmatrix} \times 10^{-9}$	$\begin{bmatrix} -13 & 6.3 \\ 6.3 & -1.9 \end{bmatrix}$ %
7	$2K_{F0}$, $0.5C_{F0}$	$\begin{bmatrix} 9.93 & -0.786 \\ -0.786 & 0.0624 \end{bmatrix} \times 10^{-10}$	$\begin{bmatrix} 28 & 18 \\ 18 & -18 \end{bmatrix}$ %

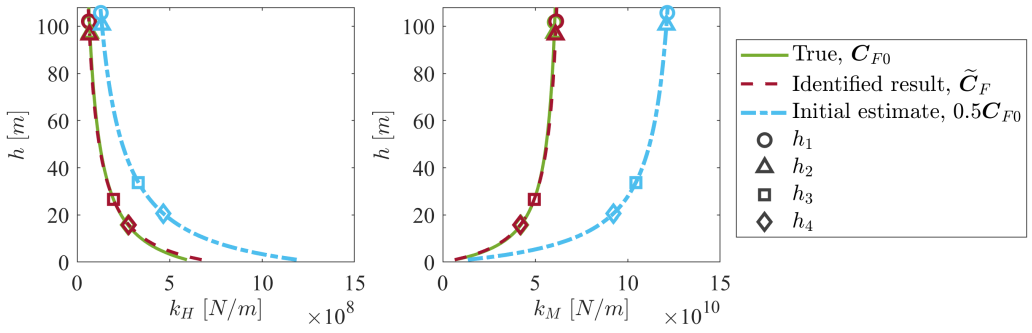
Analysis of the gradients in Figure 3.12 also predicts that $\widetilde{c}_{11}$ and $\widetilde{c}_{22}$ will have the largest and smallest identification errors respectively. This observation is broadly reflected in the cases presented in this work. This can be probed further by plot-

ting the h, k_H and h, k_M relationships, which represent the foundation behaviour. These have been plotted for cases 2, 6 and 7, showing the relationships for the true, identified and initial estimate compliance parameters (e.g. $\boldsymbol{C}_{F0}$, $\widetilde{\boldsymbol{C}}_F$ and $0.5\boldsymbol{C}_{F0}$ respectively for case 2), in Figure 3.13.

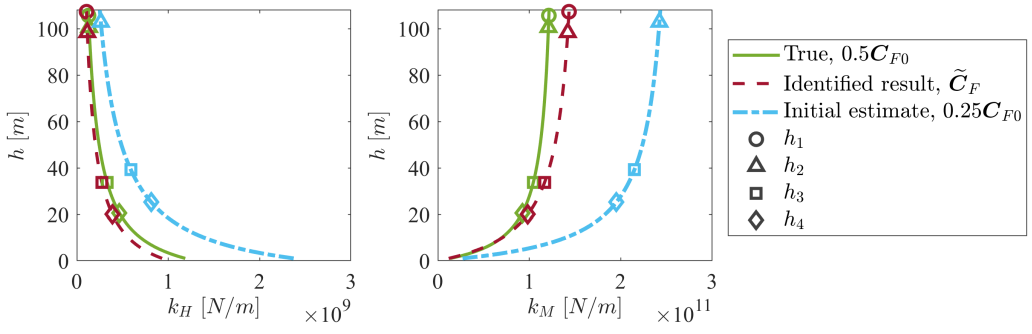
As shown by Eq. 3.9 in Section 3.2.1, for the i^{th} vibration mode an effective load eccentricity, h_i, can be calculated from the $\boldsymbol{K}_F$ (or $\boldsymbol{C}_F$) terms and the ground-level lateral and rotational displacements of the i^{th} mode shape, $v_{G,i}$ and $\theta_{G,i}$ respectively.



(a) Case 6: $2\boldsymbol{C}_{F0}$, $0.5\boldsymbol{K}_{F0}$



(b) Case 2: $\boldsymbol{C}_{F0}$, $\boldsymbol{K}_{F0}$



(c) Case 7: $0.5\boldsymbol{C}_{F0}$ $2\boldsymbol{K}_{F0}$

Figure 3.13: Variation of equivalent lateral and rotational stiffness (k_H and k_M) with load eccentricity (h), including effective modal load eccentricities (h_i), for cases 2, 6 and 7 (varying foundation stiffness).

These mode shape displacements are found using the FAST model realised with the foundation parameters of interest, e.g. $\widetilde{\boldsymbol{C}}_F$. The calculated h_i are shown in Figure 3.13 with markers. The modal properties at these effective load eccentricities are both the data available for model updating and the critical measures of performance required in order to match the model and observed behaviour. Figure 3.13 indicates that stiffer foundations present modes with higher effective load eccentricities. For case 2, h varies from approximately $18m$ for mode 4 to $108m$ for mode 1. This sparsity of data at low values of h results in greater uncertainty for the foundation parameters in this region. As a result $\widetilde{c}_{11}$, which relates to the x-intercept on the k_H plot (see Figure 3.3), is the least well identified compliance parameter. Conversely, there is a relatively large amount of information at high h, hence why $\widetilde{c}_{22}$, which relates to the vertical asymptote on the k_M plot, is generally the best identified parameter, across all seven parameter cases. This agrees with the predictions found with the error sensitivity analysis shown in Figure 3.12.

Higher order vibration modes result in lower h, so the estimated h, k_H and h, k_M relationships at low values of h would likely be improved by the inclusion of higher order tower sub-structure modes, resulting in a higher order model. However, the frequencies of these higher order modes are significantly greater than the typical frequencies of the sources of input excitation for OWT (wind, wave and rotor excitations). These higher order modes are therefore less likely to be excited by the inputs, thus have a smaller contribution to the overall OWT dynamic behaviour and are consequently of less interest from a design perspective. In addition, the lack of excitation of these modes may result in them being more difficult to identify in practice. By accurately capturing the foundation and modal behaviour at load eccentricities, h, relevant to the lower frequency modes, as in this study, the model updating process delivers a set of foundation parameters that will allow accurate modelling of the most critical structural dynamic behaviour and provide an appropriate basis for comparison with design models.

3.5 Summary

The success of model updating methods relies on how well the model represents the true nature of the system and whether a sufficient number of modal parameters are identified with adequate accuracy.

This work demonstrates that wind turbine structures exhibit significant non-proportional aerodynamic damping that causes the mode shapes to vibrate in non-orthogonal directions. A method, termed 'complex normalisation', is shown to successfully approximate the undamped mode shapes of the OWT model when applied to the damped mode shapes. By applying this complex normalisation to sensor identified mode shapes, model updating can be performed accurately using an undamped model, thus removing the need for high fidelity modelling of the physical sources of damping.

All four model frequencies and undamped mode shapes are identified well from simulated data under various conditions with the subspace state-space system identification method N4SID.

It was found that for a ground-level coupled springs foundation model the terms of the compliance matrix are better conditioned for optimisation and for the comparison of different foundations than the stiffness terms. The effective lateral and rotational stiffnesses, which govern the foundation behaviour for a given set of loads, are more simply represented by the compliance terms than the stiffness terms. For the identification or comparison of such a foundation model it is recommended that the compliance terms are adopted.

Based on simulated data for a variety of wind speed conditions and synthetic noise levels, the model updating approach performs well in identifying the foundation behaviour, via identification of the compliance terms. This is shown for three cases of an OWT model with different foundations of varying levels of compliance. It was demonstrated that the model updated foundation parameters are fairly sensitive to the modal identification errors, owing to the shallow gradient of the objective

function with respect to the foundation compliance parameters.

The four vibration modes used in this study, which are those typically primarily considered for the design of a wind turbine, have effective load eccentricities between approximately 18 and 108m. The identified foundation compliance parameters are shown to accurately replicate the behaviour of the true foundation parameters in this range, and therefore provide an effective basis for accurate modelling of the typically critical structural behaviour and comparison of the identified foundation with design models.

The problem of non-proportional damping, such as that arising from wind turbine rotor aerodynamics, is expected to persistently affect the majority of investigations related to such structures. The procedure used here for the normalisation of mode shapes can be paired with other methods for tackling complementary issues such as the problematic effects arising from closely spaced modes, operational conditions and blade flexibility. Chapters 4 and 5 will investigate those complementary issues.

Chapter 4

Effects of idling data and close modes

4.1 Introduction

The model updating method is applied in this chapter to identify the properties of two foundation models: a coupled springs macro-element and a set of depthwise-varying springs. These two foundations models are statically equivalent but not dynamically equivalent, and are both commonly used in the design and analysis of OWT to represent the soil-structure interaction of the embedded monopile. Two output only system identification methods that have been widely used and proven to be robust, N4SID (Van Overschee & De Moor, 1994) and SSI-cov/ref (Peeters & De Roeck, 1999), are employed for the modal identification step.

The simplifications applied to the OWT model in Chapter 3; rigid blades, parked conditions and an altered RNA inertia, are not applied in this chapter, resulting in a more realistic representation of the NREL 5MW OWT.

Typical system identification methods work under the assumptions that the structural properties are time invariant and the excitation is of a white noise nature. Therefore data from parked conditions, where the wind turbine is not rotating, are typically favoured to avoid the introduction of harmonic components and time variance of the structural properties due to the rotor rotation. These conditions were covered in Chapter 3. However, as explained in Section 1.3.1, idling conditions, where the rotor is free to rotate but not producing power, are more common than parked conditions. In this chapter, the suitability for modal identification of data from idling conditions is explored, analysing the effect of the time variability caused by the varying azimuth angle through numerical modelling.

Owing to their quasi-axisymmetric nature, wind turbines exhibit pairs of modes with closely spaced natural frequencies, herein referred to as close modes. In Chapter 3, the RNA inertia was altered to increase the separation between the frequencies of the modes, to avoid the issues introduced by close modes. In this chapter, this inertia alteration is not imposed, and the implications of the inherent close modes on the modal and foundation identification of the OWT are investigated. The mode

shape identification results are analysed using both the MAC (Allemang & Brown, 1982) and the S2MAC (D'Ambrogio & Fregolent, 2003), introduced in Section 1.3.2. Two approaches are shown for initially investigating the existence of the close modes, firstly by comparing the MAC and S2MAC, and secondly by analysing the identification uncertainties predicted by the SSI-cov/ref method.

The OWT model, system identification and mode shape correlation methods are detailed in Section 4.2. In Section 4.3.1, the modes of specific interest from a foundation identification point of view are determined through modelling, and then identified from simulated data in Section 4.4.1. The impact of the idling rotor on the identification is analysed in Section 4.3.2, showing the difficulties introduced for the identification of modes dominated by blade vibration. Another key focus is the effect of the close modes on the identification and the comparison of the MAC vs the S2MAC for the mode shape inspection, found in Section 4.4.1. Furthermore, two approaches are outlined for investigating the presence of close modes in Section 4.4.2. Finally, the identified foundation-sensitive modes are then used to estimate the foundation properties with a model updating method in Section 4.4.3, demonstrating an application where the use of the S2MAC, in lieu of the MAC, is vital for accurate results.

4.2 Methodology

4.2.1 Model

In this chapter, the implications of using idling data and the existence of close modes are investigated using the OWT sub-model FB, as presented in Section 2.2.3, modelled using FAST v7 (J. Jonkman & Buhl, 2005). The DOF of sub-model FB are shown in Figure 4.1 and the dimensions and tower accelerometer locations are shown in Figure 4.2a. Sub-model FB will simply be referred to as the model or OWT model for the remainder of this chapter. The OWT has been modelled to reproduce

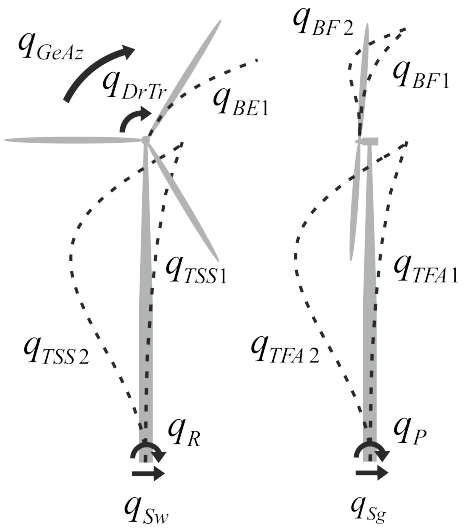
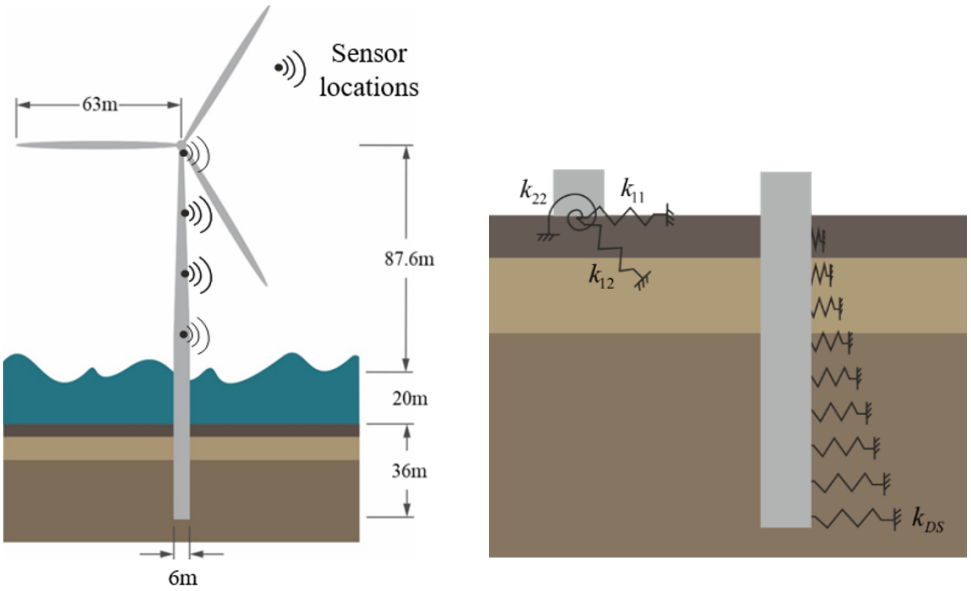


Figure 4.1: Model degrees of freedom.



(a) (b)

Figure 4.2: OWT model dimensions (a) and foundation representations (b).

idling conditions with a blade pitch of 14°, resulting in an average simulated rotor speed of $3rpm$.

To recap, the soil-structure interaction of a monopile is typically modelled as a set of depthwise-varying or ground level statically equivalent coupled springs that provide reaction to the specified loading. In this chapter both forms of the foundation model are investigated, termed DS and CS respectively. These foundation representations were explained in Sections 2.2.1 and 3.2.1 and are shown in 4.2b. All

soil properties are assumed to be axisymmetric about the vertical axis. The DOF that correspond to the translation and rotation of the base of the OWT model, q_{Sg}, q_{Sw}, q_P and q_R, are located at the base of the monopile for DS foundation case and at the mudline for the CS foundation case (as the monopile is not modelled).

The model updating procedure in this chapter aims to estimate the properties of the three coupled springs for the CS model, and the individual base spring for the DS model. These spring properties are updated in the form of the compliances as these were found to be better conditioned for optimisation and provide a better basis for comparison of the macro-element foundation behaviour, compared to the stiffnesses, in Chapter 3.

4.2.2 Calculation of modal parameters

The modal parameters are calculated as described in Chapter 3, detailed in Section 3.2.2. The only difference being that the state vector, $\boldsymbol{q}$, of Eqs. 3.10 and 3.11 consists of the 19 DOF shown in Figure 4.1. The corresponding frequencies, $\boldsymbol{f}$, damping ratios, $\boldsymbol{\zeta}$, and sensor-based mode shapes, ${}^{s}\boldsymbol{\phi}$, are calculated.

4.2.3 Identification of modal parameters

System modal parameters can be identified from measured or simulated sensor data using various methods. Two such examples of output only methods, used in this chapter, are: the subspace state space system identification method N4SID (Van Overschee & De Moor, 1994) and the reference-based covariance-driven stochastic subspace identification algorithm SSI-cov/ref (Peeters & De Roeck, 1999). The former is implemented using the System Identification Toolbox from MATLAB (MathWorks, 2021) and the latter is implemented using the MACEC toolbox from KU Leuven (Reynders, Schevenels, & De Roeck, 2021). All identified parameters in this thesis are indicated with the accent $\tilde{}$.

When supplied with only output data, $\boldsymbol{y}$, both methods identify the unknown

$\widetilde{\boldsymbol{A}}_D$, and $\widetilde{\boldsymbol{E}}$ matrices of the discrete system, describing the transition of the system between steps k and $k+1$, in state space form as:

$$\boldsymbol{x}_{k+1} = \widetilde{\boldsymbol{A}}_D \boldsymbol{x}_k + \boldsymbol{w}_k, \qquad \boldsymbol{y}_k = \widetilde{\boldsymbol{E}} \boldsymbol{x}_k + \boldsymbol{v}_k \tag{4.1}$$

where $\boldsymbol{w}$ and $\boldsymbol{v}$ are the process noise and measurement noise vectors respectively. The steps $k = 1 \ldots N$ are sampled with a finite sampling time step Δt. In addition to estimating the system matrices themselves, both methods can estimate the covariances of these matrices. In the implementation in the MACEC toolbox these covariances are then used to calculate the covariances of the corresponding modal parameters (Reynders et al., 2008), therefore providing uncertainty bounds on their identification accuracy. The uncertainty bounds on the identified frequencies are used in this work to infer whether or not a pair of consecutive modes should be considered to be close modes. This procedure is elaborated upon and implemented in Section 4.4.2.

As explained in Section 3.2.5, the identified $\widetilde{\boldsymbol{A}}_D$ matrix is converted to the state matrix of the equivalent continuous state-space system, $\widetilde{\boldsymbol{A}}_C$, using Eq. 3.30. The identified modal parameters are found by using $\widetilde{\boldsymbol{A}}_C$ in Eqs. 3.16, 3.20 and 3.21 giving $\widetilde{\boldsymbol{\psi}}_d$, $\widetilde{\boldsymbol{\zeta}}$ and $\widetilde{\boldsymbol{f}}$ respectively. The identified mode shapes are damped since the $\widetilde{\boldsymbol{A}}_C$ matrix includes damping contributions. The identified output matrix, $\boldsymbol{E}$, transforms the identified eigenvectors, $\widetilde{\boldsymbol{\psi}}_d$, into the sensor-based mode shapes, ${}^s\widetilde{\boldsymbol{\phi}}_d$ using Eq. 3.31, where the additional superscript ^{s} denotes the sensor basis.

4.2.4 Mode shape normalisation and comparison

Due to their arbitrary scaling, mode shapes must be normalised according to some adopted convention. Suggested normalisation procedures were given in Section 3.2.3. Eq. 3.23 presented a common approach for undamped mode shapes, and Eq. 3.25 demonstrated an approach, termed 'complex normalisation' for approximating the

undamped mode shapes from complex non-proportionally damped mode shapes. To recap, normalised undamped mode shapes are written as $\bar{\boldsymbol{\phi}}_{u,i}$ and complex normalised damped mode shapes are written as $\bar{\boldsymbol{\phi}}_i^C$.

Comparison of the identified and model-estimated modal parameters is fundamental to the model updating process. The individual values of the frequencies can be simply compared through the norm of their difference, however the mode shape comparison is more complicated. Commonly, the degree of correlation between a relevant pair of mode shapes is calculated with the MAC (Allemang & Brown, 1982) (also given in Eq. 3.33) which gives a value between 0 and 1 using the following equation:

$$\text{MAC}\left(\boldsymbol{\phi}_i, \widetilde{\boldsymbol{\phi}}_i\right) = \frac{\left|\boldsymbol{\phi}_i \widetilde{\boldsymbol{\phi}}_i^{\,*}\right|^2}{\boldsymbol{\phi}_i \boldsymbol{\phi}_i^{\,*} \widetilde{\boldsymbol{\phi}}_i \widetilde{\boldsymbol{\phi}}_i^{\,*}} \tag{4.2}$$

where i denotes the vibration mode in question. Typically, mode shapes are considered to 'match' if the MAC calculation result is greater than a particular value, but there is a degree of subjectivity to what this threshold should be, depending on the problem studied. Often thresholds of 0.9 and above are used.

Quasi-axisymmetric systems, such as wind turbines, often present pairs of close modes which can cause difficulties for identification methods, as was discussed in Section 1.3.2 and will be shown for this structure in Section 4.4.1. For a perfectly axisymmetric structure, identical modes are found whose mode shapes can only be uniquely defined as existing within a subspace around the axis of symmetry (Brincker & Lopez-Aenlle, 2015), as a pair of mode shapes in any two orthogonal directions are possible, as depicted in Figure 4.3. When trying to identify these mode shapes from monitoring data, there would be no guarantee which of those infinitely many and equally correct mode shapes would be identified. If the structure is instead nearly axisymmetric, despite a pair of unique orthogonal mode shapes existing, they are very susceptible to perturbations in the structural properties, easily moving within

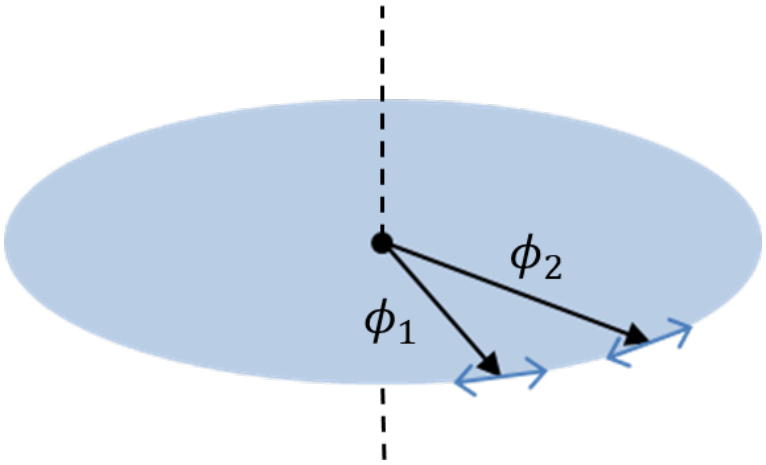


Figure 4.3: Mode shape subspace for close modes (adapted from Au and Brownjohn (2019)).

the subspace spanned by the mode shape pair. This makes identification of the mode shapes along the true orthogonal bases very challenging.

D'Ambrogio and Fregolent (2003) developed a modification of the MAC, called the S2MAC, that quantifies the correlation between an individual mode shape and the subspace spanned by a pair of mode shapes. In this chapter it is used to compare the identified mode shape, $\widetilde{\boldsymbol{\phi}}_i$, of a close mode to the subspace spanned by the mode shapes of the corresponding model-estimated close mode pair, $\boldsymbol{\phi}_i$ and $\boldsymbol{\phi}_k$. The S2MAC is calculated by:

$$\text{S2MAC}\left(\boldsymbol{\phi}_i, \boldsymbol{\phi}_k, \widetilde{\boldsymbol{\phi}}_i\right) = \frac{(\widetilde{\boldsymbol{\phi}}_i^{\,T}\boldsymbol{\phi}_i)^2 - 2(\widetilde{\boldsymbol{\phi}}_i^{\,T}\boldsymbol{\phi}_i)(\boldsymbol{\phi}_i^T\boldsymbol{\phi}_k)(\widetilde{\boldsymbol{\phi}}_i^{\,T}\boldsymbol{\phi}_k) + (\widetilde{\boldsymbol{\phi}}_i^{\,T}\boldsymbol{\phi}_k)^2}{1 - (\boldsymbol{\phi}_i^T\boldsymbol{\phi}_k)^2} \tag{4.3}$$

where all mode shapes are real-valued unit vectors and $k = i + 1$ or $i - 1$. As with MAC, S2MAC is bounded between 0 and 1, with 1 demonstrating that the individual mode shape is an exact linear combination of the pair of mode shapes. D'Ambragio and Fregolent advise that the S2MAC value is analysed by way of the improvement compared to the value obtained using the MAC. In the case where the standard MAC indicates that identified mode shapes from close modes correlate poorly to those within numerical models, the result could be mistakenly interpreted as either the consequence of a badly identified mode or a biased model. However,

the S2MAC could provide confidence that the identified modes in fact belong to the subspace spanned by the modes of the numerical model and could be used within a model updating process rather than potentially being discarded. The complex normalisation method, Eq. 3.25, is well suited to the implementation of the S2MAC formulation, since Eq. 4.3 requires real-valued mode shapes.

4.2.5 Model updating

The goal of modal-model updating is to tune a vector of parameters of the model so that its modal properties match those identified from sensor measurements. This is achieved in this chapter by minimising the following objective function, $J(\boldsymbol{\chi})$:

$$J(\boldsymbol{\chi}) = \sum_{i=1}^{m} \left[W_{F,i} \left(\frac{f_i(\boldsymbol{\chi}) - \widetilde{f}_i}{\widetilde{f}_i} \right)^2 + W_{M,i} \left(1 - \mathrm{MAC} \left({}^{s}\bar{\boldsymbol{\phi}}_{u,i}(\boldsymbol{\chi}), {}^{s}\widetilde{\bar{\boldsymbol{\phi}}}_{i}^{C} \right) \right) \right. \tag{4.4}$$
$$\left. + W_{S,i} \left(1 - \mathrm{S2MAC} \left({}^{s}\bar{\boldsymbol{\phi}}_{u,i}(\boldsymbol{\chi}), {}^{s}\bar{\boldsymbol{\phi}}_{u,k}(\boldsymbol{\chi}), {}^{s}\widetilde{\bar{\boldsymbol{\phi}}}_{i}^{C} \right) \right) \right]$$

where m is the number of identified modes used for comparison, $\boldsymbol{\chi}$ is the vector of parameters to be tuned: the foundation parameters, and $W_{F,i}$, $W_{M,i}$ and $W_{S,i}$ are boolean weights (1 or 0). These weights enable the choice of including the frequencies and the use of either the MAC or S2MAC for the mode shape comparison for each mode, i.

$f(\boldsymbol{\chi})$ and ${}^{s}\bar{\boldsymbol{\phi}}_{u}(\boldsymbol{\chi})$ are the numerical model modal parameters realised for a specific $\boldsymbol{\chi}$ following the procedures set out in Sections 4.2.2 and 4.2.4. ${}^{s}\bar{\boldsymbol{\phi}}_{u}(\boldsymbol{\chi})$ are undamped mode shapes calculated using Eq. 3.12, transformed to the sensor basis using Eq. 3.19 and finally normalised using Eq. 3.23.

$\widetilde{f}$ and ${}^{s}\widetilde{\bar{\boldsymbol{\phi}}}^{C}$ are the identified modal parameters estimated using the procedures set out in Sections 4.2.2 to 4.2.4. ${}^{s}\widetilde{\bar{\boldsymbol{\phi}}}^{C}$ are damped mode shapes calculated using Eq. 3.16, then transformed to the sensor basis using Eq. 3.31 and finally complex normalised using Eq. 3.25.

As in Chapters 3 and 5, the objective function of Eq. 4.4 is minimised using the MATLAB fminsearch optimisation algorithm.

The parameters to be optimised for the CS model, $\boldsymbol{\chi}_{CS}$, are the c_{11}, c_{12} and c_{22} terms of the foundation compliance matrix, $\boldsymbol{C}_{CS}$ (previously denoted $\boldsymbol{C}_F$), which is the inverse of the macro-element stiffness matrix, $\boldsymbol{K}_{CS}$ (previously denoted $\boldsymbol{K}_F$), and is defined in the following:

$$\boldsymbol{C}_{CS} = \boldsymbol{K}_{CS}^{-1} = \frac{1}{k_{11}k_{22} - k_{12}^2} \begin{bmatrix} k_{22} & -k_{12} \\ -k_{12} & k_{11} \end{bmatrix} = \begin{bmatrix} c_{11} & c_{12} \\ c_{12} & c_{22} \end{bmatrix} \tag{4.5}$$

The DS model consists of a linear variation of soil subgrade modulus starting at 0 at the ground level and reaching k_{DS} at the base, as explained in Section 2.2.1. Therefore, the DS model has one optimisation parameter, the lateral soil compliance at the monopile base, $\boldsymbol{\chi}_{DS} = c_{DS} = 1/k_{DS}$.

4.3 Exploring modal behaviour

4.3.1 Sensitivity to foundation stiffness

Since this study aims to identify the foundation properties, the vibration modes of interest are therefore those that are sensitive to the stiffness of the foundation. This can be investigated by varying the CS and DS model foundation stiffnesses, $\boldsymbol{K}_{CS}$ and k_{DS} respectively, using a linear scaling parameter:

$$k_{DS} = \gamma k_{DS0} \qquad\qquad \boldsymbol{K}_{CS} = \gamma \boldsymbol{K}_{CS0} \tag{4.6}$$

where γ, the foundation stiffness multiplier, is a real positive number and also represents the normalised foundation stiffness. $\boldsymbol{K}_{CS0}$ and k_{DS0} are baseline stiffnesses

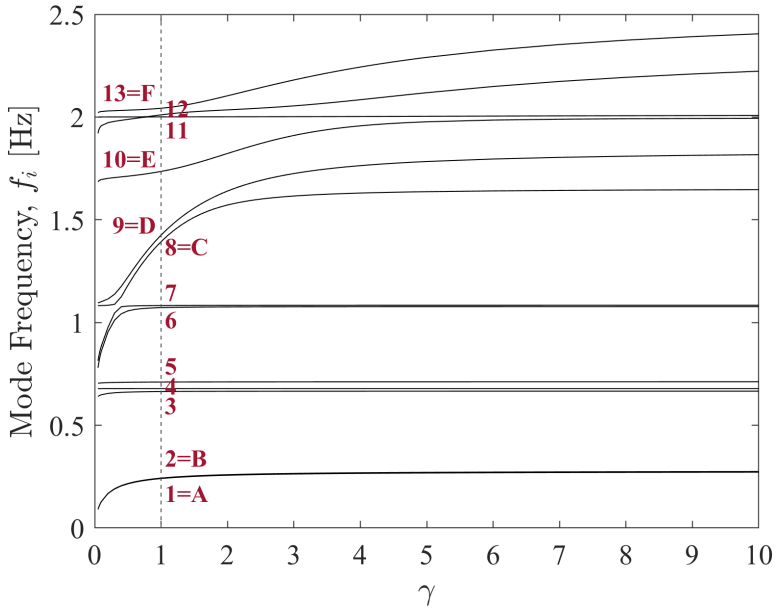
with the following values:

$$k_{DS0} = 5.50 \times 10^8 \text{ N/m} \qquad \boldsymbol{K}_{CS0} = \begin{bmatrix} 0.0139 & 0.119 \\ 0.119 & 1.66 \end{bmatrix} \times 10^{11} \text{ N/m} \quad (4.7)$$

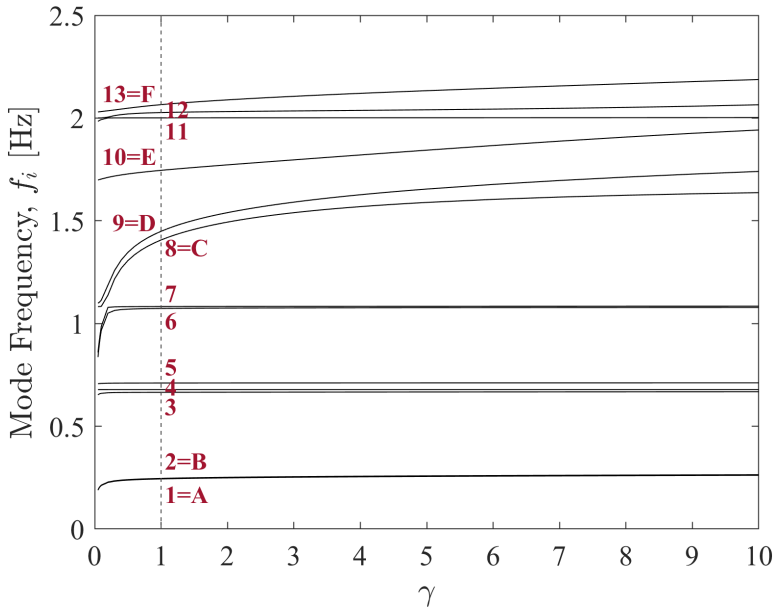
$\boldsymbol{K}_{CS0}$ is the macro-element equivalent to the embedded monopile with DS soil stiffness k_{DS0}, calculated using the Oxford 1D simplified FE model of the wind turbine. FAST is used to calculate the numerical model frequencies, $\boldsymbol{f}$, with varying γ, for the OWT model with both CS and DS foundation representations, which are plotted in Figures 4.4a and 4.4b respectively.

Figure 4.4 shows that depending on the value of γ there are a limited number of modes that are sensitive to changes in the value of the foundation stiffness as indicated with lines of non-negligible gradient. These modes are referred to as 'foundation-sensitive' modes. Focusing on a specific interval of γ, the extent of the gradient of the line indicates the degree of the foundation sensitivity of each mode; the steeper the line the greater the sensitivity. As γ varies, the frequencies of these foundation-sensitive modes change, their degree of sensitivity changes and the subset of modes which would be considered foundation-sensitive also changes. At certain points, for example, at a frequency of around 1.1 Hz and $\gamma \approx 0.3$ for the CS model (Figure 4.4a), the relative gradients of the lines are such that some of the modes almost appear to cross one another. This behaviour is investigated in more detail in Chapter 5.

The line portions in Figures 4.4a and 4.4b that have negligible gradient demonstrate that across that range of γ, the modes have negligible sensitivity to γ and are thus considered 'foundation-insensitive'. For example, the three modes with frequencies between 0.6 and 0.7 Hz, labelled as modes 3 to 5 in Figure 4.4, are seemingly foundation-insensitive across the entire investigated range of γ. Within the regions of foundation-insensitivity, the mode shapes of the foundation-insensitive modes are typically dominated by blade motion. In comparison, the modes that are seemingly



(a) CS foundation model



(b) DS foundation model

Figure 4.4: Effect of the normalised foundation stiffness, γ, on the frequencies of the NREL 5MW OWT modelled with CS (a) or DS (b) foundation models.

foundation-sensitive, tend to have larger mode shape contributions from the DOF belonging to the tower.

Each vibration mode of the OWT is characterised by a mode shape that consists of a unique combination of contributions from each DOF of the structure. The DOF of the OWT model used in this chapter are depicted in Figure 4.1. Some of the

modes are almost entirely dominated by one DOF, for example the modes labelled A and B in Figure 4.4 are dominated by q_{TFA1} and q_{TSS1} respectively, because those individual DOF have frequencies of vibration that are well separated from those of the other DOF. If the frequencies of each DOF are calculated individually, it is found that some are well separated and some are close together. This can have an impact on how the DOF contributions combine, or couple, in the mode shapes of the full structure vibration modes. For example, the frequency associated with DOF q_{TFA2} sits between, and in close proximity to, the frequencies associated with blade DOF q_{BF1} and q_{BF2}, resulting in modes with mode shapes that have significant contributions from both tower and blade bending DOF. The relative DOF contributions to the mode shapes change as γ is varied, hence changing the tower vs blade dominance and the foundation-sensitivity of each mode.

The simulated data used for identification in this chapter are generated with $\boldsymbol{K}_{CS0}$ or k_{DS0}, corresponding to $\gamma = 1$. Focusing on the region of $\gamma = 1$ in Figures 4.4a and 4.4b, visual inspection of the gradients suggest that there are six modes that are foundation-sensitive: two modes around 0.25 Hz; two modes around 1.5 Hz; one mode around 1.75 Hz and a final mode around 2.1 Hz. These six modes will be referred to as modes A to F (as indicated with the figure labels) and will be the focus of this chapter from this point on, investigating their characteristics as predicted by the FAST model and as identified from the simulated data.

Though the CS and DS foundation models are statically equivalent at $\gamma = 1$, the respective plots in Figure 4.4 are not identical for a number of reasons. Firstly, the models are not dynamically equivalent since the mass of the structure below the ground level is not captured by the CS model, so even at $\gamma = 1$ the frequencies are not identical. Secondly, at any specific $\gamma \neq 1$, $\boldsymbol{K}_{CS}$ is not statically equivalent to the corresponding DS model with base k_{DS}, since γ scales the combined soil and monopile stiffness for the CS model and only the soil stiffness for the DS model. It is also worth noting that during the modal reduction (described in Section 2.2.2),

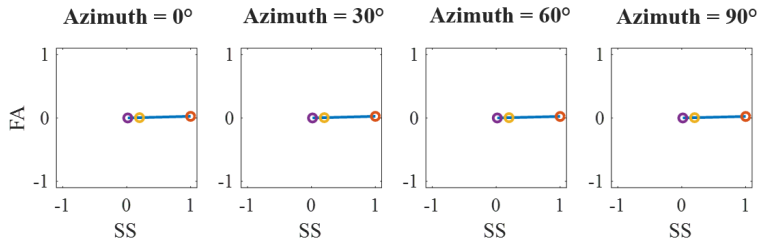
the process of approximating the mode shape with a 6^{th} order polynomial appears to be better conditioned to the CS model, so this approximation results in a slightly larger modelling error for the DS model.

4.3.2 Effect of idling rotor

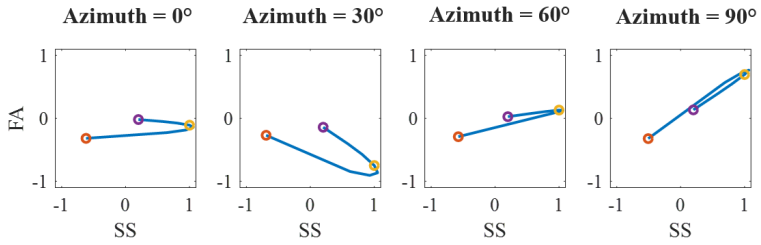
During periods of OWT idling, where the rotor is rotating but not producing power, a degree of time variability is introduced to the system as the geometry of the structure is changing with time. This could have an impact on the success of the output only identification methods used, described in Section 4.2.3, since these methods assume time invariance of the structural properties.

The effect of this time variability is explored by calculating the model-estimated modal properties at varying azimuth angles. The position of the rotor is described by the azimuth angle. A particular rotor position is defined as having an azimuth angle, az, of 0°, i.e. blade 1 at the upwards vertical position, and any other rotor position is subsequently defined with an azimuth angle equal to the angle between the current position of blade 1 and the upwards vertical position, in the direction of the rotor rotation. Therefore, $0° \leq az < 360°$, $az = 0° = 360°$ and rotational symmetry exists at 120° intervals since the blades are identical in the model. The effect of the varying azimuth angle on the frequencies was found to be negligible and is therefore not shown for brevity. However, variability was observed in the tower portion of the mode shapes, where all of the monitoring accelerometers are assumed to be mounted.

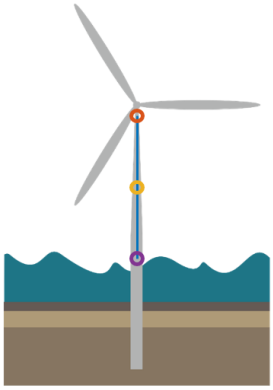
Figure 4.5 shows the undamped mode shape, ${}^{s}\bar{\boldsymbol{\phi}}_u$, of the OWT tower from above at various rotor azimuth angles for an example tower-dominant mode, mode 2/B, with a frequency of 0.246 Hz (Figure 4.5a) and an example blade-dominant mode, mode 11, with a frequency of 2.00 Hz (Figure 4.5b). While only mode shapes of the OWT model with DS foundation are shown, the CS foundation case produces the same qualitative result. The influence of the rotor azimuth angle varies depending



(a) Mode 2/B: 0.246 Hz (tower-dominant mode shape)



(b) Mode 11: 2.00 Hz (blade-dominant mode shape)



(c) Mode shape key

Figure 4.5: Effect of the rotor azimuth angle on the model tower mode shape, ${}^{s}\bar{\phi}_u$, (plan view), shown for two example modes, a tower-dominant mode (a) and a blade-dominant mode (b), of the NREL 5MW with DS foundation model. The coloured markers represent points on the tower at varying heights, as shown in the key (c).

on the extent to which the individual modes are dominated by blade vibrations.

Figure 4.5a shows that the mode shape of the tower for the tower-dominant mode is consistent regardless of the azimuth angle. Figure 4.5b, however, demonstrates that the mode shape of the tower can be sensitive to the rotor azimuth angle for modes that are dominated by blade vibration. This variation would make it difficult for an identification method to capture a stable mode shape, particularly when using tower sensors alone. Furthermore, azimuth-averaging of the model mode shape would need to be applied to provide an individual mode shape to compare against the identified mode shape. Fortunately for this study, the six 'foundation-sensitive' (at $\gamma = 1$) modes have consistent mode shapes across the tower portion, ${}^{s}\bar{\phi}_u$, regardless of the azimuth angle, for both the CS and DS realisations. Some of these modes, modes E and F in particular, only have a small contribution from the tower (see modes FB10 and 13 in Figure 2.7), but it seems that as long as there is sufficient activity of the tower vibration, the mode shape of the tower is practically time invariant when idling.

In practice, monitoring data of an idling OWT captures the variability of the structural vibrations induced by the varying azimuth angle over the recording period. On using this monitoring data, identification methods consequently estimate sensor-based mode shapes that are averaged across the variability seen over the monitoring period. For comparison to the OWT model, these 'azimuth-averaged' identified mode shapes would correspond to azimuth-averaged sensor-based model mode shapes, ${}^{s}\boldsymbol{\phi}^{AZ}$, found by calculating the model mode shapes at equal increments of azimuth angle, az, and averaging across all angles, as demonstrated by:

$$ {}^{s}\boldsymbol{\phi}_{i}^{AZ} = \frac{\sum\limits_{az \in \mathbb{S}} \frac{\pm {}^{s}\boldsymbol{\phi}_{i,az}}{||\pm {}^{s}\boldsymbol{\phi}_{i,az}||}}{p}, \qquad \mathbb{S} = \frac{120^{\circ}}{p}\{0, 1, 2... \, p-1\} \tag{4.8} $$

where p is the total number of azimuth increments. In this study, $p = 24$ resulting in 5° increments of the azimuth angle. Some processing of the mode shapes is necessary before averaging to ensure they are of consistent form. The ± in Eq. 4.8 ensures consistency of the sign of a representative DOF for each mode, across the azimuth angles. For example, ± might be chosen such that ${}^{s}\boldsymbol{\phi}(1)_{i,az}$ is always positive. The mode is then divided by the euclidean norm to ensure the consistent form, while retaining the mode shape complexity. The azimuth averaging is applied to both the undamped and damped mode shapes, giving ${}^{s}\boldsymbol{\phi}_{u}^{AZ}$ and ${}^{s}\boldsymbol{\phi}_{d}^{AZ}$ respectively. These are subsequently normalised using Eqs. 3.23 or 3.25 to give ${}^{s}\bar{\boldsymbol{\phi}}_{u}^{AZ}$ or ${}^{s}\bar{\boldsymbol{\phi}}^{C,AZ}$ respectively. The damped mode shapes are averaged before being complex normalised to reflect the process that occurs during identification, when averaged mode shapes are identified from monitoring data and then subsequently normalised.

Figure 4.6 shows the two elevation views and plan view of these undamped and damped mode shapes (tower portion only) for the six foundation-sensitive modes of the OWT model with CS foundation. The agreement between the mode shapes, ${}^{s}\bar{\boldsymbol{\phi}}_{u}^{AZ}$ and ${}^{s}\bar{\boldsymbol{\phi}}^{C,AZ}$ indicates that the complex normalisation procedure gives a good approximation of the undamped mode shapes of the foundation-sensitive modes,

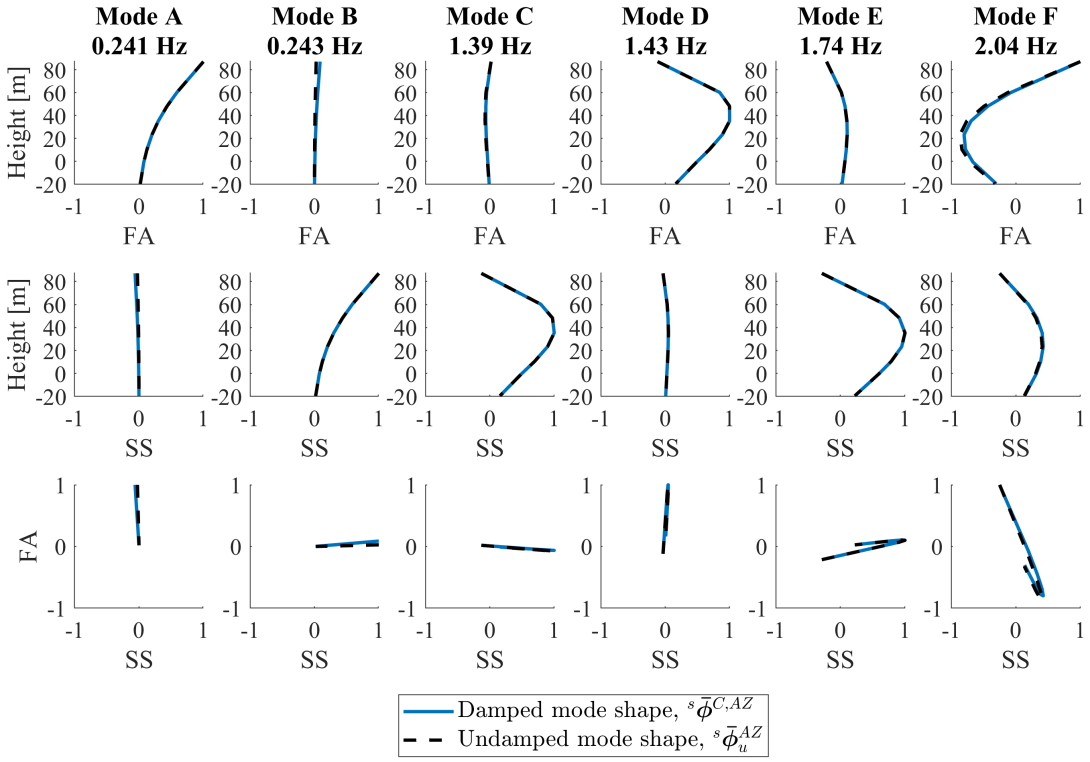


Figure 4.6: Comparison of FAST predicted damped (${}^s\bar{\phi}^C$) and undamped (${}^s\bar{\phi}_u$) mode shapes, averaged across varying azimuth angle, for the foundation-sensitive modes of the NREL 5MW with CS foundation model.

even after azimuth averaging. This averaging is successful since these mode shapes exhibit very little variation with changing azimuth angle, as was shown for mode 2/B in Figure 4.5a.

Figure 4.7 shows the azimuth-averaged undamped and damped mode shapes for the seven foundation-insensitive (and typically blade-dominant) modes of the OWT model with CS foundation. Comparison of the mode shapes for modes 4, 7 and 11 suggests that even if the identification method were able to capture the averaged damped mode shape, ${}^s\bar{\boldsymbol{\phi}}^{C,AZ}$, it would not necessarily agree with the undamped model mode shape, ${}^s\bar{\boldsymbol{\phi}}_u^{AZ}$. This highlights an additional difficulty of trying to capture the behaviour of blade-dominant modes from tower sensors alone. However, the mode shape agreement for modes 3, 5, 6, and 12 is good.

To understand why the averaging works better for some modes, Figure 4.8 shows the MAC between the damped mode shape at azimuth angle, az, compared to the

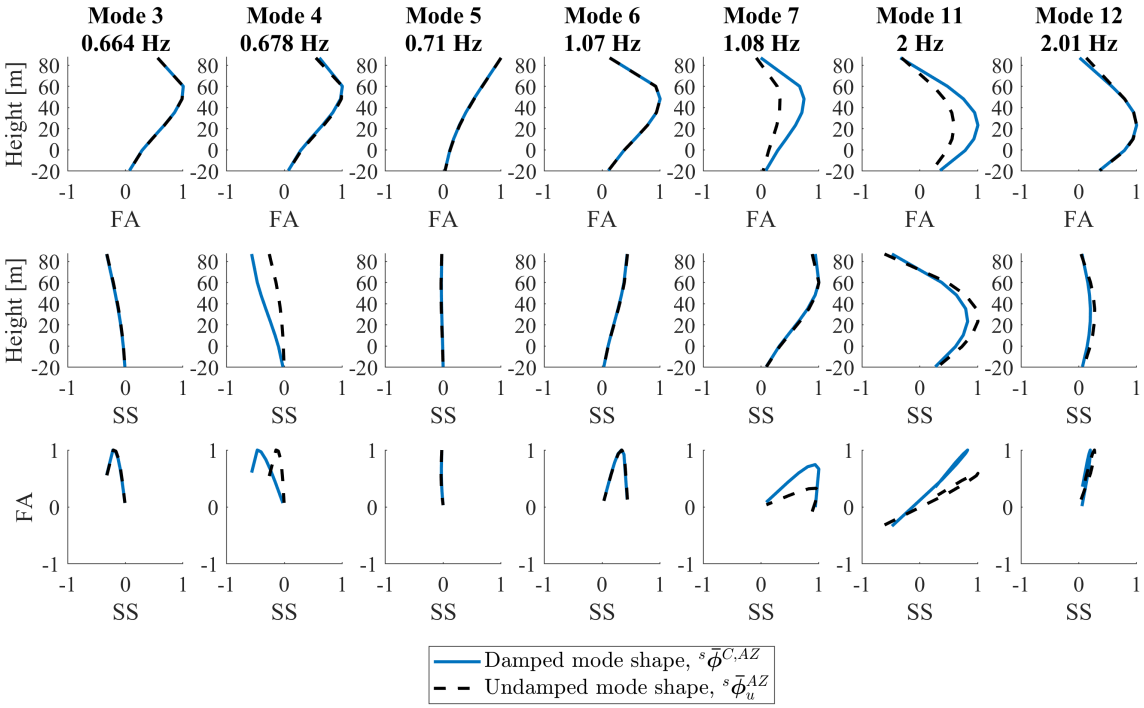


Figure 4.7: Comparison of FAST predicted damped (${}^s\bar{\phi}^C$) and undamped (${}^s\bar{\phi}_u$) mode shapes, averaged across varying azimuth angle, for the foundation-insensitive (and typically blade-dominant) modes of the NREL 5MW with CS foundation model.

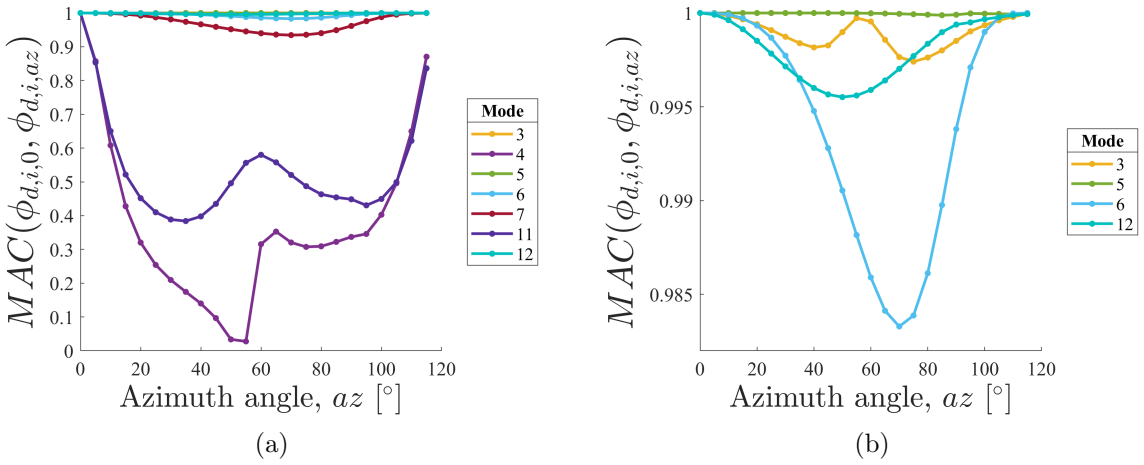


Figure 4.8: (a) MAC of damped mode shape at azimuth angle, az, compared to damped mode shape at azimuth angle, $az = 0$, for the foundation-insensitive modes of the NREL 5MW with CS foundation model. (b) y-axis scale increased to show detail at high MAC values.

damped mode shape at azimuth angle, $az = 0$, (MAC($\boldsymbol{\phi}_{d,i,0}, \boldsymbol{\phi}_{d,i,az}$)) for the same foundation-insensitive modes. The MAC values demonstrate that the mode shapes of modes 3, 5, 6, and 12 (shown in detail in Figure 4.8b) see much less significant variation with the changing azimuth angle when compared to modes 4, 7 and 11.

4.4 Application to model updating

4.4.1 Identification of modal parameters

The FAST model was used to generate simulated data for two cases, both with the blades pitched to 14°. One case has a CS foundation model with stiffness $\boldsymbol{K}_{CS0}$ and the other has a DS foundation model with base stiffness k_{DS0} (see Eq. 4.7 for the stiffness values). The foundation compliances, which are the inverse of the stiffnesses, are the model updating optimisation parameters, $\boldsymbol{\chi}$, and are as follows:

$$c_{DS0} = 1.82 \times 10^{-9} \text{ m/N} \qquad \boldsymbol{C}_{CS0} = \begin{bmatrix} 1.87 & -0.134 \\ -0.134 & 0.0156 \end{bmatrix} \times 10^{-9} \text{ m/N} \quad (4.9)$$

The environmental conditions consisted of stationary water and synthetic wind data generated as described in Section 3.3.2, with mean wind speed of 3 m/s and IEC wind turbulence category B (resulting in a wind turbulence intensity of 37%).

The simulated output data were accelerations in the FA and SS directions for four sensors, $s_j, j = 1...4$, located at heights of 10, 35, 60 and 87m respectively above the MSL, which is 20m above the seabed. The data were sampled at a frequency of 100 Hz for a period of 20 minutes. The acceleration output signals were then contaminated with 1% root-mean-square Gaussian white noise (Eqs. 3.38 and 3.39) to form eight discrete-time output signals, $\boldsymbol{y}_k$, to be supplied to the identification method as shown in Eq. 3.37 .

The system identification methods N4SID and SSI-cov/ref were applied to the simulated output data, $\boldsymbol{y}_k$, for both the cases with CS and DS foundation models. The input data, $\boldsymbol{u}_k$, are not supplied since it is not practical to measure these in reality. Therefore, the methods estimate $\widetilde{\boldsymbol{A}}_D$ and $\widetilde{\boldsymbol{E}}$ of the discrete system, given in Eq. 4.1, for a specified system order. The equivalent continuous system $\widetilde{\boldsymbol{A}}_C$ is calculated using Eq. 3.30, followed by subsequent solution of the eigenvalue problem (Eq. 3.16) to give the identified modal parameters $\widetilde{\boldsymbol{\phi}}_d$ and $\widetilde{\boldsymbol{\lambda}}_d$. $\widetilde{\boldsymbol{\phi}}_d$ are then

transformed to the sensor basis (Eq. 3.31) and complex normalised (Eq. 3.25) to give ${}^{s}\widetilde{\widetilde{\boldsymbol{\phi}}}^{C}$. Finally $\widetilde{\boldsymbol{\zeta}}$ and $\widetilde{\boldsymbol{f}}$ are calculated from $\widetilde{\boldsymbol{\lambda}}_d$ using Eqs. 3.20 and 3.21.

These modal parameters were calculated across a range of model orders. The modes were considered to be stable, and therefore likely representative of a true vibration mode, if the variation of $\widetilde{f}_i$ between consecutive model orders was less than 1%. Typically, the identified damping and mode shapes are also considered for stabilisation. However, for wind turbines the existence of non-proportional damping and close modes can affect the consistency of the damping and mode shape identification respectively. The stabilisation of the mode shapes would require an implementation that firstly characterises the modes as close or well separated and then uses the S2MAC or MAC as appropriate. Therefore, these additional stability criteria were not applied in this chapter. Modes with identified damping above 30% were excluded.

Figure 4.9 shows an example stabilisation diagram for the identification using N4SID of the NREL 5MW model with DS foundation. The identified frequencies,

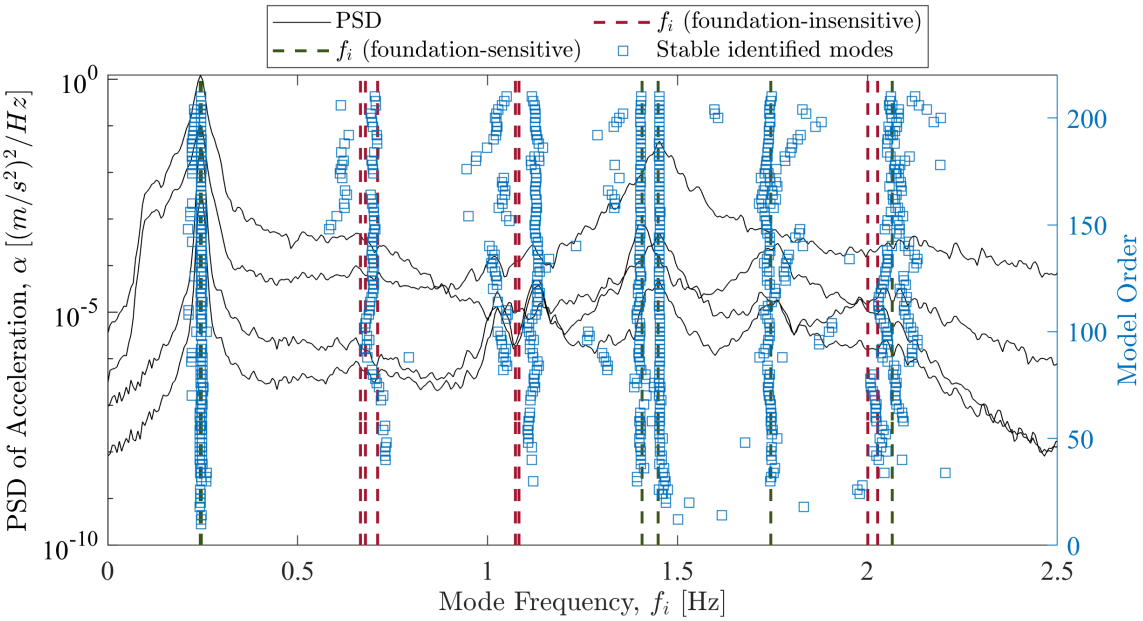


Figure 4.9: Stabilisation diagram for the NREL 5MW with DS foundation identified using N4SID (right axis), power spectral density of four simulated acceleration signals (left axis) and the model modal frequencies (dashed lines).

$\widetilde{\boldsymbol{f}}$, from a model order of 2 to 210 are shown with blue squares. Also shown on the plot, with solid lines, are the power spectral densities (PSD) of the acceleration signals of the tower-top and mid-tower sensors in both the FA and SS directions, $\boldsymbol{\alpha}_{FA}(s_4)$, $\boldsymbol{\alpha}_{SS}(s_4)$, $\boldsymbol{\alpha}_{FA}(s_2)$ and $\boldsymbol{\alpha}_{SS}(s_2)$ respectively. Finally, the dashed lines show the model-estimated modal frequencies, $\boldsymbol{f}$, with the foundation-sensitive modes shown in green and the foundation-insensitive modes shown in red. The six foundation-sensitive modes are identified well as can be seen. Whilst a small number of the foundation-insensitive modes appear to stabilise, the match with $\boldsymbol{f}$ is inferior, and the majority of them are not identified at all, which might be expected given the lack of distinct peaks in the PSD of the tower accelerometer signals, $\boldsymbol{\alpha}$. Furthermore, the identification is likely more difficult due to the variation of the mode shapes with changing azimuth angle, as depicted in Figures 4.5b and 4.8a. Though not shown for brevity, the same qualitative outcomes are seen with the SSI-cov/ref results.

The identification results shown throughout the remainder of the chapter are all identified at a model order of 190, as consistent stabilisation was seen at this order.

Tables 4.1 and 4.2 compare the model and identified frequencies, f_i and $\widetilde{f}_i$ respectively, including a percentage error, ϵ_{fi}, for the foundation-sensitive modes,

Table 4.1: Comparison of numerical ($\boldsymbol{f}_{CS}$) and identified ($\widetilde{\boldsymbol{f}}_{CS}$) frequencies, with % errors ($\boldsymbol{\epsilon}_{f,CS}$), for the NREL 5MW with CS foundation model.

Mode, i	$f_{i,CS}$, Hz	N4SID		SSI-cov/ref	
		$\widetilde{f}_{i,CS}$, Hz	$\epsilon_{fi,CS}$, %	$\widetilde{f}_{i,CS}$, Hz	$\epsilon_{fi,CS}$, %
A	0.241	0.241	0.2	0.240	-0.2
B	0.243	0.243	0.002	0.243	0.1
C	1.39	1.39	-0.4	1.39	-0.1
D	1.43	1.43	0.1	1.43	0.1
E	1.74	1.73	-0.3	1.74	0.1
F	2.04	2.05	0.6	2.03	-0.6

Table 4.2: Comparison of numerical ($\boldsymbol{f}_{DS}$) and identified ($\widetilde{\boldsymbol{f}}_{DS}$) frequencies, with % errors ($\boldsymbol{\epsilon}_{f,DS}$), for the NREL 5MW with DS foundation model.

Mode, i	$f_{i,DS}$, Hz	N4SID		SSI-cov/ref	
		$\widetilde{f}_{i,DS}$, Hz	$\epsilon_{fi,DS}$, %	$\widetilde{f}_{i,DS}$, Hz	$\epsilon_{fi,DS}$, %
A	0.244	0.246	0.8	0.242	-0.8
B	0.246	0.246	0.1	0.248	0.6
C	1.41	1.40	-0.3	1.40	-0.3
D	1.45	1.45	0.2	1.45	0.1
E	1.75	1.74	-0.3	1.75	0.1
F	2.07	2.05	-0.5	2.07	0.3

identified using N4SID and SSI-cov/ref. Table 4.1 shows the results for the CS foundation model case and Table 4.2 the DS foundation model case. The frequencies of all modes are identified well for both foundation model cases, using both identification methods.

Figures 4.10 and 4.11 compare the mode shapes identified by the two methods, ${}^s\widetilde{\bar{\boldsymbol{\phi}}}^C$, against the numerical model mode shapes, ${}^s\bar{\boldsymbol{\phi}}_u$, for the CS and DS foundation cases respectively, showing the two elevation views and the plan view.

In Figure 4.10, the mode shapes of modes A, D and E for the CS foundation cases are shown to be identified well, with both identification methods. Similarly, in Figure 4.11, for the DS cases, modes D, E and F are identified well. It can be seen by looking at the elevation views of both Figures 4.10 and 4.11 that for all the remaining modes, the 'shape' of the mode shape appears to be identified consistently. However, when looking at the plan views (bottom row) it is observed that the 'direction' of the mode shapes appear to be incorrect. As explained previously, this can be as a result of the mode frequencies being closely spaced, meaning that the identification method identifies mode shapes that belong to the subspace spanned by the close modes, which are not guaranteed to be along the FA or SS directions.

Table 4.3 shows the correlation between mode shapes ${}^s\widetilde{\bar{\boldsymbol{\phi}}}^C$ and ${}^s\bar{\boldsymbol{\phi}}_u$, as calculated

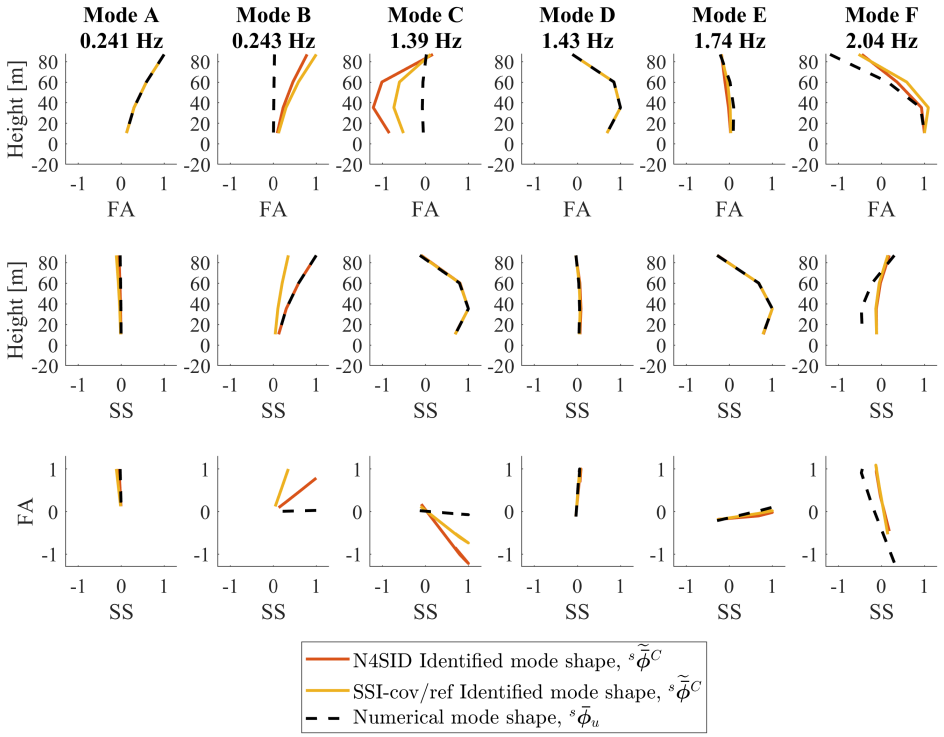


Figure 4.10: Comparison of numerical (${}^s\bar{\phi}_u$) and identified (${}^s\widetilde{\bar{\phi}}^C$) mode shapes for the NREL 5MW with CS foundation.

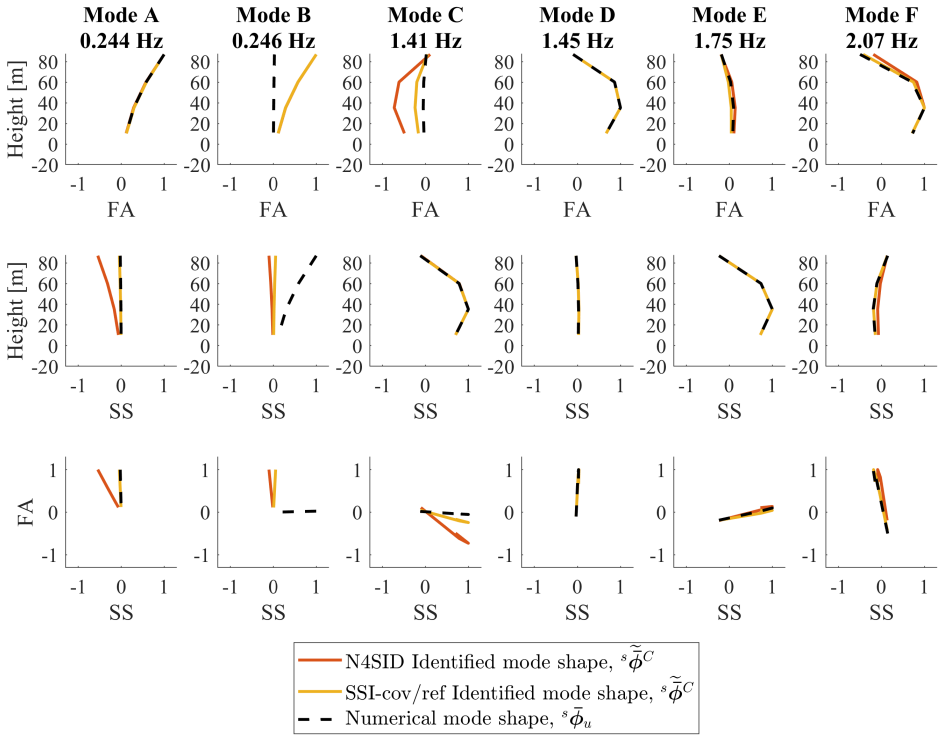


Figure 4.11: Comparison of numerical (${}^s\bar{\phi}_u$) and identified (${}^s\widetilde{\bar{\phi}}^C$) mode shapes for the NREL 5MW with DS foundation.

Table 4.3: MAC and S2MAC results for comparisons between the numerical (${}^s\bar{\boldsymbol{\phi}}_u$) and identified (${}^s\tilde{\bar{\boldsymbol{\phi}}}^C$) mode shapes, for the NREL 5MW with CS and DS foundation representations.

Mode, i	CS: N4SID		CS: SSI-cov/ref		DS: N4SID		DS: SSI-cov/ref	
	MAC	S2MAC	MAC	S2MAC	MAC	S2MAC	MAC	S2MAC
A	0.999	1.000	0.992	1.000	0.787	1.000	1.000	1.000
B	0.647	1.000	0.127	1.000	0.006	1.000	0.006	1.000
C	0.469	1.000	0.711	1.000	0.696	1.000	0.965	1.000
D	0.999	1.000	1.000	1.000	1.000	1.000	0.999	1.000
E	0.985	N/A	0.994	N/A	0.999	N/A	0.997	N/A
F	0.785	0.997	0.754	0.985	0.945	0.992	0.998	0.999

by the MAC and the S2MAC, for both foundation cases and identification methods. As mentioned in Section 4.2.4, values above 0.9 are generally considered to indicate a mode 'match'. The S2MAC compares the identified mode shape, e.g. ${}^s\tilde{\bar{\boldsymbol{\phi}}}^C_A$, with the subspace spanned by the model-estimated mode shapes of the relevant close mode pair, e.g. ${}^s\bar{\boldsymbol{\phi}}_{u,A}$ and ${}^s\bar{\boldsymbol{\phi}}_{u,B}$. The first two close mode pairs are modes A and B and modes C and D. The third pair is mode F and mode 12: a blade-dominant mode that has a frequency of 2.01 Hz in the CS case and 2.03 Hz in the DS case.

The results in Table 4.3 show that the MAC gives varying values ranging from almost 0 to 1, only just over half of which indicate mode matches, demonstrating that the individual mode shapes of the close mode pairs have not all been identified correctly by N4SID or SSI-cov/ref. However, the S2MAC results give values close to 1 across all modes, showing that for modes A to D and F, the mode shapes identified by N4SID and SSI-cov/ref all belong to the subspaces spanned by the corresponding model-estimated mode shape pair. So in essence the subspaces spanned by the close mode pairs have been identified successfully.

The sensitivity of each criterion, MAC and S2MAC, to the foundation stiffness magnitude is investigated, to determine whether they would provide a robust measure for the optimisation algorithm, in the case of close modes. The foundation

stiffness multiplier, γ, was varied for the OWT model with the DS foundation, and the model-estimated mode shapes, ${}^{s}\bar{\boldsymbol{\phi}}_u(\gamma)$, calculated for modes A to D. These were compared with the N4SID identified modes, ${}^{s}\tilde{\bar{\boldsymbol{\phi}}}^{C}$, estimated from data generated with $\gamma = 1$, of modes B and C (shown in Figure 4.11 in orange), using the MAC and S2MAC. It is reminded that the S2MAC compares the identified mode shape, ${}^{s}\tilde{\bar{\boldsymbol{\phi}}}^{C}_{B}$ or ${}^{s}\tilde{\bar{\boldsymbol{\phi}}}^{C}_{C}$, with the subspace spanned by the model-estimated mode shapes (at varying γ) of the relevant close mode pair, ${}^{s}\bar{\boldsymbol{\phi}}_{u,A}(\gamma)$ and ${}^{s}\bar{\boldsymbol{\phi}}_{u,B}(\gamma)$ or ${}^{s}\bar{\boldsymbol{\phi}}_{u,C}(\gamma)$ and ${}^{s}\bar{\boldsymbol{\phi}}_{u,D}(\gamma)$, respectively. Finally, the MAC and S2MAC results were plotted vs γ in Figure 4.12.

The plot shows that for both modes B and C, the S2MAC has a peak value at $\gamma \approx 1$ while the MAC has a peak value at $\gamma \approx 0$. This could have significant consequences in a model updating procedure that aims to optimise the value of γ. While this is elaborated further in Section 4.4.3, if one was to solely optimise based on the closeness of the MAC or the S2MAC to 1, then the S2MAC would indeed

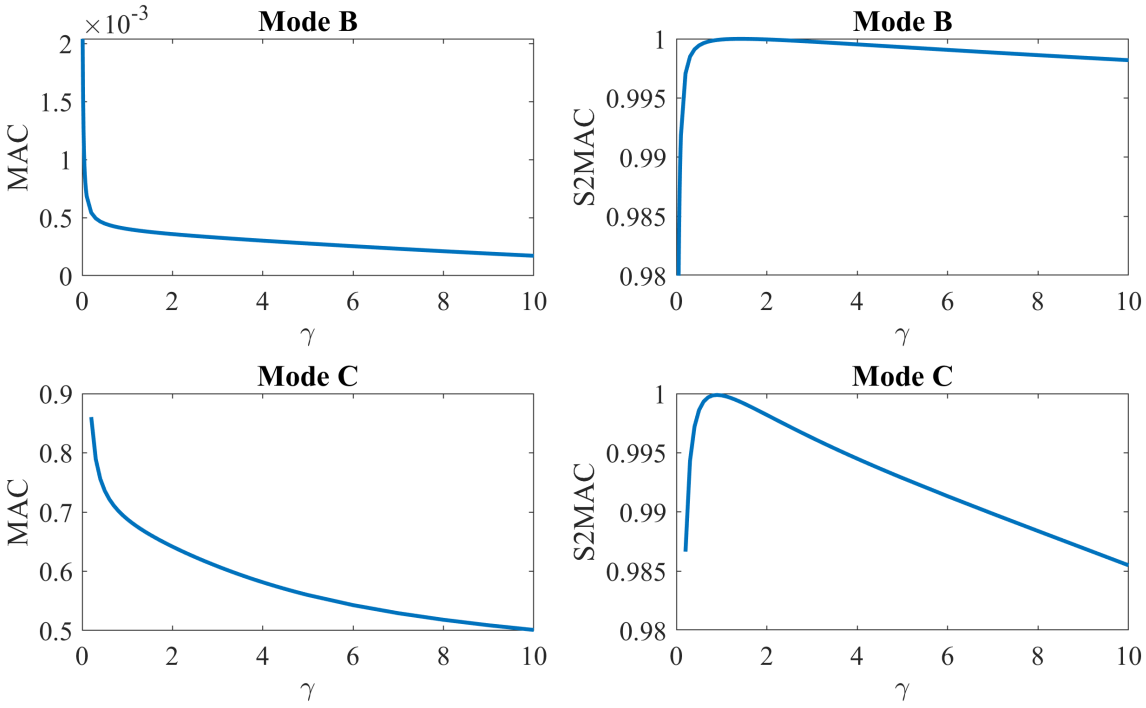


Figure 4.12: MAC (left) vs S2MAC (right) for modes B (top) and C (bottom), comparing the N4SID identified mode shapes (${}^{s}\tilde{\bar{\boldsymbol{\phi}}}^{C}$) with the numerical model mode shapes (${}^{s}\bar{\boldsymbol{\phi}}_u(\gamma)$) calculated with varying foundation stiffness multiplier (γ).

provide useful information to the optimisation algorithm as the values peak close to the true value of $\gamma = 1$, while the MAC would push the optimiser towards $\gamma = 0$, therefore producing incorrect model updating results.

The analysis in this section has demonstrated that in cases where a low MAC may suggest a poor match between model and identified modal properties, the S2MAC would provide additional information regarding the quality of the match. This can help in assessing the success of the identification and enable the use of these mode shapes in further applications. Were the applications to involve optimisation, such as a model updating method, the S2MAC would provide a robust measure for use in the objective function. Assessing the mode shapes using the MAC alone may have resulted in the rejection of specific identified modes due to their divergence from the expected behaviour from the numerical modelling. For example, without knowledge of the existence and effect of close modes, identifying the 1^{st} and 2^{nd} modes both as FA modes would result in the rejection of one of those modes, and potentially cast doubt on the entire identification set, or perhaps even the numerical model.

4.4.2 Close mode characterisation

In order to know whether to use the MAC or S2MAC in the model updating algorithm, one needs to first determine whether the identification is being affected by the presence of close modes in the structure under review. Two possible approaches are demonstrated here through application to the OWT model. The first involves comparing the identified and model-estimated mode shapes using both the MAC and S2MAC, while the second analyses the identification uncertainties predicted by the SSI-cov/ref method. These are referred to as the criterion and uncertainty approaches respectively, and are shown in detail in this section.

Criterion approach

Firstly, the criterion approach simply consists of using both the MAC and S2MAC to compare the identified and numerical model mode shapes, ${}^{s}\tilde{\bar{\boldsymbol{\phi}}}^{C}$ and ${}^{s}\bar{\boldsymbol{\phi}}_{u}$, and observing whether the S2MAC indicates a match while the MAC does not, suggesting a close mode. As this stage is prior to the model updating, the values of the structural parameters due to be updated are still unknown. So in practice, one might apply this approach multiple times across a reasonable range of estimates of the unknown structural parameter values. However, the example shown here uses the true value of the DS foundation stiffness, k_{DS0}, in order to demonstrate the process.

The approach is applied with the OWT model with DS foundation, to an example mode that has been identified by N4SID as having a frequency of 1.40 Hz (corresponding to mode 8/C, but this would not be known in practice). The elevation and plan views of the identified mode shape are shown in the left column of Figure 4.13. The shape of the bending indicates that a mode with a tower mode shape portion dominated by 2$^{\text{nd}}$ order shape bending has been identified. The next step is to use this mode shape information and the frequency magnitude to refine which model-estimated modes this identified mode could feasibly correspond to. Eliminating the tower-dominant 1$^{\text{st}}$ order shape modes around 0.25 Hz and the group of blade-dominant modes around 0.7 Hz, this leaves eight model modes (6 to 13), the mode shapes of which are also shown in Figure 4.13, that all display an element of 2$^{\text{nd}}$ order shape bending of the tower (i.e. strong contributions from either the q_{TFA2} or q_{TSS2} DOF). Looking at Figure 4.4b, these modes have frequencies between 1 Hz and 2.2 Hz depending on the value of γ, which as discussed would be unknown at this stage of the investigation.

The MAC and S2MAC are then used to compare the identified mode with the eight relevant numerical model modes, modes 6 to 13 (shown in Figure 4.13). In practice, the model modes would be calculated for the best estimate of the unknown structural parameters. However, in this example they are calculated with $\gamma = 1$, so

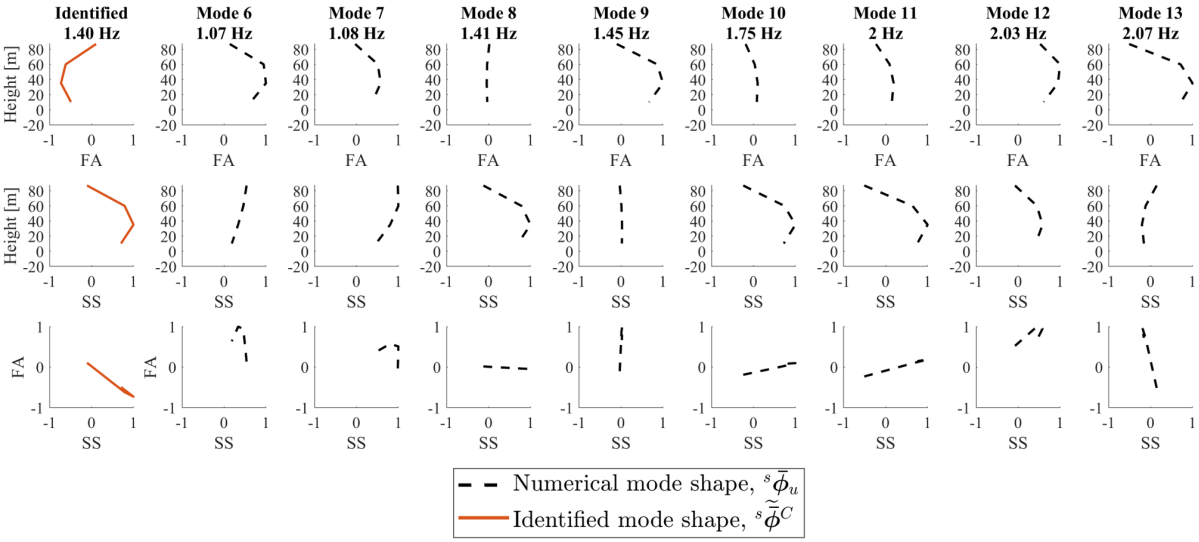


Figure 4.13: Mode shapes of N4SID identified mode with frequency of 1.40 Hz and all possible numerical model mode matches, based on qualitative assessment of the mode shape.

Table 4.4: Example determination of a close mode using MAC and S2MAC. The N4SID identified mode at 1.40 Hz is compared with the numerical model modes found with $\gamma = 1$.

Mode, i	6	7	8	9	10	11	12	13
MAC	0.07	0.07	0.69	0.33	0.54	0.41	0.01	0.51
Modes, i, k	6,7	7,8	8,9	9,10	10,11	11,12	12,13	
S2MAC	0.74	0.80	1.00	0.98	0.67	0.68	0.65	

$k_{DS} = k_{DS0}$. Table 4.4 shows the MAC and S2MAC values that would be calculated when comparing the mode shapes of the relevant model-estimated modes, found with the DS foundation case at $\gamma = 1$, with the mode shape of the N4SID identified mode at 1.40 Hz. The pairs used for the S2MAC are also noted in the Table.

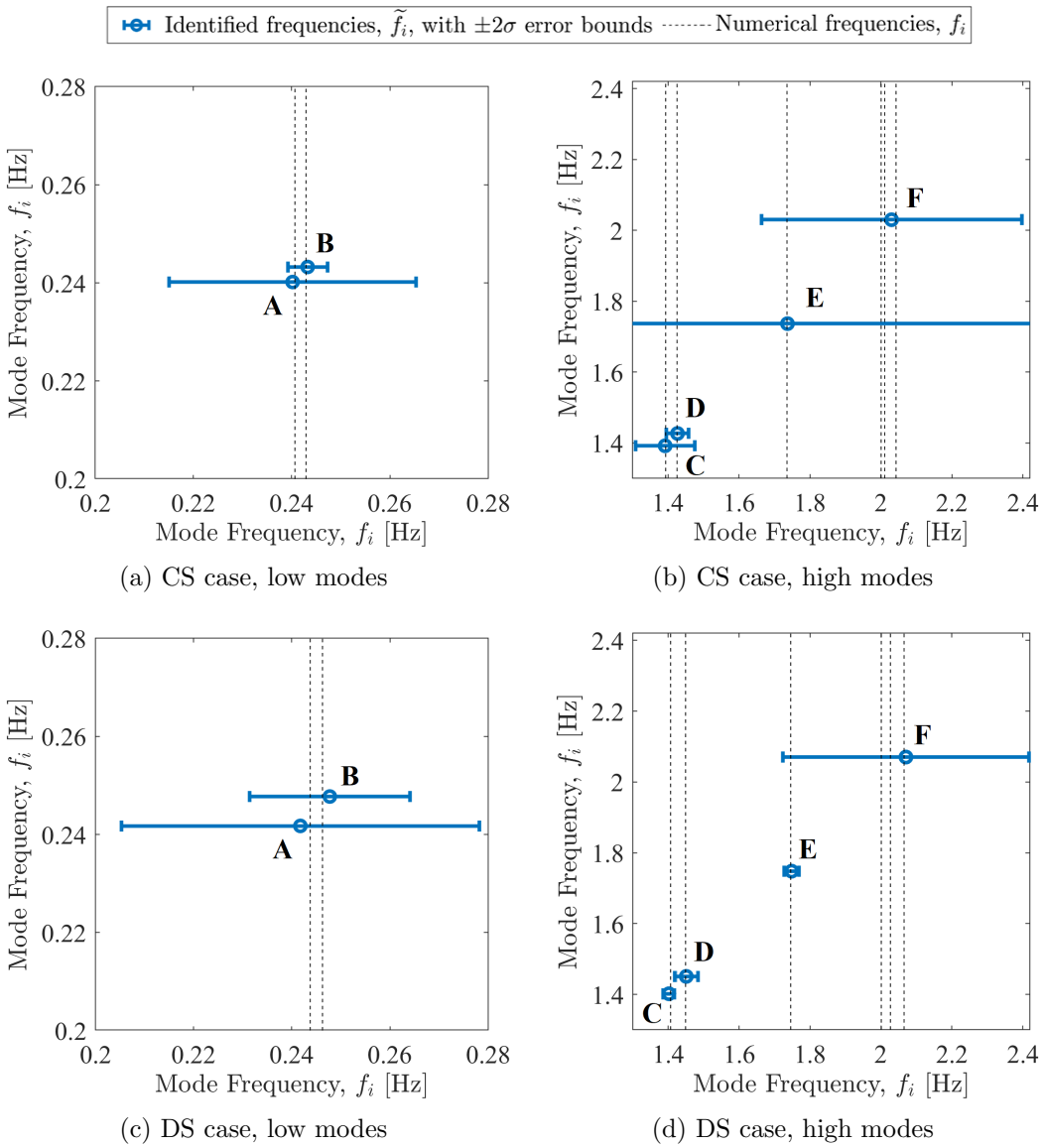
The results in Table 4.4 show that if the MAC values were analysed alone, it could lead to the conclusion that the mode had not been identified well or that it had not yet stabilised and therefore should be discarded, or the assumption that the model is wrong and should be altered. However, by calculating the S2MAC with the potential pairs of consecutive modes, the results show that the mode has been identified correctly and is one of a set of close modes, given as model modes 8 and 9 in

this case. These correspond to the two foundation-sensitive modes around the 1.40 Hz mark as would likely be expected from the frequency comparison. The success of this approach can be dependent on the initial estimate of γ, so in practice this would be applied multiple times across a reasonable range of γ estimates. The uncertainty approach does not suffer from this limitation. Observing the criterion values of Table 4.4 alone may also suggest that modes 9 and 10 form a set of close modes, therefore analysis of the proximity of the modes' frequencies and some engineering judgement is also necessary in this approach. The criterion approach is best applied to problematic identified modes that do not appear to display the correct mode shape 'direction', for investigation into the possible involvement of close modes.

Uncertainty approach

The second approach used to investigate the existence of close modes, the uncertainty approach, consists of employing an identification method that calculates the identification uncertainties, such as the SSI-cov/ref algorithm. Figure 4.14 shows the six identified frequencies, $\widetilde{f}_i$, of modes A to F (modes 1, 2, 8, 9, 10 and 13), for both CS and DS cases, where the associated uncertainties are depicted with error bars. The bars show two standard deviations, $\pm 2\sigma$, corresponding to the 95% confidence interval. The vertical dashed lines show the 'true' frequencies of all the model-estimated modes, f_i.

As shown in Figures 4.14a and 4.14c, the 95% confidence intervals overlap entirely for modes A and B (modes 1 and 2), which indicates that the modes are close. Therefore, the identified mode shapes are likely to be interchangeable, or display directions of vibration that are not coincident with the orthogonal axes, but do exist within the subspace spanned by the corresponding orthogonal close mode pair of the model. Focusing on modes C and D (modes 8 and 9), in the lower left corners of Figures 4.14b and 4.14d, the confidence intervals are seen to overlap entirely for the CS case, but not for the DS case, which agrees with the better identification of



(a) CS case, low modes

(b) CS case, high modes

(c) DS case, low modes

(d) DS case, high modes

Figure 4.14: Graphical representation of the identified frequencies ($\widetilde{\boldsymbol{f}}$) and $\pm 2\sigma$ uncertainty error bounds, found using SSI-cov/ref, for the NREL 5MW with CS (top) and DS (bottom) foundation models. The numerical model frequencies ($\boldsymbol{f}$) are shown with black dashed lines.

these mode shapes for the DS case, when using SSI-cov/ref, as shown in Table 4.3 and Figure 4.11.

Mode E (mode 10) does not belong to a close mode pair, and correspondingly exhibits a low uncertainty for the DS case. However, it does exhibit a large uncertainty for the CS case. This could be caused by a variety of factors, such as low mode excitation or poor sensor placement. The confidence interval of mode F

(mode 13) shows a large uncertainty that spans across the close set of numerical model modes in the 2 Hz vicinity, supporting the conclusion that mode F is also a close mode. While this approach does not require the use of a system model, and avoids the issue of choosing a reasonable initial estimate of γ, as mentioned there are many possible sources of uncertainty, particularly with real monitoring data. Uncertainties from other sources may therefore be mistaken as uncertainty due to close modes. As such, both approaches could be used in conjunction for the best understanding of the close modes. The uncertainty approach could be applied first to give an idea of all potential close modes, and then the criterion approach applied to investigate if being a close mode might be the source of the uncertainty.

4.4.3 Identification of foundation properties

The model updating method, described in Section 4.2.5, is applied to the OWT model for a variety of scenarios, to explore the influence of the modal identification results, $\widetilde{\boldsymbol{f}}$ and ${}^{s}\widetilde{\bar{\boldsymbol{\phi}}}^{C}$ (shown in Section 4.4.1) and use of the MAC and S2MAC, on the foundation identification results.

As discussed in Section 4.2.5, the vector of parameters, $\boldsymbol{\chi}$, to be tuned by the model updating method are the foundation compliances. Therefore $\boldsymbol{\chi}$ consists of c_{11}, c_{12} and c_{22} (the terms of the $\boldsymbol{C}_{CS}$ matrix) for the OWT model with the CS foundation and c_{DS} for the OWT model with the DS foundation. The true values of these compliances can be found in Eq. 4.9 in Section 4.4.1. The initial estimates of the compliances, passed to the optimisation algorithm, in all the presented cases are half their true value, equivalent to $\gamma = 2$.

Given the negligible influence of the azimuth angle on the foundation-sensitive modes, during optimisation the numerical model modal properties are calculated at a single azimuth angle, with one blade directly vertical, for computational efficiency.

The model updating method estimates the foundation compliances by minimising the objective function given in Eq. 4.4, which in essence computes the similarity

between the model-estimated and identified modal properties, with higher similarity reducing the objective function value. The corresponding model and identified modes must be matched to one another to enable comparison. If all the modes of a structure within the frequency range of interest (which is $0 - 2.5$Hz in this application) are identified, then a potential approach would be to sort the model and identified modes by frequency magnitude and match them in order. However, in situations where only a subset of these total modes are identified, as is the case with this OWT, the matching process is more difficult. A common approach is to use the MAC to match the modes based on the similarity between the model and identified mode shapes; this is investigated in Chapter 5. Since this work uses numerically simulated data rather than monitoring data from a real structure, this mode matching issue is bypassed by setting the objective function to compare the modes which are known, through numerical modelling, to match one another. Though contrived, this is necessary to isolate the focus of this chapter, which is to analyse the effect of the close modes on identification.

Formulating the objective function with MAC vs S2MAC

The first set of model updating scenarios compares the effect on the foundation identification results of using the MAC vs the S2MAC to compute the correlation of the mode shapes in the objective function. Though unlikely in practice, the frequencies are not included in order to isolate the effect of using the MAC vs the S2MAC for the mode shape correlation. In the two following scenarios, ***i*** and ***ii***, the objective functions are formulated as follows:

i. Only the mode shapes, for modes A to D, are used. The correlation between the corresponding identified and numerical model mode shapes is calculated using the MAC.

$$J(\boldsymbol{\chi}) = \sum_{i=\{A,B,C,D\}} \left[1 - \text{MAC}\left({}^{s}\bar{\boldsymbol{\phi}}_{u,i}\left(\boldsymbol{\chi}\right), {}^{s}\widetilde{\bar{\boldsymbol{\phi}}}_{i}^{C} \right) \right]$$

ii. Only the mode shapes, for modes A to D, are used. The correlation between the corresponding identified and numerical model mode shapes is calculated using the S2MAC.

$$J(\boldsymbol{\chi}) = \sum_{i=\{A,B,C,D\}} \left[1 - \text{S2MAC}\left({}^{s}\bar{\boldsymbol{\phi}}_{u,i}(\boldsymbol{\chi}), {}^{s}\bar{\boldsymbol{\phi}}_{u,k}(\boldsymbol{\chi}), {}^{s}\widetilde{\bar{\boldsymbol{\phi}}}_{i}^{C}\right)\right]$$

Each scenario is run with the model updating algorithm for the four cases (N4SID and SSI-cov/ref results for both the CS and DS models), populating the objective function with the relevant identified mode shapes (shown in Figures 4.10 and 4.11). A percentage error difference between the resulting model updated compliances and the true compliance parameters, $\widetilde{c}_{DS}$ and c_{DS0} and $\widetilde{\boldsymbol{C}}_{CS}$ and $\boldsymbol{C}_{CS0}$ respectively, are calculated for each case giving the foundation identification errors, $\epsilon_{F,DS}$ and $\epsilon_{F,CS}$, shown in Table 4.5.

Across all cases the foundation errors found by formulating the objective function with the S2MAC are significantly smaller than those found with the MAC, demonstrating the benefit of using the S2MAC over the MAC for situations where close modes have inhibited the mode shape identification. The errors seen with the 'S2MAC' scenario ***ii*** results are likely due to the small identification errors in the 'shape' of the identified mode shapes, i.e. the errors that would remain if the incorrect 'direction' identification due to the close modes were to be removed.

To illustrate the reason for the error differences between scenarios ***i*** and ***ii***, Figure

Table 4.5: Model updating results: Foundation identification errors, ϵ_F, for scenarios *i* and *ii*.

Scenario	$\epsilon_{F,CS}$ [%] (N4SID)	$\epsilon_{F,CS}$ [%] (SSI-cov/ref)	$\epsilon_{F,DS}$ [%] (N4SID)	$\epsilon_{F,DS}$ [%] (SSI-cov/ref)
i (MAC modes A-D)	$\begin{bmatrix} 310 & 120 \\ 120 & 23 \end{bmatrix}$	$\begin{bmatrix} 170 & 130 \\ 130 & 88 \end{bmatrix}$	520	110
ii (S2MAC modes A-D)	$\begin{bmatrix} -8 & -15 \\ -15 & -22 \end{bmatrix}$	$\begin{bmatrix} -8 & -14 \\ -14 & -21 \end{bmatrix}$	1	-1

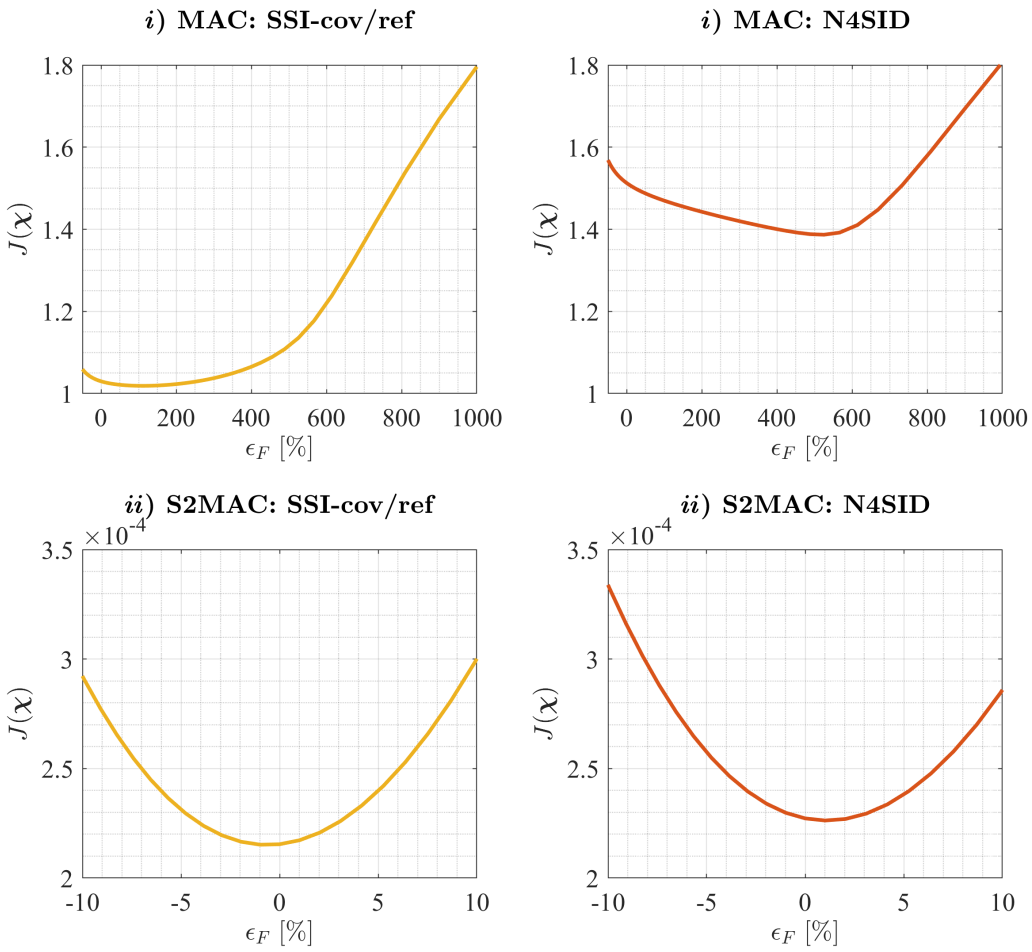


Figure 4.15: Objective function, $J(\chi)$, against foundation identification error, ϵ_F, for model updating scenarios ***i*** and ***ii***, for the cases with DS foundation model.

4.15 shows the objective function, $J(\chi)$, against the foundation identification error $\epsilon_{F,DS}$ for the model updating cases with the DS foundation model. The minimum point of the curves match the $\epsilon_{F,DS}$ results given in Table 4.5, demonstrating that the optimisation algorithm, fminsearch, is effective. Figure 4.15 shows that the combination of the MAC value contributions for both the examples of scenario ***i*** result in a minimum value of the overall objective function that does not occur at or near to the true foundation compliance, c_{DS0}. Hence, foundation compliances with large errors are identified. These are in contrast to the examples of scenario ***ii***, which use the S2MAC in the objective function and present a minimum value near to c_{DS0}.

The three-parameter CS foundation cases are more difficult to analyse as the ob-

jective function surface cannot be visualised. However, it is reasonable to presume that, as in the DS case, the 'surface minimum' does not occur at foundation compliance values near to the true values, $\boldsymbol{C}_{CS0}$, as a result of the MAC contributions computed with the erroneously identified mode shapes of modes B and C.

Realistic objective function formulations

If the analyst were not familiar with the issue of close modes and the existence of the S2MAC formulation, the modal results could prompt multiple interpretations. Various scenarios have been formulated to cover the most likely interpretations, and each then tested with the model updating algorithm to compare the outcomes on the foundation identification.

A common first approach would be to formulate the objective function with all six identified modes, using both the frequencies and mode shapes and using the MAC to calculate the mode shape correlations (**scenario *iii***). Given that the analyst may realise that the identified mode shapes are not as expected, they might decide to formulate the objective function using only the frequencies of the six identified modes (**scenario *iv***). The mode shapes of the 1$^{\text{st}}$ and 2$^{\text{nd}}$ modes (modes A and B) are particularly problematic; looking at Figure 4.11 both identification methods appear to identify both of these modes as predominantly vibrating in the FA direction. Hence, the analyst might decide to ignore their mode shapes and compare the averaged identified frequency of this pair of modes with the corresponding model predicted average. The objective function would then be formulated with these averaged frequencies of modes A and B, in addition to the frequencies and mode shapes (using MAC) of the other four identified modes (C to F) (**scenario *v***). Finally, if the analyst became aware of the presence of close modes and the possible impact on the identified mode shapes, they would use all the frequencies and mode shapes in the objective function, but use the S2MAC for the close modes (modes A, B, C, D and F) and the MAC for mode E (**scenario *vi***).

The scenarios are summarised, along with the objective function formulations, as follows:

iii. The frequencies and mode shapes of the six foundation-sensitive modes, A to F, are all included and the MAC is used for the mode shape correlation.

$$J(\boldsymbol{\chi}) = \sum_{i=\{A,B,C,D,E,F\}} \left[\left(\frac{f_i(\boldsymbol{\chi}) - \widetilde{f}_i}{\widetilde{f}_i} \right)^2 + \left(1 - \text{MAC} \left({}^s\bar{\boldsymbol{\phi}}_{u,i}(\boldsymbol{\chi}),\ {}^s\widetilde{\bar{\boldsymbol{\phi}}}_i^C \right) \right) \right]$$

iv. The frequencies of the six foundation-sensitive modes, A to F, are all included and mode shapes are ignored.

$$J(\boldsymbol{\chi}) = \sum_{i=\{A,B,C,D,E,F\}} \left[\left(\frac{f_i(\boldsymbol{\chi}) - \widetilde{f}_i}{\widetilde{f}_i} \right)^2 \right]$$

v. The user is not sure how to interpret modes A and B, so they average the identified and model frequencies and ignore their mode shapes. The frequencies and mode shapes for all modes C to F are included and the MAC is used for the mode shape correlation.

$$J(\boldsymbol{\chi}) = \left(\frac{0.5(f_A(\boldsymbol{\chi}) + f_B(\boldsymbol{\chi})) - 0.5(\widetilde{f_A} + \widetilde{f_B})}{0.5(\widetilde{f_A} + \widetilde{f_B})} \right)^2 + \sum_{i=\{C,D,E,F\}} \left[\left(\frac{f_i(\boldsymbol{\chi}) - \widetilde{f}_i}{\widetilde{f}_i} \right)^2 + \left(1 - \text{MAC} \left({}^s\bar{\boldsymbol{\phi}}_{u,i}(\boldsymbol{\chi}),\ {}^s\widetilde{\bar{\boldsymbol{\phi}}}_i^C \right) \right) \right]$$

vi. All frequencies and mode shapes are included, but S2MAC is used for the mode shape correlation of the close modes (modes A, B, C, D and F) and MAC is used for mode E.

$$J(\boldsymbol{\chi}) = \sum_{i=\{A,B,C,D,E,F\}} \left(\frac{f_i(\boldsymbol{\chi}) - \widetilde{f}_i}{\widetilde{f}_i} \right)^2 + \sum_{i=\{E\}} \left(1 - \text{MAC} \left({}^s\bar{\boldsymbol{\phi}}_{u,i}(\boldsymbol{\chi}),\ {}^s\widetilde{\bar{\boldsymbol{\phi}}}_i^C \right) \right) + \sum_{i=\{A,B,C,D,F\}} \left(1 - \text{S2MAC} \left({}^s\bar{\boldsymbol{\phi}}_{u,i}(\boldsymbol{\chi}), {}^s\bar{\boldsymbol{\phi}}_{u,k}(\boldsymbol{\chi}), {}^s\widetilde{\bar{\boldsymbol{\phi}}}_i^C \right) \right)$$

As before, each scenario is run with the model updating algorithm for the four cases (N4SID and SSI-cov/ref results for both the CS and DS models). As previ-

Table 4.6: Model updating results: Foundation identification errors, ϵ_F, for scenarios ***iii*** to ***vi***.

Scenario	$\epsilon_{F,CS}$ [%] (N4SID)	$\epsilon_{F,CS}$ [%] (SSI-cov/ref)	$\epsilon_{F,DS}$ [%] (N4SID)	$\epsilon_{F,DS}$ [%] (SSI-cov/ref)
iii	$\begin{bmatrix} -83 & -28 \\ -28 & 84 \end{bmatrix}$	$\begin{bmatrix} -87 & -38 \\ -38 & 78 \end{bmatrix}$	-18	-2
iv	$\begin{bmatrix} -18 & 13 \\ 13 & -3 \end{bmatrix}$	$\begin{bmatrix} 59 & -34 \\ -34 & 6 \end{bmatrix}$	-0.4	1
v	$\begin{bmatrix} -79 & -22 \\ -22 & 81 \end{bmatrix}$	$\begin{bmatrix} -86 & -37 \\ -37 & 80 \end{bmatrix}$	-18	-2
vi	$\begin{bmatrix} 10 & -8 \\ -8 & 1 \end{bmatrix}$	$\begin{bmatrix} -41 & 3 \\ 3 & 10 \end{bmatrix}$	-11	-5

ously mentioned, the initial estimates of the compliances are half the true values, and the correct corresponding identified and numerical model modes are matched manually to circumvent the issue of how to automatically match them. The foundation identification errors, $\epsilon_{F,DS}$ and $\epsilon_{F,CS}$, calculated by finding the percentage difference between the model updated and the true foundation compliance parameters, $\widetilde{c}_{DS}$ and c_{DS0} and $\widetilde{\boldsymbol{C}}_{CS}$ and $\boldsymbol{C}_{CS0}$ respectively, with each of the scenarios, are shown in Table 4.6.

In the majority of cases, scenario ***vi***, in which the S2MAC is used, provides the best identified foundation, especially for the cases with the CS foundation. The 'frequency only' scenario, ***iv***, performs the best for the DS foundation cases, but for the more complex three-parameter optimisation involved with the CS foundation cases, it appears beneficial to provide additional information in the form of the S2MAC mode shape comparison.

Looking back at Figure 4.4, it is clear that the frequencies of modes C to E have a higher sensitivity to the foundation compliance than modes A and B, around $\gamma = 1$. This might help explain why the use of the S2MAC does not improve the results for the DS SSI-cov/ref case. It can be seen from Table 4.3 that for this specific case, the S2MAC formulation is not required in the objective function for the more

highly sensitive modes, C to E, as the MAC is already sufficient. The erroneous objective function contribution from mode shape B is, therefore, not significant enough to corrupt the overall objective function surface that results from the other contributions. This is in contrast to scenario ***i*** seen previously (Figure 4.15), and the N4SID cases of scenarios ***iii*** and ***v***, where the MAC contributions of the erroneously identified mode shapes are sufficient to corrupt the objective function surface.

As with scenarios ***i*** and ***ii***, the CS foundation cases cannot be easily analysed due to the complex three-parameter optimisation. However, it is reasonable to presume once again that the larger errors of scenarios ***iii*** and ***v*** are caused by a similar corruption of the objective function 'surface' with the malinformed use of the MAC, resulting in the 'surface minimum' not occurring at foundation compliance values near to the true values, $\boldsymbol{C}_{CS0}$. Though the identified and model-estimated modes are matched manually at the start of the model updating process, there is a chance that during the updating of the $\boldsymbol{C}_{CS}$ parameters, the modes cross one another, rendering these matches incorrect and possibly inducing errors in the results. This is investigated in more detail in Chapter 5. Nonetheless, the important outcome from the CS cases is that using the S2MAC for comparison of the close modes (scenario ***vi***) rather than the MAC, gives more accurately identified foundation properties.

4.5 Summary

This chapter has shown that the modal parameters necessary for inferring OWT foundation stiffness can be identified from simulated idling data. Furthermore these parameters can be used to update the foundation parameters of the OWT foundation model, in two different forms: a macro-element with coupled springs and depthwise-varying springs.

Analysis using the NREL 5MW OWT model has shown that the time variability introduced by idling causes time variability in some mode shapes as the rotor az-

imuth angle is varied. This effect is particularly prominent for blade-dominant modes, when observing the tower portion of their mode shapes. However, the foundation-sensitive modes have consistent tower mode shapes regardless of the azimuth angle.

Only a subset of the OWT modes are sensitive with respect to the parameters of the foundation, at any given realisation of those parameters. At the specific foundation stiffness modelled in this chapter, there appear to be six foundation-sensitive modes. The frequencies of these foundation-sensitive modes are all identified well from simulated tower acceleration data, of a 5MW OWT (sub-model FB) idling at $3rpm$, using N4SID and SSI-cov/ref. The foundation-insensitive blade-dominant modes are not generally identified well, if at all.

The quasi-axisymmetric nature poses a challenge for the identification of the OWT's mode shapes due to the presence of close modes. Two approaches are demonstrated to investigate their presence, and use of the MAC and S2MAC shows that despite incorrect identification of the individual mode shape for some modes, the mode shape subspaces spanned by the pairs of close modes are identified successfully. This enables the extraction of useful information from mode shapes that may otherwise have been disregarded if the MAC alone had been assessed.

An application of the identified modal data is demonstrated through the identification of the foundation parameters with a model updating approach. A range of modal data interpretation scenarios were investigated, to see their impact on the identified foundation parameters, importantly including scenarios where the existence of close modes was acknowledged or ignored. These results show that adopting the S2MAC gives consistently better foundation identification results, for the situations where close modes have inhibited the mode shape identification. For the common application of a system with close modes, employment of the S2MAC has been shown to enable the use of identified modal information that might otherwise have been thought incorrect and discarded.

Chapter 5

Mode veering and crossing during optimisation

5.1 Introduction

When estimating parameters that describe the mechanical properties of a structure through model optimisation, it is common to update a vector of model parameters, $\boldsymbol{\chi}$, until the model modal properties agree with those identified from sensor measurements, within a reasonable tolerance (Mottershead & Friswell, 1993). The model and identified modal properties must be referenced or matched in some way. This means that given a set of model estimated modes and a separate set of identified modes from data, one must choose which modes of the model set are to be compared to each of the modes in the identified set. This process can be non-trivial because the model modal properties will change as the model parameters are tuned, each to a different extent depending on its sensitivity to the varying parameters. Hence, mode veering and/or mode crossing can occur, as introduced in Sections 1.3.3 and 2.3.3. As a model parameter is varied, mode veering is when the frequencies of the modes approach one another and then veer away without crossing (Leissa, 1974). In comparison, when the frequencies of the modes approach and then cross one another, such that their rank (with respect to their frequency) changes, this is referred to as mode crossing. It is therefore important to understand the mode veering or crossing behaviour, herein referred to jointly as mode crossing behaviour, of the system in question and the likely cause. This may affect the implementation of the optimisation, for example the choice of optimisation algorithm, or the inclusion of a mode tracking technique.

This chapter presents an OWT system that exhibits both mode veering and crossing. Furthermore, the OWT presents different mode crossing behaviour depending on whether the modes have been calculated from the damped or undamped version of the system state-space matrix. The potential source of this behaviour is first demonstrated through the use of a simple analytical 2DOF system. Potential impacts of mode veering and crossing are investigated with the foundation identification model updating application used in Chapters 3 and 4, applied here on the

undamped OWT sub-model FB system with CS foundation.

If the model can be symbolically expressed in terms of the optimisation parameters, $\boldsymbol{\chi}$, then the eigenvalue problem can be solved in terms of those parameters. By choosing a specific consistent root of the determinant, the frequency and mode shape of a consistent mode of the structure can be expressed as a function of $\boldsymbol{\chi}$. This analytical solution of the problem allows each unique mode to be consistently tracked for any value of $\boldsymbol{\chi}$. However, this is often impractical. Firstly, because models are often assembled numerically, as in the case of the OWT in this thesis. Secondly, the symbolic computation of eigenvalues and eigenvectors can be limited to systems of lower order due to computational capabilities (De Jager, 1995).

Due to these constraints, the modal properties of a system are typically defined numerically. As a result, determination of the crossing behaviour is not straightforward, as solving the eigenvalue problem numerically only provides information at discrete $\boldsymbol{\chi}$ values. To determine the crossing behaviour, one needs additional information about continuity, i.e. how the frequencies transition between these discrete points. Various existing methods for tracking the numerical model modes or calculating eigenderivatives were introduced in Section 1.3.3. In this chapter, Nelson's original method for calculating the eigenvalue and eigenvector derivatives of undamped systems (Nelson, 1976) and Friswell's extension, for non-proportionally damped non-self-adjoint systems (M. I. Friswell & Adhikari, 2000), are employed. They are applied to the undamped and damped systems respectively, for both the OWT and the 2DOF systems, to predict the mode crossing behaviour.

As introduced in Section 1.3.4, Lallement and Inman (1995) showed that when a system is non-proportionally damped, the natural frequencies calculated by taking the absolute values of the complex eigenvalues of the damped system are not exactly equivalent to those calculated from the same system with no damping. The OWT model investigated in this study is such a system, and interestingly the two sets of frequencies (calculated with and without the system damping) suggest opposing

mode crossing outcomes. This phenomenon is explored further with the simple analytical 2DOF model.

As previously explained, optimising parameters, $\boldsymbol{\chi}$, using model updating requires the corresponding model and identified modal properties to be matched for each realisation of $\boldsymbol{\chi}$, and two such approaches are explored in the chapter. The first approach, commonly employed in literature, uses the MAC (Allemang & Brown, 1982) to match the identified mode to the model mode with the best MAC value. The other approach classifies the model and identified modes by sorting their frequencies in ascending order. Though not always applicable in practice, this acts as a baseline for comparison with the MAC approach. Both are detailed in Section 5.4.1. This chapter demonstrates that matching the modal properties using the MAC, for this OWT model updating application, results in inaccuracies in the updated structural parameters.

The methodology is outlined in Section 5.2, including the procedures for calculating and processing the modal parameters, and applying Nelson's formulations for eigenderivatives to track consistent modes while $\boldsymbol{\chi}$ varies. The mode crossing problem is demonstrated in Section 5.3.1 and then explored with the 2DOF system in Section 5.3.2. Nelson's method is shown to successfully predict the crossing behaviour for the 2DOF problem and is thus applied to the OWT system in Section 5.3.3. Nelson's method indicates that the undamped and damped OWT systems show contradicting mode crossing behaviour. Finally, Section 5.4 applies model updating to the undamped OWT system, highlighting the importance of knowledge of the veering/crossing behaviour.

5.2 Methodology

5.2.1 Wind turbine model

In this chapter, the implications of the mode crossing behaviour on the model udpating method are investigated using the OWT sub-model FB, as presented in Section 2.2.3, modelled using FAST v7 (J. Jonkman & Buhl, 2005). The DOF of sub-model FB are shown in Figure 5.1 and the dimensions and tower accelerometer locations are shown in Figure 5.2a. Sub-model FB will simply be referred to as the OWT model for the remainder of this chapter.

This model is used to calculate the model modal properties. These are typically compared to modal properties identified from sensor measurements from the structure, as was demonstrated with simulated sensor data in Chapters 3 and 4. However, in this chapter the modal properties calculated by the model, using the 'true' structural parameters, are used as the 'identified' modal properties. This simplification is implemented to remove the effect of identification errors. The model has a sensor configuration consisting of four biaxial accelerometers, measuring in both the FA and SS directions. The sensors are placed at heights of 10, 35, 60 and 87m above the MSL, which is 20m above the seabed. These virtually placed sensors

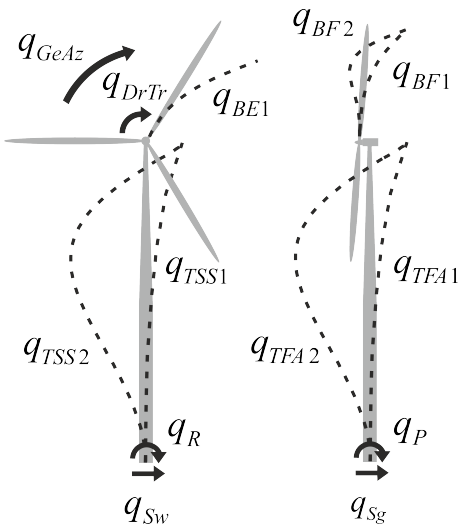
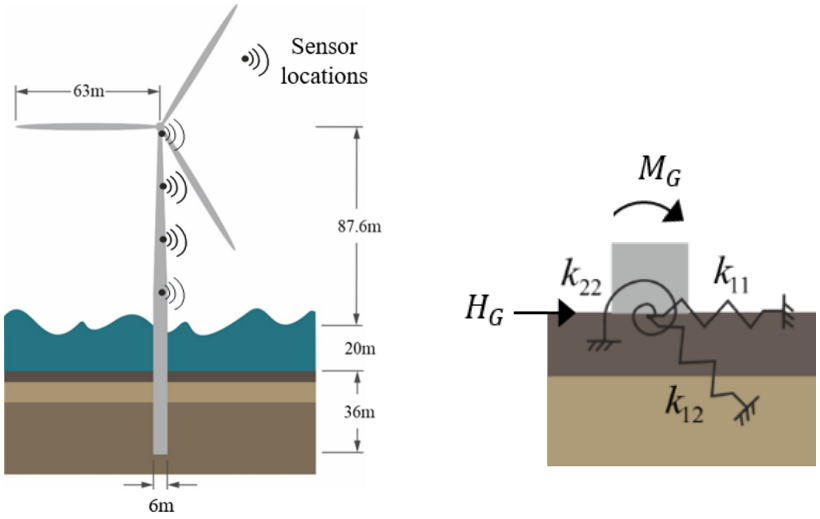


Figure 5.1: Model degrees of freedom.



(a) (b)

Figure 5.2: OWT model dimensions (a) and foundation representation (b).

in the model are used for obtaining the mode shapes of the structure in the sensor basis.

In this chapter, the foundation is represented by the coupled springs macro-element model, shown in Figure 5.2b and explained in Sections 2.2.1 and 3.2.1. As with Chapters 3 and 4, all soil properties are assumed to be axisymmetric about the vertical axis and the model updating procedure aims to estimate the three coupled spring stiffnesses of $\boldsymbol{K}_F$ (k_{11}, k_{12} and k_{22}).

FAST calculates the numerical mass, $\boldsymbol{M}$, damping, $\boldsymbol{D}$, and stiffness, $\boldsymbol{K}$, matrices of the OWT by linearising the nonlinear equations of motion about a specific operating point (see Section 3.2.4), as presented in the FAST user guide (J. Jonkman & Buhl, 2005). In this chapter the operating point used is the steady state vector of the OWT states under gravitational loading.

5.2.2 Calculation of modal parameters

The modal parameters are calculated in the same way as in Chapter 3, detailed in Section 3.2.2. However, the formulation of Nelson's method applied in this work for damped systems requires the calculation of both the left and right eigenvectors,

and the frequencies calculated from the undamped and damped systems are treated independently.

So the calculation of the modal parameters for this chapter firstly follows Eqs. 3.10 to 3.17 from Section 3.2.2. The eigenvectors calculated in those equations implicitly corresponded to the right eigenvectors, $\boldsymbol{\psi}_{R,d}$ and $\boldsymbol{\phi}_{R,d}$. For self-adjoint systems, where the structural matrices are symmetric, the left and right eigenvectors are equal (M. I. Friswell & Lees, 1998). For non-self-adjoint systems, the left eigenvectors can be calculated by solving:

$$\boldsymbol{\psi}^*_{L,d,i}\boldsymbol{A} = \boldsymbol{\psi}^*_{L,d,i}\lambda_{d,i} \quad \boldsymbol{\psi}_{L,d,i} \neq 0 \quad i = 1, 2, ...2n \tag{5.1}$$

where * denotes the complex conjugate transpose. The first order form left eigenvectors, $\boldsymbol{\psi}_{L,d}$, are related to the second order form left eigenvectors, $\boldsymbol{\phi}_{L,d}$, by:

$$\boldsymbol{\psi}_{L,d,i} = \left\{ \begin{array}{c} -(1/\lambda_{d,i})\boldsymbol{K}\boldsymbol{\phi}_{L,d,i} \\ \boldsymbol{M}\boldsymbol{\phi}_{L,d,i} \end{array} \right\} \tag{5.2}$$

The undamped systems used in this work are considered to be self-adjoint, as the $\boldsymbol{M}$ and $\boldsymbol{K}$ matrices are either exactly or approximately symmetric. Therefore $\boldsymbol{\phi}_{L,u} = \boldsymbol{\phi}_{R,u}$ and will be referred to simply as $\boldsymbol{\phi}_u$. The formulations of Nelson's method applied in this study, outlined in Section 5.2.4, require eigenvectors of the second order form. The formulation for undamped systems assumes self-adjoincy and therefore requires $\boldsymbol{\phi}_u$. However, the formulation applied for the damped systems is more generic in not assuming self-adjoincy and requires the provision of $\boldsymbol{\phi}_{L,d}$ and $\boldsymbol{\phi}_{R,d}$. These are found by firstly solving the eigenvalue problems given by Eqs. 3.16 and 5.1 to give $\boldsymbol{\psi}_{R,d}$ and $\boldsymbol{\psi}_{L,d}$ respectively. Then Eqs. 3.17 and 5.2 are used to transform these 1$^{\text{st}}$ order form eigenvectors to the 2$^{\text{nd}}$ order form, $\boldsymbol{\phi}_{R,d}$ and $\boldsymbol{\phi}_{L,d}$, respectively.

$\boldsymbol{\lambda}_d$ and $\boldsymbol{\lambda}_u$ are the diagonal matrices of eigenvalues for the damped and undamped

cases respectively, defined in Eqs. 3.13 and 3.12 respectively. The damping ratios, $\boldsymbol{\zeta}$, are calculated from $\boldsymbol{\lambda}_d$ using Eq. 3.20. The undamped natural frequencies, $\boldsymbol{f}_u$, can be calculated from $\boldsymbol{\lambda}_u$ using:

$$f_{u,i} = \frac{\omega_{u,i}}{2\pi} = \frac{\sqrt{\lambda_{u,i}}}{2\pi} \tag{5.3}$$

where $\boldsymbol{\omega}_u$ are the undamped circular natural frequencies. The natural frequencies for the damped system, $\boldsymbol{f}_c$, can be calculated from $\boldsymbol{\lambda}_d$ using the following equation:

$$f_{c,i} = \frac{\omega_{c,i}}{2\pi} = \frac{|\lambda_{d,i}|}{2\pi} \tag{5.4}$$

where $\boldsymbol{\omega}_c$ are the circular natural frequencies for the damped system. $\boldsymbol{\omega}_c$ are not to be confused with the damped circular natural frequencies, typically denoted $\boldsymbol{\omega}_d$, which are calculated using $\omega_{d,i} = \omega_{u,i}\sqrt{1-\zeta_i^2}$ and will not be used in this study.

$f_{u,i}$ and $f_{c,i}$ are often mistakenly assumed to be exactly equivalent (Lallement & Inman, 1995). While this holds true for proportionally damped systems, it is not true for non-proportionally damped systems. Proportional damping allows the equations of motions to decouple from one another, resulting in equivalent frequencies and mode shapes for the undamped and damped systems, that is $\boldsymbol{f}_u = \boldsymbol{f}_c$ and $\boldsymbol{\phi}_u = \boldsymbol{\phi}_d$.

5.2.3 Mode shape normalisation and comparison

Due to their arbitrary scaling, eigenvectors (or mode shapes) must be normalised according to some adopted convention.

The formulations of Nelson's method, which are outlined in Section 5.2.4, require specific normalisation conventions. For Nelson's formulation for undamped systems, the undamped real-valued eigenvectors utilised must be mass normalised such that

$$\bar{\boldsymbol{\phi}}_{u,i}^T \boldsymbol{M} \bar{\boldsymbol{\phi}}_{u,i} = 1 \tag{5.5}$$

where $\bar{}$ denotes the normalised form. For Friswell's formulation of Nelson's method for damped non-self-adjoint systems, the normalisation used is

$$\bar{\boldsymbol{\phi}}_{L,d,i}^{T} \left[2\lambda_{d,i}\boldsymbol{M} + \boldsymbol{D}\right] \bar{\boldsymbol{\phi}}_{R,d,i} = 1 \tag{5.6}$$

where ^{T} is the nonconjugate transpose.

In Section 5.4 a model updating application is demonstrated on the OWT system. This involves comparison of identified and model mode shapes. Mode shapes identified from sensor data are intrinsically found in the sensor basis form, i.e. they correspond to the locations and measurement type (e.g. acceleration) of the sensors. The model mode shapes, which initially exist in model DOF basis, must be transformed to the equivalent virtual sensor basis, for comparison with the identified mode shapes in the model updating algorithm. The output matrix, $\boldsymbol{E}$, calculated by FAST through the linearisation process, is used to transform the 1$^{\text{st}}$ order form mode shapes, $\boldsymbol{\psi}$, from the state-space basis, $\boldsymbol{x}$, to the output vector basis, $\boldsymbol{y}$, (sensor basis) using Eq. 3.18.

The mode shapes used in the model updating procedure of the undamped system are then normalised using:

$${}^{s}\bar{\boldsymbol{\phi}}_{u,i} = \frac{{}^{s}\boldsymbol{\phi}_{u,i}}{\max({}^{s}\boldsymbol{\phi}_{u,i})} \tag{5.7}$$

As discussed, comparison of modal parameters is fundamental to the model updating process, for example comparing numerical model modal parameters with those identified with a system identification method. The mode shapes are compared using the MAC, given in Eq. 4.2. For the MAC to be meaningful the relevant pair of mode shapes must be in the same basis.

5.2.4 Nelson's method

Nelson's method (Nelson, 1976) enables the calculation of the derivatives of numerical model frequencies and mode shapes symbolically. Different formulations are required for undamped and damped systems. Firstly the original method developed for undamped systems is shown, followed by an outline of the extension of the method to non-proportionally damped non-self-adjoint systems by M. I. Friswell and Adhikari (2000).

Suppose the system defined in Eq. 3.10 is dependent on a set of parameters, $\boldsymbol{\chi}$, such that the system matrices, $\boldsymbol{M}$, $\boldsymbol{K}$ and $\boldsymbol{C}$, are functions of $\boldsymbol{\chi}$. The undamped eigenvalue, $\omega_{u,i}$, and eigenvector, $\boldsymbol{\phi}_{u,i}$, derivatives with respect to an individual system parameter, χ_j, are calculated using the following expressions:

$$\frac{\partial \omega_{u,i}}{\partial \chi_j} = \frac{1}{2\omega_{u,i}} \bar{\boldsymbol{\phi}}_{u,i}^T \left(\frac{\partial \boldsymbol{K}}{\partial \chi_j} - \omega_{u,i}^2 \frac{\partial \boldsymbol{M}}{\partial \chi_j} \right) \bar{\boldsymbol{\phi}}_{u,i} \tag{5.8}$$

$$\frac{\partial \bar{\boldsymbol{\phi}}_{u,i}}{\partial \chi_j} = \left(\boldsymbol{I} - \bar{\boldsymbol{\phi}}_{u,i} \bar{\boldsymbol{\phi}}_{u,i}^T \boldsymbol{M} \right) \boldsymbol{G}^{\dagger -1} \boldsymbol{H}^{\dagger} - \frac{1}{2} \bar{\boldsymbol{\phi}}_{u,i} \bar{\boldsymbol{\phi}}_{u,i}^T \frac{\partial \boldsymbol{K}}{\partial \chi_j} \bar{\boldsymbol{\phi}}_{u,i} \tag{5.9}$$

The matrix $\boldsymbol{G}^{\dagger}$ is derived through modification of the $\boldsymbol{G}$ matrix (Eq. 5.10 below), by replacing the r^{th} row and column elements with zeros and the $(r,r)^{th}$ element with 1, where r is the index of the element of $|\bar{\boldsymbol{\phi}}_{u,i}|$ with the highest value. The vector $\boldsymbol{H}^{\dagger}$ is found by replacing the r^{th} element of vector $\boldsymbol{H}$ (Eq. 5.11 below) with zero.

$$\boldsymbol{G} = \boldsymbol{K} - \omega_{u,i}^2 \boldsymbol{M} \tag{5.10}$$

$$\boldsymbol{H} = - \left(\boldsymbol{I} - \boldsymbol{M} \bar{\boldsymbol{\phi}}_{u,i} \bar{\boldsymbol{\phi}}_{u,i}^T \right) \left(\frac{\partial \boldsymbol{K}}{\partial \chi_j} - \omega_{u,i}^2 \frac{\partial \boldsymbol{M}}{\partial \chi_j} \right) \bar{\boldsymbol{\phi}}_{u,i} \tag{5.11}$$

For the damped systems, we apply a formulation of Nelson's method that was

extended to non-proportionally damped systems with complex modes (M. I. Friswell & Adhikari, 2000). This formulation is applicable to non-self-adjoint systems, where the left and right eigenvectors are not equal. The complex eigenvalue, $\lambda_{c,i}$, derivatives with respect to χ_j are calculated using:

$$\frac{\partial \lambda_{c,i}}{\partial \chi_j} = -\bar{\boldsymbol{\phi}}_{L,d,i}^T \left(\lambda_{c,i}^2 \frac{\partial \boldsymbol{M}}{\partial \chi_j} + \lambda_{c,i} \frac{\partial \boldsymbol{D}}{\partial \chi_j} + \frac{\partial \boldsymbol{K}}{\partial \chi_j} \right) \bar{\boldsymbol{\phi}}_{R,d,i} \tag{5.12}$$

An additional constraint exists on the form of the eigenvectors for this non-self-adjoint formulation of Nelson's method. After applying the normalisation shown in Eq. 5.6, one corresponding element in both the left and right eigenvectors must be set to be equal. This element is arbitrary, but should have a relatively large magnitude in both the eigenvectors. The damped eigenvector derivatives with respect to χ_j are then calculated using:

$$\frac{\partial \bar{\boldsymbol{\phi}}_{R,d,i}}{\partial \chi_j} = \boldsymbol{L}_i^{\dagger -1} \boldsymbol{N}_i^{\dagger} + p_i \bar{\boldsymbol{\phi}}_{R,d,i} \tag{5.13}$$

$$\frac{\partial \bar{\boldsymbol{\phi}}_{L,d,i}}{\partial \chi_j} = \left(\boldsymbol{Q}_i^{\dagger} \boldsymbol{L}_i^{\dagger -1} \right)^T + p_i \bar{\boldsymbol{\phi}}_{L,d,i} \tag{5.14}$$

As with the undamped system, the $\boldsymbol{L}^{\dagger}$ matrix is derived by replacing the r^{th} row and column elements of $\boldsymbol{L}$ (Eq. 5.15 below) with zeros and the $(r,r)^{th}$ element with 1, where r is the index of the element of $|\bar{\boldsymbol{\phi}}_{L,d,i}|$ or $|\bar{\boldsymbol{\phi}}_{R,d,i}|$ with the highest value. The vectors $\boldsymbol{N}^{\dagger}$ and $\boldsymbol{Q}^{\dagger}$ are found by replacing the r^{th} element of vector $\boldsymbol{N}$ (Eq. 5.16 below) or $\boldsymbol{Q}$ (Eq. 5.17 below) respectively with zero. $\boldsymbol{L}$, $\boldsymbol{N}$ and $\boldsymbol{Q}$ are defined by:

$$\boldsymbol{L} = \lambda_{c,i}^2 \boldsymbol{M} + \lambda_{c,i} \boldsymbol{D} + \boldsymbol{K} \tag{5.15}$$

$$\boldsymbol{N} = \left(\lambda_{c,i}^2 \frac{\partial \boldsymbol{M}}{\partial \chi_j} + \lambda_{c,i} \frac{\partial \boldsymbol{D}}{\partial \chi_j} + \frac{\partial \boldsymbol{K}}{\partial \chi_j}\right) \bar{\boldsymbol{\phi}}_{R,d,i} + \left(2\lambda_{c,i}\boldsymbol{M} + \boldsymbol{D}\right) \bar{\boldsymbol{\phi}}_{R,d,i} \frac{\partial \lambda_{c,i}}{\partial \chi_j} \tag{5.16}$$

$$\boldsymbol{Q} = -\bar{\boldsymbol{\phi}}_{L,d,i}^T \left(\lambda_{c,i}^2 \frac{\partial \boldsymbol{M}}{\partial \chi_j} + \lambda_{c,i} \frac{\partial \boldsymbol{D}}{\partial \chi_j} + \frac{\partial \boldsymbol{K}}{\partial \chi_j}\right) - \bar{\boldsymbol{\phi}}_{L,d,i}^T \left(2\lambda_{c,i}\boldsymbol{M} + \boldsymbol{D}\right) \frac{\partial \lambda_{c,i}}{\partial \chi_j} \tag{5.17}$$

Finally, the scalar p_i is defined as:

$$\begin{aligned} p_i = \frac{1}{2}\Big[&-\bar{\boldsymbol{\phi}}_{L,d,i}^T \left(2\lambda_{c,i}\boldsymbol{M} + \boldsymbol{D}\right) \left(\boldsymbol{L}_i^{\dagger -1} \boldsymbol{N}_i^{\dagger}\right) - \left(\boldsymbol{Q}_i^{\dagger} \boldsymbol{L}_i^{\dagger -1}\right) \left(2\lambda_{c,i}\boldsymbol{M} + \boldsymbol{D}\right) \bar{\boldsymbol{\phi}}_{R,d,i} \\ &-\bar{\boldsymbol{\phi}}_{L,d,i}^T \left(2\boldsymbol{M} \frac{\partial \lambda_{c,i}}{\partial \chi_j} + 2\lambda_{c,i} \frac{\partial \boldsymbol{M}}{\partial \chi_j} + \frac{\partial \boldsymbol{D}}{\partial \chi_j}\right) \bar{\boldsymbol{\phi}}_{R,d,i} \Big] \end{aligned} \tag{5.18}$$

When the model parameters, $\boldsymbol{\chi}$, undergo a small perturbation, $\boldsymbol{\Delta\chi} = \{\Delta\chi_1, \Delta\chi_2 \dots\}$, the changed i^{th} eigenvalue, $\omega_{u,i}(\boldsymbol{\chi} + \boldsymbol{\Delta\chi})$, can be approximated using:

$$\begin{aligned} \omega_{u,i}(\boldsymbol{\chi} + \boldsymbol{\Delta\chi}) &\approx \omega_{u,i}(\boldsymbol{\chi}) + \boldsymbol{\Delta\chi} \nabla \omega_{u,i} \\ &\approx \omega_{u,i}(\boldsymbol{\chi}) + \{\Delta\chi_1, \Delta\chi_2 \dots\} \left\{ \frac{\partial \omega_{u,i}}{\partial \chi_1}, \frac{\partial \omega_{u,i}}{\partial \chi_2} \dots \right\}^T \end{aligned} \tag{5.19}$$

or the changed i^{th} complex eigenvalue, $\lambda_{c,i}(\boldsymbol{\chi} + \boldsymbol{\Delta\chi})$, can be found in the same way by substituting $\omega_{u,i}$ with $\lambda_{c,i}$ in the above expression. The process is often referred to as Euler integration. The changed i^{th} undamped eigenvector, $\bar{\boldsymbol{\phi}}_{u,i}(\boldsymbol{\chi} + \boldsymbol{\Delta\chi})$, can similarly be approximated using:

$$\begin{aligned} \bar{\boldsymbol{\phi}}_{u,i}(\boldsymbol{\chi} + \boldsymbol{\Delta\chi}) &\approx \bar{\boldsymbol{\phi}}_{u,i}(\boldsymbol{\chi}) + \left[\nabla \bar{\boldsymbol{\phi}}_{u,i}\right] \boldsymbol{\Delta\chi}^T \\ &\approx \bar{\boldsymbol{\phi}}_{u,i}(\boldsymbol{\chi}) + \left[\frac{\partial \bar{\boldsymbol{\phi}}_{u,i}}{\partial \chi_1}, \frac{\partial \bar{\boldsymbol{\phi}}_{u,i}}{\partial \chi_2} \dots \right] \{\Delta\chi_1, \Delta\chi_2 \dots\}^T \end{aligned} \tag{5.20}$$

or the changed i^{th} left or right complex eigenvectors, $\bar{\boldsymbol{\phi}}_{L,d,i}(\boldsymbol{\chi} + \boldsymbol{\Delta\chi})$ or $\bar{\boldsymbol{\phi}}_{R,d,i}(\boldsymbol{\chi} + \boldsymbol{\Delta\chi})$ respectively, can be found by substituting $\bar{\boldsymbol{\phi}}_{L,d,i}$ or $\bar{\boldsymbol{\phi}}_{R,d,i}$ for $\bar{\boldsymbol{\phi}}_{u,i}$ in the above expression. To start this process, an eigenanalysis of the system model must be performed to calculate the initial modal parameters. Eqs. 5.19 and 5.20 are then used to predict the subsequent realisations of the modal parameters with each $\boldsymbol{\Delta\chi}$

step, without the need to rerun an eigenanalysis of the model.

The system matrix derivatives, $\frac{\partial \boldsymbol{M}}{\partial \chi_j}$, $\frac{\partial \boldsymbol{K}}{\partial \chi_j}$ and $\frac{\partial \boldsymbol{D}}{\partial \chi_j}$ can be found analytically or numerically depending on the nature of the model of the system in question. Numerically, $\frac{\partial \boldsymbol{K}}{\partial \chi_j}$ can be found using:

$$\frac{\partial \boldsymbol{K}}{\partial \chi_j} \approx \frac{\boldsymbol{K}(\chi_j + \Delta\chi_j) - \boldsymbol{K}(\chi_j)}{\Delta\chi_j} \tag{5.21}$$

and $\frac{\partial \boldsymbol{M}}{\partial \chi_j}$ or $\frac{\partial \boldsymbol{D}}{\partial \chi_j}$ can be found by substituting $\boldsymbol{M}$ or $\boldsymbol{D}$ respectively for $\boldsymbol{K}$ in the above expression.

When the eigenvalue problem (e.g. Eq. 3.16) is solved for a numerically assembled model, the order of the resulting eigenvalues and eigenvectors is arbitrary, so they are typically ordered by the relative magnitude of the eigenvalues. This means that when recalculated upon a change in $\boldsymbol{\chi}$, one cannot follow the underlying system modes from one realisation of $\boldsymbol{\chi}$ to the next, as it is not possible to know if the order of the mode eigenvalues has changed. The expressions given in Eqs. 5.19 and 5.20 enable tracking of the system eigenvalues and eigenvectors with incremental discrete changes in the system parameters, $\boldsymbol{\chi}$. It is therefore possible, given a sufficiently small increment $\boldsymbol{\Delta\chi}$, to follow the underlying system modes and determine their crossing behaviour as $\boldsymbol{\chi}$ varies. This is possible because Nelson's method preserves the order of the system's DOF, following a consistent root of the eigenvalue problem.

5.2.5 Model updating

The goal of the model updating algorithm used in this study is to tune a vector of parameters of the model, $\boldsymbol{\chi}$, so that its modal properties match those identified from sensor measurements. This is achieved in this chapter by minimising the following objective function, $J(\boldsymbol{\chi})$:

$$J(\boldsymbol{\chi}) = \sum_{i=1}^{m} \left[\left(\frac{f_{u,i}\left(\boldsymbol{\chi}\right) - \widetilde{f}_{u,i}}{\widetilde{f}_{u,i}} \right)^2 + \left(1 - \mathrm{MAC}\left({}^{s}\bar{\boldsymbol{\phi}}_{u,i}\left(\boldsymbol{\chi}\right), {}^{s}\widetilde{\bar{\boldsymbol{\phi}}}_{i} \right) \right) \right] \tag{5.22}$$

where m is the number of identified modes used for comparison.

$\boldsymbol{\chi}$, are the c_{11}, c_{12} and c_{22} terms of the foundation compliance matrix, $\boldsymbol{C}_F$, which is the inverse of the foundation macro-element stiffness matrix, $\boldsymbol{K}_F$, and is defined in Eq. 3.6, as the compliance matrix terms were found to be a superior basis for comparison of the foundation behaviour within Chapter 3.

$\boldsymbol{f}_u(\boldsymbol{\chi})$ and ${}^s\bar{\boldsymbol{\phi}}_u(\boldsymbol{\chi})$ are the model modal parameters realised for a specific $\boldsymbol{\chi}$ following the procedures set out in Sections 5.2.2 and 5.2.3. ${}^s\bar{\boldsymbol{\phi}}_u(\boldsymbol{\chi})$ are undamped mode shapes calculated using Eq. 3.12, transformed to the sensor basis using Eq. 3.19 and finally normalised using Eq. 5.7.

$\widetilde{\boldsymbol{f}}_u$ and ${}^s\widetilde{\bar{\boldsymbol{\phi}}}$ are the identified modal parameters, typically identified from monitoring data obtained from structural sensors. As previously described, it is assumed in this chapter that the identification is perfectly accurate, so the 'identified' modal parameters are therefore taken as the model modal parameters, calculated with the 'true' foundation parameters, $\boldsymbol{C}_{F0}$. Therefore, $J(\boldsymbol{\chi}) = 0$ when $\boldsymbol{\chi} = \boldsymbol{C}_{F0}$. The work in this chapter has therefore removed the effect of identification errors or modelling errors or bias (Song et al., 2019) on the model updating to isolate and demonstrate an application where understanding of the crossing behaviour of modes would be beneficial. An issue that has been removed is that of close modes affecting the mode shape identification, as covered in Chapter 4. Hence, the use of the MAC in the objective function for this chapter is applicable.

As in Chapters 3 and 4, the objective function of Eq. 5.22 is minimised using the MATLAB fminsearch optimisation algorithm.

5.3 Exploring mode crossing behaviour

5.3.1 Demonstrating mode crossing behaviour of an OWT system

During structural optimisation procedures, such as model updating applications, as the underlying structural parameters are varied the modal frequencies also vary, which can result in the crossing or veering of modes. It is important to understand if this is the case prior to optimisation, so that necessary procedures can be implemented for tracking the modes. In this section the mode crossing behaviour, with respect to the ground-level macro-element foundation stiffness, is demonstrated for the OWT system. The behaviour is investigated by varying $\boldsymbol{K}_F$ using the equation:

$$\boldsymbol{K}_F = \gamma \boldsymbol{K}_{F0} \tag{5.23}$$

where $\boldsymbol{K}_{F0}$ is the baseline stiffness and has the following values:

$$\boldsymbol{K}_{F0} = \begin{bmatrix} 0.0139 & 0.119 \\ 0.119 & 1.66 \end{bmatrix} \times 10^{11} \text{ N/m} \tag{5.24}$$

and γ is a real positive number that represents the normalised foundation stiffness. Linearisation of the OWT system in FAST was used to calculate the numerical model frequencies, $\boldsymbol{f}_u$ and $\boldsymbol{f}_c$, with varying γ. $\boldsymbol{K}_{F0}$ is the statically equivalent macro-element to the embedded monopile with soil stiffness varying linearly with depth from zero at the seabed to 5.5×10^8 N/m at the pile toe. This was calculated using the Oxford 1D FE model of the OWT, which uses Euler-Bernoulli elements.

Figure 5.3 shows the undamped frequency variation with γ for two altered versions of the OWT model. The solid lines correspond to the OWT model with flexible foundation and tower, but rigid blades, and the dashed lines correspond to the OWT model with flexible blades, but a rigid tower and foundation. Therefore,

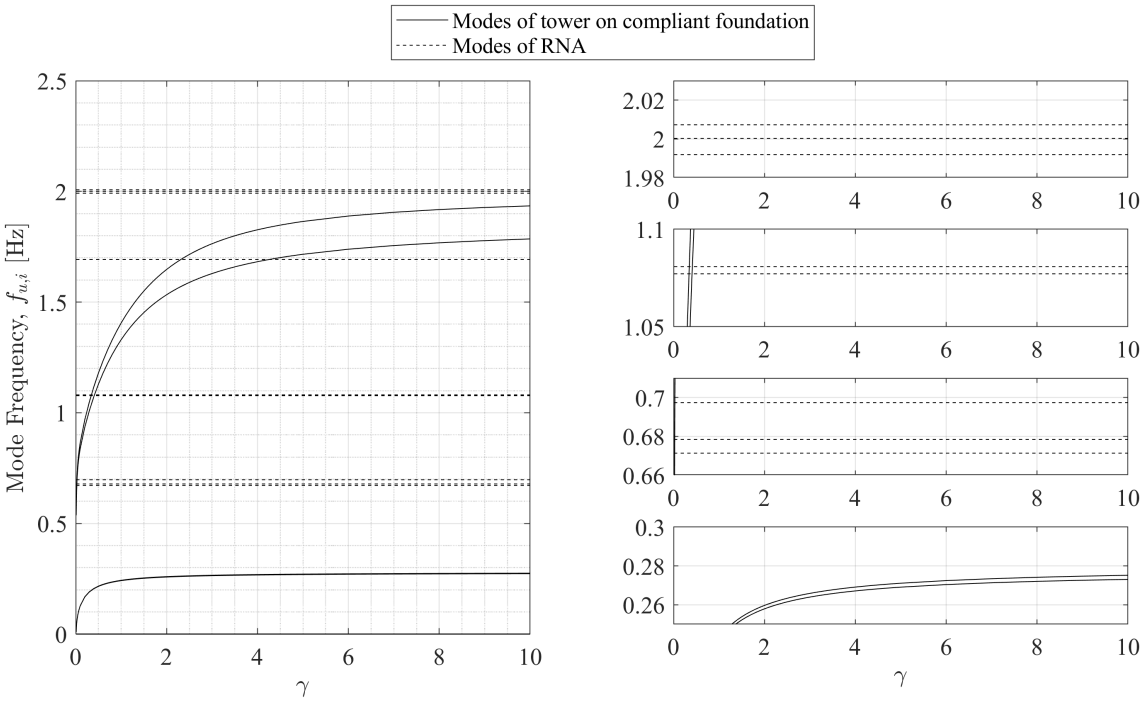


Figure 5.3: Effect of the normalised foundation stiffness, γ, on the frequencies of the undamped OWT system with flexible foundation and tower and rigid blades (solid lines). Also shown are the frequencies of the undamped OWT system with flexible blades and rigid tower and foundation (dashed lines). The y-axis scale is increased on the right for observation of the modes with close frequencies.

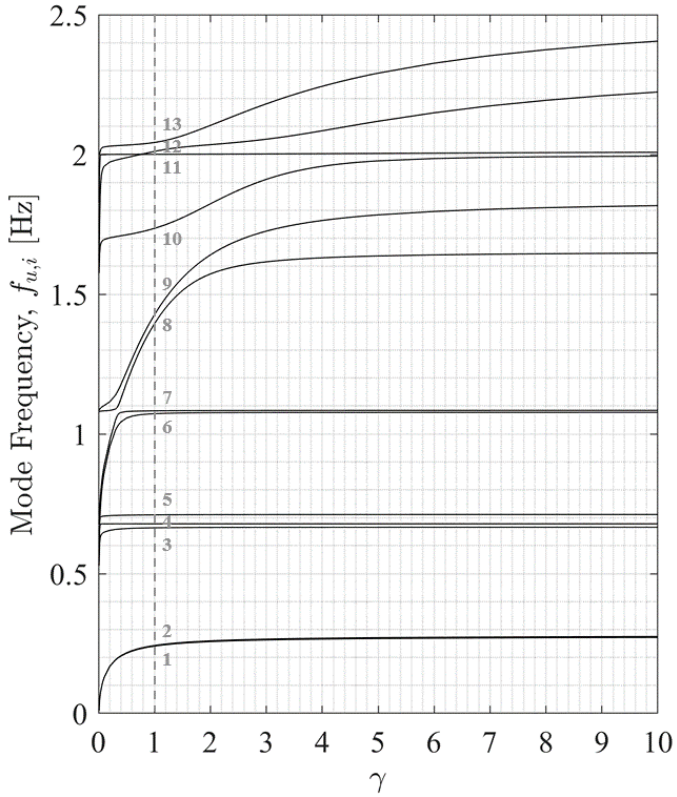
the solid lines show the bending modes of the tower on a compliant foundation, and the dashed lines show the bending modes of the RNA sub-structure.

This figure demonstrates the proximity between the underlying frequencies of vibration of the individual tower and blade sub-structures. This is particularly pertinent for the modes dominated by the 2$^{\text{nd}}$ order tower DOF, q_{TFA2} and q_{TSS2} (the top two solid lines), as their vibration frequencies tend to sit between the frequencies of the modes dominated by the 1$^{\text{st}}$ and 2$^{\text{nd}}$ order blade bending DOF (q_{BF1}, q_{BE1} and q_{BF2}). As a result, when the full OWT is modelled, the 2$^{\text{nd}}$ order tower DOF strongly couple with the blade bending DOF in the mode shapes. This coupling means that certain modes of vibration of the wind turbine will feature contributions from multiple DOF, i.e. bending of both the tower and the blades, rather than solely tower or blade bending.

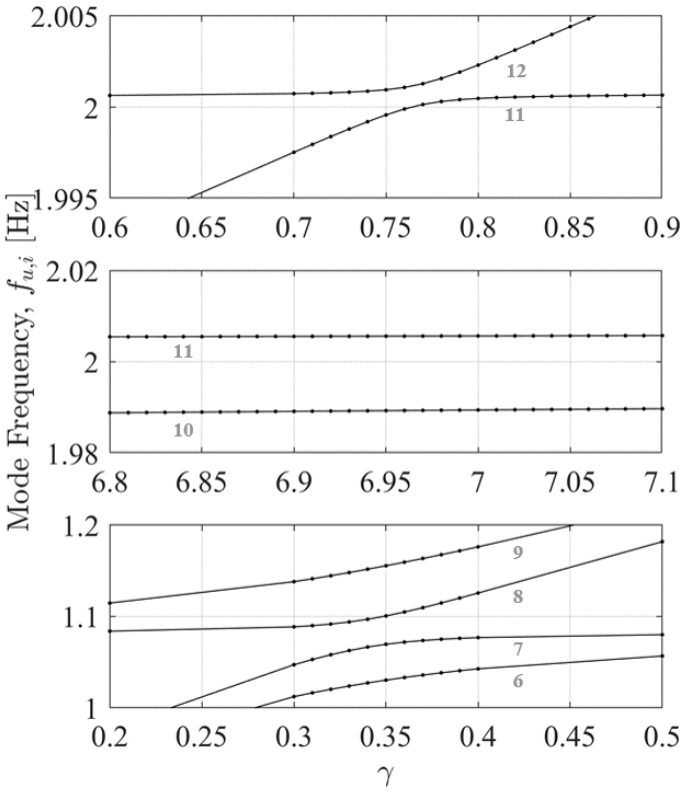
This coupling behaviour can be seen in Figures 5.4a and 5.5a, which show the

frequencies of the full undamped and damped OWT systems, respectively, varying with the normalised foundation stiffness, γ. Note that the frequencies of this non-proportionally damped system, $\boldsymbol{f}_c$, are the absolute value of the eigenvalues, as shown in Eq. 5.4, as opposed to the original complex-valued eigenvalues. As discussed the modal behaviour features many coupled modes, rather than solely tower or blade bending modes. 13 of the OWT system modes are of interest in this study, which are shown in Figures 5.4a and 5.5a. The modes will be referred to from 1 to 13, numbered in ascending order of their frequency values at $\gamma = 1$, as labelled in grey on the figures. At this stage the modes are all shown in black, as colouring the modes would require assumptions about their crossing behaviour, which has not yet been established.

Figures 5.4a and 5.5a show that depending on the value of γ there are a limited number of modes that are sensitive to the changes in the foundation stiffness magnitude, referred to as 'foundation-sensitive' modes. In a particular interval of γ, the insensitive modes have a practically zero gradient and conversely the more sensitive modes are indicated by lines of substantive gradient. As γ varies, the frequencies of these foundation-sensitive modes change rapidly and they interact with other nearby modes as they approach them, as a result of the coupling between the model's DOF. Those nearby modes are therefore rendered sensitive to the foundation stiffness variation in the specific region of γ. For example in both Figures 5.4a and 5.5a, at $\gamma = 1$ there are two closely spaced frequencies around 1.4Hz, modes 8 and 9, that have a steep gradient, indicating foundation sensitivity. As γ increases these frequencies gradually become less foundation sensitive, but mode 10 directly above them gradually becomes more sensitive, and past $\gamma = 4$ mode 12 starts to become more sensitive. There are certain regions where the modes almost appear to cross one another, and these important regions have been scaled up and shown in the subfigures of Figures 5.4b and 5.5b. The subfigures of 5.4b demonstrate that the step size of γ is refined sufficiently to see $\boldsymbol{f}_u$ veer away from one another, and

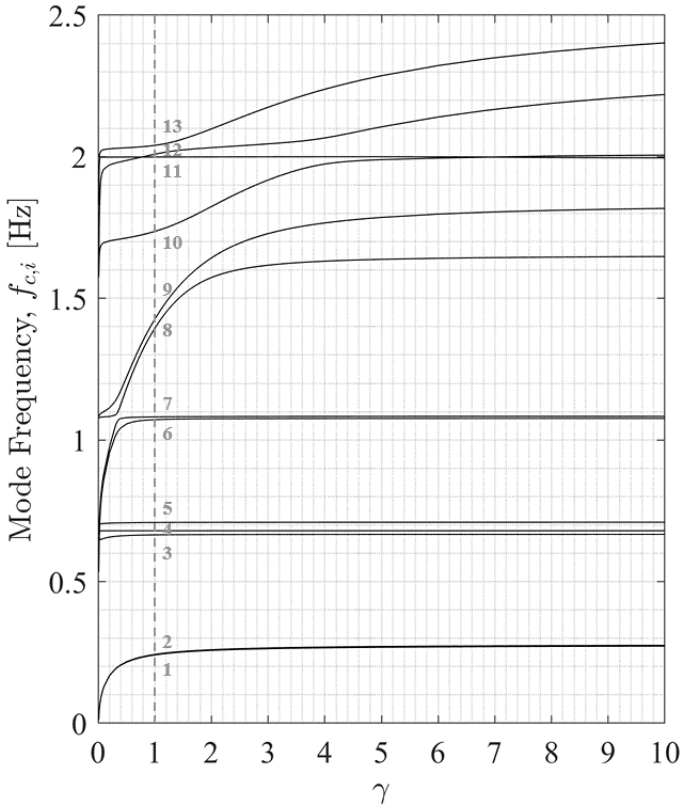


(a) Overall results

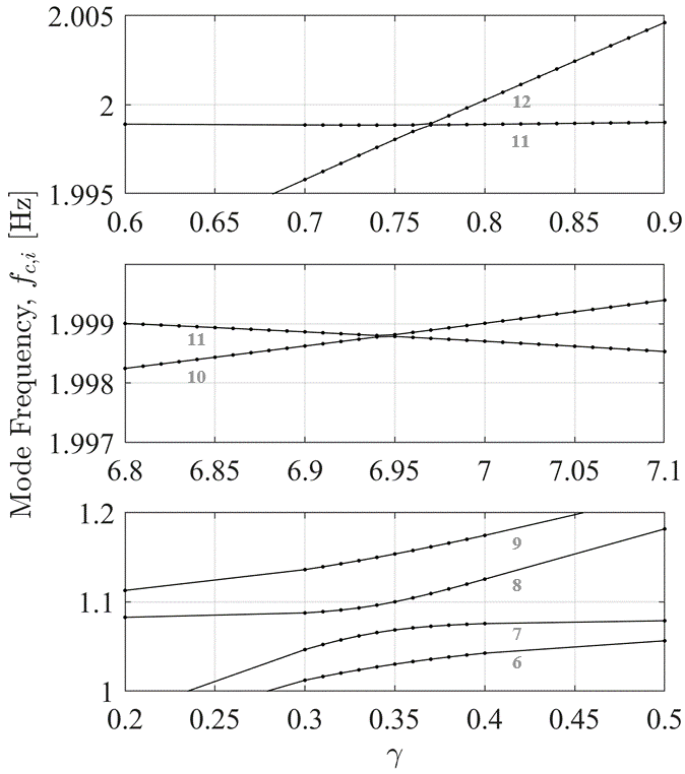


(b) Scaled up regions of interest

Figure 5.4: Effect of the normalised foundation stiffness, γ, on the frequencies of the undamped OWT system.



(a) Overall results



(b) Scaled up regions of interest

Figure 5.5: Effect of the normalised foundation stiffness, γ, on the frequencies of the damped OWT system.

within the explored region of $\gamma = 0.001 : 10$ the frequencies never cross one another.

The two sets of frequencies seen in Figures 5.4 and 5.5, $\boldsymbol{f}_u$ and $\boldsymbol{f}_c$ respectively, are slightly different due to the presence of non-proportional damping. At a specific γ the differences between $\boldsymbol{f}_u$ and $\boldsymbol{f}_c$ are around 0.1% to 0.2% (shown in Table 2.3), which would be significantly smaller than the accuracy with which the frequencies can be identified from data. However, Figures 5.4 and 5.5 appear to imply different crossing behaviour. While Figure 5.4b confirmed no crossing for the undamped OWT system, the presented sampling resolution of γ in Figure 5.5b does not confirm that $\boldsymbol{f}_c$ veer away, but also does not explicitly show that they cross one another, as a smaller γ resolution might confirm veering. This is seen for modes 10 and 11 around $\gamma = 6.95$ and modes 11 and 12 around $\gamma = 0.75$ (Figure 5.5b). One could continue to refine the resolution of γ, but at some point the limit of computational precision would be reached. In summary, the observation of mode veering confirms that the modes do not cross; however, the absence of veering does not confirm that they do cross.

Therefore the OWT model is a system that exhibits slightly differing $\boldsymbol{f}_u$ and $\boldsymbol{f}_c$ values, that potentially imply different mode crossing behaviour. However, it is not possible to confirm these observations through the evaluation of FAST simulations alone. Understanding whether the modes cross or not is essential to the development and implementation of a model updating or optimisation procedure that compares modal properties. If the numerical model modes do not cross at all, then the model and identified modes can be matched at the beginning of the procedure and then sorting each set by their frequencies would allow for consistent comparison as the procedure advances. However, if the numerical model modes cross one another as the procedure advances, then the same modes will not be consistently compared unless methods are implemented for recognising the mode crossing and correctly updating the 'matches' between the model and identified modes. In Section 5.3.3, Nelson's method is used to predict the crossing behaviour for the damped

and undamped OWT systems, after the work in Section 5.3.2 demonstrates that this method successfully predicts the behaviour for an analytical 2DOF system.

5.3.2 Exploring mode crossing behaviour of a 2DOF system

In this section, mode crossing behaviour will be investigated with a simple 2DOF analytical model. The question of why the modes do or do not cross will be explored through alteration of the stiffness, mass and damping matrices of the model, and subsequent solution of the eigenvalue problem both numerically and symbolically. Nelson's method will be applied to each case, demonstrating correct prediction of the crossing behaviour.

This simpler 2DOF system is used as its size is small enough to allow for symbolic solutions to the eigenvalue problem, yet it still allows for demonstration of the effects of varying the model parameters on the crossing behaviour. This model is comprised of 2×2 mass, $\boldsymbol{M}$, stiffness, $\boldsymbol{K}$, and damping, $\boldsymbol{D}$, matrices. Five realisations of the analytical 2DOF model are explored. They are referred to as systems $\boldsymbol{i}$ to $\boldsymbol{v}$ and are defined with the $\boldsymbol{M}$, $\boldsymbol{K}$ and $\boldsymbol{D}$ matrices given in Table 5.1. The structural properties of the system are perturbed by varying the stiffness matrix term, k_α,

Table 5.1: 2DOF analytical systems $\boldsymbol{i}$ to $\boldsymbol{v}$.

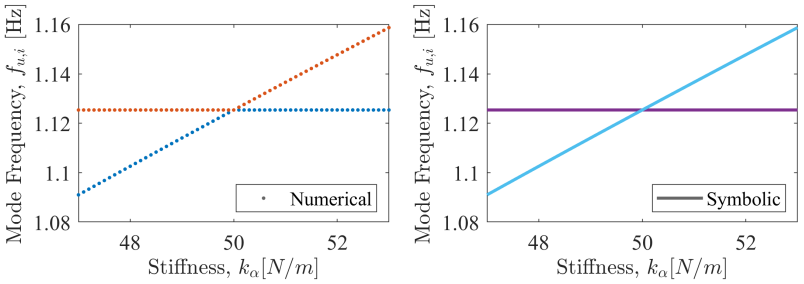
System	$\boldsymbol{M}$	$\boldsymbol{K}$	$\boldsymbol{D}$
$\boldsymbol{i}$	$\begin{bmatrix} 1 & 0 \\ 0 & 1 \end{bmatrix}$	$\begin{bmatrix} k_\alpha & 0 \\ 0 & 50 \end{bmatrix}$	$\begin{bmatrix} 0 & 0 \\ 0 & 0 \end{bmatrix}$
$\boldsymbol{ii}$	$\begin{bmatrix} 1 & 0.002 \\ 0.002 & 1 \end{bmatrix}$	$\begin{bmatrix} k_\alpha & 0 \\ 0 & 50 \end{bmatrix}$	$\begin{bmatrix} 0 & 0 \\ 0 & 0 \end{bmatrix}$
$\boldsymbol{iii}$	$\begin{bmatrix} 1 & 0 \\ 0 & 1 \end{bmatrix}$	$\begin{bmatrix} k_\alpha & 0.1 \\ 0.1 & 50 \end{bmatrix}$	$\begin{bmatrix} 0 & 0 \\ 0 & 0 \end{bmatrix}$
$\boldsymbol{iv}$	$\begin{bmatrix} 1 & 0 \\ 0 & 1 \end{bmatrix}$	$\begin{bmatrix} k_\alpha & 0.1 \\ 0.1 & 50 \end{bmatrix}$	$\begin{bmatrix} 0.5 & 0 \\ 0 & 0.5 \end{bmatrix}$
$\boldsymbol{v}$	$\begin{bmatrix} 1 & 0 \\ 0 & 1 \end{bmatrix}$	$\begin{bmatrix} k_\alpha & 0.1 \\ 0.1 & 50 \end{bmatrix}$	$\begin{bmatrix} 0.5 & 0.2 \\ 0.3 & 0.6 \end{bmatrix}$

between the range of 47 and 53. This perturbation causes changes in the modal properties of the system, which are calculated as outlined in Section 5.2.2.

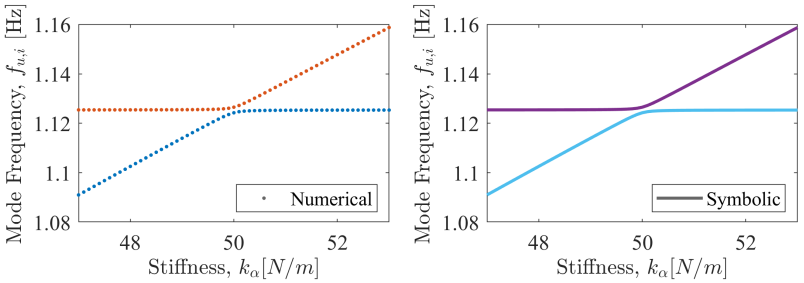
Tracking modes symbolically

Figure 5.6 shows the frequencies, $\boldsymbol{f}_u$ or $\boldsymbol{f}_c$, of these 2DOF systems against k_α, calculated both numerically (left column) and symbolically (right column) using the symbolic toolbox of MATLAB. As noted previously the frequencies of the damped systems, $\boldsymbol{f}_c$, shown in the plots are found by taking the absolute value of the original complex-valued eigenvalues (Eq. 5.4). The numerical model frequencies are coloured by relative value, the smaller being blue and the larger being orange. In the right column of Figure 5.6 the colour of the solid lines, light blue or purple, follows the consistent symbolic mode. As explained in Section 5.3.1, the numerical calculation can indicate mode veering, but cannot confirm mode crossing, hence the importance of the symbolic calculation, which allows conclusive determination of whether the modes cross one another or not. This is because the eigenvalue problem is solved symbolically, resulting in equations of the frequencies of each mode as functions of k_α.

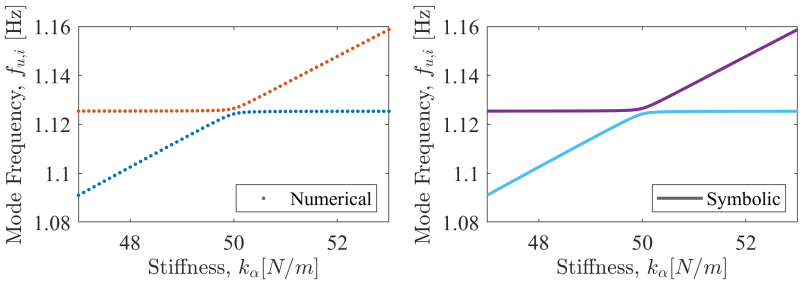
Figure 5.6a shows that for the undamped uncoupled system, ***i***, the frequencies cross one another at $k_\alpha = 50$. However, for the undamped systems ***ii*** (Figure 5.6b) and ***iii*** (Figure 5.6c), for which mass or stiffness coupling is added between the two DOF, the modes approach one another and then veer away. It is worth noting that this veering behaviour has been observed with the introduction of any non-zero value in the off-diagonal terms of $\boldsymbol{M}$ or $\boldsymbol{K}$, tested down to a value of 1×10^{-6}. Figure 5.6d shows that the addition of proportional damping in system ***iv*** gives the same result as system ***iii***. This is expected as $\boldsymbol{f}_u$ and $\boldsymbol{f}_c$ are equivalent when the system is proportionally damped, regardless of the damping magnitude. However, for system ***v*** (Figure 5.6e), which has stiffness coupling and also exhibits non-proportional damping, the frequencies cross one another, hence showing an example where the addition



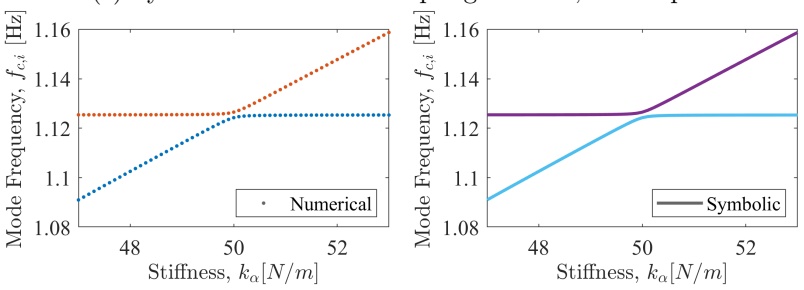
(a) System ***i***: No coupling of DOF, undamped



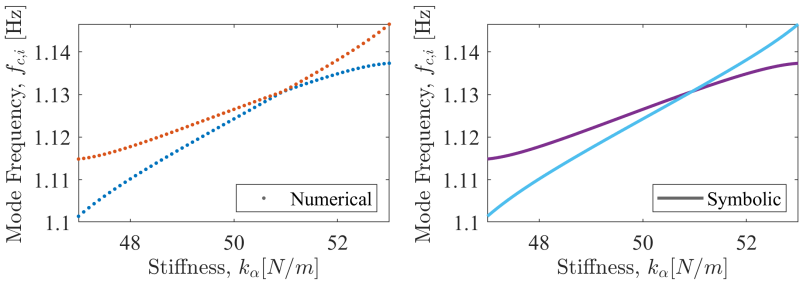
(b) System ***ii***: Mass coupling of DOF, undamped



(c) System ***iii***: Stiffness coupling of DOF, undamped



(d) System ***iv***: Stiffness coupling of DOF, proportionally damped



(e) System ***v***: Stiffness coupling of DOF, non-proportionally damped

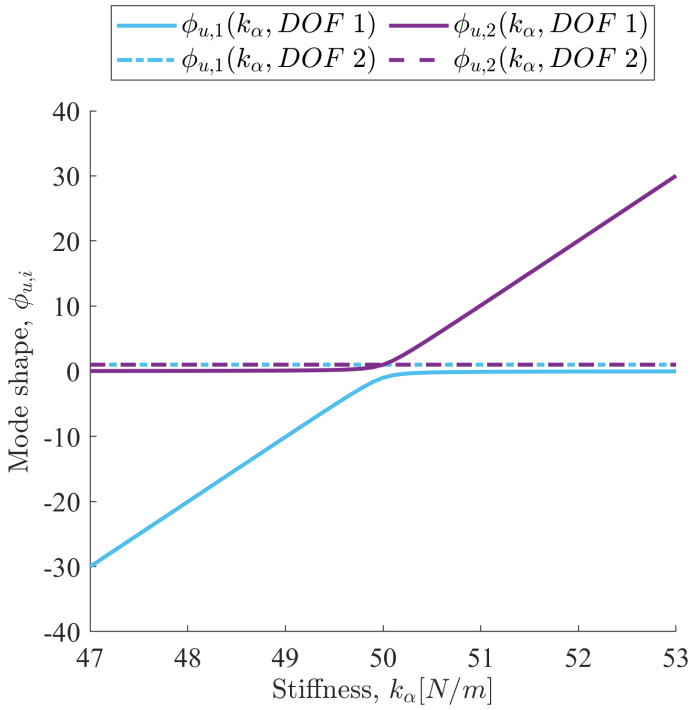
Figure 5.6: System frequencies, calculated both numerically and symbolically, for 2DOF systems ***i*** to ***v*** with varying k_α. In the left column of figures the numerical model frequencies are coloured by relative value, the smaller being blue and the larger being orange. In the right column of figures the colour, light blue or purple, follows the consistent symbolic mode hence confirming veering or crossing.

of damping actually causes $\boldsymbol{f}_u$ and $\boldsymbol{f}_c$ to display contrasting crossing behaviour.

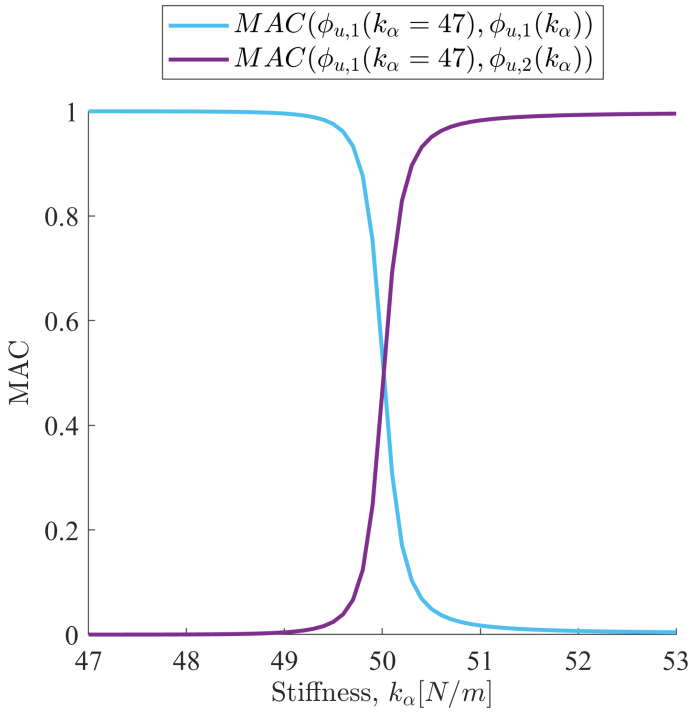
The rapidly changing behaviour of the mode frequencies during mode veering, shown in Figure 5.6, is also seen for the mode shapes, as demonstrated in Figure 5.7. Figure 5.7a shows how each element (DOF 1 and DOF 2) of the two mode shapes ($\boldsymbol{\phi}_{u,1}$ and $\boldsymbol{\phi}_{u,2}$) of the stiffness coupled 2DOF system ***iii*** change with varying k_α. The mode shapes are normalised so that the DOF 2 element is equal to 1.

It can be seen that the mode shapes gradually vary as k_α varies, but change rapidly around $k_\alpha = 50$ with the modes appearing to swap mode shape 'characteristics' with one another. This 'swapping of characteristics' is demonstrated by Figure 5.7b which shows $\text{MAC}(\boldsymbol{\phi}_{u,1}(k_\alpha = 47), \boldsymbol{\phi}_{u,i}(k_\alpha))$ for $i = 1:2$. This is the MAC value calculated between the mode shape of mode 1 or 2, varying with k_α, and a baseline mode shape. This baseline is the mode shape of mode 1 at $k_\alpha = 47$. The MAC gives a correlation between two mode shapes i.e. a measure of similarity. Figure 5.7b shows that mode shape 1 initially remains very consistent (shown in light blue), until a rapid change is seen in the region of $k_\alpha = 50$ as mode veering occurs, indicated by the rapid decrease in the MAC value. At the same time, a rapid increase is seen in the MAC of mode shape 2 with respect to the baseline mode shape 1 (shown in purple), indicating a high degree of similarity and therefore showing that the characteristics of the mode shapes have swapped. It is interesting to note here that if the MAC were used to track the modes as the stiffness, k_α, were varied, it would suggest that the modes cross one another. This is in contradiction with the symbolic calculation of the frequencies shown in Figure 5.6c which shows that they do not cross one another. Hence, this is an example where using the MAC to match the modes may lead to erroneous results. Matching modes using the MAC is investigated for the OWT system in Section 5.4.1.

This investigation has shown that coupling of the system DOF, with off-diagonal stiffness or mass matrix elements, can result in a difference in the system crossing behaviour when compared to the uncoupled system. In this example the addition



(a)



(b)

Figure 5.7: 2DOF system ***iii***: (a) Effect of varying stiffness, k_α, on mode shapes, (b) MAC value calculated between each mode shape, varying with k_α, and a baseline mode shape (mode 1 at $k_\alpha = 47$)

of off-diagonal elements led to the behaviour changing from mode crossing to mode veering. The OWT system matrices contain numerous off-diagonal elements of varying magnitudes, and are therefore the likely cause of some of the veering instances seen for the OWT. The majority are a result of the physics of this intrinsically complex coupled multiple-DOF system. However, as the structural matrices are assembled numerically by FAST through a procedure of linearisation, there are likely to be small non-zero values for terms that would be zero if the matrices were derived symbolically. This may artificially result in additional coupling between the DOF. Since it appears that the presence of any non-zero coupling can cause mode veering, it is possible that in some instances the occurrence of mode veering may be the result of numerical or computational errors, as postulated by Leissa (1974).

Analysis of the 2DOF system, in Figure 5.6, also highlights that some realisations of non-proportional damping can cause the frequencies from the undamped and damped systems to show differing crossing outcomes, comparing Subfigures 5.6c and 5.6e. This indicates that it is therefore possible for the OWT system to be showing $\boldsymbol{f}_c$ crossing while $\boldsymbol{f}_u$ do not.

Tracking modes with Nelson's method

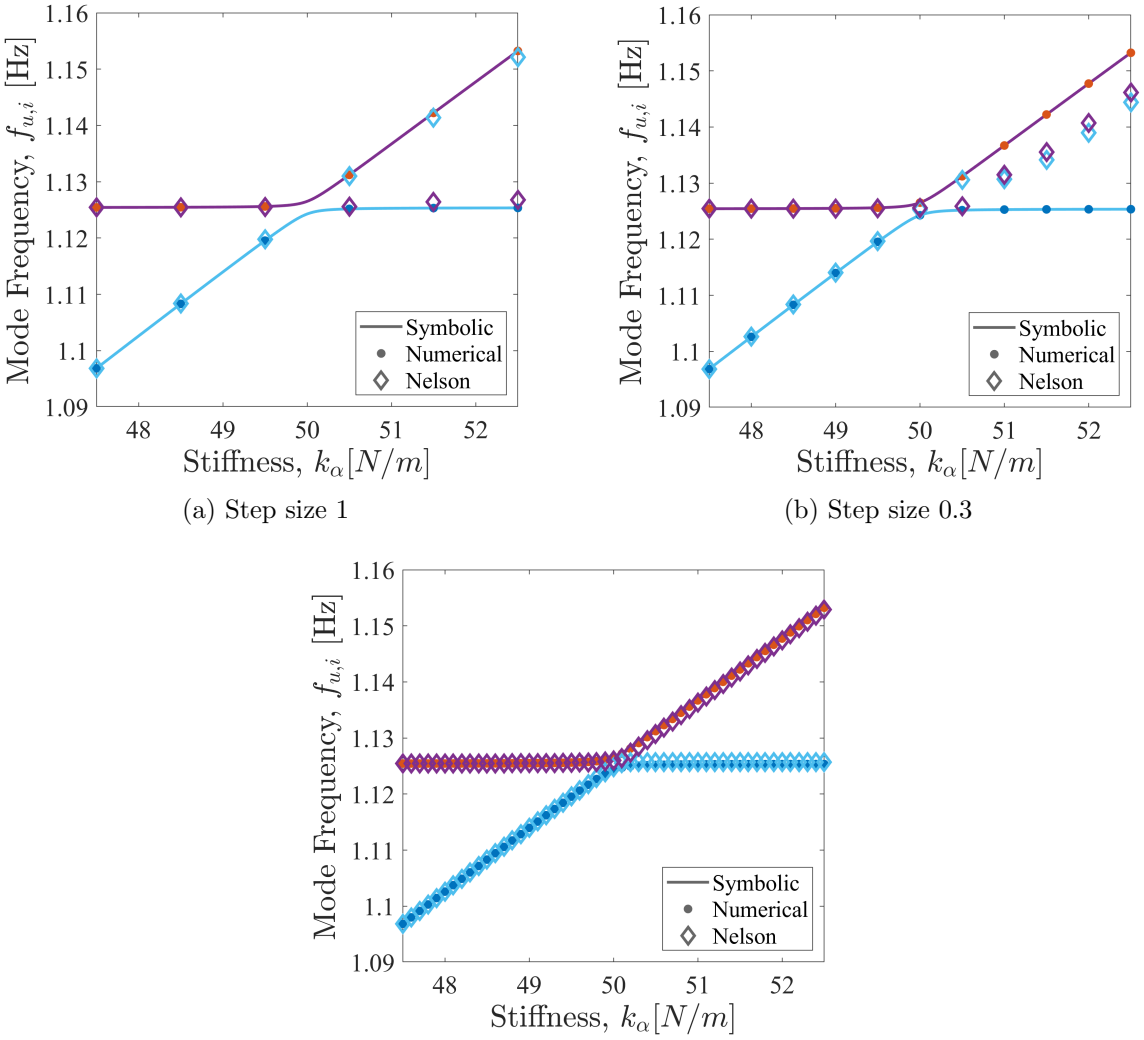
Both formulations of Nelson's method, presented in Section 5.2.4, for both damped and undamped systems are now used to predict the crossing behaviour of the 2DOF system realisations. For the 2DOF system, the varying model parameter, $\chi = k_\alpha$. The processes outlined in Section 5.2.2 are used to calculate the initial eigenvalues and eigenvectors at the chosen initial value of k_α, and then the equations described in Section 5.2.4 are used to calculate the derivatives, given a specified step size, Δk_α. The system matrix derivatives are found analytically and given by:

$$\frac{\partial \boldsymbol{M}}{\partial \chi_j} = \frac{\partial \boldsymbol{M}}{\partial k_\alpha} = \begin{bmatrix} 0 & 0 \\ 0 & 0 \end{bmatrix}, \frac{\partial \boldsymbol{K}}{\partial \chi_j} = \frac{\partial \boldsymbol{K}}{\partial k_\alpha} = \begin{bmatrix} 1 & 0 \\ 0 & 0 \end{bmatrix}, \frac{\partial \boldsymbol{D}}{\partial \chi_j} = \frac{\partial \boldsymbol{D}}{\partial k_\alpha} = \begin{bmatrix} 0 & 0 \\ 0 & 0 \end{bmatrix} \quad (5.25)$$

The predicted eigenvalues and eigenvectors at each increment of k_α are calculated using the Euler integration as shown in Eqs. 5.19 and 5.20.

An important factor is that the Euler integration method needs to have a sufficiently small step size to achieve convergence. Figure 5.8 shows three different frequency, $\boldsymbol{f}_u$, calculations for system ***iii***, using three different step sizes, Δk_α, to show its importance. The solid lines show the analytical symbolic solutions, the dots show numerical solutions (using Eqs. 3.12 and 5.3) and the diamonds show the solutions using Nelson's method. Figure 5.8 shows that Nelson's method converges towards the symbolic and numerical solutions as the step size is decreased. This shows the particular importance of reaching convergence, as the result from a step size of 1 (Figure 5.8a) might suggest that the modes cross. When a symbolic solution is not available, it is important to check Nelson against the numerical solution, as the drift of the diamonds away from the dots in Figure 5.8a indicates to the user that convergence has not been reached.

Figure 5.9 shows the successful frequency tracking of each 2DOF system case using Nelson's method, with $\Delta k_\alpha = 0.005$. The solid lines and the dots show the symbolically and numerically calculated frequencies respectively, and the diamonds show the frequencies calculated with Nelson's method. The undamped system formulation is applied to systems ***i***, ***ii*** and ***iii*** (Figures 5.9a, 5.9b and 5.9c respectively), and the non-self-adjoint damped system formulation is applied to systems ***iv*** and ***v*** (Figures 5.9d and 5.9e respectively). The close match between the diamonds and the lines in all subfigures shows that Nelson's method agrees strongly with the symbolic solutions, and therefore correctly predicts the veering or crossing behaviour for each case. This indicates that Nelson's method can be used to determine the crossing nature of modes within systems where an analytical model is not available, and therefore where the modal properties can only be calculated numerically and not symbolically. The OWT in question in this study is such a system.

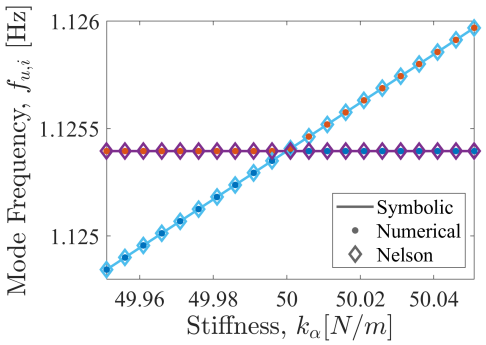


(a) Step size 1

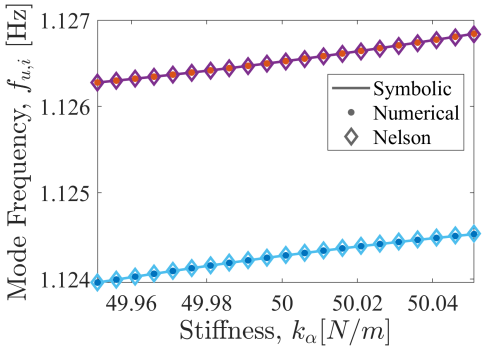
(b) Step size 0.3

(c) Step size 0.1

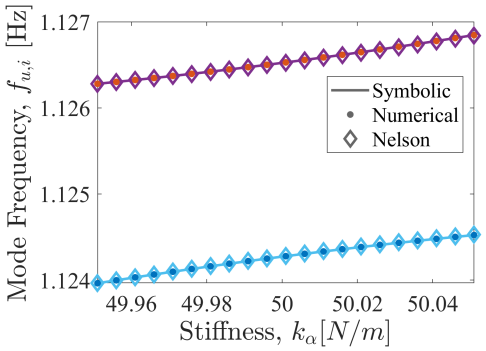
Figure 5.8: Frequencies vs stiffness parameter k_α for 2DOF system ***iii***, calculated numerically, symbolically, and using Nelson's method with varying step size. The light blue and purple lines follow the symbolically determined modes and the light blue and purple diamonds follow Nelson's method's prediction of a consistent mode.



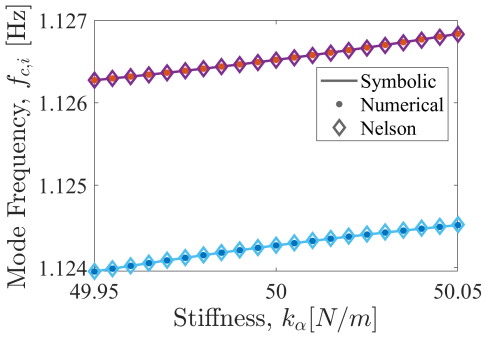
(a) System ***i***: No coupling of DOF, undamped



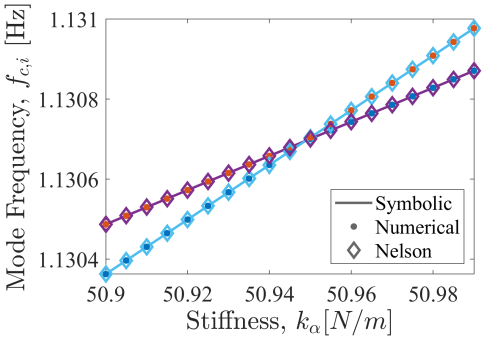
(b) System ***ii***: Mass coupling of DOF, undamped



(c) System ***iii***: Stiffness coupling of DOF, undamped



(d) System ***iv***: Stiffness coupling of DOF, proportionally damped



(e) System ***v***: Stiffness coupling of DOF, non-proportionally damped

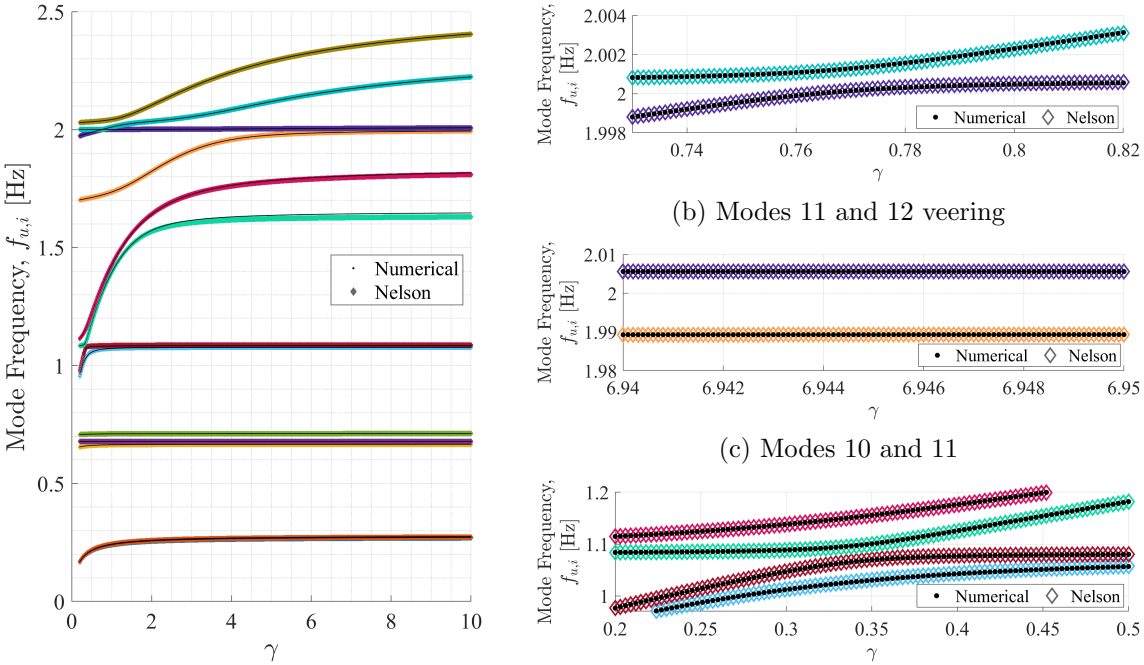
Figure 5.9: Frequencies vs stiffness parameter k_α for all 2DOF system realisations ***i*** to ***v***, calculated numerically, symbolically and using Nelson's method. The light blue and purple lines follow the symbolically determined modes and the light blue and purple diamonds follow Nelson's method's prediction of a consistent mode. Subfigures (a) and (e) show mode crossing while (b) to (d) show mode veering (at a focused region around $k_\alpha = 50$).

5.3.3 Exploring mode crossing behaviour of an OWT system

The two formulations of Nelson's method can now be applied to the undamped and damped OWT systems to predict whether the modes cross or veer away from one another. As with the 2DOF system, the processes given in Section 5.2.2 are used to calculate the initial eigenvalues and eigenvectors at the chosen initial value of the varying physical parameter, χ_j, and then the equations in Section 5.2.4 are used to calculate the derivatives given a specified step size, $\Delta\chi_j$. For this example with the OWT system, there is a single varying parameter, $\chi = \gamma$. The system matrix derivatives, $\frac{\partial \boldsymbol{M}}{\partial \gamma}$, $\frac{\partial \boldsymbol{K}}{\partial \gamma}$ and $\frac{\partial \boldsymbol{D}}{\partial \gamma}$, are found using Eq. 5.21. The predicted eigenvalues and eigenvectors at each increment of γ are calculated using the Euler integration as shown in Eqs. 5.19 and 5.20.

Figures 5.10 and 5.11 show how the natural frequencies of the undamped and damped OWT systems, respectively, vary with γ, as calculated numerically using FAST (black dots) and as predicted by Nelson's method (coloured diamonds). Both Figures 5.10a and 5.11a demonstrate that Nelson's method predicts the frequencies well across the investigated γ range. Figures 5.10b to 5.10d and 5.11b to 5.11d show detail over specific areas of interest for veering/crossing, across smaller ranges of γ. These confirm that for the undamped OWT system (Figure 5.10) all the modes veer away from one another and there are no crossing points within the examined region of γ. For the damped OWT system (Figure 5.11), Nelson's method predicts that the modes do in fact cross one another in the two regions of interest around 2 Hz, which confirms that the undamped and damped systems exhibit contrasting crossing behaviour in these regions.

Considering the analysis of the 2DOF system in Section 5.3.2, it can be hypothesised that the interference seen between the modes, the veering together and apart, could be a result of the complicated coupling between the different system DOF, either in terms of the masses or the stiffnesses. This coupling of the OWT system DOF is in part due to the physical properties of the system, but is also likely due



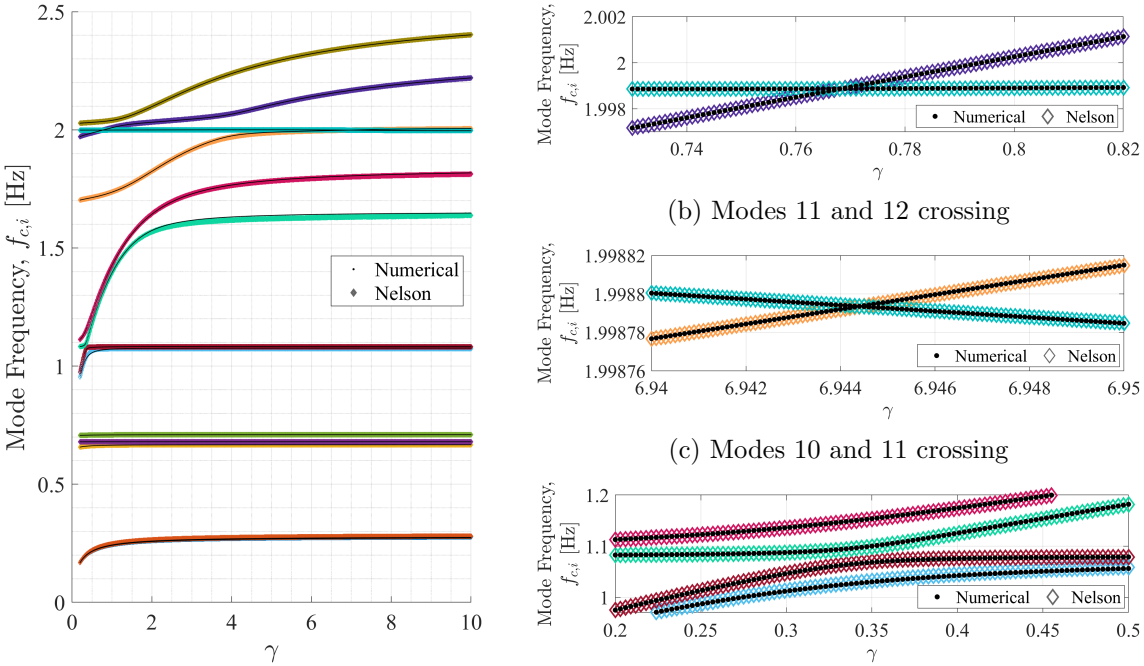
(a) Modes 1 to 13

(b) Modes 11 and 12 veering

(c) Modes 10 and 11

(d) Modes 6 to 9 veering

Figure 5.10: Frequencies vs normalised foundation stiffness, γ, for the undamped OWT system, calculated numerically and using Nelson's method.



(a) Modes 1 to 13

(b) Modes 11 and 12 crossing

(c) Modes 10 and 11 crossing

(d) Modes 6 to 9 veering

Figure 5.11: Frequencies vs normalised foundation stiffness, γ, for the damped OWT system, calculated numerically and using Nelson's method.

to numerical or computational errors arising during the numerical assembly and linearisation of the model. These errors are possibly causing small non-zero coupling terms seen in various $\boldsymbol{M}$, $\boldsymbol{K}$ and $\boldsymbol{D}$ elements, that might otherwise have been zero had the matrices been derived symbolically.

5.3.4 Discussion

The investigation in this section raises the question of how a 'mode' is defined when the parameters of the model are altered. Whilst Figure 5.10 shows that the modes of the undamped OWT system do not cross one another, they clearly interfere, and in the regions where they come close to one another, rapid changes in the behaviour of the modes are seen, such as in the mode shape (see Figure 5.13). Given that a mode is often characterised by its shape, it would be natural to suppose that the path of a mode could be followed using information related to its mode shape, for example with use of the MAC (Eq. 4.2). Looking at Figure 5.7, which demonstrated rapid mode shape change for the 2DOF system, if the mode shapes were evaluated at $k_\alpha = 49$ and $k_\alpha = 51$, calculation of the MAC would suggest that the modes must cross one another. However, evaluation of the frequencies symbolically, or numerically with a sufficiently small k_α increment, shows that the modes veer and do not cross. Comparing 2DOF systems ***i*** with ***ii*** and ***iii***, looking at Figures 5.6a, 5.6b and 5.6c, shows that a very small addition to the off-diagonal terms of the mass or stiffness matrix results in mode veering, and hence results in a very different interpretation of the modes. An off-diagonal term like this could feasibly be introduced by a computational precision error for example. It is easy to see why this may result in speculation as to whether modes should be considered to be 'crossing' or not, especially if it is suspected that the source of them 'not crossing' is a numerical error, as discussed by Leissa (1974).

In reality, the model being optimised is never a perfect model of the physical reality, it inevitably has approximations and errors, so the optimisation must deal

with the model that is available, along with the various shortcomings it may have. Hence, if the numerical model to be updated contains imperfections that result in mode veering, even if the modes of the 'perfect' model would have crossed, what matters for the optimisation is the ability to follow the path of those veering modes in the available 'imperfect' model. Therefore, as a model parameter is varied, the optimisation must follow each mode corresponding to the consistent definition that a symbolic solution for that model would provide. It has been shown that, in the absence of an analytical model, Nelson's method allows us to do that numerically.

So, whilst it is possible that an imperfect model may show mode veering when the underlying physical system might be suspected to exhibit mode crossing, the definition of the mode is limited to what the symbolic solution (or Nelson's method) would calculate for that actual model, and any other conclusion would be conjecture.

Even if a method is implemented in the optimisation for the purpose of tracking the modes across the iterations, as a first step it is necessary to match the identified modes to the modes of the initial numerical model, realised with initial estimates of the optimisation parameters. A common approach is to compare the mode shapes of the identified and model modes using the MAC, presuming matches from the highest MAC values. As explained above, this will not necessarily give the same mode as that which Nelson's method would suggest is the consistent mode. The implications of this approach are investigated with the OWT model updating example in Section 5.4.

5.4 Application to model updating

Modelling damping is highly challenging (Rao, 2011) and in practice typical aerodynamic rotor models are unlikely to accurately capture the aerodynamic damping. Furthermore, accurate modal identification of damping is significantly challenging (P. T. Brewick & Smyth, 2013). Though Section 5.3.3 concluded that the frequen-

cies from the undamped and damped models give different mode crossing behaviour, it was discussed in Section 5.3.1 that at an individual realisation of the models, for example at a specific γ, the differences between the two sets of frequencies are relatively small. Furthermore in Chapter 3, it was shown that the undamped mode shapes can be approximated well from the damped mode shapes through application of the complex normalisation technique (Fillod, 1980). Therefore, it can be assumed that the frequencies and mode shapes identified from the sensor data (which inherently includes the effect of damping) are a good approximation of the undamped frequencies and mode shapes. For all of these reasons, it is sensible to base the model updating on the undamped system, and this section will thus demonstrate a model updating application on the undamped OWT model.

Furthermore, as previously explained, to remove the effect of identification errors the identification is assumed to be perfect, so the 'identified' frequencies, $\widetilde{f}_{u,i}$, and mode shapes, ${}^{s}\widetilde{\overline{\boldsymbol{\phi}}}_i$, are taken to be the numerical model frequencies and mode shapes realised at the 'true' value of the optimisation parameters, χ, corresponding to $\gamma = 1$. These modal properties are calculated by:

1. setting up the FAST model with the 'true' foundation parameters;
2. running a linearisation of the FAST model to export the structural matrices;
3. using the equations referenced in Section 5.2.2, for an undamped system.

The mode shapes are then transformed to the sensor basis and normalised using Eqs. 3.19 and 5.7 respectively. For reference, the full mode shapes of the undamped OWT system used in this chapter (sub-model FB) can be found in Figure 2.7.

5.4.1 Mode matching

Though not carried out in this study, in practice the first step in the model updating process is to identify the modal parameters from sensor data. This can be

performed with various system identification methods, for example frequency domain decomposition (Brincker et al., 2001) or subspace state space methods e.g. N4SID (Van Overschee & De Moor, 1994). It is unlikely that all of the modes of the system will be identified, due to factors such as the quality of sensors, placement of sensors, or insufficient excitation at particular frequencies. Therefore, the next step would be to match the corresponding numerical model modes with those that have been identified, as previously discussed in Section 5.3.4. This will be referred to as 'mode matching'. It can be necessary to perform this mode matching process at every step of the optimisation procedure. Two approaches are described and employed in this chapter, referred to as the MAC and ordering approaches. Nelson's method could be implemented in such a way that it tracks the modes during optimisation within the model updating method, so that the mode matching only need be undertaken once at the beginning. However, this implementation has not been applied in this work.

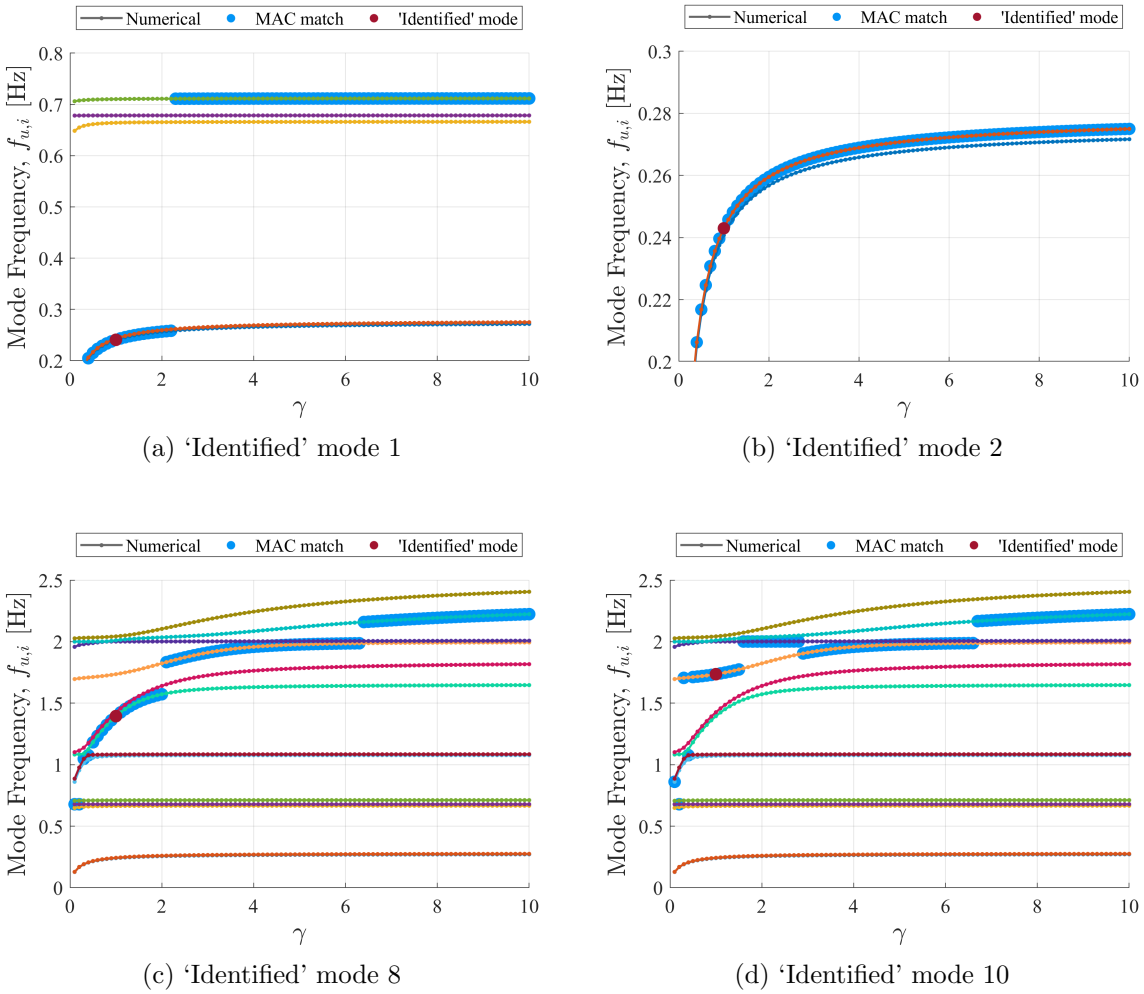
MAC approach

A frequent approach to the mode matching process consists of using the MAC to compare each identified mode shape in turn with each model mode shape, and matching those with the greatest resulting MAC values. This will be referred to as the MAC matching approach. This MAC approach to the mode matching process is applied here to the undamped OWT system. It is assumed that perfect identification has occurred, so the properties of the numerically calculated modes of the undamped OWT at $\gamma = 1$ are used as the 'identified' modal properties, i.e. $\widetilde{f}_{u,i} = f_{u,i}(\gamma = 1)$ and ${}^{s}\widetilde{\bar{\boldsymbol{\phi}}}_i = {}^{s}\bar{\boldsymbol{\phi}}_{u,i}(\gamma = 1)$. At each realisation of $\gamma = \{0.1, 0.2...10\}$, the resulting numerical model mode shapes, ${}^{s}\bar{\boldsymbol{\phi}}_{u,i}(\gamma)$ where $i = 1 : 13$, are compared in turn with each of the 'identified' mode shapes, ${}^{s}\widetilde{\bar{\boldsymbol{\phi}}}_i$, with the highest MAC result being considered to indicate the matching mode.

Figure 5.12 shows the MAC matching outcomes for four example identified

modes, modes 1, 2, 8 and 10. The coloured lines show the numerically calculated frequencies against γ (these lines are now shown with colours following confirmation using Nelson's method of how the consistent modes vary with γ). At each value of γ, the enlarged blue circle highlights the mode considered to be the best match (the mode with the highest MAC result) when compared with the 'identified' mode at $\gamma = 1$ (highlighted with an enlarged red circle).

Figure 5.12b shows the 2nd mode of the system, a 1st order shape SS tower-dominant mode (see Figure 2.7 for the full system mode shapes). The MAC indication follows what Nelson's method predicted to be a consistent mode (Figure 5.10a) with no interference with other modes, as might be expected. However, Fig-



(a) 'Identified' mode 1

(b) 'Identified' mode 2

(c) 'Identified' mode 8

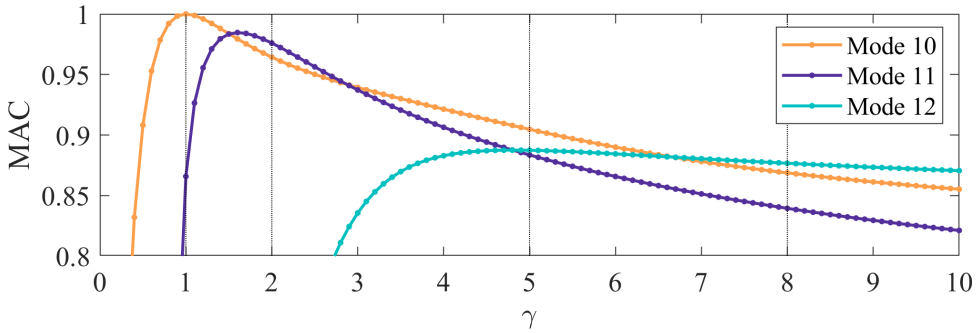
(d) 'Identified' mode 10

Figure 5.12: The 'MAC' matched mode (blue circle) with varying γ as compared with the 'identified' mode at $\gamma = 1$ (red circle), for the undamped OWT system. The coloured lines show the numerical model frequencies vs γ.

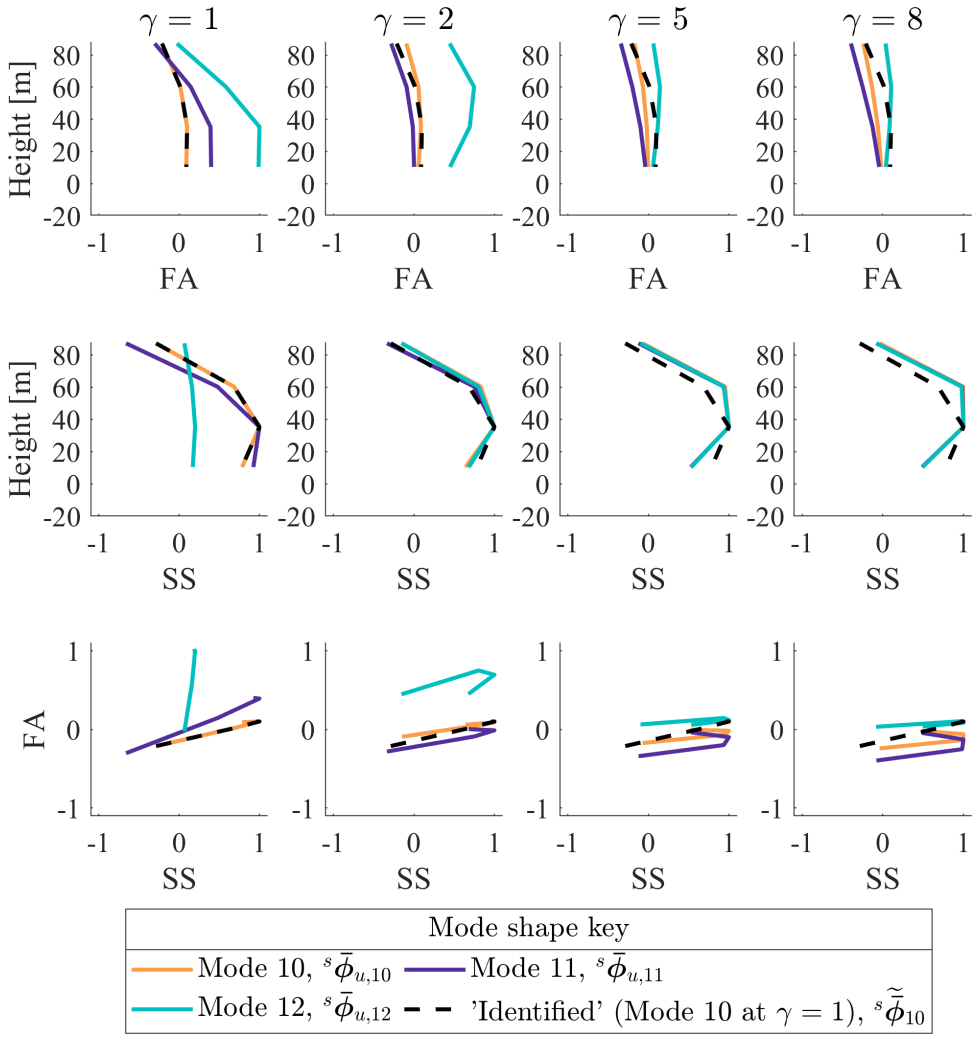
ure 5.12a shows that the 1st order shape FA tower-dominant mode (mode 1) is not tracked consistently when using the MAC. By comparing the tower-portion of the mode shapes alone, for values of $\gamma > 2.3$ the mode shape that is most similar is that of mode 5, a blade-dominant mode with a frequency around 0.7Hz. While this issue could be a result of using sensors located on the tower alone, it is still important to notice that the wrong mode would be matched to the identified 1st mode. This inconsistency of the MAC matching approach is also observed for other modes. Figure 5.12c shows mode 8, a 2nd order shape SS tower-dominant mode. Increasing from $\gamma = 1$, initially the MAC matching process follows the expected frequency in a smooth manner, but at $\gamma = 2$ it jumps up to mode 10, the next mode with SS tower bending, and then jumps again to mode 12 at $\gamma = 6.4$. This mode jumping appears to be following the characteristic of foundation-sensitivity, as it follows the modes with steeper gradients. Figure 5.12d shows another mode with 2nd order shape SS tower bending (mode 10) which exhibits the same trend as mode 8, other than around $\gamma = 2$ where the MAC matched mode swaps to an apparently foundation-insensitive blade-dominant mode (mode 11).

Figure 5.13 explores this MAC matching behaviour for the 'identified' mode 10. Subfigure 5.13a shows the MAC value found by comparing 'identified' mode 10 with numerical model modes 10 to 12 at $\gamma = \{0.1, 0.2...10\}$. Subfigure 5.13b shows the normalised sensor based mode shapes, ${}^{s}\bar{\boldsymbol{\phi}}$, for model mode shapes 10 to 12 and 'identified' mode shape 10, at pertinent values of γ, highlighted with the vertical black lines in Subfigure 5.13a.

From Figure 5.13 it can be seen that for $\gamma = 1.5 : 2.8$, the MAC suggests that the most correlated mode shape to 'identified' mode shape 10 is that belonging to numerical model mode 11, which happens to be a foundation-insensitive (frequency-wise) blade-dominant mode. By evaluating only tower sensors the blade-dominance of this mode would not be apparent. Subfigure 5.13a shows that mode 11 does exhibit a degree of foundation-sensitivity in the mode shape, as the MAC has a



(a) MAC of numerical model modes 10 to 12 with 'identified' mode 10, varying with γ. Pertinent γ values for subfigure (b) are indicated with the vertical black lines.



(b) Mode shapes of numerical model modes 10 to 12 at specific values of γ, compared to 'identified' mode 10 mode shape at $\gamma = 1$

Figure 5.13: Investigation of MAC matching approach for 'identified' mode 10

gradient with respect to γ, whereas Subfigure 5.12d shows its lack of sensitivity with respect to the frequency. For $\gamma = 2.9 : 6.6$ the MAC matched mode drops back to mode 10, causing another discontinuity, and possibly a local minimum in the objective function surface. Finally, for $\gamma = 6.7 : 10$, the MAC matched mode swaps to mode 12, which from Subfigure 5.12d appears to be the mode taking on the foundation-sensitive behaviour. Subfigure 5.13b shows how similar the tower portion of the mode shapes of different modes can be and therefore how sensitive the MAC matching approach is to jumping between modes and incorrectly indicating the underlying mode. Focusing on mode 12, particularly from $\gamma = 1$ to 2, demonstrates how rapidly the mode shapes can change as the modes interfere with one another as γ varies.

If a model updating method were using this MAC approach to match the modes at each optimisation step, there would be jumps in the objective function, making it non-smooth, and there might even be local minima as the jumping could cause the objective function to increase. Furthermore, only one foundation parameter has been varied in this analysis, so when the three foundation parameters, c_{11}, c_{12} and c_{22} are updated independently, the optimisation complexity will increase along with the failure likelihood. Section 5.4.2 and 5.4.3 demonstrate model updating examples, the former updating γ and the latter updating all three foundation compliance parameters of the matrix $\boldsymbol{C}_F$.

Ordering approach

If all modes were identified, then an alternative matching approach would be to simply sort the identified and numerical model modes in ascending order with respect to their frequencies and compare the modes in order. This will be referred to as the ordering approach. For success, this approach requires that there is no crossing of the modes as the optimisation parameters change. This has been shown to be true for the undamped OWT system when the varying parameter is γ, but not for the

variation of all three foundation compliance parameters.

In some examples in this chapter, only a subset of the modes will be compared in the objective function. In these cases, the 'ordering' approach simply matches the subset of 'identified' modes with those from the numerical model that are known, through the analysis of Section 5.3.3, to correspond to the consistent mode. Though contrived, these provide baseline cases for comparison against the results found through matching modes using the MAC approach.

Furthermore, this could be replicated for a real case with a multi-objective function analysis. Supposing only a subset of modes were identified from sensor data, then an objective function would be generated for every reasonable combination of matches between the identified and model modes. One of the objective functions would consist of the correctly matched modes, and would likely give the lowest overall objective function value upon completion.

5.4.2 Foundation identification: one parameter

The first model updating example updates the normalised foundation stiffness parameter, so $\chi = \gamma$. As the identification is assumed to be perfect, there is a minimum for this problem corresponding to $J(\gamma = 1) = 0$. Given that analysis has shown that the modes do not cross one another with varying γ for the undamped system (Figure 5.10), it follows that for any initial estimate of the foundation parameters, the ordering approach would correctly match the modes, giving the optimisation algorithm a route to this minimum point. The MAC approach, on the other hand, will not necessarily match the consistent modes, as demonstrated in Figure 5.12. This inconsistent matching can generate local minima, although if these happen to be avoided the optimisation could succeed regardless.

A common starting point when estimating the boundary conditions of a model, might be to start with the boundary condition fixed, reflecting a complete lack of information about the compliance. For this OWT application, that would be

equivalent to giving a very high stiffness for the foundation, equivalent to a high γ. So the initial estimate for this first set of model updating examples is chosen as $\gamma = 10$. Two approaches are taken for matching the model and 'identified' modes, as previously described:

- the MAC approach;
- the ordering approach.

Three subsets of 'identified' modes are tested:

- all modes 1 to 13;
- modes 1, 2, 8, 9, 10 and 13 (considered to be foundation sensitive at $\gamma = 1$);
- mode 10 alone.

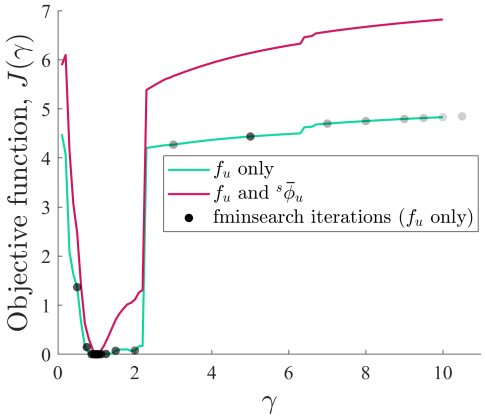
For each subset of modes, and each mode matching approach, the objective function is assembled in two ways:

- using only the frequencies;
- using both the frequencies and mode shapes.

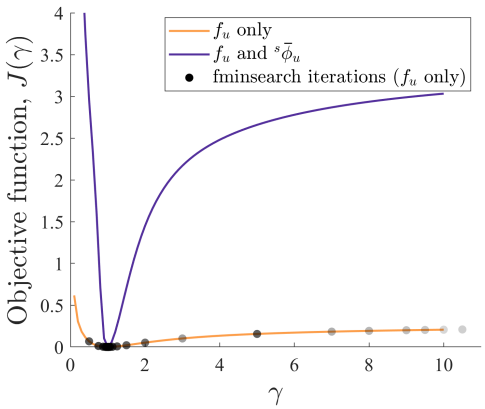
This results in 12 model updating cases overall.

With the initial estimate of $\gamma = 10$, all 12 cases successfully update the foundation parameter using fminsearch, finding $\widetilde{\gamma} = 1$, with a relative error on the order of 10^{-8} or smaller. These results are explored in Figure 5.14 which shows the value of the objective function against γ from 0.1 to 10 at increments of 0.1, for all 12 cases described above. For the cases where the frequencies alone were used in the objective function, the fminsearch iterations are also plotted with grey dots, the darkening shade of which corresponds to the progression of the optimisation.

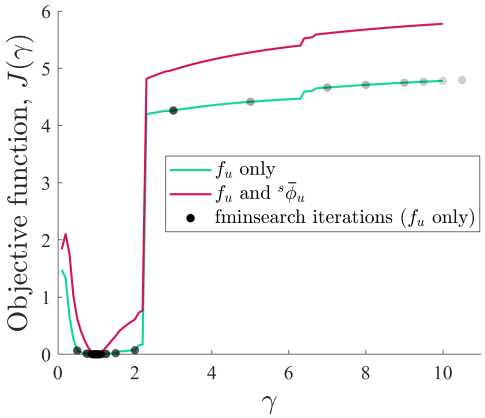
As expected, the ordering approach (Figures 5.14b, d and f) results in smooth objective function surfaces, while the MAC approach (Figures 5.14a, c and e) results



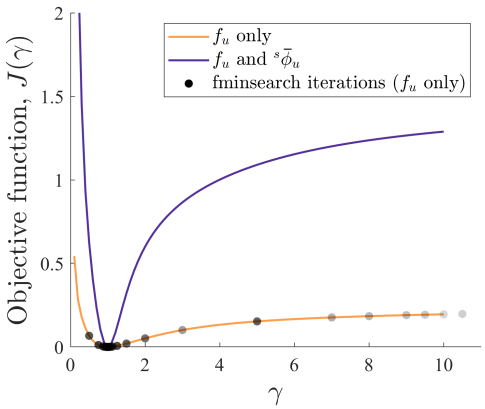
(a) Modes 1 to 13: MAC approach



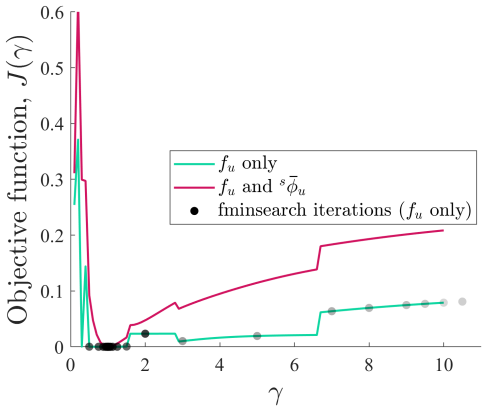
(b) Modes 1 to 13: ordering approach



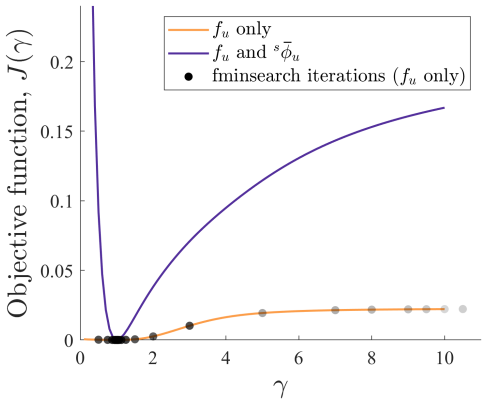
(c) Modes 1, 2, 8, 9, 10, 13: MAC approach



(d) Modes 1, 2, 8, 9, 10, 13: ordering approach



(e) Mode 10: MAC approach



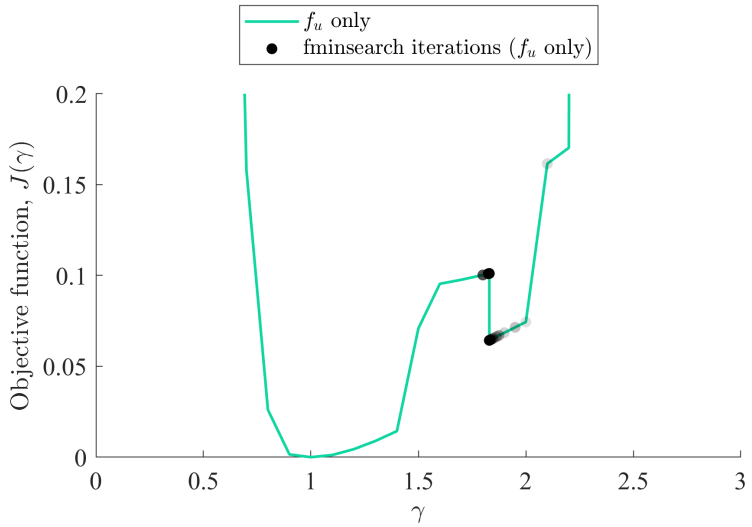
(f) Mode 10: ordering approach

Figure 5.14: Objective function, $J(\gamma)$, against normalised foundation stiffness, γ, for all 12 model updating cases. Solid lines show calculated $J(\gamma)$ for $\gamma = \{0.1 : 0.1 : 10\}$. Grey dots show fminsearch iterations for frequency only cases, where darkening shade corresponds to optimisation progression.

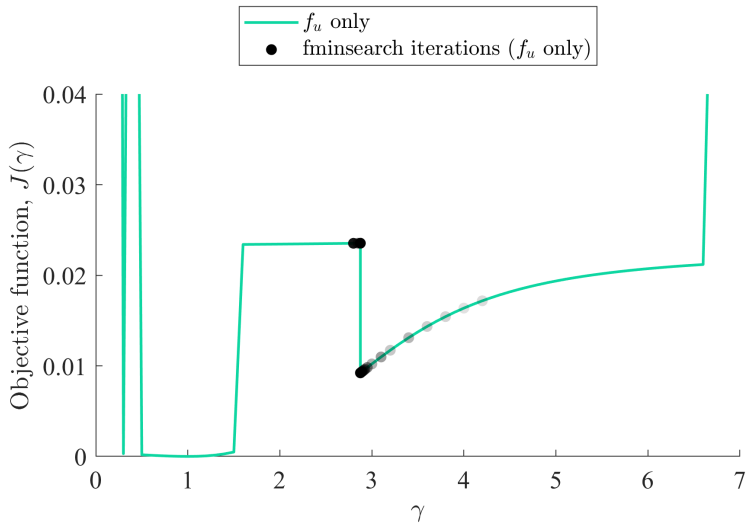
in non-smooth surfaces as the mode matching jumps from one mode to another. Furthermore, in some cases a local minimum is formed, where the route towards the true value of γ involves an increase in the gradient of the objective function surface. This is seen in Figure 5.14e for $2.9 < \gamma < 6.6$ and $\gamma \approx 0.3$, which shows mode 10 alone (see Figure 5.12d for the mode matching of mode 10), and in Figure 5.14a for $\gamma \approx 2$ (for the $\boldsymbol{f}_u$ only case). The grey dots in the figures, showing the fminsearch iterations, demonstrate that by initiating the model updating procedure with an initial estimate of $\gamma = 10$, fminsearch happens to avoid getting stuck in these local minima. However, there is no guarantee that the algorithm would have skipped the problematic region had a different initial estimate been chosen.

Figure 5.15 again shows the objective function against γ and the fminsearch iterations of the model updating procedure, for two cases identified above as having local minima when the MAC approach is applied for mode matching. This time the initial estimates of γ for the model updating procedure are specifically chosen to be located in the vicinity of the local minima. Figure 5.15a demonstrates how fminsearch remains stuck in the local minimum at $\gamma \approx 2$ for the case with the objective function assembled with the frequencies of all modes 1 to 13. In this case the initial estimate of γ is 2. Similarly Figure 5.15b demonstrates how fminsearch remains stuck in the local minimum at $\gamma \approx 3$, given an initial estimate of $\gamma = 4$, for the case that compares the frequency of mode 10 alone.

These cases highlight the shortcomings of using the MAC approach to match the modes in the model updating algorithm. Depending on the specifics of the model and application there could be multiple local minima in the objective function, resulting in sensitivity to the initial estimates of the optimisation parameters. Some cases do work well, for example for all cases with the subset of foundation sensitive modes (modes 1, 2, 8, 9, 10 and 13), the objective function surface is free of local minima. However, it just happens to be the case that the local minima observed in the individual modes (such as mode 10) are cancelled out with the inclusion



(a) Modes 1 to 13: MAC approach



(b) Mode 10: MAC approach

Figure 5.15: Objective function, $J(\gamma)$, against normalised foundation stiffness, γ, two model updating cases with local minima. Green lines show calculated $J(\gamma)$ for $\gamma = \{0.1 : 0.1 : 10\}$. Grey dots show fminsearch iterations, where darkening shade corresponds to optimisation progression.

of the other objective function contributions. A different weighting between the contributions could easily lead to local minima.

Looking across all the cases, even for a simple example that updates one parameter only and uses the exact 'identified' properties for comparison, some initial estimates were successful and others were not, indicating the low reliability of the MAC matching approach. It is likely that updating multiple parameters and us-

ing inexact identified properties could exacerbate the problems and increase the likelihood of failure.

5.4.3 Foundation identification: three parameters

The following model updating example updates all three compliance parameters, $\chi = \{c_{11}, c_{12}, c_{22}\}$, of the foundation macro-element model. It is assumed that all 13 modes of the undamped OWT model (shown in Figures 5.4 or 5.10) have been identified, and as previously explained it is assumed that the identification is perfect, so $J(\boldsymbol{\chi} = \boldsymbol{C}_{F0}) = 0$. The matrix $\boldsymbol{C}_{F0}$ corresponds to the compliance terms of the true foundation used in the OWT model, and is found by inverting the true foundation stiffness matrix, $\boldsymbol{K}_{F0}$, giving:

$$\boldsymbol{C}_{F0} = \begin{bmatrix} 1.87 & -0.134 \\ -0.134 & 0.0156 \end{bmatrix} \times 10^{-9} \text{ m/N} \tag{5.26}$$

The model updating method is run eight times with the following permutations. The MAC approach and the ordering approach are each used for matching the model and 'identified' modes, as previously described, at each iteration of the optimisation algorithm, which aims to minimise the objective function given in Eq. 5.22. The optimisation is given initial estimates of both $2\boldsymbol{C}_{F0}$ and $10\boldsymbol{C}_{F0}$. Finally, for each mode matching approach and each initial estimate, the objective function is assembled either with the frequencies alone or with both the frequencies and mode shapes, resulting in eight cases overall.

Table 5.2 shows the results of the model updating example, for all eight permutations, showing the percentage error, $\boldsymbol{\epsilon}_F$, found when comparing each identified compliance matrix, $\widetilde{\boldsymbol{C}}_F$, to the true compliance matrix, $\boldsymbol{C}_{F0}$.

The results in Table 5.2 show that neither the ordering nor MAC approaches for mode matching enable consistent successful identification of the foundation compliance terms. Despite giving very low errors across three of the cases, when construct-

Table 5.2: Model updating results: Foundation identification errors, $\boldsymbol{\epsilon}_F$, for eight cases with different combinations of mode matching approach (MAC or ordering), initial estimate and modal parameters used to construct the objective function.

Objective function	**Initial estimate**	$\boldsymbol{\epsilon}_F$ [%] Ordering approach	$\boldsymbol{\epsilon}_F$ [%] MAC approach
Frequencies only	$2\boldsymbol{C}_{F0}$	$\begin{bmatrix} 5 & -4 \\ -4 & 0.9 \end{bmatrix} \times 10^{-7}$	$\begin{bmatrix} -84 & -20 \\ -20 & -55 \end{bmatrix}$
Frequencies only	$10\boldsymbol{C}_{F0}$	$\begin{bmatrix} 4 & -3 \\ -3 & 0.5 \end{bmatrix} \times 10^{-7}$	$\begin{bmatrix} -89 & -63 \\ -63 & -8 \end{bmatrix}$
Frequencies and mode shapes	$2\boldsymbol{C}_{F0}$	$\begin{bmatrix} 4 & -4 \\ -4 & 0.3 \end{bmatrix} \times 10^{-6}$	$\begin{bmatrix} -8 & 7 \\ 7 & 1 \end{bmatrix} \times 10^{-6}$
Frequencies and mode shapes	$10\boldsymbol{C}_{F0}$	$\begin{bmatrix} -19 & 17 \\ 17 & 4 \end{bmatrix}$	$\begin{bmatrix} -3 & 3 \\ 3 & -1 \end{bmatrix} \times 10^{-5}$

ing the objective function with both the frequencies and mode shapes and giving an initial estimate of $10\boldsymbol{C}_{F0}$, the ordering approach results in erroneous foundation identification. Since the ordering approach cannot follow mode crossing, this result could suggest that mode crossing may have occurred during optimisation. Nelson's method was used in Section 5.3.3 to confirm the absence of crossing for the undamped modes of the OWT when varying the foundation stiffness multiplier, γ, but the presence or absence of mode crossing has not been confirmed when independently varying the three compliance parameters of $\boldsymbol{C}_F$.

Employing the MAC approach for mode matching results in large errors for the frequency only cases, likely due to the presence of local minima in the objective function due to discontinuous mode matching, as depicted in Figure 5.12. The MAC approach does happen to identify the foundation with small errors when both the frequencies and mode shapes are used. A possible reason is that the addition of the mode shapes to the objective function can have the effect of removing local minima from the objective function surface. It is likely that the contribution of the mode shape comparison in the objective function (see Eq. 5.22) will decrease as the optimiser moves towards the true solution, because the MAC approach implicitly minimises the residual MAC error at each iteration. An example of this effect can

be seen for the one parameter example in Figure 5.14a. The green line shows that the surface of the objective function constructed with frequencies alone has a local minimum at $\gamma \approx 2$ (see Figure 5.15a for more detail), but this minimum does not exist when the mode shapes are included with the frequencies in the objective function, shown with the pink line.

Overall, the results in Table 5.2 give further evidence of the shortcomings of using the MAC approach to match the modes in the model updating method. This frequently applied approach has been shown to give inconsistent results for the updating of the foundation parameters of the undamped OWT model, whether updating γ or c_{11}, c_{12} and c_{22}. The results are sensitive to the initial estimate of the parameters and the particular construction of the objective function, be that the subset of modes chosen or the inclusion of frequencies and/or mode shapes. The ordering approach, whose application is fairly limited for non-trivial cases, serves as a baseline for comparison in this study. This approach requires that there is no mode crossing along the optimisation path from the initial parameter estimate to the optimal value. The inconsistency in the results implies that this condition may not have been satisfied for all cases. This highlights the importance of understanding the mode crossing behaviour of the system in question. Furthermore, if it were necessary to update the damped OWT system, then not only would the MAC approach be inappropriate (as the same non-smooth erratic matching behaviour is seen as with the undamped system), but the ordering approach would also not be applicable, even for the γ optimisation case, since some modes have been shown to cross one another, thus changing order.

For the unlikely situation in which all the modes within a frequency range of interest are identified, and the modes are known not to cross one another in the likely optimisation parameter range, then the ordering approach could be applied successfully. If only a subset of the total modes are identified, but the modes are known not to cross, then a 'brute force' multi-objective function method could be

used. In both of these situations the modes would be matched once at the beginning of the optimisation. For a case where the existence of mode crossing is uncertain, Nelson's eigenderivatives could be implemented to act as a mode tracking technique, matching the modes at each step of the optimisation. This would need to be combined with a multi-objective function method to circumvent the issue of matching the initial numerical model modes with the successfully identified modes. For any of these situations, the use of the MAC approach for initially matching the modes, or tracking them through the optimisation, could induce large errors in the optimised parameters, as this chapter has shown.

5.5 Summary

This chapter has demonstrated that the FAST model of the NREL 5MW OWT (sub-model FB) presents interesting unforeseen mode veering and crossing characteristics when the foundation stiffness is varied.

Initial investigation of an analytical 2DOF system indicated that stiffness and mass coupling, regardless of how small, between the DOF of a system can cause the frequencies of the modes to veer rather than cross one another. This type of coupling could be the source of the mode veering seen in the OWT system. In practice, this coupling could be a result of modelling or numerical inaccuracies or could be due to the physics of the system.

Undamped natural frequencies calculated from the corresponding undamped and damped systems are not exactly equivalent when the system is non-proportionally damped. This chapter has demonstrated an example where the particular non-proportional damping matrix for the 2DOF system results in the frequencies of the damped system crossing as a stiffness property is varied, where the frequencies of the undamped system were shown to veer away from one another. The two sets of frequencies are very similar at each realisation of the stiffness property, so

this different crossing behaviour would not be easily apparent by observing the frequencies at discrete realisations.

Nelson's method was shown to successfully track the veering and crossing of the frequencies for the 2DOF system, and was therefore used to predict the veering and crossing of the OWT system. This approach predicted that as the foundation macro-element stiffness multiplier is varied, the frequencies of the undamped OWT system always veer away from one another and do not cross at all. However, the frequencies of the damped OWT system were shown to cross in some instances.

As it was shown to be the source for the 2DOF system, it is presumed that the mode veering of the OWT system also occurs as a result of coupling between the model's DOF. This is likely due to the nature of the physical system it represents, and numerical inaccuracies. In the context of model optimisation or updating, while it is possible that an imperfect model may show mode veering when the underlying physical system might be suspected to exhibit mode crossing, the definition of the mode is limited to what the symbolic solution (or Nelson's method) would calculate for that actual model.

The OWT model demonstrates a case where care must be taken when employing approaches to match the identified and model modal properties during model updating optimisation. It is shown how using the MAC to perform this matching at each iteration can induce discontinuities in the optimisation problem. This can result in poorly estimated optimisation parameters, shown in this chapter with a foundation compliance model updating example on the undamped OWT model. The existence and impacts of the problem have been demonstrated, and a brute force solution requiring the implementation of a multi-objective function optimisation with Nelson's eigenderivatives to track the modes has been suggested, though not demonstrated. The issue of how to successfully match modes, and the danger of using the MAC, is likely to have implications for the model optimisation of a wide variety of applications.

Chapter 6

Conclusions

6.1 Introduction

This chapter summarises the key contributions and recommendations that can be drawn from the work in this thesis; detailed conclusions are presented at the end of each chapter. Possible extensions and ideas for future work, that have arisen from this research, are also suggested.

6.2 Key contributions

Estimation of foundation properties from monitoring data

For a coupled springs formulation, the compliance parameters were found to provide better conditioned optimisation parameters, and act as a better basis for comparison between foundation realisations, than the stiffness parameters (Sections 3.2.1 and 3.4.1). The effective lateral and rotational stiffnesses, which govern the foundation behaviour for a given set of loads, are more simply represented by the compliance terms than the stiffness terms. For the identification or comparison of such a foundation model it is recommended that the compliance terms are adopted.

It was found that it is possible to identify the compliance terms of a coupled springs foundation model, and a depthwise linearly varying foundation model, from simulated monitoring data. The results are shown to accurately replicate the typically critical behaviour of the true foundation. The work in Chapter 5, which utilised the exact identified modal properties, showed that the foundation compliance parameters are identifiable, with various combinations of the frequencies and mode shapes of different modes. Chapters 3 and 4 gave an indication of the magnitude of errors introduced in the updated foundation parameters when modal identification errors are introduced. Although the identified foundation errors were found to be quite sensitive to small modal identification errors (Section 3.4.2), the errors are reasonable considering the general level of uncertainty involved with foundation assessment and design.

Optimisation of a multiple-flexible-bodied system

The FAST model of the NREL 5MW OWT was shown to present mode veering and crossing characteristics when the foundation stiffness is varied, as a result of the coupling of its numerous rigid and flexible DOF (Section 5.3.3). Analysis indicated that stiffness and mass coupling between the DOF of a system, regardless of how small, can cause the frequencies of the modes to veer rather than cross one another (Section 5.3.2). The coupling of the OWT system DOF is likely due to the nature of the physical system it represents, and numerical inaccuracies. In the context of model optimisation or updating, while it is possible that an imperfect model may show mode veering when the underlying physical system might be suspected to exhibit mode crossing, the definition of the mode corresponds to what the symbolic solution would calculate for that model. Nelson's method was shown to successfully track the veering and crossing of the frequencies of a system model, as verified with symbolic calculations.

The optimisation of system models often requires the matching of two sets of modes, for example, identified and numerical modes. This work showed that when optimising these coupled system models, the mode crossing and veering make the matching of the relevant modes very challenging. The OWT model updating method demonstrated a case where using the MAC to perform this matching at each iteration resulted in inconsistent and often poorly estimated optimisation parameters (Section 5.4). Though not demonstrated, a brute force solution requiring a multi-objective function optimisation using Nelson's eigenderivatives has been suggested. The issue of how to successfully match modes, and the danger of using the MAC, is likely to have implications for the model optimisation of a wide variety of applications.

Identification of a quasi-axisymmetric system

The quasi-axisymmetric nature of the OWT structure was shown to result in the presence of close modes that are challenging to identify. Use of mode shape cor-

relation criteria showed that despite the poor identification of the shape for some modes, qualified using the MAC, the mode shape subspaces spanned by the close mode pairs, qualified using the S2MAC, were identified successfully from simulated monitoring data (Section 4.4.1). This identified mode shape data was utilised with the OWT foundation model updating method, demonstrating that in situations where close modes had inhibited the mode shape identification, the accuracy of the updated foundation was consistently improved through adoption of the S2MAC (Section 4.4.3).

It is recommended that the existence of close modes be explored for analyses involving quasi-axisymmetric systems, and that the S2MAC be employed in place of the MAC for the assessment and subsequent utilisation of any close modes. Two approaches were demonstrated for investigating the presence of close modes in a system, one using the MAC and S2MAC to compare the identified mode shapes with those from a representative model, and a second using the uncertainties predicted by the covariances identified with a modal identification method (Section 4.4.2).

Identification of a non-proportionally damped system

The problem of non-proportional damping, such as that arising from wind turbine rotor aerodynamics, is expected to persistently affect the majority of investigations related to such structures. When undertaking modal identification of such a structure, an approach for approximating the undamped mode shapes from the identified complex-valued mode shapes is recommended, given the likely inaccurate and inconsistent identification of the damping contributions. In light of the difficulties in accurately modelling damping, if the identified properties are to be utilised in conjunction with an undamped model, then the approximation of undamped properties is even more pertinent. The 'complex normalisation' method utilised in this thesis was found to be successful in approximating the undamped mode shapes of the simulated OWT, subject to non-proportional aerodynamic damping (Sections

3.3.1 and 3.3.2).

The mode crossing behaviour of the OWT was found to differ when analysing the damped or undamped systems, as a result of the non-proportional damping (Section 5.3.3). The mode crossing behaviour can have implications for optimisation, so this is another characteristic to be aware and cautious of for non-proportionally damped systems.

Assessment of OWT

In addition to the conclusions drawn so far, when analysing wind turbine structures in particular, there are a few additional insights.

Firstly, the importance of using a fully integrated aero-elastic model with structural representation of all elements of the OWT has been demonstrated. With a simplified version, many of the complexities that have been illustrated in this work would not be apparent, and the difference between the model predictions and the true structural behaviour it aims to represent could be significant.

The modal identification of the OWT model using simulated data from parked and idling conditions was analysed. Given the use of sensors on the tower alone, the modes that sufficiently excite these sensors, corresponding to modes that have significant tower mode shape contributions, were identified well (Section 4.4.1). The time variability introduced by the idling rotor was shown to cause time variability in some mode shapes as the rotor azimuth angle varies (Section 4.3.2). This effect was particularly prominent for blade-dominant modes, when observing the tower portion of their mode shapes. Identification of blade-dominant modes from idling data, using tower sensors alone, was therefore not generally successful.

A key insight is the inconsistent nature of the vibration directions of the OWT modes. Given typical sensor placement, only the tower portion of the modes is likely to be identified in practice. The tower portions of various OWT modes have been shown to change vibration direction when the rotor is free to rotate as opposed to

locked, and/or when the blade pitch is varied (Chapter 2). Furthermore, the existence of non-proportional damping and the existence of close modes has been shown to affect the interpretation of the vibration direction of the identified mode shapes. Therefore, identified modes from monitoring data could easily be incorrectly characterised as fore-aft or side-to-side modes, having large implications on the subsequent application of those modes. Thus, it is of paramount importance to use an accurate model, adapted to the specific operational mode, to understand the expected characteristics of those modes, in particular their expected vibration direction. It is vital for those working on wind turbines to be aware of the effects of non-proportional damping and close modes on the interpretations of the identification results. Despite the fact that the MAC and real normalisation methods have lead to robust results in many applications, this thesis has demonstrated that an OWT can propose many situations where they do not perform as robustly.

6.3 Key recommendations

The key recommendations as a result of the work in this thesis are summarised in this section. The explanations have been outlined above and are elaborated upon in the body of the thesis.

- For non-proportionally damped systems, use an appropriate method to approximate the real-valued undamped mode shapes from the complex-valued damped mode shapes.
- If working with coupled springs macro-element models, use the compliance terms for their identification and assessment.
- For quasi-axisymmetric systems, use the S2MAC to assess the mode shape identification and for any subsequent mode shape comparison applications.
- When varying model parameters, be wary using the MAC to match modes

(e.g. identified and model modes), particularly with coupled multiple-flexible-bodied systems.

- When working with OWT, beware of the inconsistent nature of the vibration direction of the tower mode shapes, from both modelling and identification perspectives.

6.4 Future work

Mode matching approach for optimisation

The work in Chapter 5 demonstrated a model updating application in which use of the MAC to match the identified and numerical model mode shapes for comparison could induce errors in the updated parameters. Though a brute force method was suggested, the determination of a satisfactory mode matching approach for applications of this type, i.e. coupled multiple-flexible-bodied systems, would be of great value. The matching process is often sensitive to the initial estimate of the model parameters, so investigation into a suitable global optimisation method could be useful to circumvent this issue.

Sensitivity to modelling error

The aim of the foundation identification in this thesis was to investigate the general feasibility, so the only unknown in the model was the foundation stiffness. It is likely that the introduction of other unknowns or errors in the model would result in larger errors in the identified foundation properties. Although the foundation behaviour is thought to be one of the largest sources of uncertainty, exploration of the impact on the modal properties of other common uncertainties, such as a realistic crack in the structure or weakening of a joint, would be useful. This could be taken further by including uncertainties in the simulated data, such as a crack, and investigating the

impact on the foundation estimation errors of not accounting for that uncertainty in the updated model.

Application to real monitoring data

The model updating application and its complications have been investigated with simulated data alone, and the method has not been applied to real monitoring data in this thesis. This was necessary for the isolation of issues to aid analysis, and for scrutinising the success of the modal and foundation identification steps, since a true answer existed for comparison. However, it would be valuable to apply the method to real monitoring data, to test the application in practice. The superior mode matching approach, described above, would be essential, or perhaps a 'brute force' global multi-objective function optimisation. It is likely that the inevitable modelling errors introduced would compound into larger errors in the updated foundation parameters. The complex normalisation and S2MAC solutions from this thesis have been applied in collaborative work within the research group on the analysis of field monitored data, and this work is in preparation for submission as a journal article. Further application of these solutions to real monitoring data would provide valuable insight on their use in practice.

Monitoring data type

This thesis has explored monitoring data from accelerometers only. Investigation into using data from other types of sensors, such as strain gauges or inclinometers, in the foundation identification would be worthy of attention. Some system identification methods even allow the use of multiple types of data in conjunction, known as data fusion. Although it is uncommon to place accelerometers below the water level of OWT structures, some have strain gauges below the water level or even below the mudline. This would enable identification of sensor-based mode shapes covering a much larger portion of the tower and monopile, and the subsequent impact on the

foundation property estimation would be interesting to investigate.

Foundation identification

The extension of modal identification to structural identification of the OWT has been performed in this thesis with a model updating method alone. As introduced in Section 1.2.2, various state-of-the-art methods have been developed in recent years for identifying structural parameters from monitoring data. Future work could therefore explore the application of these methods, e.g. input-state-parameter estimation Kalman Filters, to the foundation parameter identification of OWT. Valuable insight could also be gained through calculation of the parameter identification uncertainties, enabled by applying stochastic identification methods, as opposed to deterministic as applied in this thesis.

The model updating method was applied to the estimation of two foundation models with linear springs: a coupled springs macro-element model and a depthwise-linearly-varying springs model. Future work into the identifiability of higher fidelity foundation representations would be interesting. This could include piece-wise linear depth-wise varying springs models or even the direct identification of underlying soil parameters, e.g. the void ratio or the small strain shear modulus.

A potential use for the identified in-situ foundation stiffness would be in re-analysing the fatigue life of the structure, as part of a lifetime extension analysis. Another useful input to the fatigue calculation would be the in-situ foundation damping. Therefore, exploration of the feasibility of foundation damping identification from monitoring data would be worthwhile. However, this would likely require identification of the modal damping, and application to the damped OWT model. These have been avoided in this thesis due to the challenge of successfully identifying damping from monitoring data, the difficulty of accurately modelling damping, and the complications introduced with complex damped mode shapes.

The work in Chapter 3 concluded that, in practice, the compliance terms of the

coupled springs macro-element foundation matrix are better suited to the optimisation and comparison of such foundation models, compared to the stiffness terms. Further investigation into the theoretical reasoning behind this observation would be valuable.

6.5 Summary

This thesis has explored the complexities presented by OWT systems from a modelling and identification point of view, through the application of a model updating method. This model updating method compared the numerically calculated modal properties using FAST to the modal properties identified from simulated monitoring data using output-only subspace methods. The difference between these two sets of modal properties was minimised by updating the unknown properties of the foundation model, in a coupled springs form and a depthwise-varying springs form.

Valuable insight has been provided for those working on the structural health monitoring of OWT, and other systems that exhibit the explored complexities, namely non-proportional damping, modes with close frequencies and multiple coupled degrees of freedom. Finally, in successfully estimating the properties of two foundation models from simulated data, and tackling various complications that arose in the process, this work has provided the first steps into a new area of research on the identification of OWT foundation properties from monitoring data.

References

Adhikari, S. (1999). Rates of change of eigenvalues and eigenvectors in damped dynamic system. *AIAA journal*, *37*, 1452-1458.

Adhikari, S. (2000). *Damping models for structural vibration.*

Allemang, B. J., & Brown, D. L. (1982). A correlation coefficient for modal vector analysis. *Proceedings of the International Modal Analysis Conference*, 110-116.

Anderson, E. F., McAdam, R. A., & Chatzis, M. N. (2021). Identifying close modes of idling offshore wind turbines on compliant foundations. *Proceedings of the 10th International Conference on Structural Health Monitoring of Intelligent Infrastructure*.

Antoniadou, I., Dervilis, N., Papatheou, E., Maguire, A. E., & Worden, K. (2015). Aspects of structural health and condition monitoring of offshore wind turbines. *Philosophical transactions. Series A, Mathematical, physical, and engineering sciences*, *373*.

API. (2010). *Rp 2a-wsd - recommended practice for planning, designing and constructing fixed offshore platforms.*

Arany, L., Bhattacharya, S., Macdonald, J. H., & Hogan, S. J. (2016). Closed form solution of eigen frequency of monopile supported offshore wind turbines in deeper waters incorporating stiffness of substructure and ssi. *Soil Dynamics and Earthquake Engineering*, *83*, 18-32.

Argyris, C., Papadimitriou, C., Panetsos, P., & Tsopela, P. (2020, 6). Bayesian

model-updating using features of modal data: Application to the metsovo bridge. *Journal of Sensor and Actuator Networks*, *9*.

Ashuri, T., Zaaijer, M. B., Martins, J. R., Van Bussel, G. J., & Van Kuik, G. A. (2014). Multidisciplinary design optimization of offshore wind turbines for minimum levelized cost of energy. *Renewable Energy*, *68*, 893-905.

Au, S. K., & Brownjohn, J. M. (2019). Asymptotic identification uncertainty of close modes in bayesian operational modal analysis. *Mechanical Systems and Signal Processing*, *133*.

Au, S. K., Li, B., & Brownjohn, J. M. (2021). Achievable precision of close modes in operational modal analysis: Wide band theory. *Mechanical Systems and Signal Processing*, *147*.

Avendaño-Valencia, L. D., Abdallah, I., & Chatzi, E. (2021). Virtual fatigue diagnostics of wake-affected wind turbine via gaussian process regression. *Renewable Energy*, *170*, 539-561.

Bauchau, O. A. (2011). *Flexible multibody dynamics* (Vol. 176). Springer.

Bhattacharya, S. (2014). Challenges in design of foundations for offshore wind turbines. *Engineering & Technology Reference*, 1-9.

Bir, G. S. (2007). *User's guide to bmodes (software for computing rotating beam coupled modes).*

BP. (2021). *Statistical review of world energy – all data, 1965-2020.* Retrieved from `https://www.bp.com/content/dam/bp/business-sites/en/global/corporate/xlsx/energy-economics/statistical-review/bp-stats-review-2021-all-data.xlsx`

Brewick, P., & Smyth, A. (2015). Exploration of the impacts of driving frequencies on damping estimates. *Journal of Engineering Mechanics*, *141*.

Brewick, P. T., & Smyth, A. W. (2013). An investigation of the effects of traffic induced local dynamics on global damping estimates using operational modal analysis. *Mechanical Systems and Signal Processing*, *41*, 433-453.

Brincker, R., & Kirkegaard, P. H. (2010). Special issue on operational modal analysis. *Mechanical Systems and Signal Processing*, *24*, 1209-1212.

Brincker, R., & Lopez-Aenlle, M. (2015). Mode shape sensitivity of two closely spaced eigenvalues. *Journal of Sound and Vibration*, *334*, 377-387.

Brincker, R., Zhang, L., & Andersen, P. (2001). Modal identification of output-only systems using frequency domain decomposition. *Smart Materials and Structures*, *10*, 441-445.

Brownjohn, J. M. W., Raby, A., Bassitt, J., Antonini, A., Hudson, E., & Dobson, P. (2018). Experimental modal analysis of british rock lighthouses. *Marine Structures*, *62*, 1-22.

Byrne, B. W., Houlsby, G. T., Burd, H. J., Gavin, K. G., Igoe, D. J. P., Jardine, R. J., ... Zdravkovic, L. (2020). Pisa design model for monopiles for offshore wind turbines: application to a stiff glacial till. *Geotechnique*, *70*, 1030-1047.

Byrne, B. W., McAdam, R. A., Burd, H., Houlsby, G., Martin, C., Zdravkovic, L., ... Gretlund, J. S. (2015). New design methods for large diameter piles under lateral loading for offshore wind applications. *Proc. 3rd Intern. Symp. of Frontiers in Offshore Geotech*.

Byrne, B. W., McAdam, R. A., Burd, H., Houlsby, G., Martin, C., Zdravkovic, L., ... Gretlund, J. S. (2017). Pisa: New design methods for offshore wind turbines monopiles. *8th International Conference for Offshore Site Investigation and Geotechnics*, 142-161.

Carswell, W., Johansson, J., Løvholt, F., Arwade, S. R., Madshus, C., Degroot, D. J., & Myers, A. T. (2015). Foundation damping and the dynamics of offshore wind turbine monopiles. *Renewable Energy*, *80*, 724-736.

Chatzis, M., Chatzi, E., & Smyth, A. (2015). An experimental validation of time domain system identification methods with fusion of heterogeneous data. *Earthquake Engineering & Structural Dynamics*, *44*, 523-547.

Clough, R. W., & Penzien, J. (2003). *Dynamics of structures* (Third ed.). Computers

& Structures, Inc.

D'Ambrogio, W., & Fregolent, A. (2003). Higher-order mac for the correlation of close and multiple modes. *Mechanical Systems and Signal Processing*, *17*, 599-610.

Damgaard, M., Ibsen, L. B., Andersen, L. V., & Andersen, J. K. F. (2013). Cross-wind modal properties of offshore wind turbines identified by full scale testing. *Journal of Wind Engineering and Industrial Aerodynamics*, *116*, 94-108.

De Jager, B. (1995). The use of symbolic computation in nonlinear control: is it viable? *IEEE Transactions on Automatic Control*, *40*, 84-89.

Devriendt, C., Jordaens, P. J., De Sitter, G., & Guillaume, P. (2013). Damping estimation of an offshore wind turbine on a monopile foundation. *IET Renewable Power Generation*, *120*, 96-106.

Devriendt, C., Magalhaes, F., Weijtjens, W., De Sitter, G., Cunha, A., & Guillaume, P. (2014). Structural health monitoring of offshore wind turbines using automated operational modal analysis. *Structural Health Monitoring*, *13*, 644-659.

Devriendt, C., Weijtjens, W., El-Kafafy, M., & De Sitter, G. (2014). Monitoring resonant frequencies and damping values of an offshore wind turbine in parked conditions. *IET Renewable Power Generation*, *8*, 433-441.

DNV. (2022). *https://www.dnv.com/services/wind-turbine-design-software-bladed-3775.*

DNV GL. (2016). *Dnvgl-st-0126 - support structures for wind turbines.*

Doherty, P., & Gavin, K. (2012). Laterally loaded monopile design for offshore wind farms. *Proceedings of Institution of Civil Engineers: Energy*, *165*, 7-17.

DTU. (2022). *https://www.hawc2.dk/.*

Eldred, M. S., Lerner, P. B., & Anderson, W. J. (1992). Higher order eigenpair perturbations. *AIAA Journal*, *30*, 1870-1876.

Eldred, M. S., Venkayya, V. B., & Anderson, W. J. (1995). Mode tracking issues in

structural optimization. *AIAA Journal*, *33*, 1926-1933.

Fallais, D., & Lourens, E. (2016). Vibration-based identification of hydrodynamic loads and system parameters for offshore wind turbine support structures. *Proceedings of 13th Deep Sea Offshore Wind R&D Conference*.

Farrar, C. R., & Worden, K. (2012). *Structural health monitoring: A machine learning perspective*. John Wiley & Sons, Ltd.

Fillod, R. (1980). *Contribution on identification of linear mechanical structures.*

Fox, R. L., & Kapoor, M. P. (1968). Rates of change of eigenvalues and eigenvectors. *AIAA Journal*, *6*, 2426-2429.

Friswell, M., & Mottershead, J. (1995). *Finite element model updating in structural dynamics*. Kluwer Academic Publishers.

Friswell, M. I., & Adhikari, S. (2000). Derivatives of complex eigenvectors using nelson's method. *American Institute of Aeronautics and Astronautics Journal*, *38*, 2355-2357.

Friswell, M. I., & Lees, A. W. (1998). Resonance frequencies of viscously damped structures. *Journal of Sound and Vibration*, *217*, 950-959.

Gibson, W. C. (1992). *Astros-id: Software for system identification using mathematical programming.*

GWEC. (2021). *Global wind report 2021.* Retrieved from `https://gwec.net/wp-content/uploads/2021/03/GWEC-Global-Wind-Report-2021.pdf`

Ibrahim, S. R. (1983). Computation of normal modes from identified complex modes. *AIAA*, *21*.

IEC. (2005). *Wind turbines-part 1: Design requirements* (3rd editio ed.). International Electrotechnical Commission.

Jacobsen, N.-J., Anderson, P., & Brincker, R. (2007). Eliminating the influence of harmonic components in operational modal analysis. *IMAC-XXIV : A Conference and Exposition on Structural Dynamics*.

James, G. H., Carne, T. G., & Lauffer, J. P. (1995). The natural excitation technique

(next) for modal parameter extraction from operating structures. *International Journal of Analytical and Experimental Modal Analysis*, *10*, 260-277.

Jonkman, B. J., & Kilcher, L. (2012). *Turbsim user's guide: Version 1.06.00.*

Jonkman, J., & Buhl, M. (2005). *Fast user's guide nrel/el-500-38230.*

Jonkman, J., Butterfield, S., Musial, W., & Scott, G. (2009). *Definition of a 5-mw reference wind turbine for offshore system development.*

Jonkman, J., Butterfield, S., Passon, P., Larsen, T., Camp, T., Nichols, J., ... Martinez, A. (2008). *Offshore code comparison collaboration within iea wind annex xxiii: Phase ii results regarding monopile foundation modeling.*

Jonkman, J., & Musial, W. (2010). *Offshore code comparison collaboration (oc3) for iea task 23 offshore wind technology and deployment.*

Kallehave, D., Byrne, B. W., Thilsted, C. L., & Mikkelsen, K. K. (2015). Optimization of monopiles for offshore wind turbines. *Phil. Trans. R. Soc. A*, *373*.

Kallehave, D., LeBlanc Thilsted, C., & Troya, A. (2015). Observed variations of monopile foundation stiffness. *Frontiers in Offshore Geotechnics III*, 717-722.

Kalman, R. E. (1960). A new approach to linear filtering and prediction problems. *Journal of Basic Engineering*, *82*, 35-45.

Kane, T., & Levinson, D. (1985). *Dynamics: Theory and applications.* McGraw-Hill Inc.

Lagarias, J. C., Reeds, J. A., Wright, M. H., & Wright, P. E. (1998). Convergence properties of the nelder-mead simplex method in low dimensions. *SIAM Journal of Optimization*, *9*, 112-147.

Lallement, G., & Inman, D. J. (1995). A tutorial on complex eigenvalues. *Proceedings of the 13th International Modal Analysis Conference (IMAC)*, 490-495.

Leblanc, C., Houlsby, G. T., & Byrne, B. W. (2010). Response of stiff piles in sand to long-term cyclic lateral loading. *Geotechnique*, *60*, 79-90.

Lee, I., Kim, D., & Jung, G. (1999). Natural frequency and mode shape sensitivities

of damped systems: Part i, distinct natural frequencies. *Journal of Sound and Vibration*, *222*, 399-412.

Leishman, J. G., & Beddoes, T. S. (1989). A semi-empirical model for dynamic stall. *Journal of the American Helicopter Society*, *34*, 3-17.

Leissa, A. W. (1974). On a curve veering aberration. *Journal of Applied Mathematics and Physics*, *25*, 99-111.

Ljung, L. (1987). *System identification: Theory for the user*. Prentice-Hall.

Lombardi, D., Bhattacharya, S., & Muir Wood, D. (2013). Dynamic soil-structure interaction of monopile supported wind turbines in cohesive soil. *Soil Dynamics and Earthquake Engineering*, *49*, 165-180.

Lourens, E., Papadimitriou, C., Gillijns, S., Reynders, S., De Roeck, G., & Lombaert, G. (2012). Joint input-state estimation for structural systems based on reduced-order models and vibration data from a limited number of sensors. *Mechanical Systems and Signal Processing*, *29*, 310-327.

Manzato, S., Devriendt, C., Weijtjens, W., Di Lorenzo, E., Peeters, B., & Guillaume, P. (2014). Removing the influence of rotor harmonics for improved monitoring of offshore wind turbines. *Dynamics of civil structures*, *4*, 299-312.

Mariani, S., & Corigliano, A. (2005). Impact induced composite delamination: state and parameter identification via joint and dual extended kalman filters. *Computer Methods in Applied Mechanics and Engineering*, *194*, 5242-5272.

MathWorks. (2021). *System identification toolbox™: User's guide (r2021b).*

Mayall, R. O., McAdam, R. A., Byrne, B. W., Burd, H. J., Sheil, B. B., & Cassie, P. (2018). Experimental modelling of the effects of scour on offshore wind turbine monopile foundations. *Proceedings of 9th International Conference on Physical Modelling in Geotechnics*, 725-730.

McAdam, R. A., Bajrić, A., Chatzis, M. N., Byrne, B. W., & Vanden Haute, C. (2020). Data driven assessment of offshore wind turbine foundation stiffness. *Proc. 4th Intern. Symp. of Frontiers in Offshore Geotech.*.

McAdam, R. A., Chatzis, M. N., Kuleli, M., Anderson, E. F., & Byrne, B. (2022). Identification of offshore wind foundation stiffness from monitored data. *TBC*. (Submitted)

Moireau, P., Chapelle, D., & Le Tallec, P. (2008). Joint state and parameter estimation for distributed mechanical systems. *Computer Methods in Applied Mechanics and Engineering*, *197*, 659-677.

Mottershead, J., & Friswell, M. (1993). Model updating in structural dynamics: A survey. *Journal of Sound and Vibration*, *167*, 347-375.

Nadim, F. (2015). Accounting for uncertainty and variability in geotechnical characterization of offshore sites. *Proc of the 5th Int. Symp. Geotechnical Safety and Risk*.

Naets, F., Croes, J., & Desmet, W. (2015). An online coupled state/input/parameter estimation approach for structural dynamics. *Computer Methods in Applied Mechanics and Engineering*, *283*, 1167-1188.

Nelson, R. B. (1976). Simplified calculation of eigenvector derivatives. *AIAA Journal*, *14*, 1201-1205.

NREL. (2016). *Nrel forum.* Retrieved from `https://forums.nrel.gov/t/fast-theory-manual/1322`

NREL. (2022). *Fast model.* Retrieved from `https://www.nrel.gov/wind/nwtc/fast.html`

Oliveira, G., Magalhaes, F., Cunha, A., & Caetano, E. (2018). Continuous dynamic monitoring of an onshore wind turbine. *Engineering Structures*, *164*, 22-39.

Palanisamy, R. P., & Sim, S. (2015). Bridge scour monitoring using extended kalman filter. *Proceedings of 6th International Conference on Advances in Experimental Structural Engineering*.

Pappa, R. S., Elliott, K. B., & Schenk, A. (1993). Consistent-mode indicator for the eigensystem realization algorithm. *Journal of Guidance, Control, and Dynamics*, *16*, 852-858.

Peeters, B., Cornelis, B., Janssens, K., & Van der Auweraer, H. (2007). Removing disturbing harmonics in operational modal analysis. *Proceedings of IOMAC*.

Peeters, B., & De Roeck, G. (1999). Reference-based stochastic subspace identification for output-only modal analysis. *Mechanical Systems and Signal Processing*, *13*, 855-878.

Peterka, V. (1981). *Bayesian approach to system identification.* Pergamon.

Rao, S. S. (2011). *Mechanical vibrations* (5th ed.). Pearson.

Rayleigh, J. W. S. B. (1877). *The theory of sound*. Macmillan.

Reddy, J. N. (2019). *Introduction to the finite element method* (Fourth ed.). McGraw-Hill Education.

Reese, L. C., & Matlock, H. (1956). Nondimensional solutions for laterally loaded piles with soil modulus assumed proportional to depth. *Proceedings of the 8th Texas Conference on Soil Mechanics and Foundation Engineering*.

Reynders, E. (2012). System identification methods for (operational) modal analysis: review and comparison. *Archives of Computational Methods in Engineering*, *19*, 51-124.

Reynders, E., Pintelon, R., & De Roeck, G. (2008). Uncertainty bounds on modal parameters obtained from stochastic subspace identification. *Mechanical Systems and Signal Processing*, *22*, 948-969.

Reynders, E., Schevenels, M., & De Roeck, G. (2021). *Macec 3.4 the matlab toolbox for experimental and operational modal analysis.*

Sanayei, M., & Davis, N. (2016). Bridge foundation stiffness identification. *Geotechnical and Structural Engineering Congress 2016*, 1897-1909.

Shabana, A. (2020). *Dynamics of multibody systems* (Fifth ed.). Cambridge University Press.

Shirzadeh, R., Weijtjens, W., Guillaume, P., & Devriendt, C. (2015). The dynamics of an offshore wind turbine in parked conditions: a comparison between simulations and measurements. *Wind Energy*, *18*, 1685-1702.

Shokravi, H., Shokravi, H., Bakhary, N., Heidarrezaei, M., Rahimian Koloor, S. S., & Petru, M. (2020). Application of the subspace-based methods in health monitoring of civil structures: A systematic review and meta-analysis. *Applied Sciences*, *10*.

Simoen, E., De Roeck, G., & Lombaert, G. (2015). Dealing with uncertainty in model updating for damage assessment: A review. *Mechanical Systems and Signal Processing*, *56-57*, 123-149.

Sinha, S. (2005). *Techniques for real normalization of complex modal parameters for updating and correlation with fem models.*

Skau, K., Kaynia, A., Page, A., Løvholt, F., Norén-Cosgriff, K., Sturm, H., ... Eichler, D. (2018). Redwin – reducing cost in offshore wind by intregrated structural and geotechnical design. *Journal of Physics: Conference Series*, *1104*.

Song, M., Behmanesh, I., Moaveni, B., & Papadimitriou, C. (2019). Modeling error estimation and response prediction of a 10-story building model through a hierarchical bayesian model updating framework. *Frontiers in Built Environment*, *5*, 1-15.

Sunder, S. S., & Sanni, R. (1984). Foundation stiffness identification for offshore platforms. *Applied Ocean Research*, *6*, 148-156.

Tarp-Johansen, N. J., Andersen, L., Christensen, E., Mørch, C., Kallesøe, B., & Frandsen, S. (2009). Comparing sources of damping of cross-wind motion. *Proceedings of European Offshore Wind 2009 : Conference & Exhibition*, 1-10.

Tatsis, K., Chatzi, E., & Lourens, E. (2017). Reliability prediction of fatigue damage accumulation on wind turbine support structures. *Eccomas Proceedia UNCECOMP*, 76-89.

Tcherniak, D., Chauhan, S., & Hansen, M. H. (2011). Applicability limits of operational modal analysis to operational wind turbines. *Structural Dynamics and*

Renewable Energy, *1*, 317-327.

Van der Valk, P. L. C., & Ogno, M. G. L. (2014). Identifying structural parameters of an idling offshore wind turbine using operational modal analysis. *Proceedings of the 32nd IMAC*.

Van Overschee, P., & De Moor, B. (1994). N4sid: Subspace algorithms for the identification of combined deterministic- stochastic systems. *Automatica*, *30*, 75-93.

Van Overschee, P., & De Moor, B. (1996). *Subspace identification for linear systems*. Kluwer Academic.

Versteijlen, W., Metrikine, A. V., Hoving, J., Smid, E., & De Vries, W. (2011). Estimation of the vibration decrement of an offshore wind turbine support structure caused by its interaction with soil. *EWEA Offshore 2011 Conference*.

Versteijlen, W. G., Metrikine, A. V., & Van Dalen, K. N. (2016). A method for identification of an effective winkler foundation for large-diameter offshore wind turbine support structures based on in-situ measured small-strain soil response and 3d modelling. *Engineering Structures*, *124*, 221-236.

Versteijlen, W. G., Renting, F. W., Van der Valk, P. L. C., Bongers, J., Van Dalen, K. N., & Metrikine, A. V. (2017). Effective soil-stiffness validation: Shaker excitation of an in-situ monopile foundation. *Soil Dynamics and Earthquake Engineering*, *102*, 241-262.

Wei, M. L., Allemang, R. J., & Brown, D. L. (1986). A time domain subspace iteration method for the normalization of measured complex modes. *Proceedings of 12th International Seminar on Modal Analysis*.

Weijtjens, W., Iliopoulos, A., Helsen, J., & Devriendt, C. (2015). Monitoring the consumed fatigue life of wind turbines on monopile foundations. *Proceedings of the EWEA Offshore Conference*.

Weijtjens, W., Verbelen, T., De Sitter, G., & Devriendt, C. (2016). Foundation

structural health monitoring of an offshore wind turbine—a full-scale case study. *Structural Health Monitoring*, *15*, 389-402.

Wilkinson, J. H. (1965). *The algebraic eigenvalue problem*. Oxford University Press.

Wind Europe. (2021). *Offshore wind in europe key trends and statistics 2020.*

Woodhouse, J. (1998). Linear damping models for structural vibration. *Journal of Sound and Vibration*, *215*, 547-569.

Zaaijer, M. B. (2006). Foundation modelling to assess dynamic behaviour of offshore wind turbines. *Applied Ocean Research*, *28*, 45-57.

Zdravković, L., Taborda, D., Potts, D., Jardine, R., Sideri, M., Schroeder, F., ... Gretlund, J. (2015). Numerical modelling of large diameter piles under lateral loading for offshore wind applications. *3rd Intern. Symp. of Frontiers in Offshore Geotech.*.

Zhang, L., Brincker, R., & Andersen, P. (2009). An overview of operational modal analysis: major development and issues. *Mechanical Systems and Signal Processing*.

Appendix A

Mode shape DOF contributions for Chapter 2

Table A.1: Mode shape values of the undamped OWT sub-model RB with rotor free to rotate, for modes RB 1 to 4, corresponding to Figure 2.6.

DOF	RB 1	RB 2	RB 3	RB 4
q_{Sg}	0.023	2.1E-07	-0.074	-1.7E-08
q_{Sw}	-4.9E-07	-0.023	2.2E-08	0.070
q_{R}	5.5E-08	0.003	-2.1E-09	-0.007
q_{P}	0.003	2.3E-08	-0.007	-1.6E-09
q_{TFA1}	1	9.0E-06	-0.114	1.5E-08
q_{TSS1}	2.1E-05	1	-8.9E-08	-0.149
q_{TFA2}	4.9E-05	-3.2E-08	1	1.9E-07
q_{TSS2}	9.7E-08	0.003	3.4E-07	1
q_{GeAz}	-2.9E-07	-0.015	-4.5E-09	-0.017

Table A.2: Mode shape values of the undamped OWT sub-model FB with rotor free to rotate, for modes FB 1 to 13, corresponding to Figure 2.7.

DOF	FB 1	FB 2	FB 3	FB 4	FB 5	FB 6	FB 7	FB 8	FB 9	FB 10	FB 11	FB 12	FB 13
q_{Sg}	0.023	-0.001	-0.001	-1.4E-05	-4.8E-04	0.002	4.2E-04	0.003	0.023	0.001	1.1E-04	0.004	-0.002
q_{Sw}	-0.001	-0.023	8.8E-05	-7.8E-05	4.7E-05	0.001	0.001	-0.044	0.001	0.006	-3.2E-04	0.001	0.001
q_{R}	6.3E-05	0.003	-9.4E-06	8.2E-06	-4.9E-06	-5.9E-05	-6.8E-05	0.004	-1.1E-04	-0.001	2.7E-05	-5.3E-05	-8.7E-05
q_{P}	0.003	-7.3E-05	-6.8E-05	-1.4E-06	-5.1E-05	1.8E-04	4.2E-05	3.1E-04	0.002	6.7E-05	9.7E-06	3.2E-04	-2.0E-04
q_{TFA1}	1	-0.028	-0.015	-3.2E-04	-0.013	0.016	0.003	-0.002	-0.023	-0.008	-0.001	-0.049	0.034
q_{TSS1}	0.024	1	-0.003	0.002	-0.001	-0.009	-0.009	0.118	-0.001	0.034	-0.004	0.006	0.012
q_{TFA2}	0.001	1.9E-04	0.017	3.0E-04	0.003	-0.035	-0.009	-0.041	-0.256	-0.007	4.8E-04	0.011	-0.002
q_{TSS2}	4.5E-05	0.001	0.001	-0.002	0.001	0.007	0.010	-0.654	0.019	0.043	-0.001	-0.001	3.2E-04
q_{GeAz}	-0.001	-0.019	3.8E-05	3.8E-05	-0.002	-2.5E-05	0.000	0.029	-0.002	0.018	3.4E-05	0.003	0.003
q_{DrTr}	1.5E-05	2.6E-04	-3.8E-06	-4.0E-06	2.1E-04	6.7E-06	3.2E-05	-0.013	0.001	-0.012	-3.1E-05	-0.002	-0.003
q_{B1F1}	0.751	0.182	1	-0.068	1	0.195	0.093	0.059	1	-0.311	0.007	0.041	-0.122
q_{B2F1}	0.247	-0.048	-0.556	-0.972	0.936	-0.059	-0.087	-0.220	-0.373	-0.354	0.040	-0.069	-0.027
q_{B3F1}	0.312	-0.126	-0.472	1	0.988	-0.129	0.009	-0.428	-0.227	-0.326	-0.044	-0.056	-0.033
q_{B1E1}	0.110	-0.154	0.024	-0.004	0.103	-0.807	-0.654	0.431	0.436	1	0.004	0.120	-0.120
q_{B2E1}	0.074	0.064	-0.014	-0.016	0.101	-0.197	1	1	-0.125	0.927	0.110	-0.107	-0.020
q_{B3E1}	0.027	0.054	-0.016	0.015	0.110	1	-0.353	0.777	-0.580	0.915	-0.141	-0.086	-0.010
q_{B1F2}	-0.039	-0.025	0.032	-0.003	0.053	-0.055	-0.057	0.143	0.704	-0.181	-0.093	-0.601	1
q_{B2F2}	-0.024	0.010	-0.014	-0.028	0.045	-0.035	0.099	0.056	-0.205	-0.259	-0.847	1	0.313
q_{B3F2}	-0.032	0.014	-0.012	0.029	0.048	0.091	-0.039	-0.089	-0.176	-0.203	1	0.788	0.362

Table A.3: Mode shape values of mode FB 9 with changing blade pitch, for the undamped OWT sub-model FB with rotor free to rotate, corresponding to Figure 2.10.

DOF	0°	15°	30°	45°	60°	75°	90°
q_{Sg}	0.021	0.023	0.026	0.018	0.006	0.002	-0.001
q_{Sw}	0.001	0.001	-0.001	-0.008	-0.026	-0.040	-0.044
q_{R}	-7.9E-05	-1.1E-04	1.0E-04	0.001	0.002	0.004	0.004
q_{P}	0.002	0.002	0.002	-0.002	-0.001	2.2E-04	-9.2E-05
q_{TFA1}	-0.015	-0.024	-0.041	-0.034	-0.005	-0.001	3.5E-04
q_{TSS1}	-0.002	-0.001	0.003	0.009	0.045	0.083	0.091
q_{TFA2}	-0.241	-0.257	-0.272	-0.177	-0.060	-0.024	0.010
q_{TSS2}	0.013	0.019	-0.011	-0.097	-0.354	-0.571	-0.621
q_{GeAz}	-0.001	-0.002	-0.003	-0.005	4.7E-04	0.009	0.011
q_{DrTr}	3.6E-04	0.001	0.002	0.002	-1.9E-04	-0.004	-0.005
q_{B1F1}	1	1	1	0.896	1	1	1
q_{B2F1}	-0.391	-0.369	-0.242	0.254	0.724	0.694	0.652
q_{B3F1}	-0.316	-0.218	-0.028	0.404	0.743	0.716	0.706
q_{B1E1}	0.102	0.460	0.738	0.276	-0.358	-0.171	0.061
q_{B2E1}	0.134	-0.144	-0.460	-0.739	-0.560	-0.078	0.330
q_{B3E1}	-0.323	-0.599	-0.885	-1	-0.814	-0.456	-0.079
q_{B1F2}	0.619	0.709	0.808	0.674	0.574	0.616	0.664
q_{B2F2}	-0.153	-0.207	-0.218	0.006	0.279	0.325	0.374
q_{B3F2}	-0.186	-0.174	-0.112	0.101	0.259	0.275	0.328

Table A.4: Mode shape values of the undamped OWT sub-model RB with rotor locked, for modes RB 1 to 4, corresponding to Figure 2.11.

DOF	RB 1	RB 2	RB 3	RB 4
q_{Sg}	9.3E-14	0.023	-9.6E-16	-0.074
q_{Sw}	-0.023	-2.1E-15	0.077	5.1E-17
q_R	0.003	2.3E-16	-0.007	-1.2E-18
q_P	1.0E-14	0.003	-1.1E-16	-0.007
q_{TFA1}	4.1E-12	1	5.1E-14	-0.114
q_{TSS1}	1	8.9E-14	-0.102	-3.1E-15
q_{TFA2}	-6.9E-14	4.9E-05	-3.8E-14	1
q_{TSS2}	-6.1E-05	1.7E-16	1	3.3E-15

Table A.5: Mode shape values of the undamped OWT sub-model FB with rotor locked, for modes FB 1 to 13, corresponding to Figure 2.12.

DOF	FB 1	FB 2	FB 3	FB 4	FB 5	FB 6	FB 7	FB 8	FB 9	FB 10	FB 11	FB 12	FB 13
q_{Sg}	0.004	0.023	-3.1E-04	-0.001	-2.5E-05	-0.001	0.002	4.2E-04	0.023	0.003	0.001	7.4E-05	-0.003
q_{Sw}	-0.023	0.004	0.002	9.5E-05	-6.3E-05	-0.001	0.001	0.001	-0.002	0.044	0.001	-0.001	3.8E-04
q_{R}	0.003	-3.9E-04	-2.2E-04	-1.0E-05	6.6E-06	8.1E-05	-5.4E-05	-6.0E-05	2.0E-04	-0.004	-6.1E-05	4.4E-05	-3.3E-05
q_{P}	4.0E-04	0.003	-3.3E-05	-6.7E-05	-2.6E-06	-5.7E-05	1.7E-04	4.2E-05	0.002	2.9E-04	9.9E-05	6.4E-06	-2.9E-04
q_{TFA1}	0.154	1	-0.010	-0.015	-0.001	-0.014	0.016	0.003	-0.023	-0.012	-0.013	-0.001	0.047
q_{TSS1}	1	-0.153	-0.049	-0.003	0.001	0.013	-0.006	-0.006	-0.005	0.224	0.009	-0.007	0.006
q_{TFA2}	3.9E-04	0.001	0.001	0.017	4.1E-04	0.003	-0.035	-0.009	-0.259	-0.029	0.008	3.4E-04	-0.006
q_{TSS2}	0.002	1.2E-04	0.048	0.001	-0.001	-0.018	0.004	0.006	-0.017	0.312	-0.002	0.001	-3.2E-04
q_{DrTr}	0.003	-3.1E-04	0.009	3.5E-05	6.0E-05	-0.003	-3.1E-05	-1.1E-04	1.6E-04	-0.010	-0.002	5.0E-06	-0.001
q_{B1F1}	0.456	0.707	0.957	1	-0.041	1	0.194	0.095	1	-0.183	0.033	0.007	-0.082
q_{B2F1}	0.118	0.245	1	-0.531	-0.936	0.989	-0.058	-0.090	-0.386	-0.320	0.022	0.042	0.039
q_{B3F1}	0.056	0.319	0.974	-0.456	1	0.986	-0.131	0.010	-0.257	-0.065	0.024	-0.045	0.029
q_{B1E1}	-0.231	0.149	-0.310	0.024	-0.004	0.266	-0.799	-0.646	0.461	1	-0.222	0.004	-0.210
q_{B2E1}	-0.011	0.073	-0.322	-0.014	-0.017	0.269	-0.200	1	-0.056	0.400	-0.319	0.115	-0.034
q_{B3E1}	-0.029	0.028	-0.319	-0.016	0.015	0.281	1	-0.339	-0.527	0.457	-0.297	-0.140	-0.034
q_{B1F2}	-0.044	-0.032	-0.014	0.033	-0.002	0.079	-0.055	-0.056	0.720	0.047	0.258	-0.091	1
q_{B2F2}	-0.005	-0.024	-0.020	-0.014	-0.028	0.073	-0.035	0.100	-0.203	-0.136	1	-0.873	-0.207
q_{B3F2}	-0.003	-0.032	-0.019	-0.013	0.030	0.074	0.091	-0.038	-0.187	0.090	0.898	1	-0.087